Poly(ionic liquid) Block Copolymer Gated Organic Thin-Film Transistors

By

Alexander Peltekoff

A THESIS

SUBMITTED TO THE UNIVERSITY OF OTTAWA

IN PARTIAL FULFILMENT OF THE REQUIREMENTS FOR THE

DOCTORATE OF PHILOSOPHY DEGREE

IN CHEMICAL ENGINEERING

DEPARTMENT OF CHEMICAL AND BIOLOGICAL ENGINEERING

UNIVERSITY OF OTTAWA

Ph.D. in Chemical Engineering (2021) University of Ottawa

Chemical and Biological Engineering Ottawa, Ontario, Canada

TITLE: Poly(ionic liquid) Block Copolymer Gated Organic Thin-Film Transistors

AUTHOR: Alexander Peltekoff

B.A.Sc., Chemical Engineering and Applied Chemistry

University of Toronto (Toronto, Ontario, Canada)

SUPERVISOR: Professor Benoît Lessard

NUMBER OF PAGES: 184

Abstract

Since the discovery of organic semiconductors (OSCs) over four decades ago, the field of organic electronics has broken our misconceptions regarding the possibilities of modern electronics. The synthetic toolkit of organic chemistry enables the creation of a limitless number of unique OSCs that can be specifically tailored and engineered with the specific and desired properties for unique applications. The rapid adoption of modern information systems, "Internet of Things," in which smart devices and sensors ubiquitously collect and exchange data has resulted in a need for low-cost sensors to be deployed everywhere from the monitoring of food supply chains, environmental conditions, to human health. Organic thin-film transistors (OTFTs) are a necessary component to support these technologies. However, their mass adoption will require reduction in cost and improved compatibility with low voltage generating printed batteries or flexible and ultrathin photovoltaics.

This thesis is focused on the development of high performing solid state polymer electrolytes to be employed as the gating medium in OTFTs. The choice of conventional gating materials often leads to a tradeoff between high capacitance, operating speed and material softness. For example liquid electrolyte gating materials have high capacitance but low operating speed and are liquid at room temperature which is unacceptable for many electronics application. Polymer gating materials often have lower capacitance but fast operating conditions and solid at room temperature. In this thesis we establish structure property relationships which aid in the design of novel block copolymer-based gating materials which simultaneously enable the increase in capacitance and switching speed while remaining solid at room temperature. In the first study I established a styrene-based ionic liquid monomer can be using as a controlling monomer in the nitroxide mediated copolymerization of methacrylates. The second study then focuses on the integration of these materials into OTFT devices; the morphology (block vs random copolymers) effect on device performance is assessed. The last study builds on the findings of the previous study and further explores the structural elements of block copolymers on device performance.

The work presented here outlines the development of advanced poly(ionic liquid) based solid electrolyte materials that enables both reduced operating voltages and fast switching. Finally, we establish structure-property relationships that relate the molecular architecture to OTFT device

performance paving the way for the adoption of a new generation of high performing, printable and flexible electronics.

Abstrait

Depuis la découverte des semi-conducteurs organiques (OSC) il y a plus de quatre décennies, le domaine de l'électronique organique continue à évoluer nos idées concernant les possibilités de l'électronique moderne. La boîte à outils synthétique de la chimie organique permet la création d'un nombre illimité d'OSC uniques qui peuvent être spécifiquement adaptés et conçus avec les propriétés spécifiques et souhaitées pour des applications uniques. L'adoption rapide des systèmes d'information modernes, « l'Internet des objets », dans lesquels les appareils intelligents et les capteurs collectent et échangent des données de manière omniprésente a entraîné un besoin de capteurs à peu coûteux à déployer partout, pour exemple la surveillance des chaînes d'approvisionnement alimentaire, les conditions environnementales, et la santé humaine. Les transistors organiques à couche mince (OTFT) sont un composant nécessaire de ces technologies. Cependant, leur adoption nécessitera une réduction des coûts et une meilleure compatibilité avec les batteries imprimées génératrices de basse tension ou les photovoltaïques flexibles et ultrafins.

Cette thèse se concentre sur le développement de polymères électrolytes à état solide de haute performance à utiliser comme milieu de déclenchement dans les OTFT. Le choix des matériaux de déclenchement conventionnels conduit souvent à un compromis entre une capacité élevée, une vitesse de fonctionnement et la douceur du matériau. Par exemple, les matériaux de déclenchement à électrolyte liquide ont une capacité élevée mais une faible vitesse de fonctionnement et sont liquides à température ambiante, ce qui est inacceptable pour de nombreuses applications électroniques. Les matériaux déclenchement de polymère ont souvent une capacité inférieure mais des conditions de fonctionnement rapides et solides à température ambiante. Dans cette thèse, nous établissons des relations de propriétés de structure qui aident à la conception de nouveaux matériaux de déclenchement à base de copolymère séquencé qui permettent simultanément l'augmentation de la capacité et de la vitesse de commutation tout en restant solides à température ambiante. Dans la première étude, j'ai établi qu'un monomère liquide ionique à base de styrène peut être utilisé comme monomère de contrôle dans la copolymérisation de méthacrylates à médiation par le nitroxyde. La seconde étude porte ensuite sur l'intégration de ces matériaux dans des dispositifs OTFT ; l'effet de la morphologie (copolymères séquencés vs aléatoires) sur les performances du dispositif est évalué. La dernière étude s'appuie sur les

conclusions de l'étude précédente et explore davantage les éléments structurels des copolymères séquencés sur les performances du dispositif

Le travail présenté ici décrit le développement de matériaux d'électrolyte solide à base de poly(liquide ionique) avancés qui permettent à la fois des tensions de fonctionnement réduites et une commutation rapide. Enfin, nous établissons des relations structure-propriété qui relient l'architecture moléculaire aux performances des dispositifs OTFT, ouvrant la voie à l'adoption d'une nouvelle génération d'électronique haute performance, imprimable et flexible.

Acknowledgements

I would like to begin by expressing my deepest gratitude to my supervisor, Dr. Benoit Lessard, for his support and guidance throughout my degree. You had always given me the freedom to explore my research interests with a guiding hand. I will always appreciate your mentorship. Thank you for the opportunity and for your tireless work to fund our science. It has been an amazing experience growing the lab with you to where it is today - I have no doubt the group will continue to develop and make grand discoveries under your supervision. Thank you for your trust, guidance, patience and understanding.

I would like to thank Dr. Timothy Bender at the University of Toronto for initially inviting me to work in his laboratory where my research career began. Here, I developed my passion for research. Your research mantra of practicality & scalability was and always will be model for my research endeavors.

Without the help of many other people, my work on this project would not have been possible - I would like to thank all my colleagues in the Lessard Research Group (LRG). Particularly Dr. Owen Melville and Dr. Trevor Grant, for helping to build a positive research atmosphere. It has been a blast bringing the lab from the early days to where it is now. Special thanks to Owen, for coaching me through device fabrication and characterization – the knowledge I learnt was instrumental in further developing our device characterization capabilities after you graduated from the group.

I also thank my father, Peter Peltekoff, your career and accomplishments continue to be a motivational goal I aspire to. I would like to thank my Granddad, Ron Rogers, for his mathematics tutoring during my undergraduate years – undoubtedly, I would not have made it through undergrad without the large amount of time spent solving math problems together.

Finally, I want to address my sincerest thanks to my fiancé, Katie, for her unwavering support throughout my graduate studies. While I'm able to convey my scientific findings in this dissertation, I find that my words cannot do the same in expressing my admiration and appreciation for you. You epitomize the image of a truly dedicated, driven person and you have constantly served as a true inspiration in my career. I look forward to the next chapter of our lives.

List of Peer Reviewed Journal Article Contributions

Author contributions are found preceding each chapter.

Nitroxide Mediated Polymerization of 1-(4-vinylbenzyl)-3-butylimidazolium Ionic Liquid Containing Homopolymers and Methyl Methacrylate Copolymers. Alexander J. Peltekoff, Ian Therrien, Benoît H. Lessard*. *The Canadian Journal of Chemical Engineering,* **2019**, 97 (1), 5-16 (*Chapter 2*)

Unipolar Polymerized Ionic Liquid Copolymers as High-Capacitance Electrolyte Gates for n-Type Transistors. Alexander J. Peltekoff, Victoria E. Hiller, Gregory P. Lopinski, Owen A. Melville, Benoît H. Lessard*. *ACS Applied Polymer Materials,* **2019***,* 1 (11), 3210-3221 (*Chapter 3*)

Ionic Liquid Containing Block Copolymer Dielectrics: Designing for High-Frequency Capacitance, Low-Voltage Operation, and Fast Switching Speeds. Alexander J. Peltekoff, Samantha Brixi, Jukka Niskanen, Benoît H. Lessard*. *JACS Au,* **2021**, 1, 7, 1044-1056. (*Chapter 4*)

For the following publications, the full abstracts, statement of contributions, and links to publications are found in Chapter 6.

Improving thin-film properties of poly (vinyl alcohol) by the addition of low-weight percentages of cellulose nanocrystals. Mathieu N. Tousignant, Nicole A. Rice, Alexander J. Peltekoff, Chithiravel Sundaresan, Chuanwei Miao, Wadood Y. Hamad, Benoît H. Lessard*. *Langmuir,* **2020***,* 36 (13), 3550-3557.

Contact Engineering Using Manganese, Chromium, and Bathocuproine in Group 14 Phthalocyanine Organic Thin-Film Transistors. Owen A. Melville, Trevor M. Grant, Kate Lochhead, Benjamin King, Ryan Ambrose, Nicole A. Rice, Nicholas T. Boileau, Alexander J. Peltekoff, Mathieu N. Tousignant, Ian G. Hill, Benoît H. Lessard*. *ACS Applied Electronic Materials,* **2020**, 2 (5), 1313-1322.

Controlled Synthesis of Poly(pentafluorostyrene-ran-methyl methacrylate) Copolymers by Nitroxide Mediated Polymerization and Their Use as Dielectric Layers in Organic Thin-film Transistors. Alexander J. Peltekoff, MN Tousignant, Victoria E. Hiller, Owen A. Melville, Benoît H Lessard***.*** *Polymers, **2020**,* 12 (6), 1231

1, 2, 3-triazole based poly (ionic liquids) as solid dielectric materials
Jukka Niskanen, Mathieu N. Tousignant, Alexander J. Peltekoff, Benoît H Lessard
Polymer, **2020**, 123144.

Cyanophenoxy-Substituted Silicon Phthalocyanines for Low Threshold Voltage n-Type Organic Thin-Film Transistors. Benjamin King, Andrew J. Daszczynski, Nicole A. Rice, Alexander J. Peltekoff, Nathan J. Yutronkie, Benoît H. Lessard*, Jaclyn L. Brusso*. *ACS Applied Electronic Materials* **2021**, 3, 5, 2212-2223.

Enthalpy of the Complexation in Electrolyte Solutions of Polycations and Polyzwitterions of Different Structures and Topologies. Jukka Niskanen*, Alexander J. Peltekoff, Jean-Richard Bullet, Benoît H. Lessard, Francoise M. Winnik. *Macromolecules* **2021**, 54, 14, 6678-6690.

Contents

List of Figures

Figure captions listed are abbreviated for brevity. Please refer to the actual figures for full descriptions.

List of Tables

Table headings listed are abbreviated for brevity. Please refer to actual tables for full titles.

List of Schemes

List of Abbreviations

BC	Bottom Contact
BG	Bottom Gate
C_i	Capacitance Density
DSC	Differential Scanning Calorimetry
I_{DS}	Source-Drain Current
I_{OFF}	Off Current
I_{ON}	On Current
$I_{ON/OFF}$	On/Off Current Ratio
L	Channel Length
μ_e	Electron Mobility
μ_h	Hole Mobility
OLED	Organic Light-Emitting Diode
OPV	Organic Photovoltaic
OSC	Organic Semiconductor
OTFT	Organic Thin-Film Transistor
PVD	Physical Vapour Deposition
SD	Source-Drain
T_g	Glass Transition Temperature
TC	Top Contact
TG	Top Gate
V_{DS}	Source-Drain Voltage
V_{GS}	Gate Voltage
V_T	Threshold Voltage
W	Channel Width

Chapter 1: Background

1.1 Overview

1.1.1 Organic Electronics

In 1947 scientists at Bell Laboratories created the first transistor, and with this constructed the first solid-state amplifier. This development intensified research on semiconductors, which ultimately led to the metal-oxide-semiconductor field-effect transistor (MOSFET) in 1959.[1] Transistors have since become the fundamental component of all modern electronics. The technologies produced by modern electronics have profoundly impacted humanity, especially concerning how we record, store, analyze, and communicate information globally. Transistors, without debate, hold the title as the most important development of the 20th century.

The development of polymers, or plastics, has similarly made an enormous impact in our world. Stemming from their robust mechanical properties, relatively low manufacturing cost and ease of processing, polymeric materials have superseded conventional time-honoured materials like glass, metals, wood, and ceramics in their prior applications. Traditionally, in the realm of electronics, polymers have been utilized as insulating materials. However, the deep-rooted belief that plastics are solely insulating was put to rest in 1976 by Hideki Shirakawa, Alan MacDiarmid, and Alan J. Heeger with their synthesis of polyacetylene, which exhibited the conductivity near that of metals when doped.[2] The advent of conducting polymers gave rise to the potential of a new class of materials that possess the electrical properties of traditional semiconductors and metals while maintaining the mechanical robustness and ease of processing provided by plastics. This sparked the field of *Organic Electronics,* which encompasses the development and use of organic semiconducting materials as the active material in electronic applications.

Many organic semiconductors can be processed from solutions as inks and dyes, which enables the potential for high-volume and low-cost manufacturing of electrical devices using well-established printing methods, such as flexography, inkjet, gravure, and screen printing.[3,4] This is in contrast to the fabrication of inorganic semiconductors that require high temperatures (T > 2000 °C) to grow the silicon single crystals needed for conventional electronics. Additionally, the

physical and chemical properties of organic semiconductors can be finely tuned and tailored for a specific application by modifying their chemical structure using organic chemistry.[5]

The progress in organic electronics to date has been remarkable; for example, small molecule based organic light-emitting diodes (OLEDs) have been fully commercialized and are ubiquitous in modern television and smartphone displays. They are preferred for their reduced power consumption, increased brightness, flexibility, and ultra-thin screen thickness.[6] Organic photovoltaics (OPVs) have demonstrated efficiencies up to 18.6%[7] approaching those offered by commercial silicon photovoltaics but offer the potential for greatly reduced manufacturing costs. Organic thin-film transistors (OTFTs) have been underrealized; however, they undoubtedly provide the broadest range of potential applications. For example, RFID tags,[8] active display backplanes,[9] and flexible or printed memory devices[10,11] are on the brink of commercialization.

However, it must be emphasized that OTFTs do not offer the same electrical performance as silicon devices. Although OTFT performance has been significantly improved, it is apparent that they will not approach those of their inorganic counterparts used in modern high-end and high-processing power microprocessors. As a consequence, the future of OTFTs lies in niche applications where either low-cost is required or for the exploitation of their unique properties such as flexibility, stretchability, and biocompatibility. These applications include smart packaging,[12] e-skins,[13,14] and chemical & biological sensors.[15–17] The commercial realization of many of these applications requires improvements in solution processing compatibility and power consumption. As these problems are resolved, we will move closer to a smart future.

1.1.2 Scope & Aim of Thesis

This thesis focuses on the development of novel polymer materials for the insulating medium in OTFTs that, in effect, lower device operating voltages without negatively impacting responsiveness while maintaining compatibility with large scale printing methods. The first part of the thesis (Chapter 1) provides the necessary background for understanding the research findings of Chapters 2 – 4 and presents concepts from electrical, materials, and polymer reaction engineering. An overview of OTFTs, characteristic equations, the case for electrolyte-gated transistors, and the need for improvement of electrolyte materials is introduced. Following, electrolyte materials are introduced with a thorough explanation of electrical double layers and

conductivity, along with their retrospective characterization techniques. Finally, a background on the nitroxide mediated polymerization mechanism used to synthesize the polymeric materials in this thesis works is provided. Additionally, selected literature is reviewed alongside the corresponding background as they are introduced.

In the following three chapters, scientific studies and findings are examined. In Chapter 2, the synthetic chemistry to develop imidazolium-based ionic liquid containing polymers by nitroxide mediated polymerization is explored. Multiple synthetic pathways to reach the same final material are studied with an emphasis on polymerization kinetics and the determination of reactivity ratios. The research work following (Chapter 3) outlines the polymer reaction engineering of the optimal polymer synthetic route along with the integration of the final materials into capacitors and OTFTs. In devices, the materials effectively achieve the reduced operating voltages desired but are slow responding.

The final research study (Chapter 4) works to improve the responsiveness of the materials developed in the preceding chapter. A methodical and thorough study is performed with the goals of determining structure-property relationships between the polymer structural elements and ultimate OTFT device performance metrics. A series of design principles are established outlining which specific polymeric structural elements influence a corresponding transistor performance metric along with an in-depth scientific understanding of the structure-relationships proposed.

Chapter 5 provides a brief summary of the research included in Chapters 2 – 4 and proposes future research direction and investigations building off work explored, and findings established in the thesis. Chapter 6 presents abstracts to papers from other studies I have directed and/or contributed to during my time in the *Lessard Research Group* as part of my doctoral studies.

1.2 Organic Thin-Film Transistors

This section contains the technical background information that is relevant to the understanding the significance of the research presented in Chapters 2 – 3.

1.2.1 Organic Semiconductors

Organic semiconductors (OSC) are materials composed of π-bonded carbon atoms, which often feature heteroatoms such as nitrogen, oxygen, and sulphur. They are divided into two classes: small molecules and polymers. Analogous to inorganic semiconductors, they are referenced as behaving like n-type or p-type materials based on their ability to transport negative charge carriers (electrons) or positive charge carriers (holes), respectively. Electron mobility in OSCs tends to be low resulting from inefficient charge injection and more efficient trapping from electrochemical reactions (in the presence of water and oxygen), consequently OSCs tend to perform as p-type in electrical devices. However, the organic electronics field has made remarkable progress in this regard; air stable n-type materials of both small molecule and polymeric types have been developed. Notably, the *Lessard Research Group* developed silicon bispentafluorophenoxy phthalocyanine (F_{10}-SiPc) a small molecule exhibiting electron mobility up to 0.54 cm^2/Vs. Significant progress on polymeric n-type materials has also been achieved, for example poly{[N,N'-bis(2-octyldodecyl)-naphthalene-1,4,5,8-bis(dicarboximide)-2,6-diyl]-alt-5,5'-(2,2'-bithiophene)}, P(NDI2OD-T2) (**Figure 1.1**) has exhibited electron mobility up to 0.85 $cm^2\ V^{-1}\ s^{-1}$.[18] The works included in this thesis utilize P(NDI2OD-T2) n-type polymer semiconductor, selected due to its air stability and due to its high prevalence in the literature to make a better comparison of the device performance achieve herein.

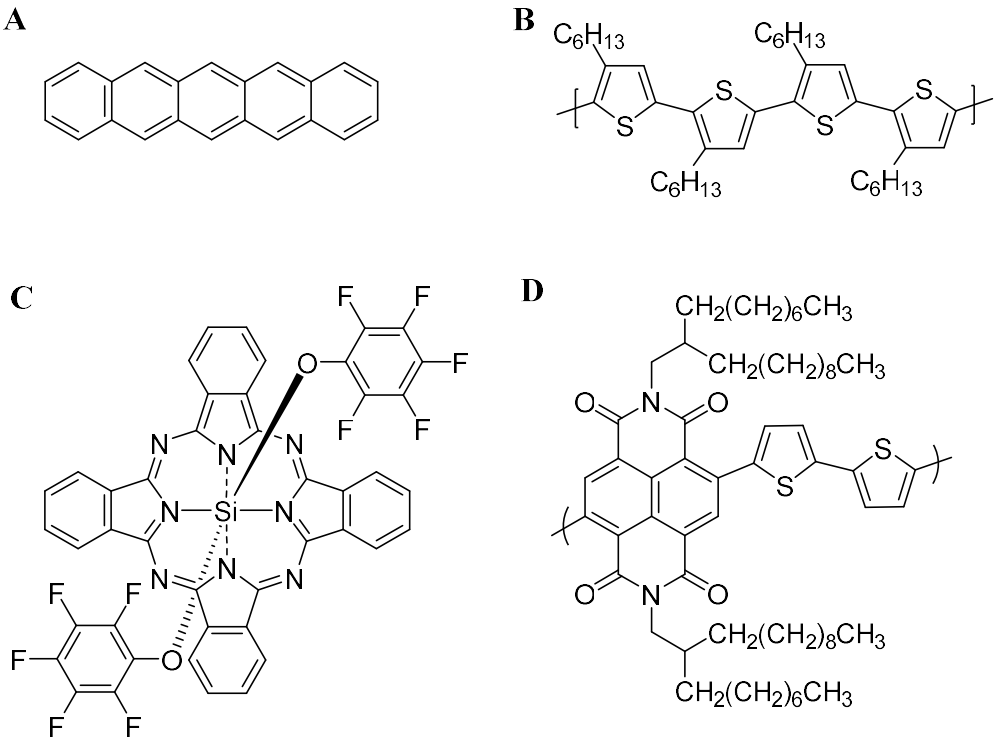

Figure 1.1. Chemical structures of some common organic semiconductors. (a) Pentacene. (b) Regioregular poly(3-hexylthiophene), P3HT. (c) silicon bispentafluorophenoxy phthalocyanine, F_{10}-SiPc. (d) poly{[N,N'-bis(2-octyldodecyl)-naphthalene-1,4,5,8-bis(dicarboximide)-2,6-diyl]-alt-5,5'-(2,2'-bithiophene)}, P(NDI2OD-T2).

Historically organic materials were thought to be exclusively insulating materials until the seminal work by Shirakawa and coworkers[2] in 1977, which showed that polyacetylene exhibited semiconducting electrical properties. Organic semiconducting materials all possess a similar structural feature where electrons are delocalized through a series of carbon atoms joined by alternating single (σ) and double bonds (σ + π bond), which is referred to as π-conjugation. When a carbon atom is involved in the formation of a double bond, it is sp^2 hybridized. The sp^2 orbitals form strongly localized σ-bonds, which governs the molecular structure, and delocalized π-electrons that occupy a single plane perpendicular to the chain of carbon atoms. The π-electron clouds overlap forming π-orbitals that extend along the conjugated chain, and thus the π-electrons are not bound (i.e. delocalized) to a specific atom or bond (**Figure 1.2a**). The π-orbital with the highest energy electrons is referred to as the highest occupied molecular orbital (HOMO). The closest (higher energy) orbital that is unoccupied is likewise referred to as the lowest unoccupied

molecular orbital (LUMO). The bandgap (energy difference between frontier orbitals) decreases with increasing conjugation,[19,20] and therefore it is generally found that the more conjugation, the better the semiconducting properties of the material (**Figure 1.2b**). However, when it comes to integrating these materials into devices, charge transport in the semiconducting films is dictated by more than solely semiconducting energetics, for example, differences in solid-state arrangements can make a drastic difference. Charge transport in devices is also negatively affected by inefficient charge injection from electrodes or charge trapping from impurities in the film.

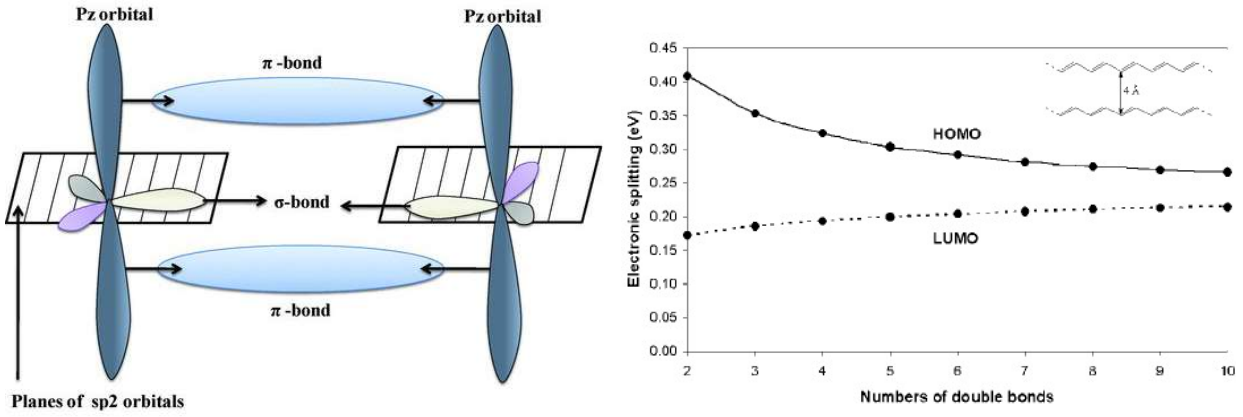

Figure 1.2. a) sp^2 hybridization of two carbon atoms, reproduced from Kumar et al.[21] and b) interchain interactions in organic pi-conjugated materials, reproduced from Cornil et al.[19]

Charge carrier transport in an organic semiconducting polymer is a combination of two mechanisms; along the polymer backbone, facilitated by electron delocalization, or by charge-hopping between adjacent polymer chains facilitated by π-orbital overlap.[22] A polymeric OSC film comprises of both ordered aggregates and amorphous domains. The ordered regions consist of conductive sheets of π-stacked chains. Charge transport in conjugated polymers is much faster along the backbone compared to charge-hopping between adjacent chains and as a result the charge transport within aggregates greatly varies depending on the direction of transport.[23,24] To enable efficient charge transport on the macroscale in the thin-film, neighboring crystallites must be connected by individual tie chains.[25] The presence of these tie chains is governed both by single-chain attributes (rigidity and length), as well as fabrication methods which influences the size, fraction, and distance between ordered regions.[26,27] This leads to a multi-scale charge transport process, where the rate limiting mechanism is differentiated depending on the length scale of

concern. Charge transport along the polymer backbone is limited by intrachain electronic coupling between connected monomeric units whereas charge transport in ordered regions is limited by interchain electronic coupling which requires multiple interchain hopping events. Macroscopic charge transport within the material bulk is limited by the amorphous regions where π-stacking is not present, unless they are connected by tie chains.

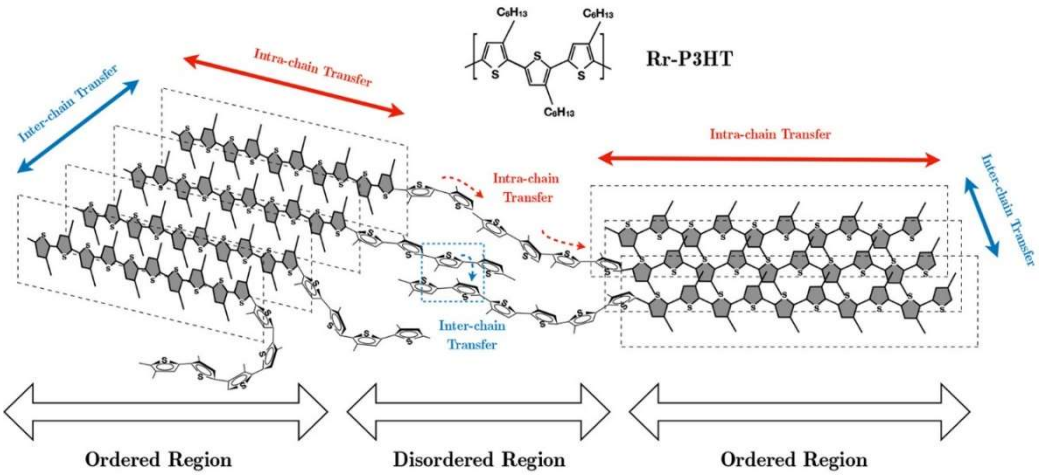

Figure 1.3. Charge transport processes and disorder at different length scales in a two-dimensional sheet of edge-on regioregular P3HT. Figure reproduced from Segatta et al.[28]

Charge transport in small molecule OSCs is more simplistic compared to polymers as charge is exclusively transported via hopping mechanisms. Charge transport by hopping is two to three orders of magnitude slower than intrachain charge transport in conjugated polymers.[29] Consequently, conjugated polymers have the greater potential in high performing organic electronic devices. Additionally, conjugated small molecules typically have poor solubility compared to conjugated polymers, which means devices cannot be fabricated using low-cost solution processing and must be deposited by physical vapour deposition. For these reasons, I believe the future of organic electronic circuitry (OTFTs) will be dependent on polymeric technologies and have directed my research on these materials.

1.2.2 Basic Operation of Organic Thin-Film Transistors

An organic thin-film transistor (OTFT) is a three-electrode solid state device that is comprised of a semiconducting layer that is separated from the gate electrode with a gating insulator. The source and drain electrodes are in direct contact with the semiconductor. The region

area between these electrodes is the channel, which has a length (L) and width (W) given from the distance between the electrodes and their dimensions. A schematic of a thin-film transistor is provided in **Figure 1.4**.

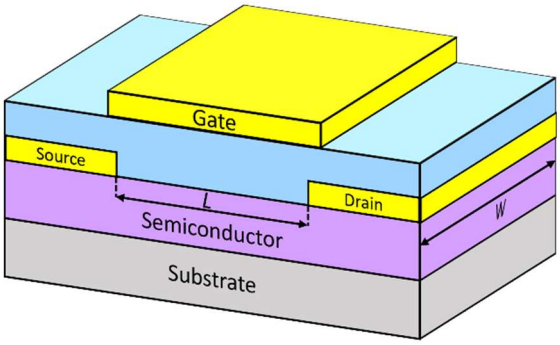

Figure 1.4. Schematic of a thin-film transistor with channel length and width of W and L.

The difference in potential between the gate and source is denoted as V_{GS} and is commonly referred to as the gate voltage. In a similar fashion, the difference in potential between the source and drain is termed the drain-source voltage and denoted at V_{DS}. Furthermore, the three electrode currents, denoted as I_D, I_S, & I_G, are defined as positive if the electron flow directed into the device; by Kirchhoff's law, the sum of all three currents is zero.

The gate-insulator-semiconductor stack is representative of a capacitor. The capacitance per unit area, C_i, of a traditional *dielectric* gate insulator is described by:

$$C_i = \frac{\varepsilon_0 k}{d} \qquad (1.1)$$

where ε_0 and k are the vacuum permittivity and relative permittivity, commonly referred to as the dielectric constant, respectively, and d is the insulator thickness. Charges can be induced at the semiconductor-insulator interface by application of a potential to the gate electrode. Application of a positive gate voltage will induce negative charges (electrons) in the semiconductor, whereas applying a negative voltage will induce positive charges (holes) in the semiconductor. These induced charges are confined to the monolayer next to the semiconductor-insulator interface,[30] increasing the electrical conductivity (of the semiconductor), and as a result, a conductive *channel* between the source and drain electrodes are formed. When a positively charged channel is formed (by induction of holes), it is deemed as p-type, and a negatively charged channel (from induction

of electrons) is deemed n-type. The conductance of this channel is modulated by the gate voltage. Some organic semiconductors will only form p- or n-channels and are termed p-type or n-type in an analogous fashion to their inorganic counterparts, and some are *ambipolar* meaning they can exhibit both types of behaviour.[31]

Nevertheless, before the conductive channel is formed, the gate voltage must exceed a specific voltage termed the *threshold voltage* V_T. The mobile charge per unit area, Q, induced by application of a gate voltage is therefore derived as:

$$Q = C_i(V_{GS} - V_T) \tag{1.2}$$

This equation describes the charge density induced in the channel when the semiconductor is grounded (i.e. $V_{DS} = 0$). However, if the charge is to flow from the source to drain, a V_{DS} potential will need to be applied. The created potential V at a specific point in the semiconductor (x) will linearly increase from a value of 0 at the source ($x = 0$) to V_{DS} at the drain ($x = L$). The charge density is therefore a function of the position in the channel and is described by:

$$Q(x) = C_i\big(V_{GS} - V_T - V(x)\big) \tag{1.3}$$

The basic operation of an OTFT is summarized by applying a gate voltage exceeding V_T, which induces a uniform layer of charge carriers (holes or electrons) in the semiconductor, forming a conductive pathway (**Figure 1.5a**). The application of a V_{DS} will produce a flow of charge carriers through the channel from the source to the drain and in accordance with **Eq. (1.3)** the density of charge carriers will gradually decrease as the drain electrode approaches. If the applied drain voltage is small ($V_{DS} \ll V_{GS} - V_T$) resistance in the channel will be negligible. The transistor output, or drain current I_D, will be proportional to the drain voltage (**Figure 1.5a**), and therefore, the transistor is described to be operating in the *linear regime*.

However, increasing the drain voltage will lead to fewer induced charges, yet the channel resistance will increase. This results in the I_D-V_{DS} slope being reduced and curving downwards. This effect will continue until $V_{DS} = V_{GS} - V_T$ where the charge carrier density at the drain electrode becomes zero (**Figure 1.5b**). This position, where the charge carrier concentration is zero, is referred to as the pinch-off point (P) and is located at the drain electrode.[21] Beyond this condition, further increasing the drain voltage ($V_{DS} > V_{GS} - V_T$) will push the P towards the

source, leading to a depletion region between P and the drain electrode. The current flow in the depletion region is spatially limited, and therefore the number of charge carriers flowing though point P will remain constant even as V_{DS} is further increased. As a result, the drain current remains constant and the transistor is said to be operating in the *saturation regime*.

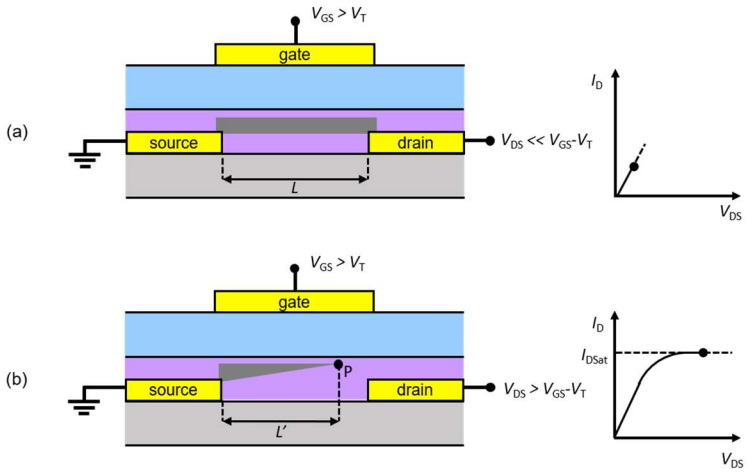

Figure 1.5. Current-voltage characteristics and associated schematic representation of the charge-distribution within the semiconductor channel in TGBC devices: (a) linear regime and (b) saturation regime

Performance Metrics

There are several performance metrics that influence the applicability of an OTFT. Some of these important metrics include the field-effect mobility (μ), V_T, and ON/OFF current ratio (I_{ON}/I_{OFF}). These parameters are influenced by a variety of factors, including device architecture, channel dimensions, material selection for the different layers (electrode, dielectric, contact), grain size of the OSC thin film, and the film morphology of the semiconductor layer. Ideally, a high μ, low V_T, and large I_{ON}/I_{OFF} are desired: The $\mu$is the average carrier drift velocity per unit of electric field. In essence, it indicates how easily charge carriers can move throughout the conductive channels. It is an importance metric used to determine the processing speed of a device. The V_T is the smallest V_{GS} needed to populate the OSC/insulator interface with charge carriers forming a conductive path between the source and drain turning the device on. V_T determines the switching behaviour of a device; hence it needs to remain constant to ensure proper operation of the device and thereby proper functioning circuits. V_T strongly depends on the insulator dielectric constant and thickness, semiconductor doping concentration and thickness, as well as the device channel length. A lower V_T is effective for reducing power consumption and therefore, useful in portable

devices. The greater the I_{ON}/I_{OFF} in accumulation to depletion modes the better the device operates as a switch or logic gate operator. A high *k* dielectric, thin semiconducting layer, and low doping concentration will all contribute to larger I_{ON}/I_{OFF}.[32]

1.2.3 Transistor Equations

The current-voltage characteristics can be analytically calculated for an ideal transistor based on the MOSFET model.[21] However, for the induced charges $Q(x)$ to flow from the source to drain a driving force is needed. An electric field $E(x)$ is therefore applied in the direction of the channel. The measured metric is the drain current I_D and is then described by equation 1.4 as a function of W and μ:

$$I_{DS} = \mu W Q(x) E(x) \tag{1.4}$$

The electric field at position x, is $E(x) = \partial V_x/\partial x$. Substituting in $E(x)$ and $Q(x)$ from Eq (1.2) equation the drain current at x is described by:

$$I_{DS} = \mu W C_i\big(V_{GS} - V_T - V(x)\big)\frac{\partial V_x}{\partial x} \tag{1.5}$$

The drain current is constant along the semiconducting channel of length *L*.[21] Integrating from source to drain ($0 \rightarrow L$) yields:

$$\int_0^L I_{DS} \cdot \partial x = \int_0^{V_{DS}} \mu W C_i\big(V_{GS} - V_T - V(x)\big) \cdot \partial V_x \tag{1.6}$$

$$I_{DS} = \frac{\mu W C_i}{L}\left[(V_{GS} - V_T)V_{DS} - \frac{V_{DS}^2}{2}\right] \tag{1.7}$$

In the linear regime (*lin*), $V_{DS} \ll V_{GS} - V_T$,[21] and we can simplify the equation to:

$$I_{D-lin.} = \frac{\mu W C_i}{L}(V_{GS} - V_T)V_{DS} \tag{1.8}$$

The mobility can be calculated by taking the derivative of (1.8) and isolating for mobility:

$$\mu_{lin.} = \frac{L}{W C_i V_{DS}}\frac{\partial I_{D-lin.}}{\partial V_{GS}} \tag{1.9}$$

In the saturation (*sat*) regime, $V_{DS} = V_{GS} - V_T$, when substituting into Eq. (1.8) yields:

$$I_{D-sat.} = \frac{\mu W C_i}{2L}(V_{GS} - V_T)^2 \quad (1.10)$$

The field effect mobility is then derived from Eq (1.10) to give:

$$\mu_{sat.} = \frac{2L}{WC_I}\left(\frac{\partial\sqrt{I_{D-sat.}}}{\partial V_{GS}}\right)^2 \quad (1.11)$$

1.2.4 Current-Voltage Characteristics

Typical current-voltage characteristics of an ideal OTFT are displayed in **Figure 1.6**. The *output curve* (**Fig. 1.6a**) is obtained by measuring I_D and sweeping V_{DS} at a fixed V_{GS}. The linear regime (low V_{DS}) and the saturation regime (high V_{DS}) are identifiable. Similarly, the transfer curve (**Fig. 1.6b**) is obtained by measuring I_D and sweeping V_{GS} while V_{DS} is held constant. The drain current is typically plotted on a logarithmic scale as the current commonly ranges over several orders of magnitude.

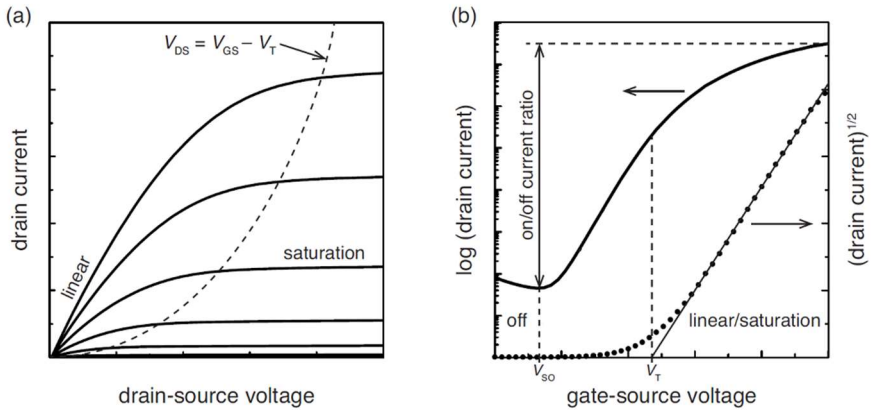

Figure 1.6. Typical current-voltage characteristics of an organic thin-film transistor. (a) Output curve with linear and saturation regime indications. (b) Transfer curve with indications of the different performance metrics; on/off drain current ratio and threshold voltage V_T. Figure reproduced from Herlogsson 2011.[33]

The V_{GS} at which the drain current first starts to increase is called the switch-on voltage (V_{SO}). However, the transistor is not functionally on until it surpasses the V_T. At voltages below V_T the drain current is very small and limited by leakage and charging currents, and the transistor is said to be in the off-state. As shown in **Figure 1.6b**, the V_T is determined by performing a linear fit to the square root of the drain current at saturation and extrapolated to the intersection of the

gate voltage axis. The V_T can be more accurately determined utilizing other methods,[34] however V_T was determined using this method in all works of this thesis.

When the device is in the on-state, above the V_T, the drain current is dependent on the V_{GS} and V_{DS} as described in Eq. (1.8) and (1.10). The field-effect μ in the linear and saturation regimes is extracted from the transfer curve using Eq. (1.9) and (1.11). It is important to perform and analyze the output characteristics first so that the correct equation is utilized when determining μ from the transfer characteristics. The I_{on}/I_{off} is determined from the transfer curve simply by dividing the greatest I_{DS} by the lowest I_{DS} at a set V_{DS}.

1.2.5 Transistor Architecture

Depending on the physical location of each active material within the OTFT there are different possible OTFT architectures, and the four most common are depicted in **Fig. 1.7**. The semiconductor, insulator (gating material), and electrode layers are positioned with respect to the gate electrode which is located on top (top-gate), or at the bottom (bottom-gate). Likewise, the source and drain contacts can be placed on top of the semiconductor (top-contact), or below (bottom-contact). Each individual architecture has some benefits and drawbacks regarding both ease of fabrication and device performance. Worth noting, transistors fabricated with the same materials but differing architectures can exhibit different performance characteristics.

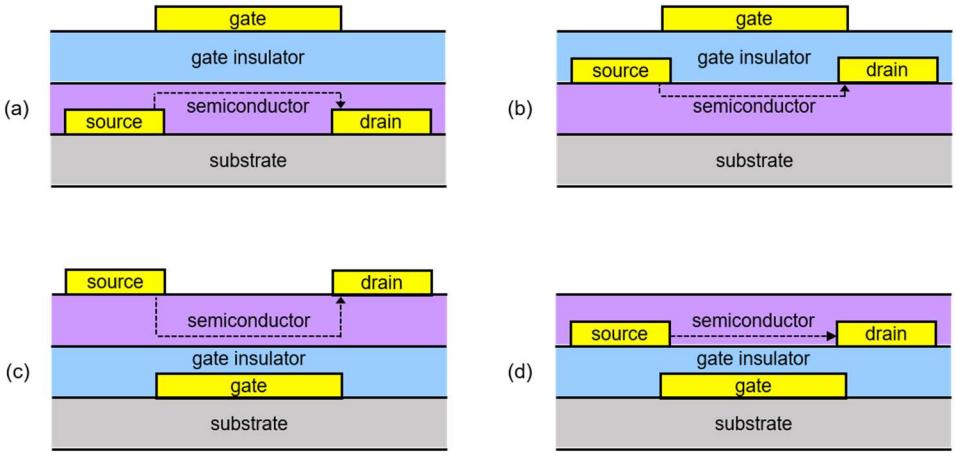

Figure 1.7. Different thin-film transistor architectures: (a) top-gate / top-contact, (b) bottom-gate / top-contact, (c) top-gate / bottom-contact, and (d) bottom-gate / bottom-contact. The dashed line indicates the charge flow in the channel.

Top-contact OTFTs (**Figure 1.7; b & c**) generally exhibit the lowest contact resistance, likely because this architecture provides an increased metal-semiconductor contact area compared to bottom contact configurations. However, in top-contact devices a major contribution to contact resistance is *access resistance*.[35] Access resistance results from the increased distance that charge carriers must travel; after injection from the source electrode at the top of the film, the charge carrier must travel down to the channel, which is at the semiconductor-insulator interface, then back up to the drain electrode. To minimize the effects of *access resistance* in top-contact configurations, the thickness of the organic semiconductor layer should not be excessively large.

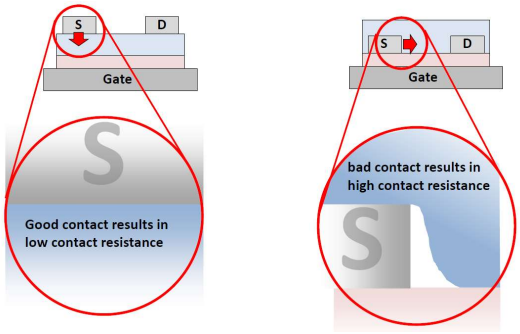

Figure 1.8. Possible source of Contact Resistance in bottom gate top contact (left) and bottom contact (right). Taken from: course notes for Organic electronics (CHG4359 – instructor: Prof. Lessard) Lecture on OTFT operation 03/2019.

With bottom-contact architectures, access resistance is not an issue because the contacts are in the same plane as the channel. However, the film morphology in the contact vicinity is often non-ideal. Bottom-contact devices fabricated by solution methods suffer from poor contact at the semiconductor/contact interface (**Figure 1.8**). In devices utilizing small molecule organic semiconductors (and thus PVD methods) the OSC gain sizes are very small near the contacts, due to heterogeneous nucleation phenomena.[36] For example, pentacene molecules deposited on SiO_2 typically "stand up" with the long axis of the molecule perpendicular to the substrate plane, [37] however, when deposited on gold contacts, strong interaction between the pentacene π-clouds and gold contacts lead to tiny grains at the contacts and, in some instances, voids are present.[37] Semiconductor film growth at the triple interface (contact-semiconductor-insulator) is complex and highly dependent on choice of materials, but it is well accepted that bottom-contact configurations more often than not, exhibit greater contact resistance than top-contact architectures.

When comparing top-gate versus bottom-gate architectures the dielectric /semiconductor interface is of most concern. With solution-processed techniques the gating medium is deposited from solution onto the semiconducting layer or vice versa. If the already deposited layer is soluble in the solvent used for the subsequent layer deposition, dissolution or swelling effects can lead to interfacial mixing and increased interface roughness. This can be prevented by cross-linking the bottom layer; however, this limits the selection of materials and requires extra consideration to circumvent introducing unwanted impurities and trapping groups.[38] A superior approach, is to select orthogonal solvents for the deposition of the multilayer structure.[39] This approach has been demonstrated to produce devices exhibiting μ as high as those fabricated with the same OSC and SiO_2, where interfacial mixing is not a concern. Identifying orthogonal processing conditions for your desired OSC and dielectric is non-trivial. However, organic semiconductors tend to require more harsh solvents compared to polymer dielectrics leading to the preference top-gate architectures when designing all organic-organic solution-processable devices.

1.2.6 Gate Insulator Materials

Charge transport in semiconductor takes place at, or very close to, the semiconductor/insulator interface. Therefore, OTFT performance depends critically on the use of high-performance dielectrics that form active interfaces with low defect densities.[40] Metrics that are thought to be intrinsic to the semiconductor like μ are influenced by interfacial phenomena. For example, it has been shown that high-k gate insulators can induce additional energetic disorder in the channel that promotes charge carrier localization, which results in a reduction of μ.[41] The μs observed in several conjugated polymers is greater when in contact with low-k dielectrics (with $k < 3$) compared to dielectrics with greater k.[42] Likewise, it has been extensively demonstrated that hydroxyl groups at the semiconductor-insulator interface, which are present in both common inorganic and polymeric dielectrics such as SiO_2 and PVP, create electron charge traps that inhibit electron conduction.[43] Therefore, implementing a low-k gating medium that does not contain hydroxyl groups can improve the performance of an OTFT. This has led to extensive research in alternative strategies such as the use of self-assembled monolayers (SAM) or by the insertion of discrete interlayers to lower the relative permittivity of the semiconductor/insulator interface.[44–46]

1.2.7 Low-Voltage Operation

The envisioned light weight and wearable applications for organic electronic-based technologies will require powering by thin-film printed batteries. These voltages provided by these are relatively low (3 to 4 V)[47], and thus OTFTs that can operate at low voltages are a requirement for the commercialization of these technologies.[48] There are two options to increase the OTFT I_{SD}: we can increase μ, by means of semiconductor and interface engineering, and/or increase the gating material capacitance. It can be argued that the field is reaching the limit of μ improvements with values approaching those obtained by single-crystal devices, which is still not satisfactory for commercialization of OTFTs in some applications. Therefore, increasing the capacitance densities of the gating medium is required.

Increasing the capacitance is traditionally done by reducing the thickness (d) of the dielectric insulator,[49] and/or implementing high-k gate insulating mediums,[50,51] as exhibited in Eq. 1.1. The ultrathin dielectric layers required are impractical for large scale fabrication due to the formation of pin holes and uneven film formation. Typically, organic materials have low k,[40] and as a result, inorganic high- k materials are commonly utilized.[52] For example, the use of SiO_2 and AlO_x oxides are common in the field. However, these materials are not solution-processable, and thus, the fabrication costs associated with these devices are higher, limiting the commercialization of organic electronic technologies, which will be required to be low-cost for their envisioned applications. Many polar, high-k polymer dielectrics, such as polyvinylphenol ($k = 4.5$), are hygroscopic and contain undesirable hydroxyl groups.[53]

In response to these limitations, there is a great need for new high-k materials that can be processed by solution methodologies. An alternative to conventional dielectric materials has been the implementation of ionically conducting electrolyte materials as the gating medium. Conceptually, this is not a new proposal, the first demonstration of an organic transistor in 1984 utilized a liquid electrolyte.[54] Furthermore, the same research group demonstrated a solid-state electrolyte in an OTFT a few years later.[55,56] Since then there has been extensive exploration of electrolyte based gating mediums in OTFTs such as ionic liquids,[57–61] ion gels,[62–69] polymer electrolytes,[70,71,80,72–79] polyelectrolytes[81,82], and traditional electrolyte solutions.[83–85] When implementing electrolyte gating mediums, there are other effects that are not of concern with

traditional dielectrics, which affect the mode of operation. Therefore, these transistors are classified as being either electrochemical transistors or field-effect transistors, which is further described in section 1.2.9.

1.2.8 Electrolyte Gate Insulators

Electrolyte gating mediums and conventional dielectrics behave differently in transistors and are schematically compared in **Figure 1.9**, which illustrates the electric field distribution inside each of the two gate insulator materials when a positive V_{GS} is applied. With the dielectric insulator (left), the electrostatic potential linearly decreases across the insulator layer and produces a uniformly constant small electric field throughout the layer. This is in stark contrast to the extremely large electric fields demonstrated at the two interfaces with the electrolyte gating medium.

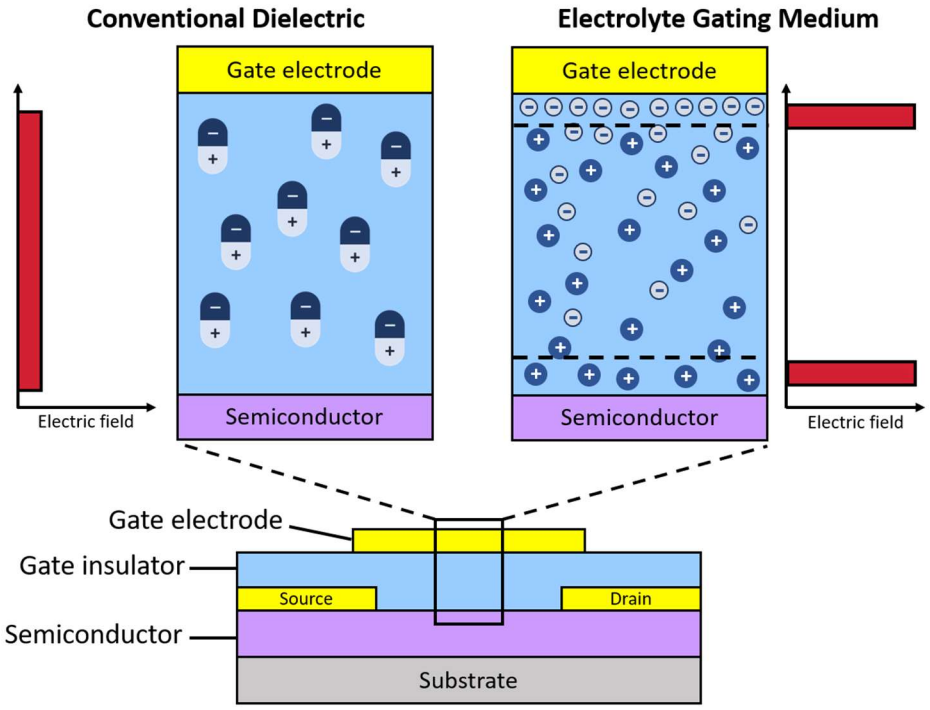

Figure 1.9. Organic thin-film transistor cross section with electric field (E) profiles for conventional dielectric & polyelectrolyte gating mediums when a positive potential is applied. Adapted from Herlogsson 2011.[86]

The large electric fields that are located at the interfaces of the electrolyte are a result of electrical double layers (EDLs), which are more thoroughly discussed in section 1.3.2. To

summarize, upon application of the potential, the ions redistribute to form EDLs at the semiconductor-electrolyte and gate-electrolyte interfaces, with a neutrally charged area in between. This results in a negligible electric field in the bulk medium and very large electric fields at each interface, creating a very large capacitance to induce charge carriers in the transistor at a low voltage. Capacitances up to 1 μF cm^{-2} have been demonstrated resulting in the operation of transistors at low voltages (< 1 V).[87] An additional benefit of EDL based transistors is that the capacitance associated with the EDL formation is independent of the layer thickness,[88] in contrast to traditional dielectrics. This thickness-independence is a significant advantage for the low cost fabrication of transistors by high throughput manufacturing printing processes such as roll-to-roll processing. However, it should be noted that as the electrolyte thickness is increased, the response time for the transistor operation is reduced.[88] Due to the greatly reduced operating voltages and ease of manufacturability enabled by electrolyte gating mediums, make them extremely attractive for printed electronics applications. This thesis focuses on the development of electrolyte-based materials for OTFTs.

1.2.9 Operating Modes in Electrolyte-Gated Transistors

There are two operational mechanisms exhibited in electrolyte-gated transistors: the first, *field-effect*, where the semiconductor is *impermeable* to ions in the electrolyte, and the electrostatic forces induce charges in the semiconductor **(Figure 1.10a**);and the second, *electrochemical doping* where the ions *permeate* the semiconductor (**Figure 1.10b**). The *field-effect* mechanism is the classic mechanism observed for conventional OTFTs while *electrochemical doping* is unique to electrolyte gated systems.

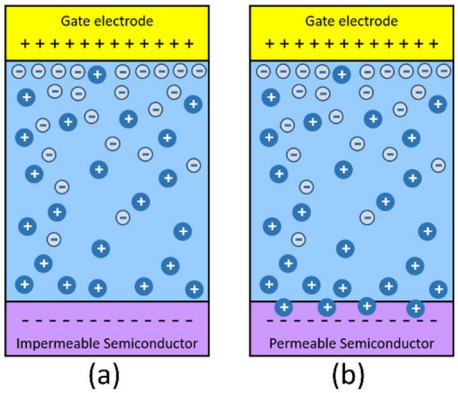

Figure 1.10. Visual representation of an electrolyte-gated organic thin-film transistor operating in (a) field-effect and (b) in the electrochemical mode. Adapted from Lodge, Frisbie, & coworkers.[89]

In electrolyte-gated transistors, upon application of a gate bias, an EDL is still formed at the gate/electrolyte interface, but at the semiconductor/electrolyte interface, ions diffuse into the semiconducting layer, and charge carriers are induced. This phenomenon is well documented in devices employing polymer semiconductors.[65] The electrochemical operation involves the reversible electrochemically doping and de-doping of the semiconductor channel by the application and removal of a gate potential, respectively. With an n-type semiconductor (electron-conducting), cations from the electrolyte penetrate the film and pair with electrons in the semiconductor.

Generally, electrochemical doping is usually undesirable due to the motion of both electronic and ionic charges in the channel leading to challenges in extracting true μ values.[90] However, recent studies have managed to elucidate the decoupling of ionic mobility and μ and have demonstrated an overall reduction in μ compared to corresponding devices operating under *field-effect* (no *electrochemical doping*).[90,91] Furthermore, electrochemical doping is undesired as it induces structural changes in the organic semiconductor film (e.g. swelling), and will likely induce disorder. Additionally, when using an electrolyte gate, the turning on and off of the transistor requires the migration of ions into and out of the semiconductor (in electrochemical doping mode) resulting in sluggish device opperation.[81] Electrochemical doping can be favoured in high current applications due to the doping of the semiconductor channel that can be three-dimensional leading to an enormous increase of the drain current (the channel is thicker).[92,93] However, this thesis focuses on the development of electrolyte gating materials, which will exclusively operate in field-effect mode to provide the benefits electrolyte gates (low-voltage operation, manufacturability) while eliminating the drawbacks of sluggish response times.

1.3 Electrolyte Materials

Electrolytes are defined as substances that contain free ions, making them conductive. These ions are formed by the dissociation of a salt giving rise to its component positive ions (cations) and negative ion (anions). They are described as weak or strong, depending on the extent to which they dissociate. Generally, electrolytes are thought of to be liquids, yet gelled, and even solid forms are common. There are five types of electrolytes: electrolyte solutions, ionic liquids, ion gels, polyelectrolytes, and polymer electrolytes.

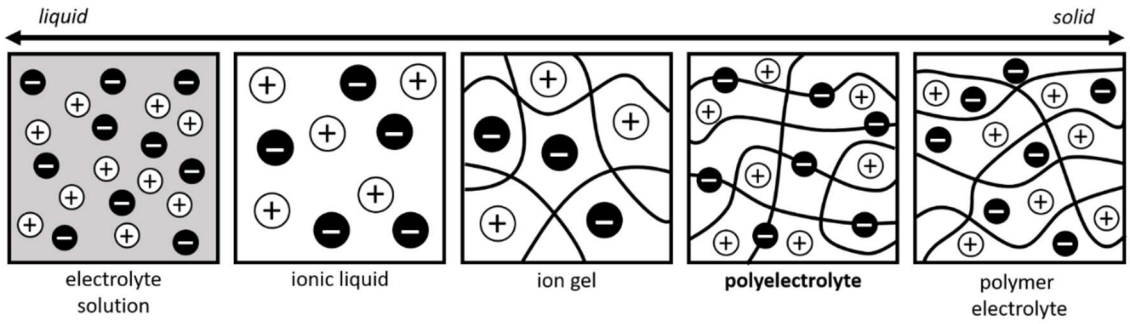

Figure 1.11 Illustrations of several types of electrolytes, ordered from left to right by increasing viscosity. Adapted from Herlogsson 2011.[33]

Electrolyte solutions are the most common type of electrolytes based on a salt that is dissolved in a liquid solvent. When dissolved, the ions are surrounded by solvent molecules, forming a solvation shell around each ion. Electrolyte solutions are commonly used in electrochemical applications, batteries, for instance. Water is usually used as the solvent, however other solvents that are non-aqueous and polar such as alcohols, ammonia, etc., are also utilized.

Ionic liquids are defined as molten salts that are liquid at temperatures under 100 °C. Generally, the ions are relatively large, and at least one of them is organic and possesses a delocalized charge. The chemical and physical properties of ionic liquids can be diverse as there is an extensive selection of anions and cations. Due to their innate liquid state, ionic liquids possess high ionic conductivities (up to 0.1 S cm^{-1})[94], making them attractive electrolytes for electrochemical devices.

Ion gels are simply ionic liquids mixed with a polymer to form a gel. Ionic liquids are not feasible to be used in solid-state devices due to their liquid nature. But, an ionic liquid can be macroscopically immobilized by combining it with a suitable polymer. The resulting material is

an ion gel, which is a polymer network swollen by an ionic liquid. Ion gels utilize only a small amount of polymer (~4 wt%), and thus the ionic conductivity of the resulting gel is often comparable to that of the ionic liquid in its pure state.

Polyelectrolytes and poly(ionic liquids)(PILs) are polymers that possess an electrolyte group in the repeat unit along the polymer backbone. By definition, polyelectrolytes and PILs are the same, differing by the approach they are synthesized: a PIL is obtained via the polymerization of an ionic liquid monomer whereas a polyelectrolyte is achieved via post-polymerization coupling of an ionic group to a polymer chain. The electrolyte groups dissociate when the polymer is in contact with a polar solvent, which results in a charged polymer chain and oppositely charged counterions. A dissociated polyelectrolyte in the solid-state (i.e. a thin film) will consist of charged polymer chains that are essentially immobile due to their large size and mobile counterions. Thus, polyelectrolytes in the solid-state are unique compared to other electrolytes as they only transport ions of one polarity. Polyelectrolytes that have a positively charged backbone (and negatively charged mobile ion) are termed polycations, whereas polyelectrolytes with a negatively charged backbone (and positively charged mobile ion) are termed polyanions.

Polymer electrolytes are like that of electrolyte solutions in the sense that salt is dissolved in a solvent but differ as polymer electrolytes comprise of a salt that is dissolved in a solvating polymer matrix rather than a liquid solvent. The most common polymer electrolytes are typically sodium or lithium salts blended with poly(ethylene oxide) (PEO).

1.3.1 Electric Double Layers

The interface between the electrolyte and a metal contact (or semiconductor in OTFTs) is of utmost importance in electrolyte applications. When there is a difference in potential between the metal electrode (or semiconductor) and bulk electrolyte, the interface will become charged, forming an EDL. The interfacial phenomena and charge distribution of EDLs in solution are well studied and commonly described by the *Goüy-Chapman-Stern* model, where the EDL is modeled by two different layers: the stern layer and the diffuse Guoy-Chapman layer (**Figure 1.12**).[95] The Stern layer consists of ions that are directly absorbed to the surface and are immobilized; in contrast, the Guoy-Chapman layer consists of mobile ions which obey Poisson-Boltzmann statistics. Figure 1.12 shows the physical form of an EDL with a plot of potential with respect to

the distance from the interface. The electrical potential within the EDL declines linearly within the Stern layer then declines exponentially in the diffuse layer.

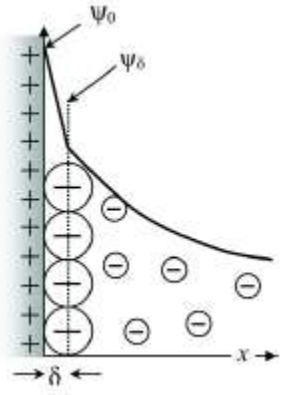

Figure 1.12. Simple version of the Stern layer for a positively charged surface. Reproduced from Surface and Interfacial Forces.[96]

An important quantity with respect to experimental verification is the differential capacitance of the total electric double layer. In the Stern model[97], it is composed of two capacitors in series: the capacity of the Stern layer, C_{St}, and the capacitance of the diffuse Guoy-Chapman layer. The total double-layer capacitance per unit area is given by:[97]

$$\frac{1}{C_{EDL}} = \frac{1}{C_{St}} + \frac{1}{C_{GC}} \tag{1.12}$$

The capacitance of the stern layer is closely approximated by the equation:[96]

$$C_{St} \approx \frac{\varepsilon_{St}\varepsilon_0}{\lambda_D} \tag{1.13}$$

where ε_{St} is the permittivity of the stern layer, ε_0 is the vacuum permittivity constant, and λ_D is the Debeye length. From an examination of the Helmholtz equation, we can see that the electric double layer behaves similar to a plate capacitor, in which the distance between the plates is given by λ_D. If we estimate C_{St} using eqn. 1.13 denoting the radius of ions by R_{ion} the distance is in the order of $R_{ion}/2$. The capacitance per unit area of the Stern layer is $C_{St} = 2\varepsilon_{St}\varepsilon_0/R_{ion}$. For an ionic liquid such as [C_2C_1Im][NTf_2] with $d = 0.38$ nm and $\varepsilon_{St} = 12$.[98] We estimate a capacitance for the Stern layer of $C_{St} = 56\ \mu F cm^{-2}$. For reference a 100 Å thin layer of SiO_2 ($k = 3.9$) will have a capacitance of $0.35\ \mu F cm^{-2}$.

With polyelectrolyte materials, electric double layers are generated at the two polyelectrolyte/metal electrode interfaces as the voltage is applies to the electrodes. In the case of polyelectrolytes only one charge is mobile and migrates towards an electrode, while the polyion will remain fixed. The two established electric double layers are not expected to be identical in terms of electric field strength since the spatial distributions of the mobile ion and oppositely charged polyion are expected to differ at the two interfaces. Consequently, the capacitance associated with each of the two double layers will not be equal. However, since the two double layers are configured in series, they are indistinguishable from each other when characterizing by electrochemical impedance spectroscopy (EIS, Section 1.3.3) and are observed as a single capacitance value:

$$C_{Total} = \frac{1}{C_{DL,ion}} + \frac{1}{C_{DL,polyion}} \quad (1.14)$$

If the capacitances of the two EDLs are not similar ($C_{DL,ion} \neq C_{DL,polyion}$), the total capacitance will be dominated by the EDL associated with the lowest capacitance. It is therefore predicted that in a polyelectrolyte system, the EDL formed by the polyion will be much lower than that of the ideal EDL formed by the mobile ions. This thesis aims to gain insights on the capacitance produced at the polyanion (charged backbone) interface as this is what is actually responsible for driving the transistor as it will be located at the semiconductor/polyelectrolyte interface during device operation.

1.3.2 Electrolyte Characterization by Electrochemical Impedance Spectroscopy (EIS)

Metal-insulator-metal (MIM) capacitors are often used to examine the conductive and capacitive properties of an electrolyte material in isolation (i.e. not incorporated into a transistor). The three ionic processes in the EDL formation process in a MIM capacitor with an electrolyte insulator are illustrated in **Figure 1.13** along with the associated voltage profile and electric field distribution inside the electrolyte layer. When a potential is first applied, there is an alignment of the permanent and induced dipoles in the electrolyte bulk, behaving analogous to conventional dielectric material. A process called dipolar relaxation where the induced charge density on the electrodes is proportional to the *k* of the material.[99] Next, ionic relaxation begins where the ions in the electrolyte bulk are redistributed. The negatively charged anions migrate towards the positive

electrode and the positively charged cations move towards the negative electrode. The electric double layers begin to form at the electrolyte/electrode interfaces and as the electrodes become more charged the potential drops at the interfacial regions and the electric field within the electrolyte bulk is reduced. The final stage is reached when the electric double layers are fully established; the electric field is highly concentrated at the interfaces and neutral within the electrolyte bulk.

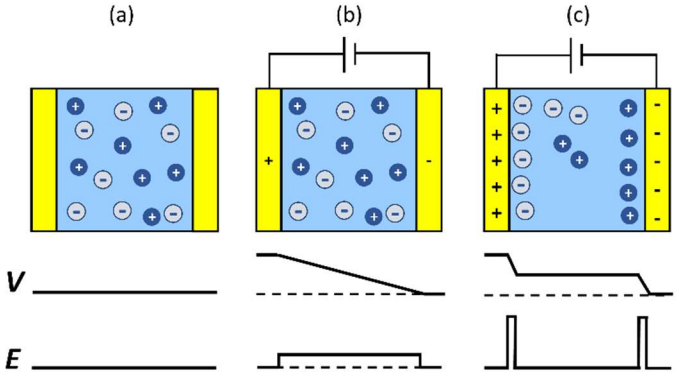

Figure 1.13 Electrolyte charge redistribution process. (a) dipolar relaxation, (b) ionic relaxation, and (c) electric double layer formation.

The electrical characteristics of electrolyte materials in capacitors is analyzed by electrochemical impedance spectroscopy (EIS). An alternating voltage of set frequency is applied, and the amplitude and phase shift of the resulting current is recorded. This is then repeated for a series of frequencies within a desired range. The total impedance (Z) is measured as a function of the frequency (f) of an applied alternating voltage. These measurements are expressed as the total impedance in the complex form:

$$Z(f) = Z_{Re} + j\,Z_{Im} \tag{1.15}$$

where Z_{Re} is the frequency-dependent real part, Z_{Im} is the frequency-dependent imaginary part, and j represent the imaginary number. The real and imaginary impedances are the embodiment of the resistive and capacitive contributions. The phase angle (θ) of the complex impedance is given by:

$$\theta(f) = \tan^{-1}\left(\frac{Z_{Im}}{Z_{Re}}\right) \tag{1.16}$$

The phase angle can therefore be used to describe if the insulating material is behaving capacitive ($\theta < -45°$) or resistive ($\theta > -45°$) at a specific frequency. For example, **Figure 1.14** shows the capacitance and phase angle (θ) as a function of the frequency of a representative capacitor made with a polyelectrolyte. Examining the phase angle (θ), three distinct regions are apparent: the first at high frequencies ($f > 10^3$) where capacitive behaviour with a low capacitance is seen, followed by resistive behaviour at intermediate frequencies ($10^1 < f < 10^3$), and another capacitive region, but with a high capacitance at low frequencies ($f < 10^1$). These three regions are associated with the ionic processes described earlier of dipolar relaxation, ionic relaxation, and EDL formation, respectively.

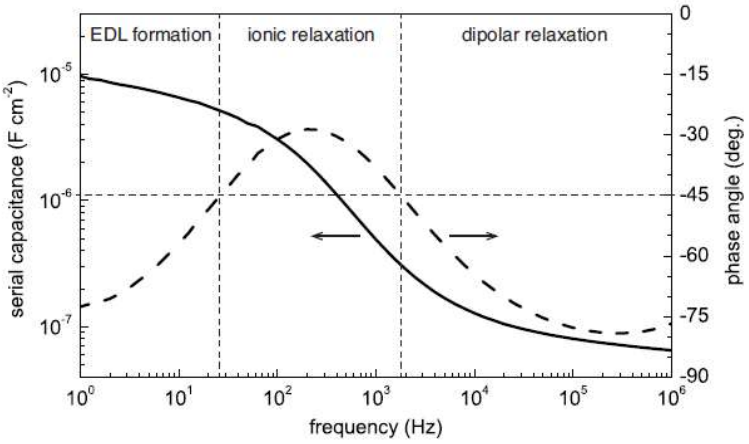

Figure 1.14 Capacitance (solid line) and phase angle (dashed line) versus voltage frequency of the impedance response for a MIM capacitor with polyelectrolyte. Adapted from Herlogsson 2011.[33]

Another format to display and interpret EIS data is in a Nyquist Plot, where the imaginary impedance component (y-axis) is plotted against the real impedance component for each frequency. The same data displayed in **Figure 1.14** is depicted as a Nyquist Plot in **Figure 1.15a**. An advantage of this plot format is that it emphasizes circuit components that are in series. For example, when charging the capacitor both charge transfer (resistive) and formation of EDL (capacitive) processes happen in parallel and hence the very apparent semicircle shape is exhibited. Once the EDLs are fully formed, and only capacitive behavior is present, the data forms a vertical line. Nyquist Plots enable further interpretation of the data by representing it as equivalent circuit models , which in this case the equivalent circuit is a resistor in series with a capacitor (**Figure**

1.14b). The experimental data can be fit to the equivalent circuit models to extract values of interest such as the double layer capacitance, bulk resistance, and ohmic resistance.

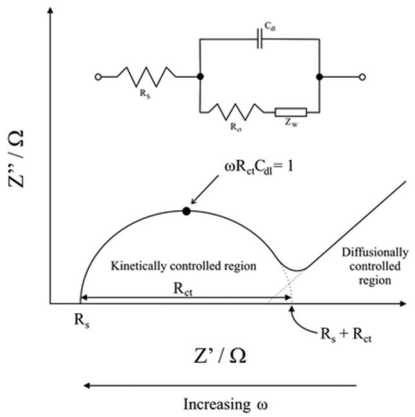

Figure 1.15 Nyquist plot of the impedance response of a MIM capacitor with simplified Randles equivalent circuit. Reproduced from Macdonald et al.[100]

In practice, experimental data does not always fit an ideal model. For example, capacitance dispersion behaviour can take place as a result from adsorption of ions on the electrode and/or roughness of the electrode surface leading to the phase angle to deviate from 90°. This causes the vertical line representing the capacitor to tilt and in order for the model to account for this deviation a constant phase element must replace the ideal capacitor in the circuit. Identifying a circuit model that accurately represents the system being analyzed can be difficult, as is often the case with polyelectrolytes. Commonly, complex circuit modeling is circumvented[101], and the *effective capacitance*[102] is calculated at each frequency using a simpler R(R||C) model from the equation: [102]

$$C = \frac{-1}{2\pi f A Z_{Im}} \qquad (1.17)$$

where f is the frequency, A is the cross-sectional area of the capacitor, and Z_{Im} is the imaginary part of the impedance. Furthermore, with respect to conductivity, as an alternative to an analysis by equivalent circuit models, the Nyquist plots are still useful in identifying key parameters. Since the semicircle stems from the ionic relaxation step, the bulk resistance can be determined from the diameter of the two intersections with the x-axis.

The conductivity can be obtained from the bulk resistance (R_b) using the following equation:

$$\sigma = \frac{l}{AR_b} \tag{1.18}$$

where l is the insulator thickness and A is the cross-sectional area of the electrodes

1.3.3 Conductivity & Ionic Charge Transport of Single-Ion Conducting Polyelectrolytes

When utilizing electrolytes as a gating medium the consideration of the time it takes for the ions in the electrolyte bulk to move to the electrolyte/electrode interface and establish a stable EDL is often the limiting factor for the switching speed of the device.[65] Therefore, to achieve short response times, a highly conductive material is desirable. Often the ionic conductivity of PILs are too low for practical application in OTFTs and thus efforts have been directed towards increasing conductivities by blending PILs, for mechanical integrity, and additional ionic liquid (for increased conductivity). This blending approach has resulted in room temperature ionic conductivities up to 10^{-3} S/cm. However, once IL are incorporated as a mixture, without being covalently bound to the polymer, the desirable unique unipolar nature of the material is lost. A brief review follows outlining conductivity considerations and developments with respect to exclusively *unipolar polymerized ionic liquids*.

The solid-state ionic conductivity of PILs has been shown to depends on several factors such as the chemical nature of the polymer backbone, the counterion, the polymer glass transition temperature (T_g), and environmental conditions (temperature & humidity). The polymerization of an ionic liquid covalently links one of the ions into the polymer backbone, and as a result the conductivity decreases several orders of magnitude relative to their non-polymerized precursors, for example the ionic conductivity decreased from ~10^{-2} to 10^{-6} Scm^{-1} for 1-ethyl-3-vinylimidazolium $TFSI^-$ after polymerization.[103] Generally, because of the ions incorporated in the polymer backbone, the conductivity is greater when the T_g is lower. For example, Elabd and coworkers showed an order of magnitude ionic conductivity increase in methacrylate-based imidazolium IL copolymers by introducing a low T_g hexyl methacrylate comonomer.[104] Along this theme, poly(1-glycidyl-3-butylimidazolium TFSI) sporting a ethylene glycol backbone exhibited ionic conductivity of 10^{-5} S cm^{-1} at 30 °C with a low-T_g of -14 °C.[105] This relation is intuitive in

the sense that a higher polymer chain flexibility better facilitates the ion transport of the materials in an analogous fashion to viscosity and ionic conductivity of ionic liquids. Evidently, the ion dynamics and structural relaxation are strongly correlated above the $T_{g,}$ leading to a significant trade-off between ionic conductivity and mechanical integrity.[106,107] These observations led to some early efforts to optimize mechanical and electrical properties of PILs by use of block copolymers.[108]

Continued efforts in developing materials with high conductivity and high elastic modulus have led to materials that undergo microphase segregation into soft and hard domains.[109–115] The hard domains provide high-elastic modulus, which enables the processing of free-standing films while the soft domains provide a pathway for ion transport. The importance of microphase separation was highlighted by Weber at al.[111], who synthesized a series of microstructured block copolymers of varying compositions and showed a conductivity had non-linear dependence on composition. The role of microphase separation was further exemplified by Choi & Ye who compared similar PIL diblock copolymers differing only in the non-ionic block (poly(styrene) vs poly(methyl methacrylate)) and found the conductivities of poly(styrene)—block-PIL block copolymers with strong microphase separation are 1.5-2 orders of magnitude higher than those of poly(methyl methacrylate)-block-PIL block copolymers with weak microphase separation at comparable PIL compositions.[112,116] These findings suggest that a strong microphase separation resulting from a higher degree of incompatibility between blocks improves ion transport properties.

1.4 Polymer Synthesis

The requirement for high-performance designer materials with complex functionalities is ever-present and evident in the field of organic electronics. Many of the envisioned applications of organic electronics require them to be low-cost, and therefore, the materials need to be compatible with large scale economical fabrication methods like roll to roll printing and they must be relatively inexpensive to synthesize. The success of organic electronics is dependent on the development of advanced functional materials at a cost comparable to commodity materials.

Ideally, blending two or more polymers or the simple addition of other additives (such as plasticizers) to achieve the desired final material properties would be the easiest approach. However, this is unsatisfactory in the advanced electrolyte gating materials for transistors, which require both the incorporation of ionically conductive moieties into the polymer backbone and morphologies tailored to the nanoscale. As mentioned, the addition of an ionic liquid to polymer results in poor performing transistor due to the resulting electrochemical doping of the semiconductor. Furthermore, the necessity of microphase separation to improve solid polymer electrolyte conductivity needed for fast responding transistor devices. In contrast to blending, the combination of various distinct segments comprising different types of polymers in a single chain can be achieved by random copolymerization or synthesizing block copolymers. To be able to obtain these tailored microstructures and advanced functionalities, the ability to control the composition, segment length, and the molecular weight distribution is crucial.

Historically, the best method to synthesize such advanced materials with the precision and microstructure control required was living techniques such as ionic polymerization.[117] However, ionic methods are cost-prohibitive due to the necessary air-free transfers and safety requirements on the industrial scale. Economically produced commodity plastics are synthesized by free-radical polymerization, but this cannot produce tailored architectures and of the narrow dispersity's required for tailored self assembly and micro structuring. Controlled radical polymerization (CRP)[118] is a technique that approaches the control and molecular weight distribution by ionic polymerization, but without the meticulous air-free transfers and excessive purification procedures.[119] The three major variants of CRP are nitroxide-mediated polymerization (NMP),[120]

atom transfer radical polymerization (ATRP),[121] and reversible addition-fragmentation transfer polymerization (RAFT).[122]

1.4.1 Nitroxide Mediated Polymerization

NMP was selected in this thesis because it does not rely on sulphur-based chain transfer agents used in RAFT, nor does it require the metallic ligands as the case with ATRP, all of which can contaminate the polymers in determinantal ways in sensitive electronic devices.[123,124] NMP, when compared to alternative CRP techniques, is conceptually the simplest.

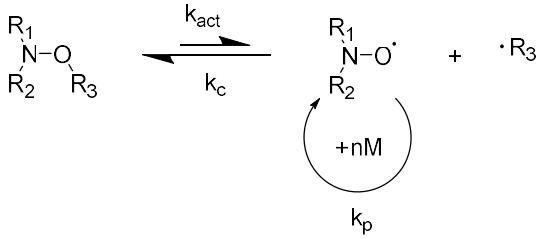

Figure 1.16. Simplified kinetic scheme for nitroxide mediated polymerization (NMP)

The polymerization of the propagating free radical is reversibly terminated with a stable nitroxide free radical. An equilibrium is then established between the propagating chains and stable free radical between its dormant state (reversibly terminates) and its active state where initiation of a monomer and chain propagation can take place(**Figure 1.16**). Irreversible termination is suppressed and the polymerization is considered controlled when the equilibrium favours the dormant state. A controlled polymerization has a low instantaneous concentration of radical-containing active chains which suppresses the irreversible chain-breaking events.[120] While termination reactions and transfer reactions are still present, they are minimized from the deactivation caused by the stability of the propagating chains capped by the stable free radical.

Traditionally NMP could only effectively control the polymerization of styrenics due to the high required polymerization temperatures. With the development of second and third generation stable free radicals NMP has been expanded to acrylates[125,126], acrylamides[127,128] and even methacrylates[129,130]. The incorporation of methacrylates, for example is of great interest due to the absence of "backbiting" reactions leading to linear chains unlike in the polymerization of acrylates.

1.4.2 Features of Controlled / "Living" Radical Polymerizations

The term *Living polymerization* was first defined by Szwarc as a chain growth process without chain breaking reactions (transfer and termination).[131] Such a polymerization enables end-group control and thus facilitates the synthesis of block copolymers by the subsequent reaction with a different batch of monomer. However, this definition does not include a requirement for molecular weight control and narrow molecular weight distributions (dispersity). To achieve these goals; the initiator needs to be reacted immediately at the initial stages of polymerization to allow for the simultaneous growth of all the polymer chains. Secondly, the exchange between species of different reactivities must be fast in comparison to the rate of propagation to ensure that all active propagating chain termini are equally susceptible to reacting with monomer promoting uniform chain growth.[132–134] A polymerization can still be defined as controlled if side reactions are present, so long as they do not significantly impact control over the molecular structure of the dispersity of polymer chains.

In a controlled polymerization the degree of polymerization and resulting number average molecular weight can therefore be predicted based on the ratio of monomer to initiator and will provide a final polymer with dispersities close to Poisson distribution. Therefore, a well-controlled polymerization will display:

(1) First-order Kinetic Behaviour

Due to the negligible contribution of non-reversible termination the concentration of actively propagating species ($[P\bullet]$) remains constant throughout the reaction. The constant $[P\bullet]$ is established by balance activation and deactivation rates, not by balancing initiation and termination rates as is the case with conventional free-radical polymerization. As a result, the rate of polymerization (R_P) with respect to the natural log of monomer concentration ($[M]$) is a liner function of time described as:

$$R_P = \frac{-d[M]}{dt} = k_p[P\bullet][M] \tag{1.19}$$

$$\ln\frac{[M]_0}{[M]} = k_p[P\bullet]t = k_p^{app}t \ (if\ [P\bullet]\ is\ contant) \tag{1.20}$$

where k_p is the propagating rate constant and k_p^{app} is the apparent rate constant. Therefore, semilogarithmic kinetic plots exhibit linear behaviour that is very sensitive to any changes in the concentration of actively propagating species. An acceleration in R_P caused by an increase in $[P\bullet]$ is exhibited as an upward curvature on the plot which indicates slow initiation whereas a deacceleration in R_P is shown as a downward curvature from a decrease in $[P\bullet]$ as a result of termination reactions increasing the persistent radical. However, these semi-logarithmic plots are not sensitive to chain transfer processes as they do not affect the number of actively propagating species.

(2) Predictable Degree of Polymerization

The degree of polymerization (DP_n), a proxy for the number average molecular weight ($\overline{M_n}$), will linearly evolve with monomer conversion:

$$DP_n = \frac{\Delta[M]}{[I]_0} = \frac{[M]_0}{[I]_0} \times (conversion) \qquad (1.21)$$

This relationship is a result from maintaining a constant number of chains throughout the polymerization caused by immediate initiation and absence of chain transfer events which increase the total number of chains. When $\overline{M_n}$ is smaller than expected, this indicates the amount of chain transfer events is significant; when $\overline{M_n}$is greater than expected there is inefficient initiation or significant termination by chain combination. Other termination mechanisms are less apparent as they do not change the total number of chains present.

(3) Narrow Molecular Weight Distribution

Polymer dispersity (Đ) is narrow due to the immediate initiation, equilibrium favouring reversibly terminated chains, and negligible chain transfer or termination. Đ will closely follow a Poisson distribution:[135]

$$Đ = \frac{M_w}{M_n} = \frac{X_w}{X_n} = 1 + \frac{X_n}{(X_n + 1)^2} \approx 1 + \frac{1}{X_n} \qquad (1.22)$$

Dispersity's should decrease with conversion when slow initiation is present, whereas dispersity's will increase with conversion when the contribution of chain break reactions becomes significant.

(4) Pseudo-Livingness of Polymer Chain with Preserved End Functionalities

Due to negligible irreversible chain transfer and termination, all polymer chains will retain their active centers after the monomer is fully consumed or the reaction is quenched. The resulting polymers are reversibly terminated by the stable free radical and therefore can be isolated, purified and used as a macroinitiator for the polymerization of a new batch of monomer. When the pseudo-livingness of the majority of the chains is preserved the macroinitiator can effectively produce block copolymers via sequential monomer addition.

1.4.3 NHS-Functionalized Initiator

Throughout the development of NMP, various nitroxide based initiators have been developed. Vinas et al. functionalized N-(2-methylpropyl)-N-(1-(diethylphosphono-2,2-dimethylpropyl)-O-(2-carboxylprop-2-yl)hydroxylamine) (commercially known as BlocBuilder-MA™, MAMA-SG1) unimolecular initiators by reacting the carboxylic acid group with a succinimidyl ester group(NHS-BB, **Figure 1.17**).[136]

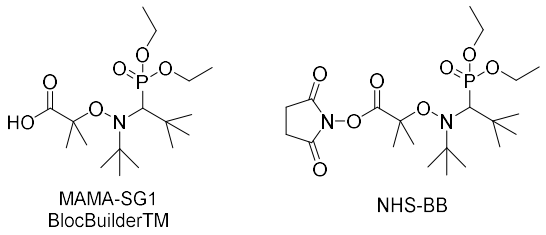

Figure 1.17. Initiators used in NMP: MAMA-SG1 (left), NHS-BB (right)

NHS-BB offers several advantages over MAMA-SG1, such as reducing the need for additional SG1 (*N*-*tert*-butyl-*N*-(1-diethyl phosphono-2,2-dimethyl-propyl) nitroxide) nitroxide while synthesizing methacrylate rich copolymers.[137] The dissociation constant of NHS-BB is 15 times greater than that of MAMA-SG1.[138] This means that NHS-BB will provide a greater amount of free SG1 nitroxide, which helps prevent the irreversible termination of methacrylates. Typically, when using MAMA-SG1 in the copolymerization of methacrylates, a 10% excess of SG1 is needed to achieve a controlled polymerization.[139]

BB-NHS can also be used as a post-functionalization approach or pre-functionalization approach to combining polymers, synthesized by NMP, with primary amine-functionalized inorganic molecules or other polymers resulting in more complex microstructures.[136] It has been demonstrated that NH_2-functionalized poly(propylene oxide) and NHS-BB to synthesize a poly(propylene oxide)-SG1 macroalkoxyamine, which was used as a macroinitiator for the NMP of styrene to obtain a poly(styrene)-b-poly(propylene oxide) block copolymer.[136] The performance of "grafting-to" and "grafting-from" reactions onto primary amine-functionalized silica particles using NHS-BB has also been demonstrated.[140]

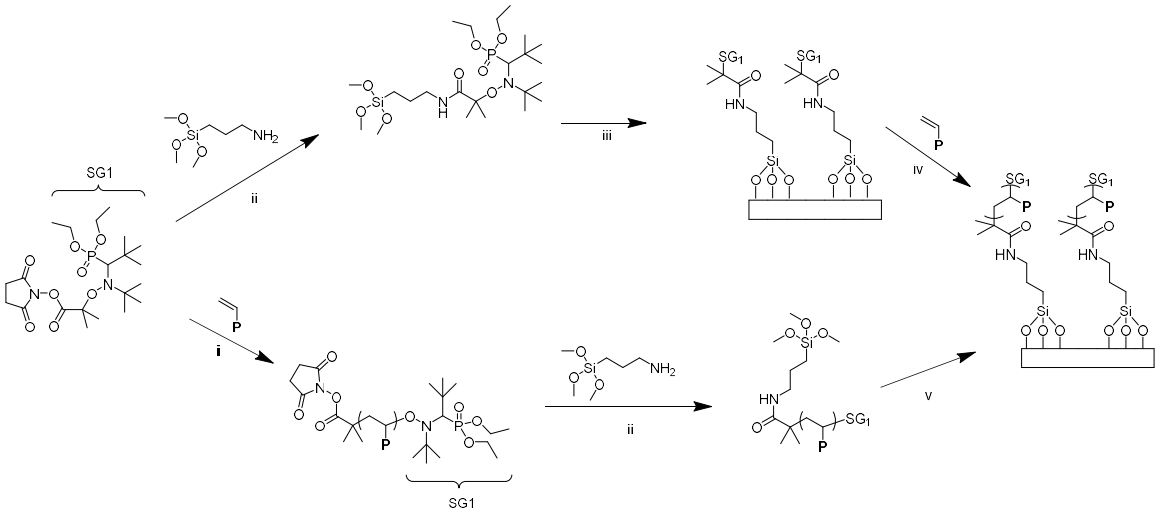

Figure 1.18. Grafting -to (bottom) and -from (top)

Although none of the specific works included in this thesis utilized grafting-to or grafting-from approaches, I synthesized several materials for other members of the *Lessard Research Group* with NHS-functionalities to implement these techniques in their device fabrication. The study *Cyanophenoxy-Substituted Silicon Phthalocyanines for Low Threshold Voltage n-Type Organic Thin-Film Transistors* by Benjamin King is one example of this, and the Abstract can be read in section 6.5 in the Additional Contributions chapter.

In the works presented in this thesis, NHS-BB was utilized only in the first study to enhance control over the polymerizations. In Chapter 3 and 4 we continued with MAMA-SG1 as we found that performing polymerizations with excess SG1 was more effective at producing pseudo-living materials with narrow dispersities.

1.5 Preface

Organic thin-film transistor-based technologies are starting to achieve acceptable performance for some commercial applications. However, there are still many gaps between academic laboratory scale device fabrication and industrial processes that must be addressed to bring these technologies to market. Notably, the reduction of operating voltage requires dielectric layer thickness to be reduced so greatly they teeter on the edge of being too thin resulting in short-circuits with high leakage current (failed devices). For the use low cost/ high throughput printing techniques obtaining ultra-thin and uniform thicknesses is a challenge. The aim of this thesis is to alleviate manufacturing concerns by molecular design, all while maintaining a level of scalability on the chemical synthesis.

Electrolyte gated transistors offer the potential to solve many of these concerns; they offer reduced operating voltages due to their high double-layer capacitances and the EDL is thickness independent, which means larger printing tolerances in the layer thickness. However, they have the downfall of electrochemical doping which eliminates the desired field-effect mechanism. Unipolar polymer electrolytes have been shown to prevent electrochemical doping, however, increased switching speeds are desired. Polyelectrolytes with greater conductivity need to be developed to increase operational frequency. Additionally, to further reduce operating voltage a greater understanding of the role polymer architecture on the polyelectrolyte/semiconductor EDL interface and ultimately OTFT performance is required. Ultimately, relationships between polymer structure and material properties (conductivity & capacitance) needs to be improved and further tying these material properties to device performance metrics (operating frequency and voltage) will help aid in optimizing OTFTs for mass production.

In my opinion, commercialization of OTFTs will require both robust fabrication and (relatively) inexpensive compounds. Advanced polymeric materials, such as the ones described, can be synthetically challenging to synthesize on large scale. Controlled free-radical polymerization techniques such as NMP have the potential to be used as a tool in the synthesis of advanced materials while maintaining scalability. The viability and development of synthetic processes using NMP to produce functional materials will be explored.

The works in this thesis aims to:(i) establish a scalable synthetic pathway of advanced polyelectrolyte materials using NMP (Chapter 2), (ii) determine a relationship between polymer structure and corresponding material capacitance & conductivity (Chapter 3 and 4), (iii) develop new fabrication methodologies (new to the Lessard Group) and integrate materials into capacitors and transistors (Chapter 3 and 4). Overall this thesis represent novel elements in polymer chemistry, thin film engineering and applied electrical engineering.

References

(1) Ayres, R. U. *The History and Future of Technology*; Springer International Publishing: Cham, 2021.

(2) Shirakawa, H.; Louis, E. J.; MacDiarmid, A. G.; Chiang, C. K.; Heeger, A. J. Synthesis of Electrically Conducting Organic Polymers: Halogen Derivatives of Polyacetylene, (CH)X. *J. Chem. Soc. Chem. Commun.* **1977**, No. 16, 578–580.

(3) Arias, A. C.; MacKenzie, J. D.; McCulloch, I.; Rivnay, J.; Salleo, A. Materials and Applications for Large Area Electronics: Solution-Based Approaches. *Chem. Rev.* **2010**, *110* (1), 3–24.

(4) Tobjörk, D.; Österbacka, R. Paper Electronics. *Adv. Mater.* **2011**, *23* (17), 1935–1961.

(5) Anthony, J. E.; Facchetti, A.; Heeney, M.; Marder, S. R.; Zhan, X. N-Type Organic Semiconductors in Organic Electronics. *Adv. Mater.* **2010**, *22* (34), 3876–3892.

(6) Chen, H. W.; Lee, J. H.; Lin, B. Y.; Chen, S.; Wu, S. T. Liquid Crystal Display and Organic Light-Emitting Diode Display: Present Status and Future Perspectives. *Light Sci. Appl.* **2018**, *7* (3), 17168.

(7) Salim, M. B.; Nekovei, R.; Jeyakumar, R. Organic Tandem Solar Cells with 18.6% Efficiency. *Sol. Energy* **2020**, *198* (October 2019), 160–166.

(8) Battiato, P.; Abdinia, S.; Jacobs, S.; Chartier, I.; Coppard, R.; Klink, G.; Cantatore, E.; Member, S.; Ragonese, E.; Member, S.; Palmisano, G.; Member, S. An Integrated 13 . 56-MHz RFID Tag in a Printed Organic Complementary TFT Technology On. **2015**, *62* (6), 1668–1677.

(9) Gelinck, G.; Heremans, P.; Nomoto, K.; Anthopoulos, T. D. Organic Transistors in Optical Displays and Microelectronic Applications. *Adv. Mater.* **2010**, *22* (34), 3778–3798.

(10) Kim, S. J.; Lee, J. S. Flexible Organic Transistor Memory Devices. *Nano Lett.* **2010**, *10* (8), 2884–2890.

(11) Leong, W. L.; Mathews, N.; Tan, B.; Vaidyanathan, S.; Dötz, F.; Mhaisalkar, S. Towards

Printable Organic Thin Film Transistor Based Flash Memory Devices. *J. Mater. Chem.* **2011**, *21* (14), 5203–5214.

(12) Grau, G.; Kitsomboonloha, R.; Swisher, S. L.; Kang, H.; Subramanian, V. Printed Transistors on Paper: Towards Smart Consumer Product Packaging. *Adv. Funct. Mater.* **2014**, *24* (32), 5067–5074.

(13) Sokolov, A. N.; Tee, B. C. K.; Bettinger, C. J.; Tok, J. B. H.; Bao, Z. Chemical and Engineering Approaches to Enable Organic Field-Effect Transistors for Electronic Skin Applications. *Acc. Chem. Res.* **2012**, *45* (3), 361–371.

(14) Wu, X.; Ma, Y.; Zhang, G.; Chu, Y.; Du, J.; Zhang, Y.; Li, Z.; Duan, Y.; Fan, Z.; Huang, J. Thermally Stable, Biocompatible, and Flexible Organic Field Effect Transistors and Their Application in Temperature Sensing Arrays for Artificial Skin. *Adv. Funct. Mater.* **2015**, *25* (14), 2138–2146.

(15) Tiwari, S.; Singh, A. K.; Joshi, L.; Chakrabarti, P.; Takashima, W.; Kaneto, K.; Prakash, R. Poly-3-Hexylthiophene Based Organic Field-Effect Transistor: Detection of Low Concentration of Ammonia. *Sensors Actuators, B Chem.* **2012**, *171–172*, 962–968.

(16) Khan, H. U.; Roberts, M. E.; Johnson, O.; Förch, R.; Knoll, W.; Bao, Z. In Situ, Label-Free DNA Detection Using Organic Transistor Sensors. *Adv. Mater.* **2010**, *22* (40), 4452–4456.

(17) White, S. P.; Dorfman, K. D.; Frisbie, C. D. Label-Free DNA Sensing Platform with Low-Voltage Electrolyte-Gated Transistors. *Anal. Chem.* **2015**, *87* (3), 1861–1866.

(18) Yan, H.; Chen, Z.; Zheng, Y.; Newman, C.; Quinn, J. R.; Dötz, F.; Kastler, M.; Facchetti, A. A High-Mobility Electron-Transporting Polymer for Printed Transistors. *Nature* **2009**, *457* (7230), 679–686.

(19) Cornil, J.; Beljonne, D.; Calbert, J. P.; Brédas, J. L. Interchain Interactions in Organic π-Conjugated Materials: Impact on Electronic Structure, Optical Response, and Charge Transport. *Adv. Mater.* **2001**, *13* (14), 1053–1067.

(20) Brédas, J. L.; Calbert, J. P.; Da Silva Filho, D. A.; Cornil, J. Organic Semiconductors: A Theoretical Characterization of the Basic Parameters Governing Charge Transport. *Proc.*

Natl. Acad. Sci. U. S. A. **2002**, *99* (9), 5804–5809.

(21) Kumar, B.; Kaushik, B. K.; Negi, Y. S. Organic Thin Film Transistors: Structures, Models, Materials, Fabrication, and Applications: A Review. *Polym. Rev.* **2014**, *54* (1), 33–111.

(22) Bronstein, H.; Nielsen, C. B.; Schroeder, B. C.; McCulloch, I. The Role of Chemical Design in the Performance of Organic Semiconductors. *Nat. Rev. Chem.* **2020**, *4* (2), 66–77.

(23) Sirringhaus, H.; Brown, P. J.; Friend, R. H.; Nielsen, M. M.; Bechgaard, K.; Langeveld-Voss, B. M. W.; Spiering, A. J. H.; Janssen, R. A. J.; Meijer, E. W.; Herwig, P.; de Leeuw, D. M. Two-Dimensional Charge Transport in Self-Organized, High-Mobility Conjugated Polymers. *Nature* **1999**, *401* (6754), 685–688.

(24) Salleo, A. Charge Transport in Polymeric Transistors. *Mater. Today* **2007**, *10* (3), 38–45.

(25) Ding, Z.; Liu, D.; Zhao, K.; Han, Y. Optimizing Morphology to Trade off Charge Transport and Mechanical Properties of Stretchable Conjugated Polymer Films. *Macromolecules* **2021**, *54* (9), 3907–3926.

(26) Gu, K.; Snyder, C. R.; Onorato, J.; Luscombe, C. K.; Bosse, A. W.; Loo, Y. L. Assessing the Huang-Brown Description of Tie Chains for Charge Transport in Conjugated Polymers. *ACS Macro Lett.* **2018**, *7* (11), 1333–1338.

(27) Duong, D. T.; Ho, V.; Shang, Z.; Mollinger, S.; Mannsfeld, S. C. B.; Dacuña, J.; Toney, M. F.; Segalman, R.; Salleo, A. Mechanism of Crystallization and Implications for Charge Transport in Poly(3-Ethylhexylthiophene) Thin Films. *Adv. Funct. Mater.* **2014**, *24* (28), 4515–4521.

(28) Segatta, F.; Lattanzi, G.; Faccioli, P. Predicting Charge Mobility of Organic Semiconductors with Complex Morphology. *Macromolecules* **2018**, *51* (21), 9060–9068.

(29) Gu, K.; Loo, Y. L. The Polymer Physics of Multiscale Charge Transport in Conjugated Systems. *J. Polym. Sci. Part B Polym. Phys.* **2019**, *57* (23), 1559–1571.

(30) Horowitz, G. Tunnel Current in Organic Field-Effect Transistors. *Synth. Met.* **2003**, *138* (1–2), 101–105.

(31) Zaumseil, J.; Sirringhaus, H. Electron and Ambipolar Transport in Organic Field-Effect Transistors. *Chem. Rev.* **2007**, *107*, 1296–1323.

(32) Sirringhaus, H.; Friend, R. H.; Li, X. C.; Moratti, S. C.; Holmes, A. B.; Feeder, N. Bis(Dithienothiophene) Organic Field-Effect Transistors with a High ON/OFF Ratio. *Appl. Phys. Lett.* **1997**, *71* (26), 3871–3873.

(33) Herlogsson, L. Electrolyte-Gated Organic Thin-Film Transistors, 2011.

(34) Boudinet, D.; Le Blevennec, G.; Serbutoviez, C.; Verilhac, J. M.; Yan, H.; Horowitz, G. Contact Resistance and Threshold Voltage Extraction in n -Channel Organic Thin Film Transistors on Plastic Substrates. *J. Appl. Phys.* **2009**, *105* (8).

(35) Braga, D.; Horowitz, G. High-Performance Organic Field-Effect Transistors. *Adv. Mater.* **2009**, *21* (14–15), 1473–1486.

(36) Kymissis, I.; Dimitrakopoulos, C. D.; Purushothaman, S. High-Performance Bottom Electrode Organic Thin-Film Transistors. *IEEE Trans. Electron Devices* **2001**, *48* (6), 1060–1064.

(37) Dimitrakopoulos, C. D.; Brown, A. R.; Pomp, A. Molecular Beam Deposited Thin Films of Pentacene for Organic Field Effect Transistor Applications. *J. Appl. Phys.* **1996**, *80* (4), 2501–2508.

(38) Drury, C. J.; Mutsaers, C. M. J.; Hart, C. M.; Matters, M.; de Leeuw, D. M. Low-Cost All-Polymer Integrated Circuits. *Appl. Phys. Lett.* **1998**, *73* (1), 108–110.

(39) Sirringhaus, H.; Kawase, T.; Friend, R. H.; Shimoda, T.; Inbasekaran, M.; Wu, W.; Woo, E. P. High-Resolution Inkjet Printing of All-Polymer Transistor Circuits. *Science (80-.).* **2000**, *290* (5499), 2123–2126.

(40) Facchetti, A.; Yoon, M. H.; Marks, T. J. Gate Dielectrics for Organic Field-Effect Transistors: New Opportunities for Organic Electronics. *Adv. Mater.* **2005**, *17* (14), 1705–1725.

(41) Veres, J.; Ogier, S. D.; Leeming, S. W.; Cupertino, D. C.; Khaffaf, S. M. Low-k Insulators

as the Choice of Dielectrics in Organic Field-Effect Transistors. *Adv. Funct. Mater.* **2003**, *13* (3), 199–204.

(42) Veres, J.; Ogier, S.; Lloyd, G.; De Leeuw, D. Gate Insulators in Organic Field-Effect Transistors. *Chem. Mater.* **2004**, *16* (23), 4543–4555.

(43) Chua, L.; Zaumseil, J.; Chang, J.; Ou, E. C. General Observation of N-Type Field-Effect Behaviour in Organic Semiconductors. *Nature* **2005**, *434* (March), 194–199.

(44) Ma, H.; Yip, H. L.; Huang, F.; Jen, A. K. Y. Interface Engineering for Organic Electronics. *Adv. Funct. Mater.* **2010**, *20* (9), 1371–1388.

(45) DiBenedetto, S. A.; Facchetti, A.; Ratner, M. A.; Marks, T. J. Molecular Self-Assembled Monolayers and Multilayers for Organic and Unconventional Inorganic Thin-Film Transistor Applications. *Adv. Mater.* **2009**, *21* (14–15), 1407–1433.

(46) Lee, H. S.; Kim, D. H.; Cho, J. H.; Hwang, M.; Jang, Y.; Cho, K. Effect of the Phase States of Self-Assembled Monolayers on Pentacene Growth and Thin-Film Transistor Characteristics. *J. Am. Chem. Soc.* **2008**, *130* (32), 10556–10564.

(47) Ng, T. N. T. Printed Organic TFT Sensor Tags. *Proc. - IEEE Int. Symp. Circuits Syst.* **2017**, 31–33.

(48) Elsobky, M.; Elattr, M.; Alavi, G.; Letzkus, F.; Richter, H.; Zschieschang, U.; Strecker, M.; Klauk, H.; Burghartz, J. N. A Digital Library for a Flexible Low-Voltage Organic Thin-Film Transistor Technology. *Org. Electron.* **2017**, *50*, 491–498.

(49) Yoon, M. H.; Yan, H.; Facchetti, A.; Marks, T. J. Low-Voltage Organic Field-Effect Transistors and Inverters Enabled by Ultrathin Cross-Linked Polymers as Gate Dielectrics. *J. Am. Chem. Soc.* **2005**, *127* (29), 10388–10395.

(50) Zirkl, M.; Haase, A.; Fian, A.; Schön, H.; Sommer, C.; Jakopic, G.; Leising, G.; Stadlober, B.; Graz, I.; Gaar, N.; Schwödiauer, R.; Bauer-Gogonea, S.; Bauer, S. Low-Voltage Organic Thin-Film Transistors with High-k Nanocomposite Gate Dielectrics for Flexible Electronics and Optothermal Sensors. *Adv. Mater.* **2007**, *19* (17), 2241–2245.

(51) Fujisaki, Y.; Mamada, M.; Kumaki, D.; Tokito, S.; Yamashita, Y. Low-Voltage and Hysteresis-Free N-Type Organic Thin Film Transistor and Complementary Inverter with Bilayer Gate Insulator. *Jpn. J. Appl. Phys.* **2009**, *48* (11).

(52) Majewski, L. A.; Schroeder, R.; Grell, M. Low-Voltage, High-Performance Organic Field-Effect Transistors with an Ultra-Thin TiO2 Layer as Gate Insulator. *Adv. Funct. Mater.* **2005**, *15* (6), 1017–1022.

(53) Sandberg, H. G. O.; Bäcklund, T. G.; Österbacka, R.; Stubb, H. High-Performance All-Polymer Transistor Utilizing a Hygroscopic Insulator. *Adv. Mater.* **2004**, *16* (13), 1112–1115.

(54) White, H. S.; Kittlesen, G. P.; Wrighton, M. S. Chemical Derivatization of an Array of Three Gold\rMicroelectrodes with Polypyrrole: Fabrication of A\rMolecule-Based Transistor. *J. Am. Chem. Soc.* **1984**, *106* (25), 5375–5377.

(55) Chao, S.; Wrighton, M. S. No Title. **1987**, No. 8, 2197–2199.

(56) Chao, S.; Wrighton, M. S. Characterization of a Solid-State Polyaniline-Based Transistor: Water Vapor Dependent Characteristics of a Device Employing a Poly(Vinyl Alcohol)/Phosphoric Acid Solid-State Electrolyte. *J. Am. Chem. Soc.* **1987**, *109* (22), 6627–6631.

(57) Ono, S.; Seki, S.; Hirahara, R.; Tominari, Y.; Takeya, J. High-Mobility, Low-Power, and Fast-Switching Organic Field-Effect Transistors with Ionic Liquids. *Appl. Phys. Lett.* **2008**, *92* (10), 2006–2009.

(58) Ono, S.; Miwa, K.; Seki, S.; Takeya, J. A Comparative Study of Organic Single-Crystal Transistors Gated with Various Ionic-Liquid Electrolytes. *Appl. Phys. Lett.* **2009**, *94* (6), 1–4.

(59) Uemura, T.; Yamagishi, M.; Ono, S.; Takeya, J. Low-Voltage Operation of n-Type Organic Field-Effect Transistors with Ionic Liquid. *Appl. Phys. Lett.* **2009**, *95* (May 2014), 103301.

(60) Uemura, T.; Yamagishi, M.; Ono, S.; Takeya, J. Very Low-Voltage Operation of Ionic Liquid-Gated n-Type Organic Field-Effect Transistors. *Jpn. J. Appl. Phys.* **2010**, *49* (1 Part

2), 2007–2010.

(61) Fujimoto, T.; Matsushita, M. M.; Awaga, K. Electrochemical Field-Effect Transistors of Octathio[8]Circulene Robust Thin Films with Ionic Liquids. *Chem. Phys. Lett.* **2009**, *483* (1–3), 81–83.

(62) Cho, J. H.; Lee, J.; He, Y.; Kim, B.; Lodge, T. P.; Frisbie, C. D. High-Capacitance Ion Gel Gate Dielectrics with Faster Polarization Response Times for Organic Thin Film Transistors. *Adv. Mater.* **2008**, *20* (4), 686–690.

(63) Lee, J.; Panzer, M. J.; He, Y.; Lodge, T. P.; Frisbie, C. D. Ion Gel Gated Polymer Thin-Film Transistors. *J. Am. Chem. Soc.* **2007**, *129* (15), 4532–4533.

(64) Cho, J. H.; Lee, J.; Xia, Y.; Kim, B.; He, Y.; Renn, M. J.; Lodge, T. P.; Daniel Frisbie, C. Printable Ion-Gel Gate Dielectrics for Low-Voltage Polymer Thin-Film Transistors on Plastic. *Nat. Mater.* **2008**, *7* (11), 900–906.

(65) Lee, J.; Kaake, L. G.; Cho, H. J.; Zhu, X. Y.; Lodge, T. P.; Frisbie, C. D. Ion Gel-Gated Polymer Thin-Film Transistors: Operating Mechanism and Characterization of Gate Dielectric Capacitance, Switching Speed, and Stability. *J. Phys. Chem. C* **2009**, *113* (20), 8972–8981.

(66) Xia, Y.; Cho, J.; Paulsen, B.; Frisbie, C. D.; Renn, M. J. Correlation of On-State Conductance with Referenced Electrochemical Potential in Ion Gel Gated Polymer Transistors. *Appl. Phys. Lett.* **2009**, *94* (1), 10–13.

(67) Braga, D.; Ha, M.; Xie, W.; Frisbie, C. D. Ultralow Contact Resistance in Electrolyte-Gated Organic Thin Film Transistors. *Appl. Phys. Lett.* **2010**, *97* (19).

(68) Xia, Y.; Zhang, W.; Ha, M.; Cho, J. H.; Renn, M. J.; Kim, C. H.; Frisbie, C. D. Printed Sub-2 V Gel-Electrolyte-Gated Polymer Transistors and Circuits. *Adv. Funct. Mater.* **2010**, *20* (4), 587–594.

(69) Hamedi, M.; Herlogsson, L.; Crispin, X.; Morcilla, R.; Berggren, M.; Ingan??s, O. Fiber-Embedded Electrolyte-Gated Field-Effect Transistors for e-Textiles. *Adv. Mater.* **2009**, *21* (5), 573–577.

(70) Taniguchi, M.; Kawai, T. Vertical Electrochemical Transistor Based on Poly(3-Hexylthiophene) and Cyanoethylpullulan. *Appl. Phys. Lett.* **2004**, *85* (15), 3298–3300.

(71) Panzer, M. J.; Frisbie, C. D. Polymer Electrolyte Gate Dielectric Reveals Finite Windows of High Conductivity in Organic Thin Film Transistors at High Charge Carrier Densities Polymer Electrolyte Gate Dielectric Reveals Finite Windows of High. *J. Am. Chem. Soc.* **2005**, *127*, 6960–6961.

(72) Panzer, M. J.; Frisbie, C. D. High Carrier Density and Metallic Conductivity in Poly(3-Hexylthiophene) Achieved by Electrostatic Charge Injection. *Adv. Funct. Mater.* **2006**, *16* (8), 1051–1056.

(73) Panzer, M. J.; Frisbie, C. D. Polymer Electrolyte-Gated Organic Field-Effect Transistors: Low-Voltage, High-Current Switches for Organic Electronics and Testbeds for Probing Electrical Transport at High Charge Carrier Density. *J. Am. Chem. Soc.* **2007**, *129* (20), 6599–6607.

(74) Dhoot, A. S.; Yuen, J. D.; Heeney, M.; McCulloch, I.; Moses, D.; Heeger, A. J. Beyond the Metal-Insulator Transition in Polymer Electrolyte Gated Polymer Field-Effect Transistors. *Proc. Natl. Acad. Sci.* **2006**, *103* (32), 11834–11837.

(75) Yuen, J. D.; Dhoot, A. S.; Namdas, E. B.; Coates, N. E.; Heeney, M.; McCulloch, I.; Moses, D.; Heeger, A. J. Electrochemical Doping in Electrolyte-Gated Polymer Transistors. *J. Am. Chem. Soc.* **2007**, *129* (46), 14367–14371.

(76) Panzer, M. J.; Frisbie, C. D. High Charge Carrier Densities and Conductance Maxima in Single-Crystal Organic Field-Effect Transistors with a Polymer Electrolyte Gate Dielectric. *Appl. Phys. Lett.* **2006**, *88* (20), 1–4.

(77) Panzer, M. J.; Newman, C. R.; Frisbie, C. D. Low-Voltage Operation of a Pentacene Field-Effect Transistor with a Polymer Electrolyte Gate Dielectric. *Appl. Phys. Lett.* **2005**, *86* (10), 1–3.

(78) Takeya, J.; Yamada, K.; Hara, K.; Shigeto, K.; Tsukagoshi, K.; Ikehata, S.; Aoyagi, Y. High-Density Electrostatic Carrier Doping in Organic Single-Crystal Transistors with

Polymer Gel Electrolyte. *Appl. Phys. Lett.* **2006**, *88* (11), 86–89.

(79) Shimotani, H.; Asanuma, H.; Takeya, J.; Iwasa, Y. Electrolyte-Gated Charge Accumulation in Organic Single Crystals. *Appl. Phys. Lett.* **2006**, *89* (20).

(80) Lee, S. W.; Lee, H. J.; Choi, J. H.; Koh, W. G.; Myoung, J. M.; Hur, J. H.; Park, J. J.; Cho, J. H.; Jeong, U. Periodic Array of Polyelectrolyte-Gated Organic Transistors from Electrospun Poly(3-Hexylthiophene) Nanofibers. *Nano Lett.* **2010**, *10* (1), 347–351.

(81) Herlogsson, L.; Crispin, X.; Robinson, N. D.; Sandberg, M.; Hagel, O. J.; Gustafsson, G. G. G. G. G. G.; Berggren, M. Low-Voltage Polymer Field-Effect Transistors Gated via a Proton Conductor. *Adv. Mater.* **2007**, *19* (1), 97–101.

(82) Said, E.; Crispin, X.; Herlogsson, L.; Elhag, S.; Robinson, N. D.; Berggren, M. Polymer Field-Effect Transistor Gated via a Poly(Styrenesulfonic Acid) Thin Film. *Appl. Phys. Lett.* **2006**, *89* (14), 10–13.

(83) Kergoat, L.; Herlogsson, L.; Braga, D.; Piro, B.; Pham, M. C.; Crispin, X.; Berggren, M.; Horowitz, G. A Water-Gate Organic Field-Effect Transistor. *Adv. Mater.* **2010**, *22* (23), 2565–2569.

(84) Lee, S.; Choi, G.; Lim, H.; Lee, K.; Lee, S.; Lee, S.; Choi, G.; Lim, H.; Lee, K. Electronic Transport Characteristics of Electrolyte-Gated Conducting Polyaniline Nanowire Field-Effect Transistors Electronic Transport Characteristics of Electrolyte-Gated Conducting Polyaniline Nanowire Field-Effect Transistors. **2009**, *013113*.

(85) Shimotani, H.; Diguet, G.; Iwasa, Y. Direct Comparison of Field-Effect and Electrochemical Doping in Regioregular Poly(3-Hexylthiophene). *Appl. Phys. Lett.* **2005**, *86* (2), 10–13.

(86) Herlogsson, L.; Crispin, X.; Tierney, S.; Berggren, M. Polyelectrolyte-Gated Organic Complementary Circuits Operating at Low Power and Voltage. *Adv. Mater.* **2011**, *23* (40), 4684–4689.

(87) Choi, J. H.; Xie, W.; Gu, Y.; Frisbie, C. D.; Lodge, T. P. Single Ion Conducting, Polymerized Ionic Liquid Triblock Copolymer Films: High Capacitance Electrolyte Gates

for N-Type Transistors. *ACS Appl. Mater. Interfaces* **2015**, *7* (13), 7294–7302.

(88) Lee, K. H.; Zhang, S.; Lodge, T. P.; Frisbie, C. D. Electrical Impedance of Spin-Coatable Ion Gel Films. *J. Phys. Chem. B* **2011**, *115* (13), 3315–3321.

(89) Kim, S. H.; Hong, K.; Xie, W.; Lee, K. H.; Zhang, S.; Lodge, T. P.; Frisbie, C. D. Electrolyte-Gated Transistors for Organic and Printed Electronics. *Adv. Mater.* **2013**, *25* (13), 1822–1846.

(90) Inal, S.; Malliaras, G. G.; Rivnay, J. Benchmarking Organic Mixed Conductors for Transistors. *Nat. Commun.* **2017**, *8* (1), 1–6.

(91) Sun, H.; Gerasimov, J.; Berggren, M.; Fabiano, S. N-Type Organic Electrochemical Transistors: Materials and Challenges. *J. Mater. Chem. C* **2018**, *6* (44), 11778–11784.

(92) Andersson, P.; Forchheimer, R.; Tehrani, P.; Berggren, M. Printable All-Organic Electrochromic Active-Matrix Displays. *Adv. Funct. Mater.* **2007**, *17* (16), 3074–3082.

(93) Andersson, P.; Nilsson, D.; Svensson, P. O. P.-O. O. P. P.-O.; Chen, M.; Malmström, A.; Remonen, T.; Kugler, T.; Berggren, M.; Andersson, B. P. Active Matrix Displays Based on All-Organic Electrochemical Smart Pixels Printed on Paper. *Adv. Mater.* **2002**, *14* (20), 1460–1464.

(94) Hagiwara, R.; Matsumoto, K.; Nakamori, Y.; Tsuda, T.; Ito, Y.; Matsumoto, H.; Momota, K. Physicochemical Properties of 1,3-Dialkylimidazolium Fluorohydrogenate Room-Temperature Molten Salts. *J. Electrochem. Soc.* **2003**, *150* (12), D195–D199.

(95) Stern, O. ZUR THEORIE DER ELEKTROLYTISCHEN DOPPELSCHICHT. *Zeitschrift für Elektrochemie und Angew. Phys. Chemie* **1924**, *30*, 508–516.

(96) Butt, H. J.; Kappl, M. *Surface and Interfacial Forces*; 2010.

(97) Butt, H.; Graf, K.; Kappl, M. *Physics and Chemistry of Interfaces*; 2003.

(98) Smith, A. M.; Lee, A. A.; Perkin, S. The Electrostatic Screening Length in Concentrated Electrolytes Increases with Concentration. *J. Phys. Chem. Lett.* **2016**, *7* (12), 2157–2163.

(99) Larsson, O.; Said, E.; Berggren, M.; Crispin, X. Insulator Polarization Mechanisms in Polyelectrolyte-Gated Organic Field-Effect Transistors. *Adv. Funct. Mater.* **2009**, *19* (20), 3334–3341.

(100) MacDonald, D. D. Reflections on the History of Electrochemical Impedance Spectroscopy. *Electrochim. Acta* **2006**, *51* (8–9), 1376–1388.

(101) Wee, G.; Larsson, O.; Srinivasan, M.; Berggren, M.; Crispin, X.; Mhaisalkar, S. Effect of the Ionic Conductivity on the Performance of Polyelectrolyte- Based Supercapacitors. *Adv. Funct. Mater.* **2010**, *20* (24), 4344–4350.

(102) Giovannitti, A.; Nielsen, C. B.; Sbircea, D.-T.; Inal, S.; Donahue, M.; Niazi, M. R.; Hanifi, D. A.; Amassian, A.; Malliaras, G. G.; Rivnay, J.; McCulloch, I. N-Type Organic Electrochemical Transistors with Stability in Water. *Nat. Commun.* **2016**, *7* (1), 13066.

(103) Ohno, H. Design of Ion Conductive Polymers Based on Ionic Liquids. *Macromol. Symp.* **2007**, *249–250*, 551–556.

(104) Chen, H.; Choi, J. H.; Cruz, D. S. D. La; Winey, K. I.; Elabd, Y. A. Polymerized Ionic Liquids: The Effect of Random Copolymer Composition on Ion Conduction. *Macromolecules* **2009**, *42* (13), 4809–4816.

(105) Hu, H.; Yuan, W.; Lu, L.; Zhao, H.; Jia, Z.; Baker, G. L.; Yuan, W. Low Glass Transition Temperature Polymer Electrolyte Prepared From Ionic Liquid Grafted Polyethylene Oxide. *J. Polym. Sci., Part A Polym. Chem* **2014**, *52*, 2104–2110.

(106) Wang, S. W.; Liu, W.; Colby, R. H. Counterion Dynamics in Polyurethane-Carboxylate Ionomers with Ionic Liquid Counterions. *Chem. Mater.* **2011**, *23* (7), 1862–1873.

(107) Snyder, J. F.; Carter, R. H.; Wetzel, E. D. Electrochemical and Mechanical Behavior in Mechanically Robust Solid Polymer Electrolytes for Use in Multifunctional Structural Batteries. *Chem. Mater.* **2007**, *19* (15), 3793–3801.

(108) Mecerreyes, D. Polymeric Ionic Liquids: Broadening the Properties and Applications of Polyelectrolytes. *Prog. Polym. Sci.* **2011**, *36* (12), 1629–1648.

(109) Schneider, Y.; Modestino, M. A.; McCulloch, B. L.; Hoarfrost, M. L.; Hess, R. W.; Segalman, R. A. Ionic Conduction in Nanostructured Membranes Based on Polymerized Protic Ionic Liquids. *Macromolecules* **2013**, *46* (4), 1543–1548.

(110) Choi, J. H.; Ye, Y.; Elabd, Y. A.; Winey, K. I. Network Structure and Strong Microphase Separation for High Ion Conductivity in Polymerized Ionic Liquid Block Copolymers. *Macromolecules* **2013**, *46* (13), 5290–5300.

(111) Weber, R. L.; Ye, Y.; Schmitt, A. L.; Banik, S. M.; Elabd, Y. A.; Mahanthappa, M. K. Effect of Nanoscale Morphology on the Conductivity of Polymerized Ionic Liquid Block Copolymers. *Macromolecules* **2011**, *44* (14), 5727–5735.

(112) Ye, Y.; Choi, J.; Winey, K. I.; Elabd, Y. A. Polymerized Ionic Liquid Block and Random Copolymers: Effect of Weak Microphase Separation on Ion Transport. *Macromolecules* **2012**, *45* (17), 7027–7035.

(113) Harris, M. A.; Heres, M. F.; Coote, J.; Wenda, A.; Strehmel, V.; Stein, G. E.; Sangoro, J. Ion Transport and Interfacial Dynamics in Disordered Block Copolymers of Ammonium-Based Polymerized Ionic Liquids. *Macromolecules* **2018**, *51* (9), 3477–3486.

(114) Allen, M. H.; Hemp, S. T.; Zhang, M.; Zhang, M.; Smith, A. E.; Moore, R. B.; Long, T. E. Synthesis and Characterization of 4-Vinylimidazole ABA Triblock Copolymers Utilizing a Difunctional RAFT Chain Transfer Agent. *Polym. Chem.* **2013**, *4* (7), 2333–2341.

(115) Mapesa, E. U.; Chen, M.; Heres, M. F.; Harris, M. A.; Kinsey, T.; Wang, Y.; Long, T. E.; Lokitz, B. S.; Sangoro, J. R. Charge Transport in Imidazolium-Based Homo- and Triblock Poly(Ionic Liquid)S. *Macromolecules* **2019**, *52* (2), 620–628.

(116) Choi, J. H.; Ye, Y.; Elabd, Y. A.; Winey, K. I. Network Structure and Strong Microphase Separation for High Ion Conductivity in Polymerized Ionic Liquid Block Copolymers. *Macromolecules* **2013**, *46* (13), 5290–5300.

(117) Lodge, T. P. Block Copolymers: Past Successes and Future Challenges. *Macromol. Chem. Phys.* **2003**, *204* (2), 265–273.

(118) Matyjaszewski, K. Controlled Radical Polymerization: State-of-the-Art in 2014. *ACS Symp.*

Ser. **2015**, *1187*, 1–17.

(119) Hadjichristidis, N.; Pispas, S.; Floudas, G. *Block Copolymers*; John Wiley & Sons, Inc.: Hoboken, USA, 2002.

(120) *Nitroxide Mediated Polymerization: From Fundamentals to Applications in Material Science*; Gigmes, D., Ed.; Polymer Chemistry Series; Royal Society of Chemistry: Cambridge, 2015.

(121) Polymerization, L. R.; Series, a C. S. S.; Society, A. C. *Controlled/Living Radical Polymerization: Progress in ATRP*; Matyjaszewski, K., Ed.; ACS Symposium Series; American Chemical Society: Washington DC, 2009; Vol. 1023.

(122) Barner-kowollik, C. *Handbook of RAFT Polymerization*; Barner-Kowollik, C., Ed.; Wiley, 2008.

(123) Hawker, C. J.; Bosman, A. W.; Harth, E. New Polymer Synthesis by Nitroxide Mediated Living Radical Polymerizations. *Chem. Rev.* **2001**, *101* (12), 3661–3688.

(124) Grubbs, R. B. Nitroxide-Mediated Radical Polymerization: Limitations and Versatility. *Polym. Rev.* **2011**, *51* (2), 104–137.

(125) Lessard, B.; Marić, M. Effect of Acrylic Acid Neutralization on 'Livingness' of Poly[Styrene- Ran -(Acrylic Acid)] Macro-Initiators for Nitroxide-Mediated Polymerization of Styrene. *Polym. Int.* **2008**, *57* (10), 1141–1151.

(126) Lessard, B. H.; Bender, T. P. Boron Subphthalocyanine Polymers by Facile Coupling to Poly(Acrylic Acid-Ran-Styrene) Copolymers Synthesized by Nitroxide-Mediated Polymerization and the Associated Problems with Autoinitiation. *Macromol. Rapid Commun.* **2013**, *34* (7), 568–573.

(127) Lessard, B. H.; Savelyeva, X.; Mari, M. Smart Morpholine-Functional Statistical Copolymers Synthesized by Nitroxide Mediated Polymerization. **2012**, *53*, 5649–5656.

(128) King, B.; Lessard, B. H. Controlled Synthesis and Degradation of Poly (N - (Isobutoxymethyl) Acrylamide) Homopolymers and Block Copolymers. *201600073*, 1–10.

(129) Ballard, N.; Aguirre, M.; Simula, A.; Leiza, J. R.; van Es, S.; Asua, J. M. High Solids Content Nitroxide Mediated Miniemulsion Polymerization of N-Butyl Methacrylate. *Polym. Chem.* **2017**, *8* (10), 1628–1635.

(130) Ballard, N.; Aguirre, M.; Simula, A.; Agirre, A.; Leiza, J. R.; Asua, J. M.; van Es, S. New Class of Alkoxyamines for Efficient Controlled Homopolymerization of Methacrylates. *ACS Macro Lett.* **2016**, *5* (9), 1019–1022.

(131) SZWARC, M. 'Living' Polymers. *Nature* **1956**, *178* (4543), 1168–1169.

(132) Quirk, R. P.; Lee, B. Experimental Criteria for Living Polymerizations. *Polym. Int.* **1992**, *27* (4), 359–367.

(133) Matyjaszewski, K. Introduction to Living Polymeriz. Living and/or Controlled Polymerization. *J. Phys. Org. Chem.* **1995**, *8* (4), 197–207.

(134) Mueller, A. H. E.; Zhuang, R.; Yan, D.; Litvinenko, G. Kinetic Analysis of "Living" Polymerization Processes Exhibiting Slow Equilibria. 1. Degenerative Transfer (Direct Activity Exchange between Active and "Dormant" Species). Application to Group Transfer Polymerization. *Macromolecules* **1995**, *28* (12), 4326–4333.

(135) Gnanou, Yves. Fontanille, M. Step-Growth Polymerizations. In *Organic and Physical Chemistry of Polymers*; pp 213–248.

(136) Vinas, J.; Chagneux, N.; Gigmes, D.; Trimaille, T.; Favier, A.; Bertin, D. SG1-Based Alkoxyamine Bearing a N-Succinimidyl Ester: A Versatile Tool for Advanced Polymer Synthesis. *Polymer (Guildf).* **2008**, *49* (17), 3639–3647.

(137) Benoit, D.; Grimaldi, S.; Robin, S.; Finet, J. P.; Tordo, P.; Gnanou, Y. Kinetics and Mechanism of Controlled Free-Radical Polymerization of Styrene and n-Butyl Acrylate in the Presence of an Acyclic β-Phosphonylated Nitroxide. *J. Am. Chem. Soc.* **2000**, *122* (25), 5929–5939.

(138) Moayeri, A.; Lessard, B. H.; Maric, M. Nitroxide Mediated Controlled Synthesis of Glycidyl Methacrylate-Rich Copolymers Enabled by SG1-Based Alkoxyamines Bearing Succinimidyl Ester Groups. *Polym. Chem.* **2011**, *2* (9), 2084.

(139) Dire, C.; Belleney, J.; Nicolas, J.; Bertin, D.; Magnet, S.; Charleux, B. β-Hydrogen Transfer from Poly(Methyl Methacrylate) Propagating Radicals to the Nitroxide SG1: Analysis of the Chain-End and Determination of the Rate Constant. *J. Polym. Sci. Part A Polym. Chem.* **2008**, *46* (18), 6333–6345.

(140) Lessard, B.; Ling, E. J. Y.; Morin, M. S. T.; Marić, M. Nitroxide-Mediated Radical Copolymerization of Methyl Methacrylate Controlled with a Minimal Amount of 9-(4-Vinylbenzyl)-9H-Carbazole. *J. Polym. Sci. Part A Polym. Chem.* **2011**, *49* (4), 1033–1045.

Chapter 2: Nitroxide Mediated Polymerization of 1-(4-vinylbenzyl)-3-butylimidazolium ionic liquid containing homopolymers and methyl methacrylate copolymers

Context

The initial goal was to synthesize copolymers containing small amounts of ionic liquid monomers by nitroxide mediated polymerization (NMP) to observe how polymerization kinetics & control are affected.

Contribution of Authors

I designed the experiments independently or in consultation with Dr. Lessard exploring the synthesis of ionic liquid polymers by NMP. I performed all the experiments and characterization with the assistance of Ian, an undergraduate thesis student, who I mentored and directed. GPC characterization I performed at McGill with postdoc Dr. Adrien Metafiot. I wrote the initial manuscript and Professor Lessard edited the final draft.

Significance of Research

This study compares a series of possible and successful routes to reach 1-(4-vinylbenzyl)-3-butylimidazolium ionic liquid containing copolymers. We explored the polymerization of the ionic liquid monomer directly, the synthesis of 1-(4-vinylbenzyl)-3-imidazole containing copolymers followed by quaternization and ion exchange as well as copolymerizing chloromethyl styrene followed by the conversion to the PIL. We studied the polymerization kinetics and copolymerization composition as a function of feed composition for the systems. We studied the relatively unique kinetic behaviour of the ionic liquid monomer, compared to non-charged monomers which is relatively unexplored in the literature.

The expertise and methodology developed in this paper to produce PILs was the basis for the rest of my research. Ample time was spent on finding *easy and scalable* isolation methods for these materials as well as figuring out how to characterize these unique materials by GPC, which

due to the charged nature of the materials are often incompatible. For my own research goals and our group, this work was significant as it established a repeatable methodology to synthesize and isolate PILs by scalable methods which are also compatible with required characterization (GPC) techniques.

*Chapter 2 has been published in The Canadian Journal of Chemical Engineering: Peltekoff, A. J., Therrien, I., & Lessard, B. H., **2019**, 97, 5-16. doi:10.1002.cjce.23348 © 2018 Canadian Society for Chemical Engineering*

2.1 Abstract

The synthesis of well-defined imidazolium-based poly(ionic liquid)s (PILs) copolymers by nitroxide mediated polymerization (NMP) is reported. The viability of three different synthetic pathways to achieve poly[1-(4-vinylbenzyl)-3-butylimidazolium bis(trifluoromethylsulphonyl)-imide-co-methyl methacrylate] (poly(VBBI$^+$TFSI$^-$-*co*-MMA)) was explored including direct polymerization of the ionic liquid monomer (VBBI$^+$TFSI$^-$) and post functionalization of precursor polymer poly(4-vinylbenzyl imidazole-co-methyl methacrylate). PILs with well-controlled molecular weight and low dispersity ($\overline{M}_w/\overline{M}_n < 1.3$) were obtained via all routes. A full synthetic, kinetic, and compositional comparison between methods is reported. These results illustrate an effective route for the synthesis of well-defined, pseudo-living functional PIL-methacrylate copolymers with tunable properties through potential methacrylate monomer substitution.

2.2 Introduction

Ionic liquids are non-volatile molten salts that have found application as electrolytes and reaction solvents.[1] Poly(ionic liquid)s (PILs) are a class of poly(electrolyte) that combine the benefits of the ionic liquid moieties and the mechanical properties of polymers.[2, 3] These ionic liquid moieties typically possess bulky cations and weakly coordinating anions.[4-7] PILs are unique compared to common neutral polymers as they exhibit properties such as high ion conductivity, chemical and thermal stability, and tunable solubility.[8] The unique properties of PILs are exploited in a variety of applications such as CO_2 separation membranes,[6, 9, 10] organic field-effect transistors[11, 12] and solid state electrolytes in electrochemical capacitors.[13]

The majority of the PILs that have been reported are prepared by conventional free radical polymerization, which results in large polymer dispersity.[3, 14, 15] Recently, some examples have emerged using reversible-deactivation radical polymerization (RDRP), also known as controlled radical polymerization (CRP), resulting in homopolymers and copolymers with well-defined architectures. Techniques such as atom transfer radical polymerization (ATRP),[16-21] organometallic-mediated radical polymerization (OMRP),[22-25] and reversible addition-fragmentation chain-transfer (RAFT) polymerization[26, 27] have been demonstrated using imidazolium based ionic liquid monomers that contain $TFSI^-$, PF_6^-, and BF_4^- counterions. Nitroxide mediated polymerization (NMP) was first discovered by Solomon et al.,[28] however, it did not receive significant attention until the seminal work by Georges et al., Veregin et al.,[29, 30] Hawker, and Hawker et al.[31, 32] NMP, when compared to alternative CRP techniques, is conceptually the simplest, often only requiring a unimolecular initiator and the monomer. NMP is an industrially scalable technique that can be used to produce well defined block copolymers without the use of air-free transfers, transition metal catalysts, or thiol transfer agents, which make it ideal for the synthesis of materials for application in sensitive electronic or biological applications.[33, 34] A disadvantage of utilizing ATRP in the synthesis of PILs is the unavoidable complex of PIL with the catalytic copper ions, a challenge that is not present when using NMP.8 Traditionally NMP was limited to the controlled homopolymerization of styrenics when using first-generation stable free radicals such as 2,2,6,6-tetramethylpiperidine-1-oxyl (TEMPO).[29, 33-35] However, the development of second-generation stable free radicals such as N-tert-butyl-N-[1-diethylphosphono-(2,2- dimethylpropyl)] nitroxide (SG1[36]) and 2,2,5-trimethyl-4-phenyl-3-

azahexane-3-nitroxide (TIPNO37) has facilitated the extension of NMP methodology to the homopolymerization of other monomers including acrylates,[38-40] acrylamides,[35] and methacrylates (when using a small amount of a controlling comonomer[41, 42]). For a controlling comonomer to be effective, in the controlled polymerization of methacrylates, it must have a low propagating rate constant, k_p,[43] relative to the methacrylate and favorable reactivity ratios with the methacrylate comonomer.[44] Styrene,[43,45] acrylonitrile,[41] 9-(4-vinylbenzyl)-9H-carbazole (VBK[46]), 2-methylene-4-phenyl-1,3-dioxolane,[47] and others have all proven to be effective controlling comonomers for a variety of methacrylates.

The incorporation of methacrylates is of great interest due to their favourable polymerization properties such as the absence of backbiting reactions, which are apparent in acrylate polymerization and result in broader molecular weight distributions, however, their copolymerization with PILs by NMP has not yet been reported. Prior to synthesizing a variety of PIL/methacrylate copolymers, it is crucial to establish that MMA (a typical case model for other methacryaltes) can be copolymerized in a controlled pseudo-living fashion using PIL based styrenics. In this study, we explore various synthetic pathways to achieve well-defined PILs copolymers based on methyl methacrylate (MMA) and 1-(4-vinylbenzyl)-3-butylimidazolium bis(trifluoromethylsulphonyl)-imide ($VBBI^+TFSI^-$) by NMP. Ease of synthesis, kinetics, reactivity ratios, and degree of functionalization were all investigated.

2.3 Results & Discussion

2.3.1 Synthetic Overview for PIL Containing Copolymer

PILs can be obtained via two synthetic approaches: direct polymerization of an ionic liquid monomer; or post-polymerization functionalization of a functional precursor polymer. In the current study, we analyze the viability of three different synthetic pathways used for the preparation of PIL copolymers via nitroxide mediated polymerization (NMP). In all cases, the use of a NHS-BlocBuilder was employed as the unimolecular initiator, due to its ability to copolymerize methacrylates and styrenics with pseudo-living behaviour (ability to reinitiate a second batch of monomer) without the need for an additional stable free radical.[51] **Scheme 2.1** illustrates the different routes that were performed and compared.

Scheme 2.1. Synthetic pathways for methyl methacrylate (MMA) and 1-(4-vinylbenzyl)-3-butylimidazolium (VBBI) copolymers by NMP.

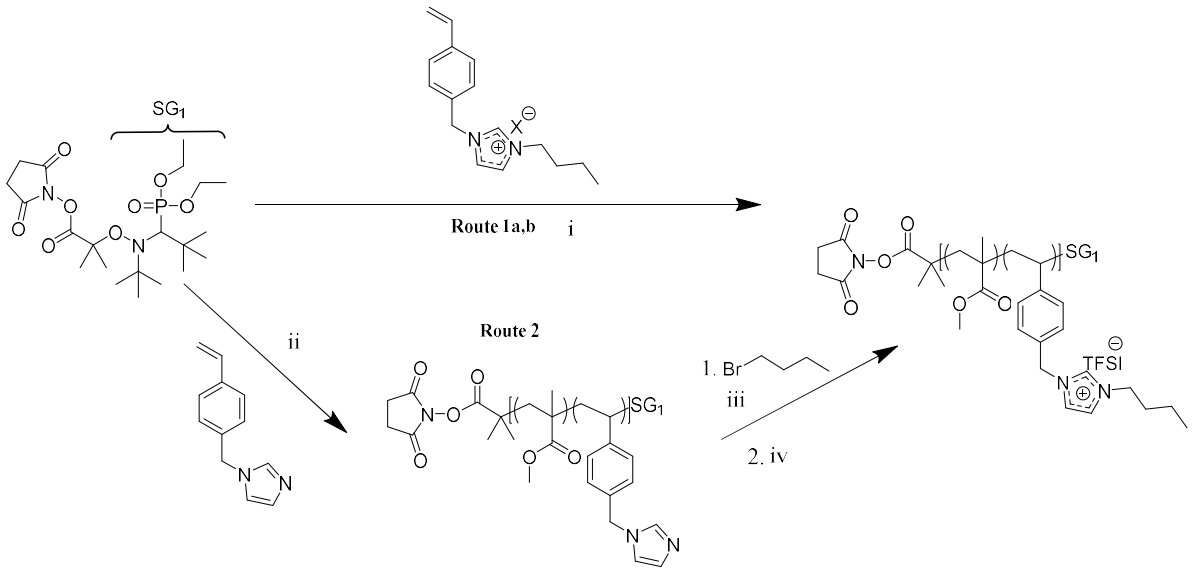

Route 1 is the copolymerization of VBBI (obtained by two different methods) and MMA, and route 2 is the copolymerization of 1-(4-vinylbenzyl)-3-imidazole (VBIm) and MMA. The conditions used for these reactions were as follows: i) VBBI and MMA (molar ratio, 1:10 to 10:1), 90 8C, DMF, 2–10 h; ii) VBIm and MMA (molar ratio, 1:10 to 10:1), 90 8C, DMF, 2–10 h; iii) 50 8C, DMF, 12-24 h; and iv) room temperature, DMA, 48 h.

Overall, post polymerization techniques of functional precursor polymers are often advantageous in terms of the final characterization of the resulting polymer. Running gel permeation chromatography on the final copolymer can be challenging due to interactions between the ionic liquid moiety and the columns, however, the pre-polymer can often be characterized prior to the coupling with ease.[52] The downside to the post polymerization strategy is that it can be very challenging to obtain 100 % coupling of the polymer reactive sites, resulting in potentially detrimental unreacted functional sites on the polymer.

One post-polymerization methodology was investigated (route 2, **Scheme 2.1**) involving the copolymerization of methyl methacrylate (MMA) and 1-(4-vinylbenzyl)-3-imidazole (VBIm) followed by a quaternization of the imidazole pendent with 1-bromobutane and then followed by ion exchange. The successful homopolymerization of VBIm has been previously reported using NMP through copolymerization with n-butyl-acrylate (BA)[53, 54] and combined with poly(styrene)

blocks via chain extensions.[55] However, its copolymerization with a methacrylate such as MMA has not yet been reported. Therefore, a series of poly(VBIm-co-MMA) copolymerizations were performed with feed ratios ranging from 5–90 mol% of VBIm. Copolymerization kinetics and copolymer compositions are discussed in the following sections. The resulting poly(VBIm-co-MMA) copolymers were found to be incompatible with the GPC columns preventing the accurate determination of molecular weight values even when the final MMA copolymer composition, F_{MMA}, ≈ 90–95 mol%. Once synthesized, the poly(VBIm-co-MMA) copolymers were reacted with 1-bromobutane followed by anion exchange with the desired salt (LiTFSI or BF_4^-), resulting in the desired PIL containing copolymer. Quaternization of the poly(VBIm-co-MMA) was adapted from a procedure utilized by Green et al.[54] in the quaternization of poly(VBIm-co-BA) pre-polymers. While the protocol in the literature did not provide NMR confirmation, the authors reported complete post functionalization of the VBIm pendent groups after 24 h. In this study, we followed the same protocol while using poly(VBIm-co-MMA) and confirmed it to be valid via ^{1}H NMR (see **Figure 2.10** in the supporting information). Quaternization was determined to be complete by NMR analysis on the precursor polymer and post-functionalized polymer. In **Figure 2.10**, the peak at δ ~4.3 corresponding to the CH_2 group bridging between the styrene aromatic group and the imidazole group has a value of 191.84 (^{1}H = 95.92). To track the quantitatively determined conversion, we track the peak shift corresponding to the H located between the two Nitrogen atoms on the imidazole moieties. The peak shifts from δ ~9.0 to ~10.25. When examining the peak at δ = 10.25 ppm and comparing this to the CH_2 bridge, this indicates a 98.7 % conversion (94.64/95.92 = 0.987). Similar to Green et al.,[50] we observed complete conversion after 24 h, when performing the functionalization in DMF. Further details on the quaternization of the VBIm moiety is discussed below.

In addition to the post-polymerization strategy, we explored the synthesis of the 1-(4-vinylbenzyl)-3-butylimidazolium (VBBI) monomer followed by the NMP copolymerization with MMA (route 1, **Scheme 2.1**). The monomer itself was synthesized via the following two routes: reacting 1-butylimidazole with chloromethylstyrene (CMS) followed by the anion exchange (route1a, **Scheme 2.2**); as well as synthesizing VBIm followed by quaternization with an alkylbromide and anion exchange (Route 1b, **Scheme 2.2**).

Scheme 2.2 Synthetic routes to obtain 1-(4-vinylbenzyl)-3-butylimidazolium bis(trifluoromethyl-sulphonyl)-imide (VBBI) monomer:

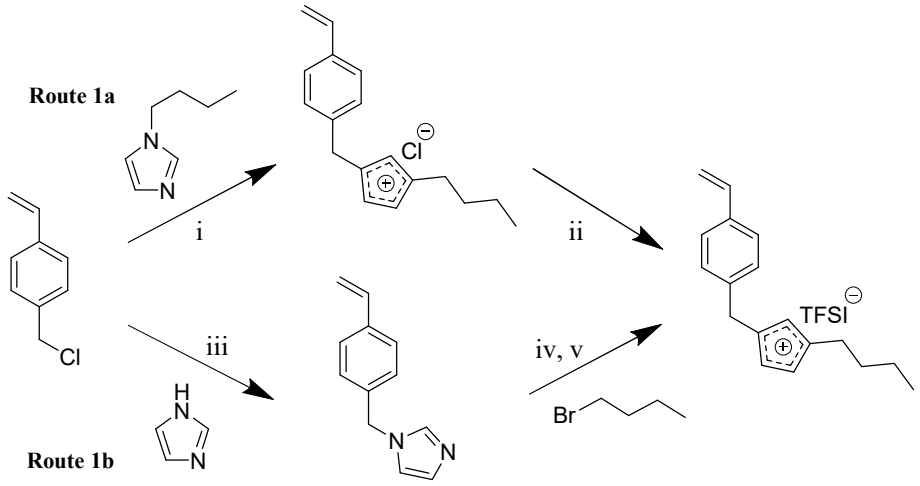

i) 45 °C, 24 h; ii) LiTFSI, water, r.t, 24 h; iii) acetone/water, K_2CO_3, 50 °C, 18 h; iv) 50 °C, 24 h; and v) LiTFSI, H_2O.

Quaternization of 1-butylimidazole with CMS monomer followed by an anion exchange with LiTFSI or $NaBF_4$ was executed according to a procedure outlined in other literature.[14] The reaction was not monitored, however, due to the difference in solubility of the final $TFSI^-$ or BF_4^- containing product and Cl^- intermediate product, the isolation of the desired product in high purity is achieved with ease with yields greater than 80 %. As was reported by Bara et al.,[14] route 1a (**Scheme 2.2**) produces the ionic liquid monomer in a straightforward manor utilizing commercially available precursors.

We decided to explore the synthesis of VBBI by adapting the post polymerization functionalization route reported by Green et al.(route 1b, **Scheme 2.2**).[54] Therefore, VBIm reacted with 1-bromobutane followed by ion exchange with LiTFSI or $NaBF_4$. Due to the persisting challenges associated with this route when performing the functionalization on the polymer (route 1b), we decided to further characterize the quaternization reaction during the monomer synthesis (route 1b). The quaternization reaction on the imidazole moiety was performed on the VBIm monomer by reacting with two equivalents of 1-bromobutane at 50 °C over 24 h in a 50 vol% acetonitrile solution and under bulk conditions. The conversion, X, was monitored by tracking the appearance of a new peak at 9.75 ppm relative to the vinyl peak at 5.7 ppm, additionally the peak

at 6.80 ppm can be seen to disappear as the reaction progresses. It was found that an elevated X (> 95 %) could be achieved within 24 h (**Figure 2.1**). The synthetic pathway (route 1b) is reproducible; however, this methodology is not optimal for several reasons; the purification of the VBIm monomer is rather time consuming due to additional acidification and neutralization steps, extra liquid extractions resulting in a much greater amount of solvent utilization, and smaller yields when compared to route 1a.

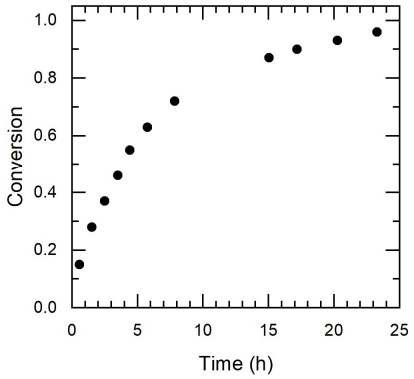

Figure 2.1 Conversion (X) versus time of VBIm quaternization reaction with bromobutane.

2.3.2 Homopolymerizations

Homopolymerizations of styrene, $VBBI^+TFSI^-$, $VBBI^+BF_4^-$, and VBIm were each performed at 110 °C to compare the relative kinetics. First order kinetic plots of $\ln[(1-X)^{-1}]$ versus the time were obtained and are shown in **Figure 2.2**. We found that the BF_4^- containing IL monomer terminated at much lower conversions (X < 20 %) compared to the other monomers. The addition of SG1 and performing the polymerization at a lower temperature also did not prevent the early termination of the BF_4^- monomer (supporting information, **Figure 2.9** and **Table 2.5**).

To compare the kinetics of each system we determined the apparent rate constant, $\langle k_p \rangle$[P •], of each polymerization. Where k_p is the propagation rate constant and [P •] is the concentration of propagating radicals. Such a parameter is frequently cited in free radical polymerization literature since it can provide insight into the pseudo-living nature of the polymerization. It is found by determining the slope of the first order kinetic plots of $\ln[(1-X)^{-1}]$ versus the time plots. When analyzing the relative kinetics, it was found that VBIm had an effective $\langle k_p \rangle$[P •] = 1.3 times greater than that of styrene, $VBBI^+TFSI^-$ had an effective

$\langle k_p \rangle$[P •] = 11.7 times greater than that of styrene, and VBBI$^+$BF$_4^-$ had an effective $\langle k_p \rangle$[P •] = 1.5 times greater than that of styrene (**Table 2.1**).

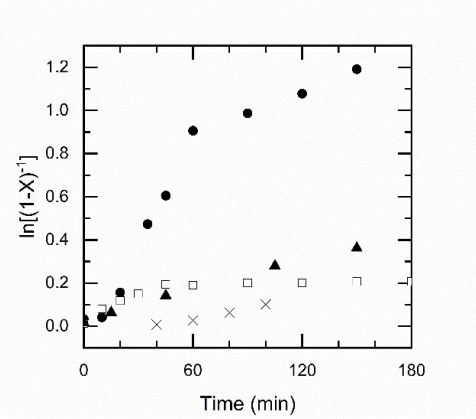

Figure 2.2 Representative kinetic plots of $\ln[(1-X)^{-1}]$ (X = conversion) versus polymerization time for homopolymerizations of monomers VBBI$^+$TFSI$^-$ (filled circles, ●), VBBI$^+$BF4$^-$ (open squares, □), VBIm (filled triangles, ▲), and styrene (cross signs, ×). All homopolymerizations were performed at 110 °C in 50 wt% DMF solutions with NHS-BlocBuilder unimolecular initiator.

Table 2.1 Homopolymerizations initiated by N- hydroxysuccinimidyl BlocBuilder at 110 °C in 50 wt% dimethylformamide solution

Monomer	k_P[P•] (s^{-1})[a)]	Time (min)	Final Conversion (X)
VBBI TFSI	$(2.9 \pm 0.1) \times 10^{-4}$	150	0.70
VBBI BF$_4^-$	$(3.8 \pm 0.8) \times 10^{-5}$	240	0.19
VBIm	$(3.5 \pm 0.2) \times 10^{-5}$	220	0.38
PS	$(2.5 \pm 0.25) \times 10^{-5}$	100	0.10

a) k_P[P•] = apparent rate constant, which was determined from the slope of the kinetic plots found in **Figure 2.2**. [Initiator]$_0$/M = 0.016 copolymerizations initiated by N- hydroxysuccinimidyl BlocBuilder at 90 °C in 50 wt% dimethylformamide solution.

The substituent effects on the polymerization kinetics of styrenics has previously been studied. Mayo et al.[56] demonstrated that during free radical copolymerization, the polymerization rate increases when the vinyl alkenes possess electron-withdrawing substituents. Following this, Imoto et al.[57] reported that the following Hammett relationship could be used in the polymerization of styrenes with para-substituents: $\log(k_{pr}/k_{pH}) = \rho\sigma$, in which σ is the Hammett constant of the substituent, ρ is the reaction constant, and k_{pr}, k_{px}, and k_{pH} are the absolute propagation rate constant of substituted styrene and unsubstituted styrene, respectively. The electronic effect of the substituent is shown by altering the electron density of the double bond via inductive and resonance effects and its ability to stabilize the active species, whether it is a radical, anion, or cation.

Substituent effects are not as present in radical reactions ($\rho < 1$) compared to ionic reactions ($\rho >> 5$).[58-60] However, radical polymerization is affected by substituents due to the participation of polar effects.

With the recent developments of controlled radical polymerization, the influence of substituent effects in these controlled systems has attracted attention. It has been demonstrated that electron-withdrawing substituent groups on styrene increase the rate of polymerization for controlled polymerization utilizing TEMPO/BPO systems, which agrees with observations in conventional free radical polymerization.[61] Further kinetic studies substituent effects in controlled polymerizations have also shown a linear correlation between the apparent rate coefficient, $k_p^{app}[M] = -d([M])/dt$, with a slope, $\rho = 1.50$, for atom transfer radical polymerization (ARTP),[62] $\rho = 1.45$ for TEMPO-mediated polymerization,[63] and $\rho = 0.60$ for conventional free-radical polymerizations[57] where this correlation was first observed. From these observation ($\rho_{controlled} > \rho_{conventional}$), it was deduced that as the higher k_p^{app} observed for styrenics with electron substituents would cause not only a larger k_p but also a larger equilibrium constant, $K_{eq} = k_d/k_c$, where k_d is the rate constant of the alkoxyamine dissociation and k_c is he rate constant for the reversible combination of the propagating radical with the nitroxide. K_{eq} represents the ratio of active propagating chains to dormant, reversibly terminated polymer chains in NMP.[64, 65] The increase in K_{eq} in NMP has been attributed to various causes; for example, Daimon et al.[63] estimated that the increase in K_{eq} is mainly caused by a decrease in k_c, while k_d would not be affected by the styrenic substituents. This is in contrast to explanations from Imoto et al.[57] who attribute the increase in K_{eq} to a increase in k_d, where k_c is much less effected by the substituents. Despite these differences, both give reasoning to explain the trend seen experimentally, where $k_p^{app}(ED) < k_p^{app}(H) < k_p^{app}(EW)$ (in which ED is an electron donating substituents, H is styrene, and EW is an electron withdrawing substituent).

This would suggest that the quaternized imidazole substituent in $VBBI^+TFSI^-$ is significantly more electron withdrawing compared to the un-functionalized imidazole substituent in VBIm. Unfortunately, to the best of our knowledge, Hammett substituent constants for imidazole attached through the nitrogen are absent from the literature.[66] Pratt et al.[67] have shown that imidazole will flexibly act to stabilize both electron-rich phenoxides by inductively

withdrawing electron density and electron-poor phenoxides by donating electron density. Using B3LYP[68, 69] the authors calculated the pK_as and used them to derive values for σ_p^- using the slope of the Hammet correlation used to define the substituent constant ($\sigma- = \Delta pK_a/2.237$),[70] which yielded a value of +0.21. To put this into context, values of σ_p^- for NO_2, F, CH_3, and OCH_3 are +1.25, +0.02, −0.14, and −0.21, respectively. This characterizes imidazole as a moderate σ-EW group corroborating the increase in k_P[P•] observed. Hammett constants of other ion containing substituent groups are significantly greater; for example, the diazonium ion ($N\equiv N^+$) possessing a Hammet constant of $\sigma_p = 1.91$, which could explain why the TFSI containing IL monomer was seen to polymerize appreciably faster compared to the others.[71] The difference observed between the two IL monomers might be due to fact that the TFSI anion is much more weakly coordinating than the BF_4 anion.[72] Substituent groups having a more coordinating mobile anion are shown to possess a lower Hammet parameter, in comparison the diazonium ion with a tetrafluoroborate anion ($N\equiv N^+BF_4^-$) $\sigma_p = 1.79$.[73] Additionally, Harrisson et al. and Carmichael[74, 75] have reported the high effect of ionic liquids as solvents to increase the polymerization rate of MMA due to the high polarity of the polymerization medium. This effect could also explain the high polymerization rates observed since the IL monomer would affect the polymerization medium. The early termination of BF_4 containing monomer still cannot be explained, however, others have noted issues with the BF_4 containing monomer by ATRP.[19] Due to the ease of the polymerization of the TFSI containing monomers, it was selected for further study in copolymers.

2.3.3 Kinetics and Molecular Weight Characterization of VBBI$^+$TFSI$^-$/MMA and VBIm/MMA: Effect of Feed Composition

Conventional radical polymerization of 1-(4-vinylbenzyl)-3-butylimidazolium bis(trifluoromethylsulphonyl)-imide (VBBI$^+$TFSI$^-$) as well as those using ATRP polymerization in bulk were already reported.[20, 76] Apart from the synthesis of a specific nitroxide exclusively devoted to methacrylate monomer,[77] the NMP of methacrylic monomers is difficult to achieve due to a too high equilibrium constant for the propagation step and/or undesired side reactions.[33, 78, 79] As was mentioned, to favour the formation of a stable chain-end alkoxyamine and obtain a controlled/living system, methacrylate monomers are usually copolymerized with a comonomer, which is well controlled by NMP. To demonstrate that the copolymerizations of

MMA/VBBI$^+$TFSI$^-$ and VBIm/MMA were well-controlled, a series of copolymerizations with the target number average molecular weight ($\overline{M}_n$) of 25 kg mol^{-1} were performed. As is summarized in **Table 2.2**, the copolymerization of VBBI$^+$TFSI$^-$ and MMA were performed in a 50 wt% solution of DMF with feed compositions ranging from 5–90 mol% VBBI$^+$TFSI$^-$ (denoted as $f_{VBBI^+TFSI^-,0}$). The copolymerization of VBIm and MMA in similar conditions is summarized in **Table 2.2** as well (feed composition denoted as $f_{VBIM,0}$). First order kinetic plots of $\ln[(1-X)^{-1}]$ versus the time at various feed compositions for the VBBI$^+$TFSI$^-$/MMA copolymerizations are shown in **Figure 2.3a**, and VBIm/MMA copolymerizations are shown in **Figure 2.3b**. At low X, when termination is negligible, the slopes of these plots represent the average apparent rate constants $\langle k_p \rangle[P\bullet]$. It is obvious that as the VBBI$^+$TFSI$^-$ or VBIm content in the feed increased, the apparent rate constants decreased (**Figure 2.3c**). The experimental values of $\langle k_p \rangle[P\bullet]$ as well as the standard deviations from the slopes of the kinetic plots are summarized in **Table 2.3**. The decrease in $\langle k_p \rangle[P\bullet]$ values indicates slower polymerization kinetics, and this is likely to contribute towards the controlled behaviour of the copolymerizations. Generally, a slow increase was observed as $f_{VBIM,0}$ and $f_{VBBI^+TFSI^-,0}$ increased followed by a sudden increase in $\langle k_p \rangle[P\bullet]$ when $f_{VBIm/MMA,0} > 0.8$. This is in agreement with other studies where a rapid increase in $\langle k_p \rangle[P\bullet]$ was observed for MMA-rich feeds at high MMA initial feed concentrations < 80 % mol% by NMP.[43] The rapid increase is likely caused by the large difference in k_p between MMA and the styrenic monomers, VBBI$^+$TFSI$^-$ or VBIm. The addition of 15 mol% of excess SG1 had no significant effect on the copolymerization kinetics (**Figure 2.11**).

To determine if the copolymerizations of VBBI$^+$TFSI$^-$/MMA exhibit controlled behaviour, samples of each copolymerization were taken periodically throughout the polymerization and were analyzed by gel permeation chromatography (GPC) to determine their molecular weight characteristics. A represented series of GPC traces taken from one experiment is shown in **Figure 2.4b**, and the corresponding number average molecular weight, $\overline{M}_n$ versus X plot is found in **Figure 2.4a**. The linear increase in $\overline{M}_n$ with conversion and the narrow GPC chromatograms suggests a controlled copolymerization. The linear behaviour of $\overline{M}_n$ versus X, suggested methacrylates can be copolymerized with VBBI$^+$TFSI$^-$, resulting in a controlled copolymerization.

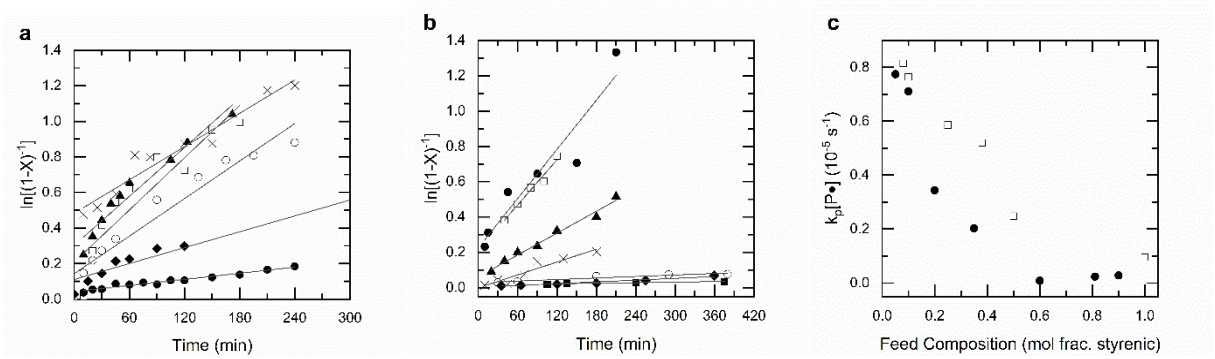

Figure 2.3 Representative kinetic plots of $\ln[(1-X)^{-1}]$ (X = conversion) versus polymerization time for: (a) 4-vinylbenzyl butylimidazole/methyl methacrylate ($VBBI^+TFSI^-$/MMA) random copolymerization at various initial $VBBI^+TFSI^-$ feed concentrations ($f_{VBBI^+TFSI^-,0}$): $f_{VBBI,0}$ = 0.08 (open squares, □); $f_{VBBI^+TFSI^-,0}$ = 0.10, (filled triangles, ▲); $f_{VBBI,0}$ = 0.25, (open circles, ○); $f_{VBBI^+TFSI^-,0}$ = 0.38 (cross signs, ×); $f_{VBBI^+TFSI^-,0}$ = 0.50 (filled diamonds, ♦); $f_{VBBI^+TFSI^-,0}$ = 1.00 (filled circles, ●) and (b) 4-vinylbenzyl/methyl methacrylate (VBIm/MMA) random copolymerization at various initial VBIm feed concentrations ($f_{VBIm,0}$): $f_{VBIm,0}$ = 0.05 (filled circles, ●); $f_{VBIm,0}$ = 0.10 (open squares, □); $f_{VBIm,0}$ = 0.20, (filled triangles, ▲); $f_{VBIm,0}$ = 0.35, (cross signs, ×); $f_{VBIm,0}$ = 0.60 (filled squares, ■); $f_{VBIm,0}$ = 0.81 (open circles, ○); $f_{VBIm,0}$ = 0.90 (filled diamonds, ♦). All copolymerizations were done at 90°C in 50 wt% DMF solutions with NHS-BlocBuilder unimolecular initiator. (c) Plot of apparent rate constant k_P[P•] (k_P = average propagation rate constant, [P·] = concentration of propagating macroradicals) as a function of various initial VBIm and $VBBI^+TFSI^-$ molar feed concentrations $f_{VBIm,0}$ for VBIm/MMA (open squares, □) and $f_{VBBI^+TFSI^-,0}$ for $VBBI^+TFSI^-$/MMA (filled circles, ●). The k_P[P•] were obtained from the slopes of the kinetic plots shown in a) and b) in the linear regions.

Table 2.2 4-vinylbenzyl imidazole/methyl methacrylate random copolymerizations and 1-(4-vinylbenzyl)-3-butylimidazolium bis(trifluoromethylsulphonyl)-imide/methyl methacrylate random copolymerizations initiated by N- hydroxysuccinimidyl BlocBuilder at 90 °C in 50 wt% dimethylformamide solution

Experimental. ID [a]	Monomer	$f_{monomer,0}$ [b]	F_{mono} [c]	k_P[P•] (s^{-1})[c)]	Polymerization Time	Final Conversion (X)[d]
VBBI/MMA-08	VBBI	0.075	0.10	$(8.15 \pm 9.75) \times 10^{-5}$	180	0.63
VBBI/MMA-10	VBBI	0.10	0.19	$(7.64 \pm 0.11) \times 10^{-5}$	172	0.64
VBBI/MMA-25	VBBI	0.25	0.49	$(5.86 \pm 6.48) \times 10^{-5}$	240	0.59
VBBI/MMA-40	VBBI	0.38	0.71	$(5.20 \pm 7.28) \times 10^{-5}$	240	0.70
VBBI/MMA-50	VBBI	0.50	0.86	$(2.48 \pm 1.13) \times 10^{-5}$	1080	0.79
VBBI/MMA-H	VBBI	1.00	1.00	$(2.92 \pm 0.13) \times 10^{-4}$	240	0.17
VBIm/MMA-5	VBIm	0.05	0.10	$(2.65 \pm 0.47) \times 10^{-4}$	210	0.74
VBIm/MMA-10	VBIm	0.10	0.25	$(7.10 \pm 0.26) \times 10^{-5}$	120	0.53
VBIm/MMA-20	VBIm	0.20	0.38	$(4.60 \pm 0.59) \times 10^{-5}$	210	0.40
VBIm/MMA-35	VBIm	0.35	0.56	$(2.79 \pm 0.28) \times 10^{-5}$	180	0.18
VBIm/MMA-60	VBIm	0.60	0.90	$(3.26 \pm 0.23) \times 10^{-6}$	375	0.03
VBIm/MMA-80	VBIm	0.81	0.96	$(2.78 \pm 0.79) \times 10^{-6}$	380	0.07
VBIM/MMA-90	VBIm	0.90	0.98	$(1.42 \pm 0.74) \times 10^{-6}$	410	0.07

a) Experimental ID, *X*/MMA-*Y*: where *X* = VBIm = 4-vinylbenzyl imidazole, VBIm = 4-vinylbenzyl imidazole, MMA = methyl methacrylate, and *Y* corresponds to the molar feed of $VBBI^+TFSI^-$ or VBIm, in all cases, $[Initiator]_0/M = 0.016$ copolymerizations initiated by N-hydroxysuccinimidyl BlocBuilder at 90 °C in 50 wt% dimethylformamide solution.

b) $f_{VBIm,0}$ = initial molar feed of VBIm, and F_{VBIm}, = final copolymer composition determined by ^1H NMR.

c) k_P[P•] = apparent rate constant, determined from the slope of the linear region of the kinetic plots found in **Figure 2.3b**.

d) Final conversion determined by gravimetry.

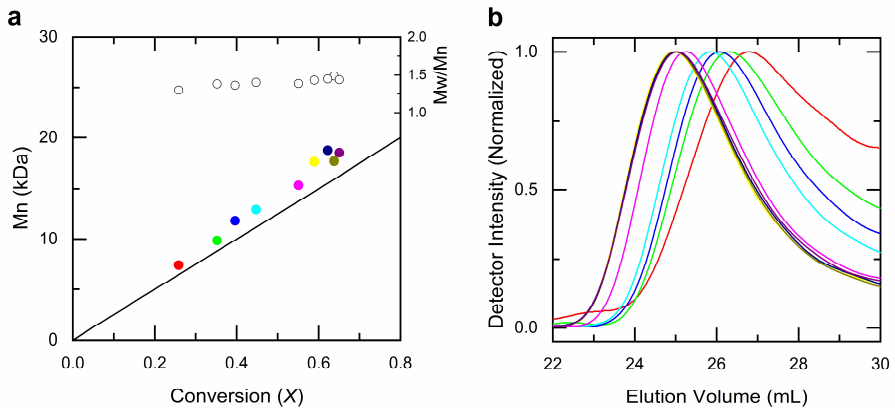

Figure 2.4 (a) Evolution of experimental number average molecular weight, $\overline{M}_n$ with X; (b) Gel permeation chromatograms (THF solution with 10 mmol L^{-1} of LiTFSI and 10 mmol L^{-1} 1-butylimidazole) of experiment $VBBI^+TFSI^-$/MMA-10 (initial molar feed fraction $f_{VBBI+TFSI-,0} = 0.10$) with samples taken at the following intervals: (red line, $X = 0.26$, $\overline{M_n} = 7.41\ kg\ mol^{-1}, \overline{M_w}/\overline{M_n} = 1.30$); 30 min (green line, $X = 0.35$, $\overline{M_n} = 9.86\ kg\ mol^{-1}, \overline{M_w}/\overline{M_n} = 1.38$); 45 min (blue line, $X = 0.40$, $\overline{M_n} = 11.83\ kg\ mol^{-1}, \overline{M_w}/\overline{M_n} = 1.36$); 60 min (cyan line, $X = 0.45$, $\overline{M_n} = 12.95\ kg\ mol^{-1}, \overline{M_w}/\overline{M_n} = 1.40$); 120 min (pink line, $X = 0.55$, $\overline{M_n} = 15.37\ kg\ mol^{-1}, \overline{M_w}/\overline{M_n} = 1.39$); 180 min (yellow line, $X = 0.59$, $\overline{M_n} = 17.63\ kg\ mol^{-1}, \overline{M_w}/\overline{M_n} = 1.43$); 240 min (dark yellow line, $X = 0.64$, $\overline{M_n} = 17.68\ kg\ mol^{-1}, \overline{M_w}/\overline{M_n} = 1.49$); 300 min (navy line, $X = 0.62$, $\overline{M_n} = 18.74\ kg\ mol^{-1}, \overline{M_w}/\overline{M_n} = 1.45$); 360 min (purple line, $X = 0.65$, $\overline{M_n} = 18.50\ kg\ mol^{-1}, \overline{M_w}/\overline{M_n} = 1.44$).

It should also be noted that polymerizations of low ionic liquid in the feed exhibited linearity when plotted versus $t^{2/3}$ rather than t. The linearity of the kinetic plots when plotted as $\ln[(1-X)^{-1}]$ versus $t^{2/3}$ rather than t lies in the persistent radical effect (PRE). According to Fischer[80] and Fukuda and Goto's[81] work, the minimization of the irreversible termination in the NMP process is governed by the PRE. Consider an alkoxyamine compound (P-SG1) that decomposes into a transient radical (P •) and a persistent radical (SG1 •). This persistent radical effect leads to two unusual rate laws for P • and SG1 • during the intermediate regimes:

$$[\text{SG1}\bullet] = \left(\frac{3k_t k_d^2 [RY]_0^2}{k_c^2}\right)^{1/3} t^{1/3} \qquad (2.1)$$

$$[\text{R}\bullet] = \left(\frac{k_d [RY]_0}{3k_t k_c}\right)^{-1/3} t^{1/3} \qquad (2.2)$$

where k_d, k_c, and k_t are the rate constants of the decomposition reaction, the combination reaction of RY and the termination reaction between two R•, respectively. Therefore, the kinetic law of monomer concentration is thus given by the following:

$$ln[(1-X)^{-1}] = \frac{3k_p}{2}\left(\frac{k_d[RY]_0}{3k_t k_c}\right)^{1/3} t^{2/3} \qquad (2.3)$$

hence, the plots of $\ln[(1-X)^{-1}]$ versus time will show a downward curvature whereas the plots of $\ln[(1-X)^{-1}]$ versus $t^{2/3}$ are linear. This persistent radical effect has been shown experimentally in the NMP of styrene and acrylates by different groups.[82-84]

Normally when dealing with high propagation rate constant monomers, an initial excess of persistent radicals is added at the beginning of the polymerization process to slow down its rate and improve polymerization control.[36, 85] Under these conditions, the concentration of the transient radicals reaches the stationary value, $[\mathrm{R}\bullet]_{stationary} = K\,[R-\mathrm{SG1}]_0/[\mathrm{SG1}\bullet]_0$ (where $K = k_d/k_c$), and the linear evolution of the polymerization index $\ln[(1-X)^{-1}]$ with time is generally observed.[86, 87] However, since the self-termination of the propagating radicals increases with the polymerization time and causes an additional [SG1•], when this released nitroxide, [SG1•], exceeds the initial one, $[\mathrm{SG1}\bullet]_0$, the behaviour of the system turns to that observed without the initial persistent species. Souaille and Fischer[87] theoretically demonstrated that if $[\mathrm{SG1}\bullet]_0 > \left(3[\ln(10)]K[RY]_0\,k_t/k_p\right)^{1/2}$, the polymerization index $\ln[(1-X)^{-1}]$ varies linearly with *t*. In contrast, if $[\mathrm{SG1}\bullet]_0 < \left(3K[R-\mathrm{SG1}]_0\,k_t/k_p\right)^{1/2}$, the initial presence of the persistent species has no influence, and the polymerization index $\ln[(1-X)^{-1}]$ increases linearly with $t^{2/3}$. Depending on the polymerization system, the propagation can take place in the first mode or could happen in both modes and in certain cases; the persistent species has no influence and the kinetics vary with time as $t^{2/3}$. In the case of $VBBI^+TFSI^-$, no values of k_p and k_t are available in the literature, thus, it is difficult to determine if $[\mathrm{SG1}]_0$ was higher than $\left(3[\ln(10)]K[NHS-BB]_0\,k_t/k_p\right)^{1/2}$ or lower than $\left(3K[NHS-BB]_0\,k_t/k_p\right)^{1/2}$. The inability to suppress this PRE with additional SG1 has been seen by others who have attempted to polymerize ionic liquid monomers via NMP.[88]

Poly(VBIm-*co*-MMA) appeared to be soluble in THF, but a very weak detector response was observed from the RI detector during GPC measurements when using THF as the eluting solvent. The imidazole groups in the copolymers are not fully soluble in THF, resulting in column interactions and, thus, significant tailing is apparent in the GPC traces. Due to the severity of this phenomenon, GPC measurements were unattainable for copolymers synthesized using $f_{VBIm,0} >$ 0.05. **Figure 2.19** in the supporting information illustrates a typical GPC spectrum of VBIm containing copolymers that stick to the column.

2.3.4 A Study of Copolymer Compositions: Reactivity Ratios

The final copolymer composition will have a significant effect on the material properties and, therefore, being able to predict the copolymer composition is crucial. For example, researchers have shown increased conductivity when controlling the molecular architecture such as the use of block/gradient PIL copolymers.[89] Therefore, knowledge of the monomer reactivity ratios for the system will facilitate the design of the desired poly(MMA-co-VBBI$^+$TFSI$^-$) copolymers. To determine the copolymer reactivity ratios, copolymerizations were conducted using the same procedure used for the kinetic experiments, except all polymerizations were intentionally stopped at low conversion ($X < 0.10$) to prevent compositional drift. Five initial feed compositions of VBBI$^+$TFSI$^-$ relative to MMA (molar feed compositions of 5, 10, 25, 38, and 50 %) and seven initial feed compositions of VBIm relative to MMA (molar feed compositions of 8, 10, 25, 38, and 50 %) were copolymerized in a 50 wt% solution of DMF at 90 °C. The resulting copolymers were analyzed by ^{1}H NMR, the results are displayed in **Figure 2.5**, where the initial molar feeds were plotted relative to the final copolymer compositions ($X < 0.10$).

Reactivity ratios of the monomer pairs were determined using the Mayo-Lewis equation:[90]

$$F_1 = \frac{r_1 f_1^2 + f_1 f_2}{r_1 f_1^2 + 2 f_1 f_2 + r_2 f_2^2 + r_2 f_2^2} \qquad (2.4)$$

$$r_1 = \frac{k_{p11}}{k_{p12}} \; and \; r_2 = \frac{k_{p22}}{k_{p21}} \qquad (2.5 \; \& \; 2.6)$$

where the copolymer composition F_1 with the initial feed composition f_1 and f_2 are defined as a function of the reactivity ratios r_1 and r_2. The subscripts 1 and 2 denote the monomer of type 1 (VBBI$^+$TFSI$^-$ or VBIm in this case) and monomer of type 2 (MMA in this case), respectively.

Therefore, $f_{x,0}$ and $F_{x,10}$ (x denoting VBBI$^+$TFSI$^-$ or VBIm) listed in **Table 2.2** were substituted into the Mayo-Lewis equation as f_1 and f_2 for reactivity ratio determination. The reactivity ratios were determined by solving the Mayo-Lewis equation through the Fineman-Ross (FR),[91] Kelen-Tüdõs (KT),[92] and the error-and-variables (EVM)[93] approaches. The resulting reactivity ratios obtained from all three techniques can be found in **Table 2.3**. Linearization methods such as the Fineman-Ross[91] approach is generally biased since not all data points are weighted equally. The Kelen and Tüdõs[92] approach reduces the bias by introducing an adjusting parameter, but it still solves the Mayo-Lewis equation indirectly via reduced variables. The solving of both the FR and KT methods, along with the linearization plots, can be found in the supporting information (Figure 2.13 to 2.18). The Mayo-Lewis equation is characteristically non-linear, thus, linearization methods such as FT and FR can be argued as inaccurate.[94-96] Nonlinear least squares (NILS) methods and more advanced error-in-variables (EVM) methods have been developed and shown to be more appropriate for use with the nonlinear Mayo-Lewis model. The EVM method was implemented to determine a more accurate estimation of the reactivity ratios using the values solved by the linearization KT method as first estimates and is displayed in **Figure 2.5**.[96-99]

Table 2.3 Reactivity ratios determined by Fineman-Ross, Kelen-Tüdõs, and error-in-variables method[a)]

Comonomers	Fineman-Ross		Kelen-Tudos		Error-in-Variables Method	
VBBI/MMA	r_{VBBI} = 12.12	r_{MMA} = 1.23	r_{VBBI} = 11.57	r_{MMA} = 1.18	r_{VBBI} = 11.71	r_{MMA} = 1.21
VBIm/MMA	r_{VBIm} = 5.45	r_{MMA} = 0.52	r_{VBIm} = 5.56	r_{MMA} = 0.56	r_{VBIm} = 3.61	r_{MMA} = 0.46

[a)] VBBI refers to VBBI$^+$TFSI$^-$

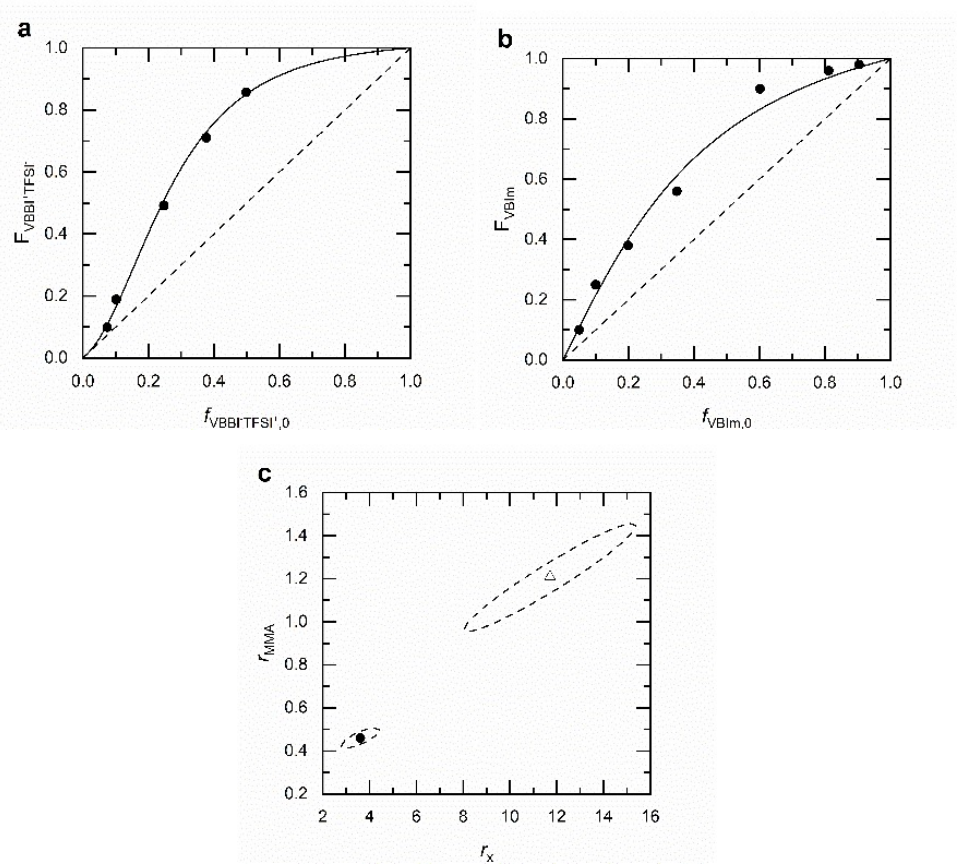

Figure 2.5 Mayo-Lewis plots of the following: (a) 4-vinylbenzyl imidazole/methyl methacrylate (VBIm/MMA); and (b) 4-vinylbenzyl butylimidazole ($VBBI^+TFSI^-$/MMA). The experimental data for copolymerizations performed in DMF at 90 °C using NHS-BB as the unimolecular initiator is indicated by the solid circles, while the solid line indicates the fit from the reactivity ratios determined by error-in-variables model fit to the Mayo-Lewis equation given in **Table 2.4**. The dashed line indicated the azeotropic composition. **Tables 2.1 and 2.2** list the experiments used for the plots. (d) The 95 % joint confidence region for $VBBI^+TFSI^-$/MMA (open triangle, Δ) and VBIm/MMA (filled circle, ●).

In both cases, $r_{VBBI} > r_{MMA}$ and $r_{VBIm} > r_{MMA}$ suggest a favourable addition of the controlling comonomer relative to MMA. In all three cases the resulting copolymer will end up as a gradient copolymer with the propagation end of the polymer, which is rich in MMA and the initiation end rich in the styrenic. Previous studies have shown that the styrenics ability to control the copolymerization of the methacrylate is directly correlated to the reactivity ratios; if the addition of the styrenic is favoured, we will have a controlled copolymerization to as high as $f_{MMA,0}$ ≈ 0.95-0.9.[44] On the contrary, if there is a strong propensity for the methacrylate to propagate over

the styrenic, then the controlled copolymerization is only possible with very high reactivity ratios; for example, methacrylic acid (MAA) and pentafluorostyrene (PFS) requires $f_{PFS,0} > 0.60$ to obtain a controlled copolymerization.[99] These results further suggest that the copolymerization of MMA and $VBBI^+TFSI^-$ or VBIm results in a controlled copolymerization over a large range of feed compositions.

2.3.5 Chain Extension of $VBBI^+TFSI^-$/MMA Random Copolymers with Styrene

Chain extensions with styrene were performed to examine the ability of the $VBBI^+TFSI^-$/MMA macroinitiators synthesized from direct polymerization of the ionic liquid monomer and from the functionalized precursor polymers to cleanly initiate a second batch of monomer. The $\bar{M}_n$ and $\bar{M}_w/\bar{M}_n$ of the samples were analyzed by GPC and compared to those of the macroinitiators. As the GPC chromatograms in **Figure 2.6** indicate, clear shifts of $\bar{M}_n$ (from 38 kg mol^{-1} to 76 kg mol^{-1}) were observed, which implied a nearly simultaneous growth of all chains, suggesting that the majority of the copolymers are pseudo-living enough to reinitiate a fresh batch of monomer (resulting in well-defined block copolymers). However, a slight increase in $\bar{M}_w/\bar{M}_n$ was observed for the block copolymer, suggesting that there was likely a small fraction of dead chains that were present in the macroinitiators. It should be noted that although the evolution of $\bar{M}_n$ with conversion of VBIm/MMA copolymerization could not be obtained due to the incompatibility of VBIm with the GPC, one could suggest these polymerizations were still of a controlled nature based on the narrow dispersity of the functionalized VBIm precursor polymers. Overall, these chain extension results illustrate the pseudo-living nature of poly($VBBI^+TFSI^-$-*co*-MMA) copolymers synthesized by both routes (direct and post functionalization) and establish a simple trajectory towards the synthesis of block copolymer containing PILs by NMP.

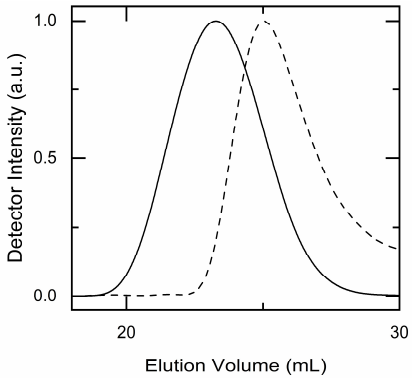

Figure 2.6 Gel permeation chromatograms (GPC) for chain extension from poly(VBBI$^+$TFSI$^-$-co-MMA) macroinitiators with a batch of styrene. The dashed line is the VBBI$^+$TFSI$^-$/MMA-10 macroinitiator ($\overline{M}_n$ = 18.50 kg mol^{-1}, $\overline{M}_w/\overline{M}_n$= 1.44) and the solid line is the block copolymer ($\overline{M}_n$ = 82.21, $\overline{M}_w/\overline{M}_n$ = 1.47). Chain extensions were performed in 50 wt% DMF solutions at 110 °C.

2.4 Conclusion

We have demonstrated that well-defined poly(VBBI$^+$TFSI$^-$-*co*-MMA) copolymers can be produced via NMP by both pre and post-functionalization approaches. All of the polymerization systems appear to proceed in a well-controlled manner, as is confirmed by several factors such as linear semi logarithmic plots of $\ln[(1-X)^{-1}]$ versus time, linear increase in the number-average molecular weight with the conversion, and narrow dispersity. The resulting copolymers were sufficiently pseudo-living to reinitiate a fresh batch of styrene and produce well-defined PIL containing block copolymers.

From the methodologies examined, we found that direct polymerization of the VBBI$^+$TFSI$^-$ monomer obtained via reaction with CMS and quaternization with butylimidazole is the ideal synthetic pathway if better methods could be developed to isolate the polymer. Any methods involving VBIm were determined to be unfavourable as it has disadvantageous qualities such as a tedious synthesis and/or lack of compatibility with GPC. In this study, we have reported the homopolymerization and copolymerization kinetics, molecular weight characteristics, and the reactivity ratios for these previously understudied materials.

This study reports the first example of a synthesis of well defined, pseudo-living methacrylate/PIL copolymers by NMP. This study establishes a protocol for obtaining PIL random

and block copolymers with methacrylic units, which will serve as an essential platform in the development of tunable PILs for next-generation applications such as in organic electronics.

2.5 Experimental

2.5.1 General Polymerization Procedure

All polymerizations were performed in a 100 mL three-neck round-bottom glass flask equipped with a condenser, thermal well, and a magnetic Teflon stir bar. The flask was placed inside a heating mantle, and the equipment was placed on a magnetic stirrer. Table 1 lists all the formulations studied. All polymerizations used a target number-average molecular weight ($\bar{M}_n$) at complete conversion of 25 kg mol^{-1}. The target degree of polymerization and hence $\bar{M}_n$ was calculated using the moles of total monomer relative to the moles of NHS-BB initiator added initially. A specific formulation for an initial feed composition of VBIm ($f_{\mathrm{VBIm},0}$) equal to 0.35 is given as an example (VBIm-*co*-MMA-35 in **Table 2.1**). 1-(4-vinylbenzyl)imidazole (VBIm) (2.99 g, 16.2 mmol), MMA (3.01 g, 30.1 mmol), NHS-BB (0.072 g, 0.15 mmol), and DMF solvent (12.00 g, 164.2 mmol) were added to the reactor, and mixing commenced with the stir bar. A thermocouple was inserted through one of the reactor ports via a temperature well and connected to a controller. To the second neck, the condenser was connected, which was connected to recirculating water to prevent the loss of the monomers and solvent due to evaporation and to a nitrogen purge. Before heating, the reactor mixture was bubbled using nitrogen for a minimum of 20 min under constant stirring to remove the dissolved oxygen. The reactor was then heated to the appropriate temperature (90 °C) at a rate of about 10 °C min^{-1} while maintaining a nitrogen purge. The initial polymerization time was taken when the reactor temperature reached 90 °C. Samples were taken with a syringe periodically for a period of 2 h, after which the reaction mixture was precipitated with diethyl ether (VBBI^{+}TFSI^{-}/MMA copolymers were unable to be isolated by precipitation). For the specific example cited, the polymerization was stopped after 2 h. After precipitation, the crude polymer was re-dissolved in tetrahydrofuran (THF) and precipitated once more into diethyl ether to remove the unreacted VBIm more effectively. After precipitation, the polymer was obtained by filtration and dried overnight in a vacuum oven at 70 °C to remove any additional solvent or unreacted monomer.

Table 2.4 Formulations for 1-(4-vinylbenzyl)-3-butylimidazolium bis(trifluoromethylsulphonyl)-imide/methyl methacrylate and for 4-vinylbenzyl imidazole/methyl methacrylate random copolymerization initiated by N- hydroxysuccinimidyl BlocBuilder at 90 8C in 50 wt% dimethylformamide solution

Experimental. ID	Monomer	$[monomer]_0$/M	$[MMA]_0$/M	$[DMF]_0$/M
VBBI/MMA-7.5	VBBI	0.2	2.2	8.7
VBBI/MMA-10	VBBI	0.2	2.0	8.8
VBBI/MMA-25	VBBI	0.4	1.2	8.9
VBBI/MMA-40	VBBI	0.5	0.7	9.0
VBBI/MMA-50	VBBI	0.5	0.5	9.0
VBIm/MMA-5	VBIm	0.2	2.9	8.6
VBIm/MMA-10	VBIm	0.3	2.6	8.7
VBIm/MMA-20	VBIm	0.5	2.2	8.7
VBIm/MMA-35	VBIm	0.9	1.6	8.8
VBIm/MMA-60	VBIm	1.3	0.9	8.9
VBIm/MMA-80	VBIm	1.6	0.4	8.9
VBIM/MMA-90	VBIm	1.7	0.2	9.0

[a] Experimental ID, *X*/MMA-*Y*: where *X* = VBIm = 4-vinylbenzyl imidazole, VBBI = 1-(4-vinylbenzyl)-3-butylimidazolium bis(trifluoromethylsulphonyl)-imide, MMA = methyl methacrylate, and *Y* corresponds to the molar feed of VBBI or VBIm in all cases. $[Initiator]_0$/M = 0.016 copolymerizations initiated by N- hydroxysuccinimidyl BlocBuilder at 90 °C in 50 wt% dimethylformamide solution.

2.5.2 Quaternization and Anion Exchange of VBIm Containing Copolymers

The quaternization of the poly(VBIm) was adapted from Green et al.[50] Poly(VBIm) / poly(VBIm-co-MMA) polymers, bromobutane (1.5 equivalent) and THF were added to a 100 mL round-bottom flask with a magnetic stir bar and placed upon a heating mantle under a nitrogen atmosphere. The flask was heated to 60 °C and left overnight. The reaction mixture was allowed to cool and precipitated into excess hexanes. The solid functionalized polymer was isolated by filtration and dried overnight in a vacuum. The functionalized polymer and LiTFSI were dissolved in DMA and left to mix at 25 °C overnight. Next, the solution was precipitated into water. The solid polymer was washed with excess water and dried overnight in a vacuum, yielding the final functionalized polymer with $TFSI^-$ salt.

2.5.3 Chain Extension of Poly(1-(4-vinylbenzyl)-3-butylimidazolium bis(trifluoro-methylsulphonyl)-imide-co-methyl methacrylate) with Styrene

The chain extensions of poly($VBBI^+TFSI^-$-*co*-MMA) with styrene were performed in a 100 mL 3 neck round-bottom glass flask equipped with a condenser, thermal well, and a magnetic Teflon stir bar similar to that of the poly($VBBI^+TFSI^-$-*co*-MMA) and poly(VBIm-co-MMA) copolymerizations. The poly($VBBI^+TFSI^-$-*co*-MMA) macroinitiators (0.25 g), styrene (10 g,

96.02 mmol), and DMF (20 g, 273.64 mmol) were added, and the reactor was then sealed with a rubber septum. A thermocouple was inserted through one of the reactor ports via a temperature well and connected to a controller. To the second neck, the condenser was connected, which was also connected to recirculating water to prevent loss of the monomers and solvent due to evaporation and to a nitrogen purge. Before heating, the reactor mixture was bubbled using nitrogen for a minimum of 20 min under constant stirring to remove dissolved oxygen. The reactor was then heated to the appropriate temperature (110 °C) at a rate of about 10 °C min^{-1} while maintaining a nitrogen purge. The polymerization was left to run overnight, after which the reaction mixture was precipitated with methanol. After precipitation, the crude polymer was re-dissolved in tetrahydrofuran (THF) and precipitated once more into methanol to remove the unreacted styrene more effectively. After precipitation, the polymer was obtained by filtration and dried overnight in a vacuum oven at 70 °C to remove any additional solvent or unreacted monomer.

2.5.4 $VBBI^{+}TFSI^{-}$ Monomer Synthesis (Alternative Route)

1-(4-vinylbenzyl)-3-butylimidazolium bis(trifluoromethylsulphonyl)-imide was synthesized via two different synthetic routes, the first being from Bara et al.[14] and the second described as follows: 4-vinylbenzyl imidazole (1.00 g, 5.4 mmol), VBIm, and 1-bromobutane (0.74 g, 5.4 mmol) were added to a 100 mL single neck round-bottom glass flask, which was then equipped with a condenser and a magnetic Teflon stir bar and was set upon a heating mantle and magnetic stirrer. The reaction vessel was heated to 50 °C and its contents were left to react for 24 h. Next, the reaction mixture was cooled and then added to 50 mL of water. LiTFSI (1.71 g, 5.94 mmol) was added to the reaction mixture and was set to stir for 24 h and an organic phase was formed. The organic phase was then separated from the aqueous phase to yield the $VBBI^{+}TFSI^{-}$ monomer. ^{1}H NMR characteristics and plots can be found in the supporting information (**Figures 2.7 and 2.8**).

2.6 Acknowledgments

The authors are very grateful for financial support from the NSERC Discovery Grant to B. H. L. The authors also thank Professor Milan Maric (McGill University) for the use of his GPC, Prof Marc Dubé for the donation of the BlocBuilder-MA, which was originally obtained from

Arkema, and for the MatLab code used for the determination of the reactivity ratios by sum of least squares.

2.7 Supporting Information

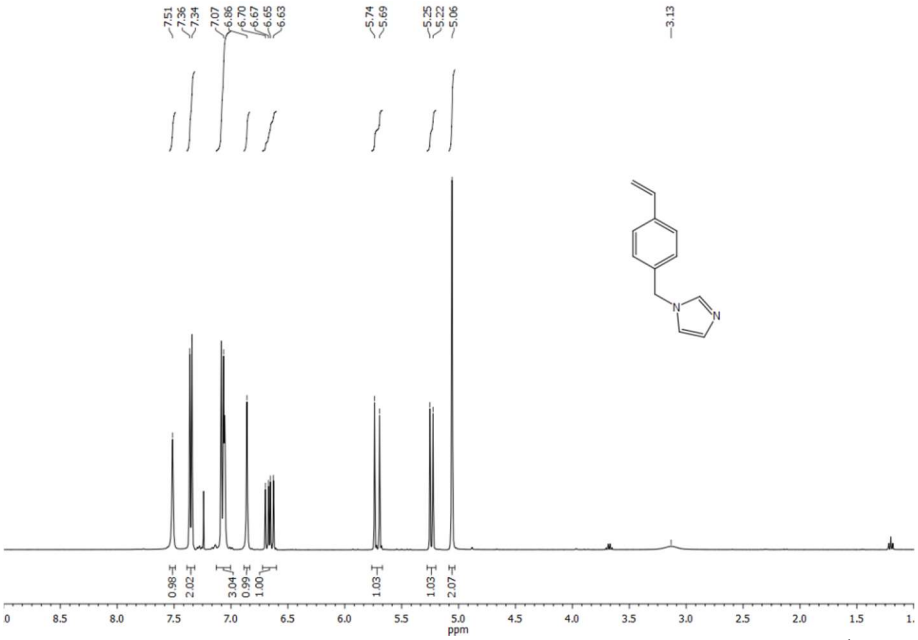

Figure 2.7. ^{1}H NMR in deuterated chlororoform of 4-vinylbenzyl imidazole (VBIm). ^{1}H NMR (400 MHz, Chloroform-*d*) δ 7.51 (s, 1H), 7.35 (d, *J* = 7.8 Hz, 2H), 7.07 (s, 3H), 6.86 (s, 1H), 6.66 (dd, *J* = 17.6, 10.8 Hz, 1H), 5.72 (d, *J* = 17.6 Hz, 1H), 5.24 (d, *J* = 10.8 Hz, 1H), 5.06 (s, 2H).

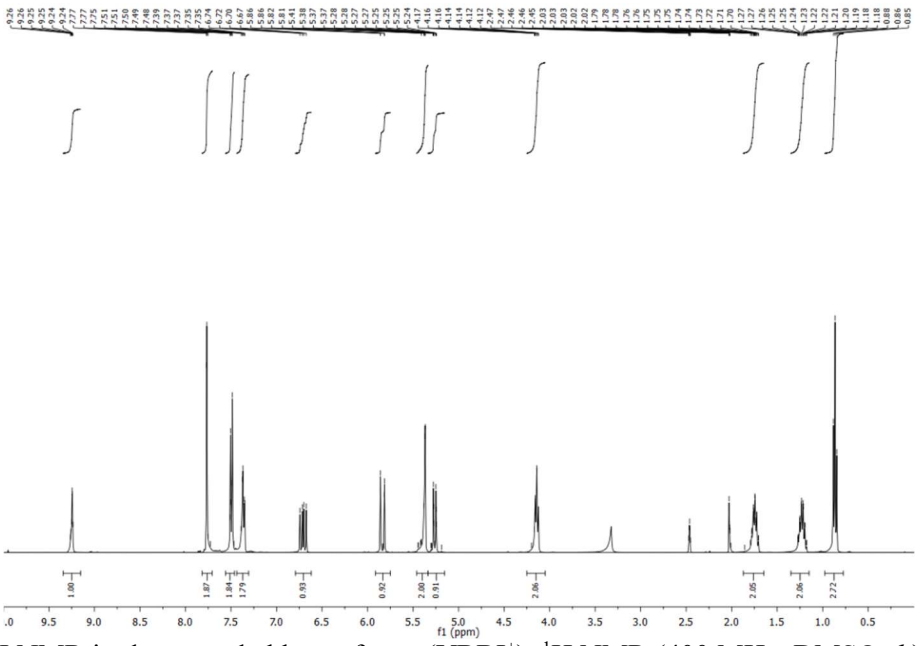

Figure 2.8. ^{1}H NMR in deuterated chlororoform (VBBI$^+$). ^{1}H NMR (400 MHz, DMSO-d_6) δ 9.25 (t, *J* = 2.3 Hz, 1H), 7.77 (d, *J* = 1.7 Hz, 2H), 7.56 – 7.46 (m, 2H), 7.36 (dd, *J* = 8.2, 1.8 Hz, 2H), 6.71 (dd, *J* = 17.7, 10.9 Hz, 1H), 5.84 (dd, *J* = 17.7, 1.0 Hz, 1H), 5.46 – 5.34 (m, 2H), 5.26 (dq, *J* = 10.8, 0.9 Hz, 1H), 4.14 (td, *J* = 7.3, 1.3 Hz, 2H), 1.87 – 1.65 (m, 2H), 1.23 (dqd, *J* = 15.5, 8.6, 7.5, 5.0 Hz, 2H), 0.86 (t, *J* = 7.4 Hz, 3H).

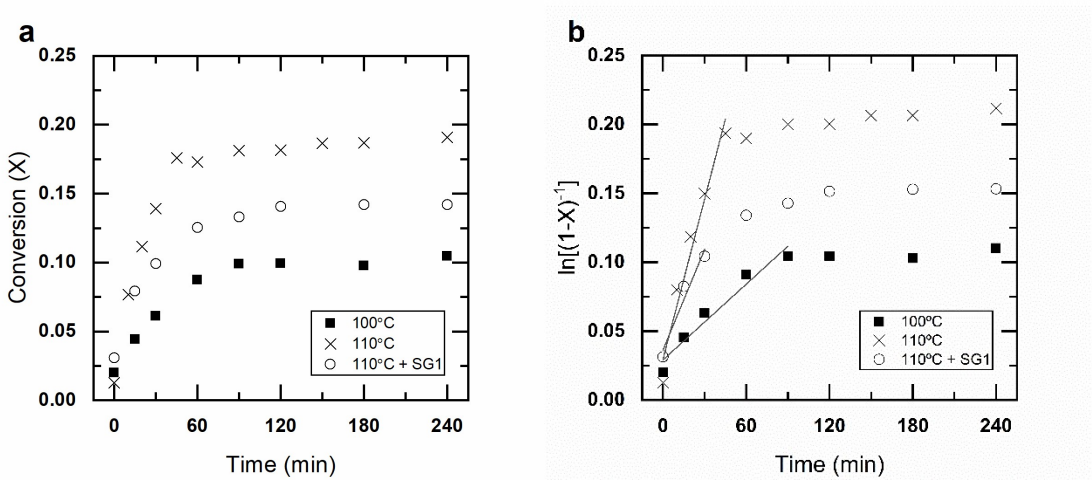

Figure 2.9. (a) Conversion (X) versus polymerization polymerization time and (b) $\ln[(1-X)^{-1}]$ versus polymerization time for homopolymerizations of $VBBI^{+}BF_4^{-}$ monomer. All homopolymerizations were performed in 50 wt% DMF solutions with NHS-BlocBuilder unimolecular initiator at 100 °C (filled squares, ■), 110°C (cross signs, ×), and 110°C (open circles, ○) with 15% excess SG1

Table 2.5. Homopolymerizations of 1-(4-vinylbenzyl)-3-butylimidazolium tetrafluoroborate initiated by N- hydroxysuccinimidyl BlocBuilder at 110°C in 50 wt % dimethylformamide solution

Monomer	**k_P[P•] (s^{-1})[a)]**	**Time**	**Final Conversion (X)**
100	$(1.5 \pm 0.2) \times 10^{-5}$	420	0.10
110	$(6.5 \pm 0.5) \times 10^{-5}$	240	0.19
110 SG1	$(6.1 \pm 0.8) \times 10^{-5}$	413	0.15

a) k_P[P•] = apparent rate constant, determined from the slope of the kinetic plots found in **Figure 2.9b**

Precursor Polymer Functionalization

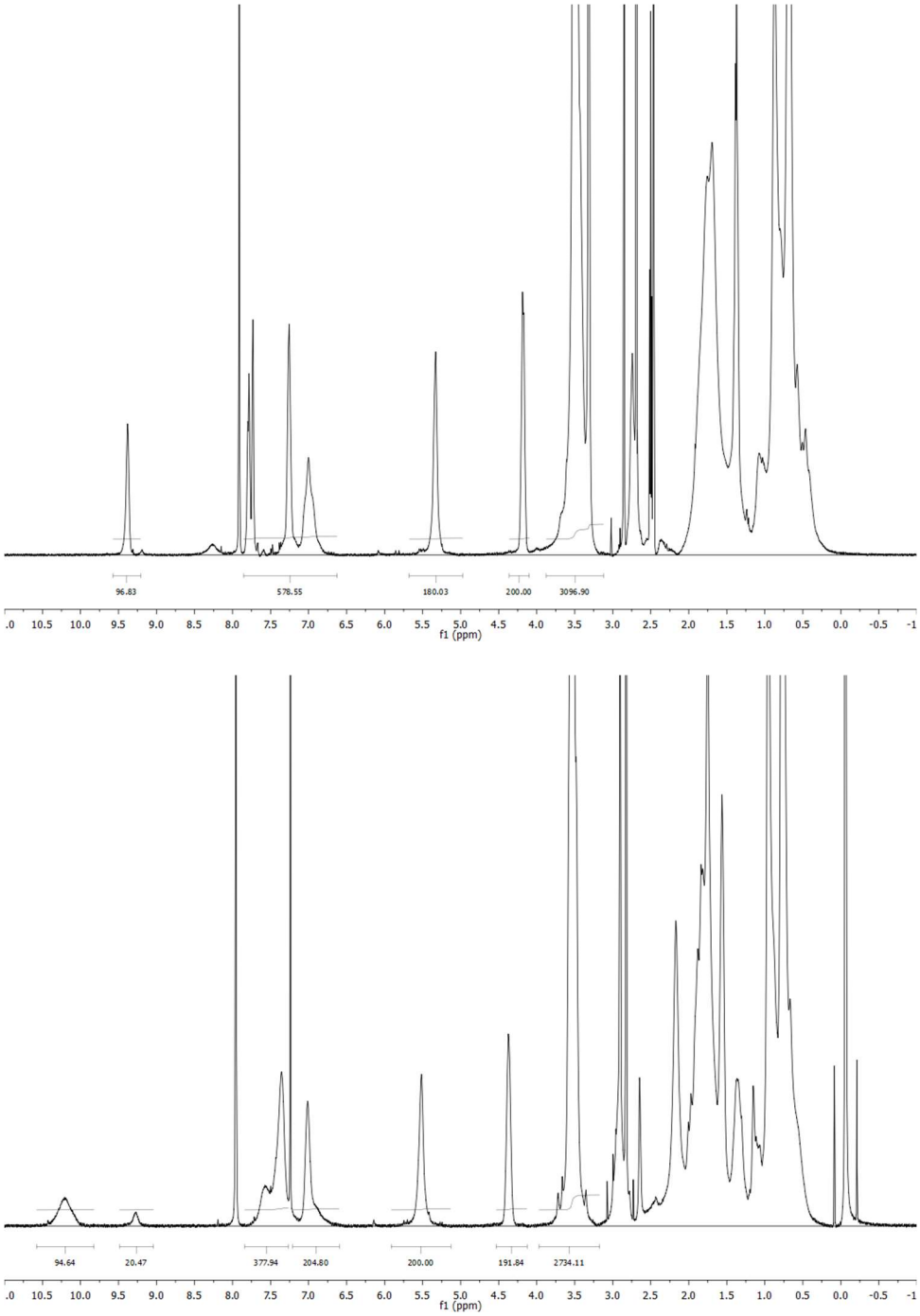

Figure 2.10. Poly(VBIm-co-MMA) before / after quaternization [to form poly(VBBI TFSI-co-MMA)].

Effect of Excess SG1 on VBBI TFSI

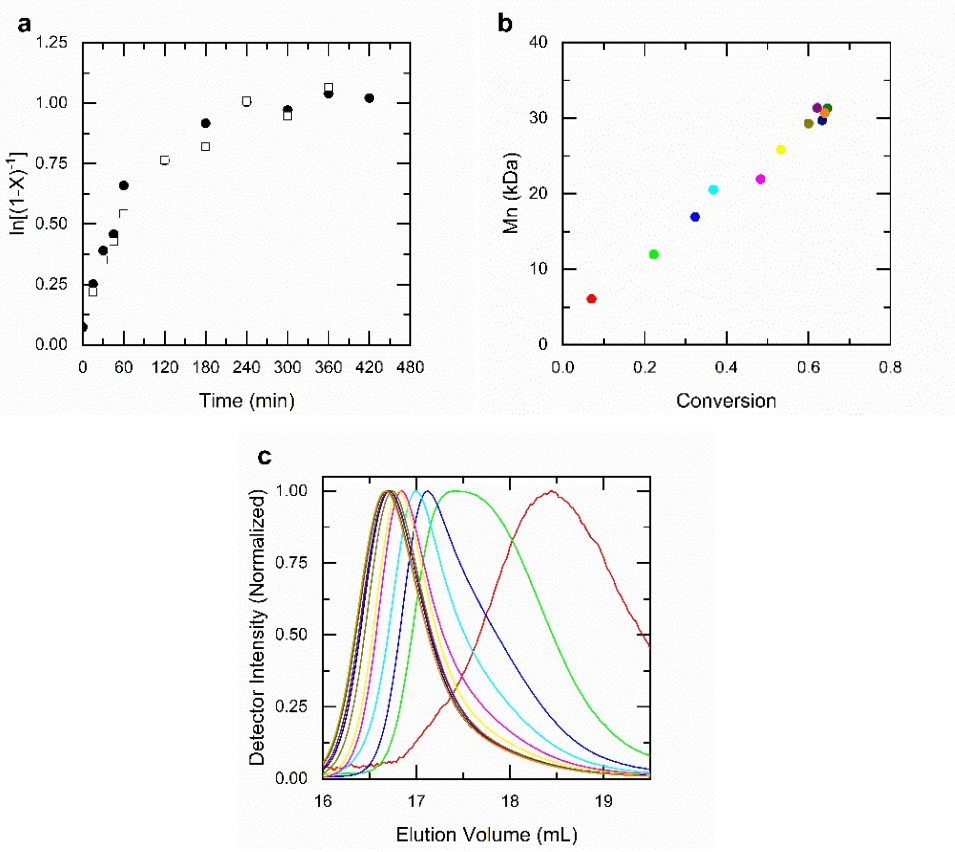

Figure 2.11. (a) Representative kinetic plots of $\ln[(1-X)^{-1}]$ (X = conversion) versus polymerization time for 10% $VBBI^{+}TFSI^{-}$ 90% MMA feed with 0.15 equivalent SG1 to BlocBuilder (filled circles, ●) and no additional SG1 (open squares, □). (b) Evolution of experimental number average molecular weight, M_n, and dispersity (D) with X with 15% excess SG1. (c) Gel permeation chromatograms (THF solution with 10 mmol L^{-1} of LiTFSI and 10 mmol L^{-1} 1-butylimidazole) of experiment VBBI/MMA-10+SG1

Determination of Reactivity Ratios (General Procedure)

With samples taken at low conversion using NHS-BB as the unimolecular initiator, Fineman-Ross[91] and Kelen-Tudos[92] plots were constructed to obtain approximate value for the reactivity ratios, assuming a terminal model was valid for the copolymer chain reactivity.[90] The Fineman-Ross approach linearizes the Mayo-Lewis equation and uses plot variables G and H that are defined by the equations given as:

$$G = \frac{f_1}{(1-f_1)}\frac{(F_1-1)}{F_1} \tag{2.7}$$

$$H = \left[\frac{f_1}{(1-f_1)}\right]^2 \frac{(1-F_1)}{F_1} \tag{2.8}$$

$$G = r_1 H - r_2 \tag{2.9}$$

where r_1 and r_2 are the reactivity ratios; f_1 and f_2 are the initial molar ratios in the feed; and F_1 and F_2 are the final molar ratios in the product for monomers 1 and 2, respectively. Thus, the reactivity ratios can be obtained from the slope and intercept in a plot of G versus A.

Since a relatively small number of compositions were used to estimate reactivity ratios, biasing of data caused by the Fineman-Ross method linearization was expected to be more severe, and thus the Kelen-Tudos method to estimate the reactivity ratios was also used. The latter method is expected to be most statistically sound method to determine the reactivity ratios. The Kelen-Tudos plot of the parameters η and ξ reveals the reactivity ratios for r_1 and r_2 (monomer 1 = styrenic comonomer, monomer 2 = methyl methacrylate) from the slope and intercept.

$$\eta = \left(r_1 + \frac{r_2}{\alpha}\right)\xi - \frac{r_2}{\alpha} \tag{2.10}$$

The Kelen-Tudos method introduces an arbitrary constant α as a scaling parameter given by $\sqrt{H_{min} \cdot H_{max}}$ while η and ξ are derived from the linearized Fineman-Ross parameters G and H as indicated in the equations above:

$$\eta = \frac{G}{\alpha + H} \tag{2.11}$$

$$\xi = \frac{H}{\alpha + H} \tag{2.12}$$

H_{min} and H_{max} correspond to the minimum and maximum values of H, respectively, determined from our data. After performing the Fineman-Ross and Kelen-Tudos fits to the data, the reactivity ratios determined were used as first estimates in sum of least squares fittings. The reactivity ratios determined by the different methods are reported in **Table 2.3** of the manuscript.

Reactivity Ratios (VBIm)

Copolymer reactivity ratios for 4-vinylbenzyl imidazole/methyl methacrylate copolymers (r_{VBIm} and r_{MMA}, respectively) were estimated from ^{1}H NMR measurements to determine the copolymer composition F_{VBIm} (in terms of 4-vinylbenzyl imidazole) at a given 4-vinylbenzyl imidazole molar feed fraction f_{VBIm}. A typical spectra of 4-vinylbenzyl imidazole/methyl methacrylate random copolymer is shown in Figure X. If the conversion is kept low, then compositional drift can be ignored and the instantaneous feed composition f_{VBIm} can be taken as approximately equal to the initial monomer molar feed fraction $f_{VBIm,0}$.

F_{VBIm} was estimated from kinetic samples, meaning the NMR spectra consisted of a mixture of polymer and unreacted monomer. To determine the polymer composition the amount of each monomer that had be polymerized was determined by subtracting the integration corresponding to the vinyl signals from the integration of the repeat unit for each polymer. For VBIm the repeat unit was taken from the integration of the signals at $= 7.5 - 8.0\ ppm$ (imidazole proton on 4-vinylbenzyl imidazole) and the monomer content was determined from the average of the integration of each vinyl signal at $\delta = 5.72\ ppm$ and $\delta = 5.24\ ppm$. For MMA the repeat unit was taken from the integration of the signals at $\delta = 3.7 - 3.66$ (3 protons from the methyl group) and the monomer content was determined from the average of the integration of each vinyl signal at $\delta = 5.5$ and $\delta = 6.05$. Thus, F_{VBIm} can be determined as follows:

$$F_{VBIm} = \frac{I_{\delta=7.5-8\ ppm} - \frac{1}{2}\left(I_{\delta=5.72\ ppm} + I_{\delta=5.24\ ppm}\right)}{\left[I_{\delta=8\ ppm} - \frac{1}{2}\left(I_{\delta=5.72\ ppm} + I_{\delta=5.24\ ppm}\right)\right] + \left[\frac{I_{\delta=3.7-3.66\ ppm}}{3} - \frac{1}{2}\left(I_{\delta=5.5\ ppm} + I_{\delta=6.05\ ppm}\right)\right]}$$

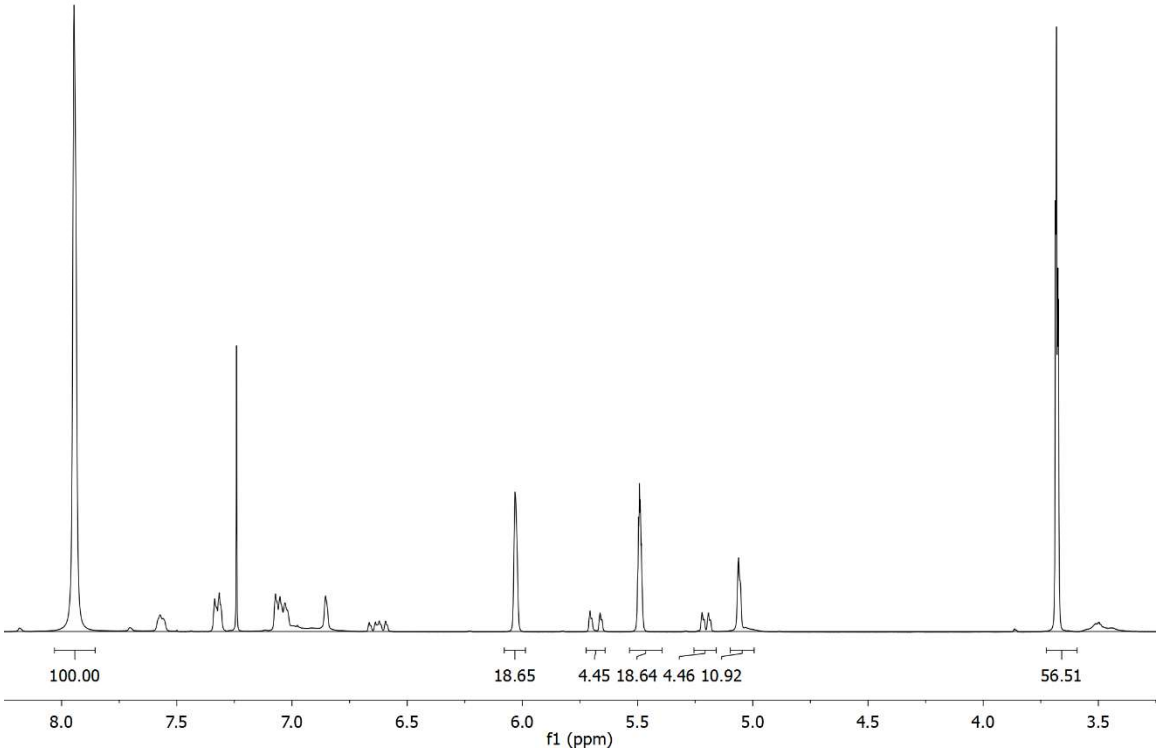

Figure 2.12. Typical ^{1}H NMR in deuterated chlororoform of a 4-vinylbenzyl imidazole-*co*-methyl methacrylate copolymer for initial molar feed of $f_{VBIm,0}$ of 20 mol%. The polymer was synthesized with NHS-BlockBuilder at 90°C in 50 wt% dimethylformamide solution. The symbol "x" corresponds to solvent.

Reactivity Ratios (VBIm)

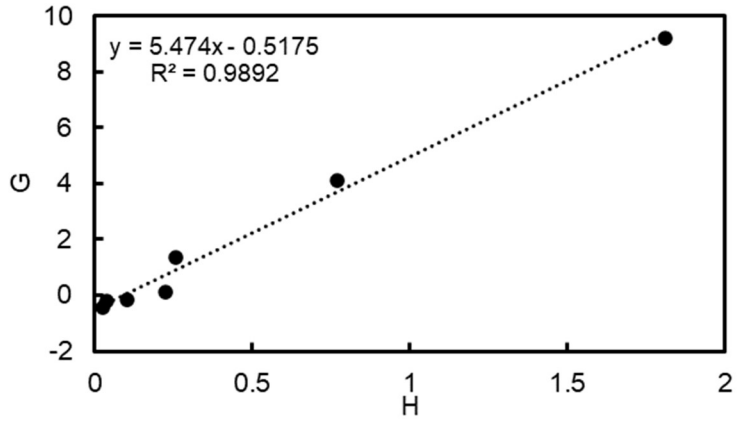

Figure 2.13. Fineman-Ross Plot to determine reactivity ratios from the intercept and slope (r_{MMA} = 0.52 and r_{VBIm} = 5.5).

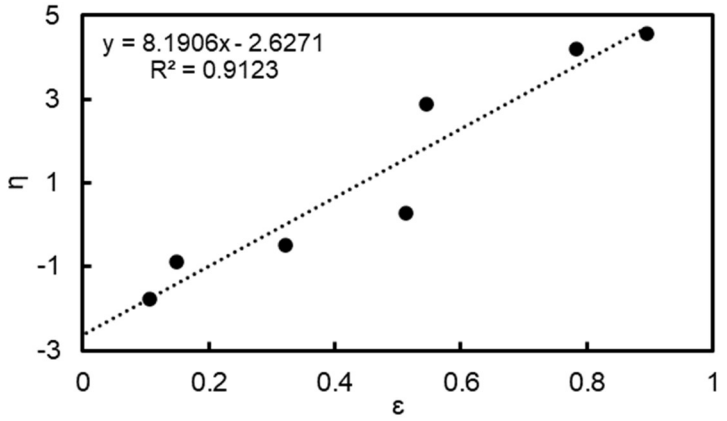

Figure 2.14. Kelen-Tudos Plot to determine the reactivity ratios from the intercept ($r_{ST}/\alpha = -2.63$) and slope ($r_{MMA} + r_{VBIm}/\alpha = 8.19$) which gives r_{MMA} = 0.56 and r_{VBIm} = 5.6.

Reactivity Ratios (VBBI TFSI)

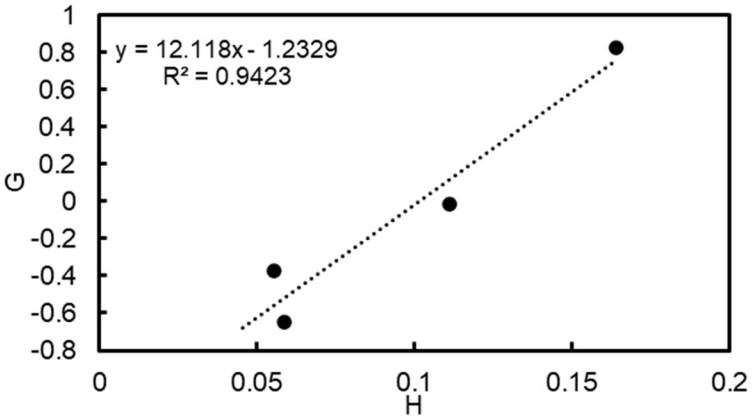

Figure 2.15. Fineman-Ross Plot to determine reactivity ratios from the intercept and slope (r_{MMA} = 1.23 and r_{VBBI} = 12.12).

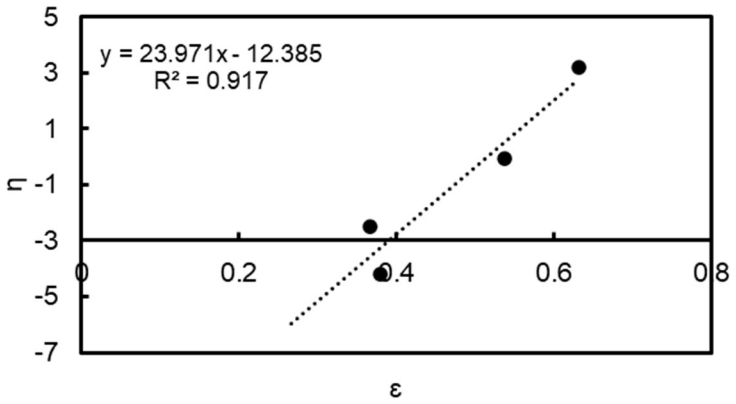

Figure 2.16. Kelen-Tudos Plot to determine the reactivity ratios from the intercept ($r_{ST}/\alpha = -12.39$) and slope ($r_{MMA} + r_{VBBI}/\alpha = 23.97$) which gives r_{MMA} = 1.18 and r_{VBBI} = 11.57.

Mayo-Lewis Plots

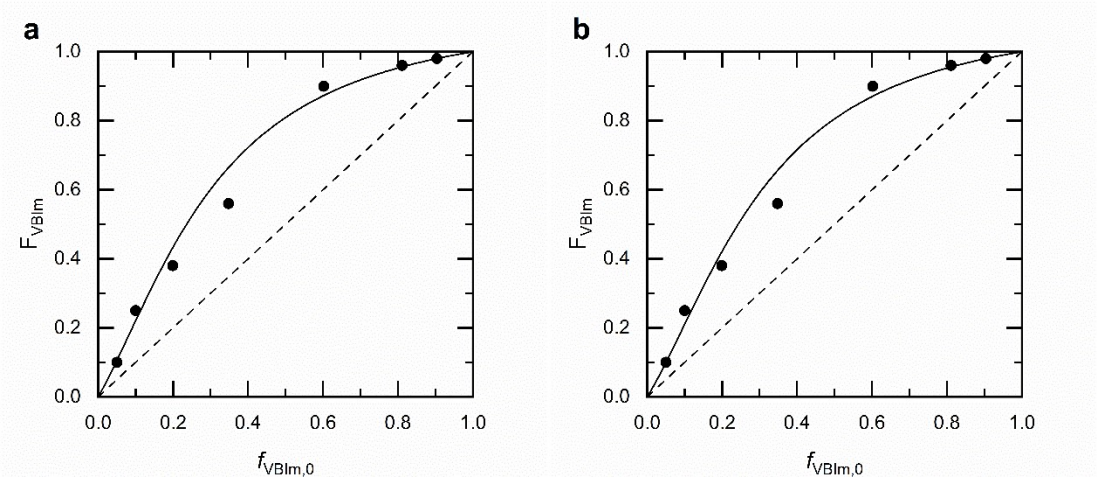

Figure 2.17. Mayo-Lewis plots of 4-vinylbenzyl imidazole/methyl methacrylate (VBIm/MMA). The experimental data for copolymerizations performed in DMF at 90 °C using NHS-BB as the unimolecular initiator is indicated by the solid circles, while the solid line indicates the fit from the reactivity ratios determined by (a) Fineman-Ross and (b) Kelen-Tudos fit to the Mayo-Lewis equation given in **Table 2.6**. The dashed line indicated the azeotropic composition. **Tables 2.1 & 2.2** list the experiments used for the plots.

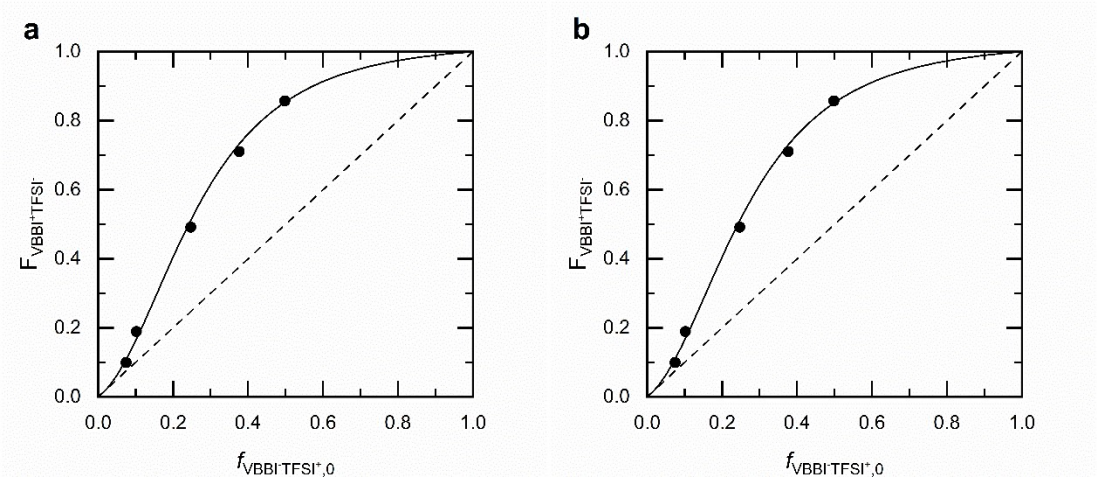

Figure 2.18. Mayo-Lewis plots of 1-(4-vinylbenzyl)-3-butylimidazolium bis(trifluoromethylsulfonyl)-imide/methyl methacrylate ($VBBI^+TFSI^-$/MMA). The experimental data for copolymerizations performed in DMF at 90 °C using NHS-BB as the unimolecular initiator is indicated by the solid circles, while the solid line indicates the fit from the reactivity ratios determined by (a) Fineman-Ross and (b) Kelen-Tudos fit to the Mayo-Lewis equation given in **Table 2.6**. The dashed line indicated the azeotropic composition. **Tables 2.1 & 2.2** list the experiments used for the plots.

VBIm GPC Traces

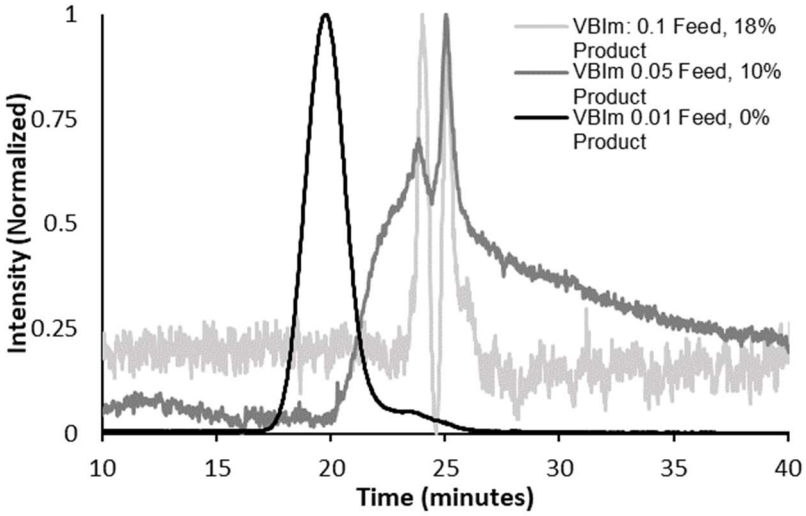

Figure 2.19. Gel permeation chromatograms of products from VBIm/MMA copolymerizations (denoted by VBIm-ran-MMA) performed at 90°C in DMF with theoretical molecular weights at complete conversion of 25 kg·mol^{-1} and with different monomer feed concentrations (initial molar feed concentration of VBIm is given by $f_{VBIm,0}$) using NHS-BB initiator: (a) $f_{VBIm,0} = 0.01$; (b) $f_{VBIm,0} = 0.05$; (c) $f_{VBIm,0} = 0.10$

2.8 References

(1) Livi, S.; Duchet-Rumeau, J.; Gérard, J. F.; Pham, T. N. Polymers and Ionic Liquids: A Successful Wedding. *Macromol. Chem. Phys.* **2015**, *216* (4), 359–368.

(2) Yuan, J.; Mecerreyes, D.; Antonietti, M. Poly(Ionic Liquid)s: An Update. *Prog. Polym. Sci.* **2013**, *38* (7), 1009–1036.

(3) Mecerreyes, D. Polymeric Ionic Liquids: Broadening the Properties and Applications of Polyelectrolytes. *Prog. Polym. Sci.* **2011**, *36* (12), 1629–1648.

(4) Men, Y.; Schlaad, H.; Yuan, J. Cationic Poly(Ionic Liquid) with Tunable Lower Critical Solution Temperature-Type Phase Transition. *ACS Macro Lett.* **2013**, *2* (5), 456–459.

(5) Jangu, C.; Long, T. E. Phosphonium Cation-Containing Polymers: From Ionic Liquids to Polyelectrolytes. *Polym. (United Kingdom)* **2014**, *55* (16), 3298–3304.

(6) Adzima, B. J.; Venna, S. R.; Klara, S. S.; He, H.; Zhong, M.; Luebke, D. R.; Mauter, M. S.; Matyjaszewski, K.; Nulwala, H. B. Modular Polymerized Ionic Liquid Block Copolymer Membranes for CO_2 /N_2 Separation. *J. Mater. Chem. A* **2014**, *2* (21), 7967–7972.

(7) Mudraboyina, B.; Obadia, M. M.; Allaoua, I.; Serghei, A.; Romdhane, H. Ben; Drockenmuller, E. 1,2,3-Triazolium-Based Poly(Ionic Liquid)S Obtained Through Click Chemistry Polyaddition Strategy. *Chem. Mater.* **2014**, No. 26, 1720–1726.

(8) Yuan, J.; Antonietti, M. Poly(Ionic Liquid)s: Polymers Expanding Classical Property Profiles. *Polymer (Guildf).* **2011**, *52* (7), 1469–1482.

(9) Bara, J. E.; Gin, D. L.; Noble, R. D. Effect of Anion on Gas Separation Performance of Polymer−Room-Temperature Ionic Liquid Composite Membranes. *Ind. Eng. Chem. Res.* **2008**, *47* (24), 9919–9924.

(10) Gu, Y.; Cussler, E. L.; Lodge, T. P. ABA-Triblock Copolymer Ion Gels for CO2 Separation Applications. *J. Memb. Sci.* **2012**, *423–424*, 20–26.

(11) Thiburce, Q.; Campbell, A. J. Low-Voltage Polyelectrolyte-Gated Polymer Field-Effect Transistors Gravure Printed at High Speed on Flexible Plastic Substrates. *Adv. Electron. Mater.* **2017**, *3* (2).

(12) Herlogsson, L.; Cölle, M.; Tierney, S.; Crispin, X.; Berggren, M.; C??lle, M.; Tierney, S.; Crispin, X.; Berggren, M. Low-Voltage Ring Oscillators Based on Polyelectrolyte-Gated Polymer Thin-Film Transistors. *Adv. Mater.* **2010**, *22* (1), 72–76.

(13) Pandey, G. P.; Hashmi, S. A. Ionic Liquid 1-Ethyl-3-Methylimidazolium Tetracyanoborate-Based Gel Polymer Electrolyte for Electrochemical Capacitors. *J. Mater. Chem. A* **2013**, *1* (10), 3372.

(14) Bara, J. E.; Lessmann, S.; Gabriel, C. J.; Hatakeyama, E. S.; Noble, R. D.; Gin, D. L. Synthesis and Performance of Polymerizable Room-Temperature Ionic Liquids as Gas Separation Membranes. *Ind. Eng. Chem. Res.* **2007**, *46* (16), 5397–5404.

(15) Ohno, H.; Yoshizawa, M.; Ogihara, W. Development of New Class of Ion Conductive Polymers Based on Ionic Liquids. *Electrochim. Acta* **2004**, *50* (2-3 SPEC. ISS.), 255–261.

(16) Ding, S.; Tang, H.; Radosz, M.; Shen, Y. Atom Transfer Radical Polymerization of Ionic Liquid 2-(1-Butylimidazolium-3-Yl)Ethyl Methacrylate Tetrafluoroborate. *J. Polym. Sci. Part A Polym. Chem.* **2004**, *42* (Copyright (C) 2014 American Chemical Society (ACS). All Rights Reserved.), 5794–5801.

(17) He, X.; Yang, W.; Pei, X. Preparation, Characterization, and Tunable Wettability of Poly(Ionic Liquid) Brushes via Surface-Initiated Atom Transfer Radical Polymerization. *Macromolecules* **2008**, *41* (13), 4615–4621.

(18) He, H.; Zhong, M.; Adzima, B.; Luebke, D.; Nulwala, H.; Matyjaszewski, K. A Simple and Universal Gel Permeation Chromatography Technique for Precise Molecular Weight Characterization of Well-Defined Poly(Ionic Liquid)S. *J. Am. Chem. Soc.* **2013**, *135* (11), 4227–4230.

(19) He, H.; Zhong, M.; Luebke, D.; Nulwala, H.; Matyjaszewski, K. Atom Transfer Radical Polymerization of Ionic Liquid Monomer: The Influence of Salt/Counterion on Polymerization. *J. Polym. Sci. Part A Polym. Chem.* **2014**, *52* (15), 2175–2184.

(20) He, H.; Averick, S.; Roth, E.; Luebke, D.; Nulwala, H.; Matyjaszewski, K. Clickable Poly(Ionic Liquid)s for Modification of Glass and Silicon Surfaces. *Polym. (United Kingdom)* **2014**, *55* (16), 3330–3338.

(21) Tang, H.; Tang, J.; Ding, S.; Radosz, M.; Shen, Y. Atom Transfer Radical Polymerization of Styrenic Ionic Liquid Monomers and Carbon Dioxide Absorption of the Polymerized Ionic Liquids. *J. Polym. Sci. Part A Polym. Chem.* **2005**, *43* (7), 1432–1443.

(22) Cordella, D.; Kermagoret, A.; Debuigne, A.; Jéroîme, C.; Mecerreyes, D.; Isik, M.; Taton, D.; Detrembleur, C. All Poly(Ionic Liquid)-Based Block Copolymers by Sequential Controlled Radical Copolymerization of Vinylimidazolium Monomers. *Macromolecules* **2015**, *48* (15), 5230–5243.

(23) Cordella, D.; Kermagoret, A.; Debuigne, A.; Riva, R.; German, I.; Isik, M.; Jérôme, C.; Mecerreyes, D.; Taton, D.; Detrembleur, C. Direct Route to Well-Defined Poly(Ionic Liquid)s by Controlled Radical Polymerization in Water. *ACS Macro Lett.* **2014**, *3* (12), 1276–1280.

(24) Allen, M. H.; Hemp, S. T.; Smith, A. E.; Long, T. E. Controlled Radical Polymerization of 4-Vinylimidazole. *Macromolecules* **2012**, *45* (9), 3669–3676.

(25) Cordella, D.; Ouhib, F.; Aqil, A.; Defize, T.; Jérôme, C.; Serghei, A.; Drockenmuller, E.; Aissou, K.; Taton, D.; Detrembleur, C. Fluorinated Poly(Ionic Liquid) Diblock Copolymers Obtained by Cobalt-Mediated Radical Polymerization-Induced Self-Assembly. *ACS Macro Lett.* **2017**, *6* (2), 121–126.

(26) Mori, H.; Yanagi, M.; Endo, T. RAFT Polymerization of N-Vinylimidazolium Salts and Synthesis of Thermoresponsive Ionic Liquid Block Copolymers. *Macromolecules* **2009**, *42* (21), 8082–8092.

(27) Vijayakrishna, K.; Jewrajka, S. K.; Ruiz, A.; Marcilla, R.; Pomposo, J. a; Mecerreyes, D.; Taton, D.; Gnanou, Y. Synthesis by RAFT and Ionic Responsiveness of Double Hydrophilic Block Copolymers Based on Ionic Liquid Monomer Units. *Macromolecules* **2008**, *41* (17), 6299–6308.

(28) Solomon, D. H.; Rizzardo, E.; Cacioli, P. Polymerization Process and Polymers Produced Thereby. US4581429A, 1986.

(29) Georges, M. K.; Veregin, R. P. N.; Kazmaier, P. M.; Hamer, G. K. Narrow Molecular Weight Resins by a Free-Radical Polymerization Process. *Macromolecules* **1993**, *26* (11), 2987–2988.

(30) Veregin, R. P. N.; Georges, M. K.; Kazmaier, P. M.; Hamer, G. K. Free Radical Polymerizations for Narrow Polydispersity Resins: Electron Spin Resonance Studies of the Kinetics and Mechanism. *Macromolecules* **1993**, *26*, 5316–5320.

(31) Hawker, C. J. " Living " Free Radical Polymerization: A Unique Technique for the Preparation of Controlled Macromolecular Architectures. *Acc. Chem. Res.* **1997**, *30* (96), 373–382.

(32) Hawker, C. J.; Elce, E.; Dao, J.; Volksen, W.; Russell, T. P.; Barclay, G. G. Well-Defined Random Copolymers by a "Living" Free-Radical Polymerization Process. *Macromolecules* **1996**, *29* (7), 2686–2688.

(33) Nicolas, J.; Guillaneuf, Y.; Lefay, C.; Bertin, D.; Gigmes, D.; Charleux, B. Nitroxide-Mediated Polymerization. *Prog. Polym. Sci.* **2012**, *38* (1), 63–235.

(34) Grubbs, R. B. Nitroxide-Mediated Radical Polymerization: Limitations and Versatility. *Polym. Rev.* **2011**, *51* (2), 104–137.

(35) Hawker, C. J.; Bosman, A. W.; Harth, E. New Polymer Synthesis by Nitroxide Mediated Living Radical Polymerizations. *Chem. Rev.* **2001**, *101* (12), 3661–3688.

(36) Benoit, D.; Grimaldi, S.; Robin, S.; Finet, J. P.; Tordo, P.; Gnanou, Y. Kinetics and Mechanism of Controlled Free-Radical Polymerization of Styrene and n -Butyl Acrylate in the Presence of an Acyclic. *J. Am. Chem. Soc.* **2000**, *122* (2), 5929–5939.

(37) Benoit, D.; Chaplinski, V.; Braslau, R.; Hawker, C. J. Development of a Universal Alkoxyamine for "living" Free Radical Polymerizations. *J. Am. Chem. Soc.* **1999**, *121* (16), 3904–3920.

(38) Lessard, B. H.; Marić, M. Water-Soluble/Dispersible Carbazole-Containing Random and Block Copolymers by Nitroxide-Mediated Radical Polymerisation. *Can. J. Chem. Eng.* **2013**, *91* (4), 618–629.

(39) Eggenhuisen, T. M.; Becer, C. R.; Fijten, M. W. M.; Eckardt, R.; Hoogenboom, R.; Schubert, U. S. Libraries of Statistical Hydroxypropyl Acrylate Containing Copolymers with LCST Properties Prepared by NMP. *Macromolecules* **2008**, *41* (14), 5132–5140.

(40) Lessard, B.; Marić, M. Effect of Acrylic Acid Neutralization on 'Livingness' of Poly[Styrene- Ran -(Acrylic Acid)] Macro-Initiators for Nitroxide-Mediated Polymerization of Styrene. *Polym. Int.* **2008**, *57* (10), 1141–1151.

(41) Nicolas, J.; Brusseau, S.; Charleux, B. A Minimal Amount of Acrylonitrile Turns the Nitroxide-Mediated Polymerization of Methyl Methacrylate into an Almost Ideal Controlled/Living System. *J. Polym. Sci. Part A Polym. Chem.* **2010**, *48* (1), 34–47.

(42) Lessard, B. H.; Savelyeva, X.; Marić, M. Smart Morpholine-Functional Statistical Copolymers Synthesized by Nitroxide Mediated Polymerization. *Polym. (United Kingdom)* **2012**, *53* (25), 5649–5656.

(43) Charleux, B.; Nicolas, J.; Guerret, O. Theoretical Expression of the Average Activation−Deactivation Equilibrium Constant in Controlled/Living Free-Radical Copolymerization Operating via Reversible Termination. Application to a Strongly Improved Control in Nitroxide-Mediated Polymerization Of . *Macromolecules* **2005**, *38* (13), 5485–5492.

(44) Lessard, B. H.; Guillaneuf, Y.; Mathew, M.; Liang, K.; Clement, J. L.; Gigmes, D.; Hutchinson, R. A.; Marić, M. Understanding the Controlled Polymerization of Methyl Methacrylate with Low Concentrations of 9-(4-Vinylbenzyl)-9 H -Carbazole Comonomer by Nitroxide-Mediated Polymerization: The Pivotal Role of Reactivity Ratios. *Macromolecules* **2013**, *46* (3), 805–813.

(45) Lessard, B. H.; Sampson, K. L.; Plint, T.; Bender, T. P. Boron Subphthalocyanine Polymers: Avoiding the Small Molecule Side Product and Exploring Their Use in Organic Light-Emitting Diodes. *J. Polym. Sci. Part A Polym. Chem.* **2015**, *53* (17), 1996–2006.

(46) Lessard, B.; Ling, E. J. Y.; Morin, M. S. T.; Marić, M. Nitroxide-Mediated Radical Copolymerization of Methyl Methacrylate Controlled with a Minimal Amount of 9-(4-Vinylbenzyl)-9H-Carbazole. *J. Polym. Sci. Part A Polym. Chem.* **2011**, *49* (4), 1033–1045.

(47) Tran, J.; Guégain, E.; Ibrahim, N.; Harrisson, S.; Nicolas, J. Efficient Synthesis of 2-Methylene-4-Phenyl-1,3-Dioxolane, a Cyclic Ketene Acetal for Controlling the NMP of Methyl Methacrylate and Conferring Tunable Degradability. *Polym. Chem.* **2016**, *7* (26), 4427–4435.

(48) Vinas, J.; Chagneux, N.; Gigmes, D.; Trimaille, T.; Favier, A.; Bertin, D. SG1-Based Alkoxyamine Bearing a N-Succinimidyl Ester: A Versatile Tool for Advanced Polymer Synthesis. *Polymer (Guildf).* **2008**, *49* (17), 3639–3647.

(49) Soulé, J.-F.; Miyamura, H.; Kobayashi, S. Copolymer-Incarcerated Nickel Nanoparticles with N -Heterocyclic Carbene Precursors as Active Cross-Linking Agents for Corriu–Kumada–Tamao Reaction. *J. Am. Chem. Soc.* **2013**, *135* (29), 10602–10605.

(50) Green, M. D.; Wang, D.; Hemp, S. T.; Choi, J. H.; Winey, K. I.; Heflin, J. R.; Long, T. E. Synthesis of Imidazolium ABA Triblock Copolymers for Electromechanical Transducers. *Polym. (United Kingdom)* **2012**, *53* (17), 3677–3686.

(51) Moayeri, A.; Lessard, B. H.; Maric, M. Nitroxide Mediated Controlled Synthesis of Glycidyl Methacrylate-Rich Copolymers Enabled by SG1-Based Alkoxyamines Bearing Succinimidyl Ester Groups. *Polym. Chem.* **2011**, *2*, 2084–2092.

(52) Coupillaud, P.; Taton, D. Imidazolium-Based Poly(Ionic Liquid) Block Copolymers. In *Applications of Ionic Liquids in Polymer Science and Technology*; Springer Berlin Heidelberg: Berlin, Heidelberg, 2015; pp 69–102.

(53) Green, M. D.; Allen, M. H.; Dennis, J. M.; Cruz, D. S. D. La; Gao, R.; Winey, K. I.; Long, T. E. Tailoring Macromolecular Architecture with Imidazole Functionality: A Perspective for Controlled Polymerization Processes. *Eur. Polym. J.* **2011**, *47* (4), 486–496.

(54) Green, M. D.; Choi, J. H.; Winey, K. I.; Long, T. E. Synthesis of Imidazolium-Containing Aba Triblock Copolymers: Role of Charge Placement, Charge Density, and Ionic Liquid Incorporation. *Macromolecules* **2012**, *45* (11), 4749–4757.

(55) Jangu, C.; Wang, J. H. H.; Wang, D.; Sharick, S.; Heflin, J. R.; Winey, K. I.; Colby, R. H.; Long, T. E. Well-Defined Imidazolium ABA Triblock Copolymers as Ionic-Liquid-Containing Electroactive Membranes. *Macromol. Chem. Phys.* **2014**, *215* (13), 1319–1331.

(56) Mayo, F. R.; Lewis, F. M.; Walling, C. Copolymerization. VIII. The Relation Between Structure and Reactivity of Monomers in Copolymerization. *J. Am. Chem. Soc.* **1948**, *1544* (70), 1529.

(57) Imoto, M.; Kinoshita, M.; Nishigaki, M. Vinyl Polymerization. 93. Polar Effects in Radical Polymerization of p-Substituted Styrenes. *Die Makromol. Chemie* **1965**, *86* (1), 217–230.

(58) Sim, B. A.; Milne, P. H.; Griller, D.; Wayner, D. D. M. Thermodynamic Significance of .Rho.+ and .Rho.- from Substituent Effects on the Redox Potentials of Arylmethyl Radicals. *J. Am. Chem. Soc.* **1990**, *112* (18), 6635–6638.

(59) Matyjaszewski, K. Correlation of the Rate Constants of Propagation With the Structures of Monomers and Active Centers in Chain-Growth Polymerization. *J. Macromol. Sci. Part C Polym. Rev.* **1986**, *26* (1), 1–32.

(60) Matyjaszewski, K. *Cationic Polymerizations: Mechanisms, Synthesis & Applications*; Marcel Dekker: New York, 1996.

(61) Kazmaier, P. M.; Daimon, K.; Georges, M. K.; Hamer, G. K. Nitroxide-Mediated "'living'" Free Radical Polymerization, Substituent Effects on the Free Radical

Polymerization of Styrene. *Am. Chem. Soc. Polym. Prepr. Div. Polym. Chem. Polym. Prepr.* **1996**, *37* (1), 485.

(62) Qiu, J.; Matyjaszewski, K. Polymerization of Substituted Styrenes by Atom Transfer Radical Polymerization. *Macromolecules* **1997**, *30* (19), 5643–5648.

(63) Daimon, K.; Kazmaier, P. M.; Georges, M. K. Substituent Effect on Styrene Polymerization in the Nitroxide Mediated Stable Free Radical Polymerization. *Polym. Prepr. (Am. Chem. Soc., Div. Polym. Chem.)* **1997**, *38* (1), 653.

(64) Lacroix-Desmazes, P.; Lutz, J. F.; Chauvin, F.; Severac, R.; Boutevin, B. Living Radical Polymerization: Use of an Excess of Nitroxide as a Rate Moderator. *Macromolecules* **2001**, *34* (26), 8866–8871.

(65) Couvreur, L.; Lefay, C.; Belleney, J.; Charleux, B.; Guerret, O.; Magnet, S. First Nitroxide-Mediated Controlled Free-Radical Polymerization of Acrylic Acid. *Macromolecules* **2003**, *36* (22), 8260–8267.

(66) Hansch, C.; Leo, A.; Taft, R. W. A Survey of Hammett Substituent Constants and Resonance and Field Parameters. *Chem. Rev.* **1991**, *91* (2), 165–195.

(67) Pratt, D. A.; Pesavento, R. P.; van der Donk, W. A. Model Studies of the Histidine-Tyrosine Cross-Link in Cytochrome c Oxidase Reveal the Flexible Substituent Effect of the Imidazole Moiety. *Org. Lett.* **2005**, *7* (13), 2735–2738.

(68) Becke, A. D. Density-Functional Thermochemistry. III. The Role of Exact Exchange. *J. Chem. Phys.* **1993**, *98* (7), 5648–5652.

(69) Lee, C.; Yang, W.; Parr, R. G. Development of the Colle-Salvetti Correlation-Energy Formula into a Functional of the Electron Density. *Phys. Rev. B* **1988**, *37* (2), 785–789.

(70) Fischer, A.; Riddolls, M. A.; Vaughan, J. Rates of Methylation of 1-Naphthoxide Ions. *J. Chem. Soc. B Phys. Org.* **1966**, No. 106, 106.

(71) Lewis, E. S.; JoHnsOn, M. D. The Substituent Constants of the Diazonium Ion Group. *J. Am. Chem. Soc.* **1959**, *81* (9), 2070–2072.

(72) Izgorodina, E. I.; Maganti, R.; Armel, V.; Dean, P. M.; Pringle, J. M.; Seddon, K. R.; MacFarlane, D. R. Understanding the Effect of the C2 Proton in Promoting Low

Viscosities and High Conductivities in Imidazolium-Based Ionic Liquids: Part I. Weakly Coordinating Anions. *J. Phys. Chem. B* **2011**, *115* (49), 14688–14697.

(73) Hoefnagel, A. J.; Hoefnagel, M. A.; Wepster, B. M. Substituent Effects. 6. Charged Groups: A Simple Extension of the Hammett Equation. *J. Org. Chem.* **1978**, *43* (25), 4720–4745.

(74) Harrisson, S.; Mackenzie, S. R.; Haddleton, D. M. Unprecedented Solvent-Induced Acceleration of Free-Radical Propagation of Methyl Methacrylate in Ionic Liquids. *Chem. Commun.* **2002**, *2* (23), 2850–2851.

(75) Carmichael, A. J.; Haddleton, D. M.; Bon, S. A. F.; Seddon, K. R. Copper(I) Mediated Living Radical Polymerisation in an Ionic Liquid. *Chem. Commun.* **2000**, No. 14, 1237–1238.

(76) He, H.; Luebke, D.; Nulwala, H.; Matyjaszewski, K. Synthesis of Poly(Ionic Liquid)s by Atom Transfer Radical Polymerization with Ppm of Cu Catalyst. *Macromolecules* **2014**, *47* (19), 6601–6609.

(77) Guillaneuf, Y.; Gigmes, D.; Marque, S. R. A.; Astolfi, P.; Greci, L.; Tordo, P.; Bertin, D. First Effective Nitroxide-Mediated Polymerization of Methyl Methacrylate. *Macromolecules* **2007**, *40* (9), 3108–3114.

(78) Dire, C.; Belleney, J.; Nicolas, J.; Bertin, D.; Magnet, S.; Charleux, B. β-Hydrogen Transfer from Poly(Methyl Methacrylate) Propagating Radicals to the Nitroxide SG1: Analysis of the Chain-End and Determination of the Rate Constant. *J. Polym. Sci. Part A Polym. Chem.* **2008**, *46* (18), 6333–6345.

(79) Matsumura, S.; Hlil, A. R.; Lepiller, C.; Gaudet, J.; Guay, D.; Shi, Z.; Holdcroft, S.; Hay, A. S. Ionomers for Proton Exchange Membrane Fuel Cells with Sulfonic Acid Groups on the End-Groups: Novel Branched Poly(Ether-Ketone)S. *Am. Chem. Soc. Polym. Prepr. Div. Polym. Chem.* **2008**, *49* (1), 511–512.

(80) Fischer, H. The Persistent Radical Effect: A Principle for Selective Radical Reactions and Living Radical Polymerizations. *Chem. Rev.* **2001**, *101* (12), 3581–3610.

(81) Goto, A.; Fukuda, T. Kinetics of Living Radical Polymerization. *Prog. Polym. Sci.* **2004**, *29* (4), 329–385.

(82) Lutz, J. F.; Lacroix-Desmazes, P.; Boutevin, B. The Persistent Radical Effect in Nitroxide Mediated Polymerization: Experimental Validity. *Macromol. Rapid Commun.* **2001**, *22* (3), 189–193.

(83) Drockenmuller, E.; Lamps, J. P.; Catala, J. M. Living/Controlled Radical Polymerization of Ethyl and n-Butyl Acrylates at 90°C Mediated by β-Sulfinyl Nitroxides: Influence of the Persistent Radical Stereochemistry. *Macromolecules* **2004**, *37* (6), 2076–2083.

(84) Chauvin, F.; Dufils, P. E.; Gigmes, D.; Guillaneuf, Y.; Marque, S. R. A.; Tordo, P.; Bertin, D. Nitroxide-Mediated Polymerization: The Pivotal Role of the Kd Value of the Initiating Alkoxyamine and the Importance of the Experimental Conditions. *Macromolecules* **2006**, *39* (16), 5238–5250.

(85) Phan, T. N. T.; Bertin, D. Synthesis of Water-Soluble Homopolymers and Block Copolymers in Homogeneous Aqueous Solution via Nitroxide-Mediated Polymerization. *Macromolecules* **2008**, *41* (5), 1886–1895.

(86) Fukuda, T.; Goto, A.; Ohno, K. Mechanisms and Kinetics of Living Radical Polymerizations. *Macromol. Rapid Commun.* **2000**, *21* (4), 151–165.

(87) Souaille, M.; Fischer, H. Rate Enhancement and Retardation Strategies in Living Free Radical Polymerizations Mediated by Nitroxides and Other Persistent Species: A Theoretical Assessment. *Macromolecules* **2002**, *35* (1), 248–261.

(88) Phan, T. N. T.; Ferrand, A.; Ho, H. T.; Liénafa, L.; Rollet, M.; Maria, S.; Bouchet, R.; Gigmes, D. Vinyl Monomers Bearing a Sulfonyl(Trifluoromethane Sulfonyl) Imide Group: Synthesis and Polymerization Using Nitroxide-Mediated Polymerization. *Polym. Chem.* **2016**, *7* (45), 6901–6910.

(89) Weber, R. L.; Ye, Y.; Schmitt, A. L.; Banik, S. M.; Elabd, Y. A.; Mahanthappa, M. K. Effect of Nanoscale Morphology on the Conductivity of Polymerized Ionic Liquid Block Copolymers. *Macromolecules* **2011**, *44* (14), 5727–5735.

(90) Mayo, F. R.; Lewis, F. M. Copolymerization I. A Basis for Comparing the Behavior of Monomers in Copolymerization; the Copolymerization of Styrene and Methyl Methacrylate. *J. Am. Chem. Soc.* **1944**, *66* (1939), 1594–1601.

(91) Fineman, M.; Ross, S. D. Linear Method for Determining Monomer Reactivity Ratios in Copolymeization. *J. Polym. Sci.* **1950**, *V* (2), 259–265.

(92) Kelen, T.; Tüdõs, K. Analysis of the Linear Methods for Determining Copolymerization Reactivity Ratios. I. A New Improved Linear Graphic Method. *J. Macromol. Sci. Part A - Chem.* **1975**, *9* (1), 1–27.

(93) Kazemi, N.; Lessard, B. H.; Marić, M.; Duever, T. A.; Penlidis, A. Reactivity Ratio Estimation in Radical Copolymerization: From Preliminary Estimates to Optimal Design of Experiments. *Ind. Eng. Chem. Res.* **2014**, *53* (18), 7305–7312.

(94) Polic, A. L.; Duever, T. A.; Penlidis, A. Case Studies and Literature Review on the Estimation of Copolymerization Reactivity Ratios. *J. Polym. Sci. Part A Polym. Chem.* **1998**, *36* (5), 813–822.

(95) Hauch, E.; Zhou, X.; Duever, T. A.; Penlidis, A. Estimating Reactivity Ratios from Triad Fraction Data. *Macromol. Symp.* **2008**, *271* (1), 48–63.

(96) Kazemi, N.; Duever, T. A.; Penlidis, A. Design of Experiments for Reactivity Ratio Estimation in Multicomponent Polymerizations Using the Error-in-Variables Approach. *Macromol. Theory Simulations* **2013**, *22* (5), 261–272.

(97) Kazemi, N.; Duever, T. A.; Penlidis, A. Reactivity Ratio Estimation from Cumulative Copolymer Composition Data. *Macromol. React. Eng.* **2011**, *5* (9–10), 385–403.

(98) Kazemi, N.; Duever, T. A.; Penlidis, A. A Powerful Estimation Scheme with the Error-in-Variables-Model for Nonlinear Cases: Reactivity Ratio Estimation Examples. *Comput. Chem. Eng.* **2013**, *48*, 200–208.

(99) Kannan, N. B.; Lessard, B. H. Copolymerization of 2,3,4,5,6-Pentafluorostyrene and Methacrylic Acid by Nitroxide-Mediated Polymerization: The Importance of Reactivity Ratios. *Macromol. React. Eng.* **2016**, 1–11.

Chapter 3: Unipolar Polymerized Ionic Liquid Copolymers as High-Capacitance Electrolyte Gates for n-type Transistors

Context

In this study we synthesized PIL containing copolymers that were soluble and and were easily isolated and purified by means of simple precipitations. The favourable post-polymerization synthetic strategy, established in Chapter 2, led to prepolymers that could be characterized by GPC PILs. Therefore, we synthesized and purified a series of random copolymers and block copolymers containing the PILs. We started by characterizing the resulting polymer thermal properties as a function of copolymer composition and established relationships. The materials were then characterized by solid state impedance spectroscopy. We had to establish new laboratory procedures including the fabrication of metal insulator metal capacitors. This involved several iterations to work out problems with short cucuits due to rough masks and other technical challenges. Finally we developed the new lab protocols to fabricate top gate bottom contact OTFT devices to characterize these materials in OTFTs. Although our lab was fabricating and testing transistors at this point, we only had experience fabricating bottom gated devices.

Contributions of Authors

I designed the experiments and the study with the guidance of Dr. Lessard. Victoria, an undergraduate student under my direct supervision, synthesized the precursor polymers, and I executed the following functionalization. I fabricated the capacitor and OTFT devices. Dr. Greg Lopinski showed me how they characterized dielectrics, and facilitated a few demos at the National Research Council of Canada, which inspired the mounting of our setup in our laboratory at uOttawa. I performed the impedance characterization and characterized the OTFTs with the assistance of Owen Melville.

Significance of Research

This research was significant as we were able to demonstrate that we could synthesize polyelectrolyte materials and successfully integrate them into transistors of comparable to others

in the literature. We showed the content of ionic liquid moieties in the material was not instrumental to achieving a high capacitance and that conductivity was linked to T_g and morphology. We also identified a minimum PL content necessary to obtain an EDL which is different for random and block copolymers further suggesting block copolymer self-assembly is key to high performance.

Chapter 3 was published in Applied Polymer Materials: Peltekoff, A. J., Hiller, V. E., Lopinski, G. P., Melville, O. A., & Lessard, B. H., 2019, 1, 11, 3210-3221. doi:10.1021/acsapm.9b00959

3.1 Abstract

A series of well-defined polymerized ionic liquid (PIL) statistical and block copolymers consisting of ionic liquid monomer, 1-(4-vinylbenzyl)-3-butylimidazolium bis(trifluoromethylsulfonyl)imide, and a nonionic monomer, methyl methacrylate (MMA), were synthesized by nitroxide-mediated polymerization (NMP) with the goal of understanding the influence of polymer structure on the thin film capacitance. Copolymer compositions were varied from 8 to 54 wt % for both statistical and block copolymers and were characterized by predictable changes in glass transition temperature (75 °C > T_g > 45 °C). When integrated into thin film capacitors, block copolymers exhibited the formation of electrical double layer (EDL) at lower frequencies compared to the statistical copolymers of similar comonomer compositions. The materials that formed an EDL all produced a similar maximum double layer capacitance value, with the only difference being the frequency at which the EDL was formed. Finally, the PIL-containing materials that were utilized in organic thin-film transistors (OTFTs) showed a significant reduction in operating voltage compared to the poly(MMA) baseline. These results indicate that not only composition but also polymer architecture plays a vital role in the formation of an EDL and determines at which frequency the resulting OTFTs can be operated.

3.2 Introduction

The growing demand for flexible, lightweight, and stretchable electronics has led to great interest in printed organic electronics. Thin-film transistors (TFTs) are foundational components of many emerging organic electronic devices such as radio frequency identification (RFID) tags, active-matrix organic light-emitting-diode-based (AMOLED) displays, and chemical and biological sensors.[1–9] In these applications, low-voltage operating TFTs are required to minimize power utilization, while maintaining the low processing temperature required to be compatible with plastic substrates. Therefore, novel gate dielectric materials that exhibit both high effective capacitance and low-temperature processing must be developed.[10–12] Electrolyte-gated transistors (EGTs)[4,13] utilize a polyelectrolyte as the gating medium which possess mobile ions that lead to the formation of an electrical double layer that significantly increases the capacitance compared to neutral polymers. EGTs can operate in field-effect mode by pairing with an appropriate semiconductor. Polycations, for example, possess an immobile positive charge pendant to the backbone that cannot diffuse into the n-type semiconductor upon application of a positive gate voltage, where the opposite is true for a polyanion and p-type semiconductor.[14,15] Other researchers have demonstrated polyelectrolyte-gated thin film transistors utilizing both inorganic[16,17] and organic semiconductors.[18–22] More recently, Thiburce and co-workers fabricated PSS-based polyelectrolyte-gated TFTs by gravure printing methods to develop low operating voltage p-type P3HT devices.[23] Additionally, polyelectrolyte-gated TFTs have been incorporated into OTFT-based pressure sensors, demonstrating the range of potential for these types of materials.[24,25]

Both n- and p-type-based semiconductors are required to produce low-power-consuming organic integrated circuits. Significant progress in the production of high-performing organic EGTs with p-type semiconductors[19,26–30] has been reported; however, fewer studies on the development of organic n-type EGTs are available.[31–35] Some existing methods include the use of lithium perchlorate/poly(ethylene oxide) (PEO)[31] and ionic liquids[32,33] as the gating medium for n-type EGTs. More recently, polyelectrolytes with bound anions and cations have also been successfully incorporated into EGTs.[34,35]

Ionic liquids have received tremendous interest over the years due to their ionic conductivity, lack of flammability, negligible vapor pressure, and chemical/thermal stability.

Poly(ionic liquid)s (PILs) are a subset of polyelectrolytes that possess ionic liquid moieties as part of the polymer backbone or as pendent side chains. PILs therefore combine the advantages of ionic liquids with the mechanical strength, processability, and flexibility of polymers, finding applications in batteries, supercapacitors, fuel cells, solar cells, and even gas separation membranes.[36–40] These advantageous properties of PILs can be influenced by altering either the polymer structure or the composition of ionic liquid. For example, it has been shown that decreasing the glass transition temperature (T_g) results in an increase in ion conductivity, although mechanical stability and processability suffer.[41,42] Therefore, the use of block copolymers possessing a low-T_g ion-conducting ionic liquid block and a high-T_g block to provide mechanical stability has proven to be beneficial.[19,43,44]

In this study, the nitroxide-mediated polymerization (NMP) was used to synthesize a series of statistical and block copolymer-based polyelectrolytes containing 1-(4-vinylbenzyl)-3-butylimidazolium bis(trifluoromethylsulfonyl)imide ($VBBI^+TFSI^-$) and methyl methacrylate (MMA). In contrast to other electrolytes like ion ionic liquids and ion gels, these poly($VBBI^+TFSI^-$-*r*-MMA) copolymers are unipolar ion conductors as the ionic liquid moieties are bound to the backbone. We first determine the necessary kinetics and copolymer reactivity ratio of the prepolymer copolymerization followed by the characterization of the T_g of the resulting polymers after post-polymerization binding of the ion functional group. We continue to investigate the effect of copolymer composition and molecular architecture (block versus statistical) on the EDL capacitance and demonstrate one of the material's ability to function as a gating medium in EGTs with relatively low operating voltages.

3.3 Results & Discussion

3.3.1 Statistical Copolymer Synthesis, Kinetics, and Reactivity Ratio Determination.

We synthesized a series of methyl methacrylate (MMA) and 1-(4-vinylbenzyl)-3-butylimidazolium bis(trifluoromethylsulfonyl)imide ($VBBI^+TFSI^-$) containing statistical (poly($VBBI^+TFSI^-$-*r*-MMA)) and block (poly(MMA-r-S)-*b*-poly($VBBI^+TFSI^-$)) copolymers at various $VBBI^+TFSI^-$ compositions. These PIL-containing statistical and block copolymers were obtained by post-polymerization functionalization of chloromethylstyrene (CMS) containing prepolymers that were first synthesized via nitroxide-mediated polymerization (NMP) a

living/controlled polymerization technique (**Schemes 3.1a and 3.1b**, respectively). The statistical copolymers precursors were prepared by copolymerizing CMS with MMA in 50 wt % solutions of DMF or 1,4-dioxane at 90 °C, and the block copolymers precursors were prepared by chain extension of poly(MMA-*r*-S) macroinitiator with CMS (**Scheme 3.1**). The CMS containing precursor polymers were then functionalized to ionic liquids bearing chloride anions via quaternization reaction of CMS moieties with 1-butylimidazole. The functionalized precursors were then subsequently converted into $TFSI^-$ counterions by anion exchange yielding $VBBI^+TFSI^-$ (**Scheme 3.1**). This approach was found to be more straightforward, and the product was easier to isolate than directly polymerizing $VBBI^+TFSI^-$ containing monomer as performed in our previous study.[46]

Scheme 3.1. Synthesis of (a) Poly(MMA-*r*-$VBBI^+TFSI^-$) Statistical Copolymers and (b) Poly(MMA-*r*-S)-*b*-Poly($VBBI^+TFSI^-$) Block Copolymers.[a]

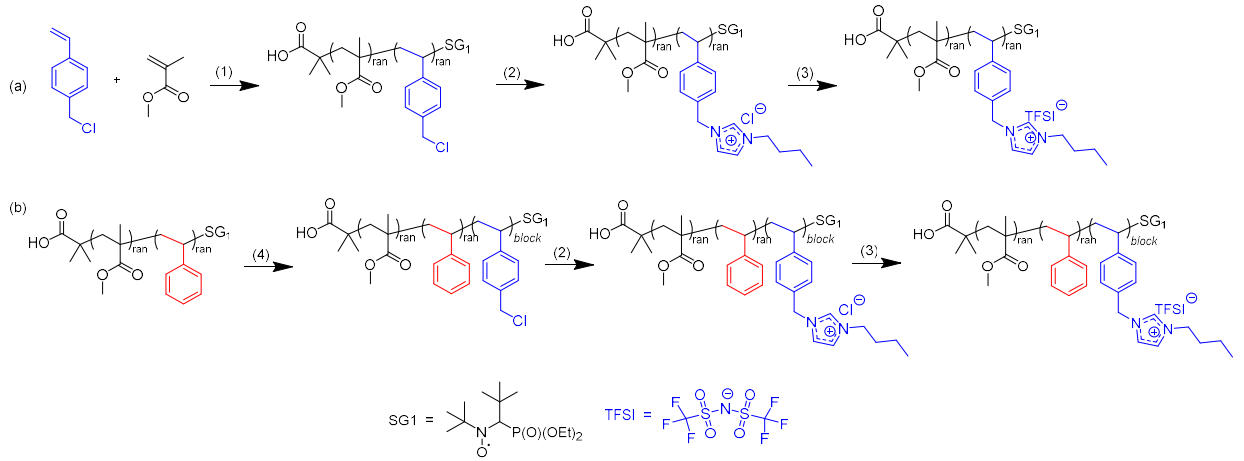

[a] Reagents and conditions: (1) BlocBuilder-MA, SG1, 1,4-dioxane, or DMF, 90 °C, 4−8 h; (2) butylimidazole, THF 60 °C, 24 h; (3) LiTFSI, 50 °C, 48 h; (4) chain extension of poly(MMA-r-S) macroinitiator using CMS: 1,4-dioxane, 110 °C, 8 h.

To achieve a conclusive study comparing block vs statistical copolymers, it is necessary that the statistical copolymers prepared are well-defined with narrow molecular weight distribution and have homogeneous copolymer composition; therefore, they must be synthesized by a controlled polymerization. In this study, NMP was selected because it is relatively simple to implement, and the final polymers can be used in sensitive electronic applications without the need for involved purification techniques such as other controlled radical polymerization techniques.[47–49] The product of k_p, the propagation rate constant, and K, the

activation−deactivation equilibrium constant, is often used to define the kinetics of an NMP system. K is defined as a ratio of the concentration of propagating radicals, [P•], and the free nitroxide concentration, [SG1], over the concentration of reversibly terminated species, [P−SG1]:

$$K = \frac{[\mathrm{P}][\mathrm{SG1}]}{[\mathrm{P}-\mathrm{SG1}]} \quad (3.1)$$

At the beginning of the polymerization, the concentration of free nitroxide radicals is high and relatively constant and is therefore substituted with the initial concentration of SG1 ([SG1] = $[SG1]_0$). The initial molar concentration of SG1 and BlocBuilder-MA is defined by r = $[SG1]_0/[BlocBuilder]_0$, and all polymerizations in this study were performed with $r \leq 0.10$ (**Table 3.1**), which reduces the rate of termination by β-hydrogen chain transfer to SG1, suggesting the major form of irreversible termination is homotermination.[50,51]

Table 3.1 Experimental Formulation for Chloromethylstyrene/Methyl Methacrylate (CMS/MMA) Statistical Copolymerizations Initiated by Using BlocBuilder-MA at 90 °C in 50 wt % Solvent Solution.[a]

Exp ID	CMS		MMA		Solvent		
	mmol	g	mmol	g		mmol	g
CMS/MMA-05/95-A	4.9	0.74	92.5	9.26	DMF	136.82	10
CMS/MMA-05/95-B	4.9	0.74	92.5	9.26	1,4-dioxane	113.49	10
CMS/MMA-10/90	9.5	1.45	85.4	8.55	1,4-dioxane	113.49	10
CMS/MMA-15/85	13.9	2.12	78.7	7.88	1,4-dioxane	113.49	10
CMS/MMA-20/80	18.1	2.76	72.3	7.24	1,4-dioxane	113.49	10
CMS-MMA-30/70-A	25.9	3.95	60.4	6.05	DMF	136.82	10
CMS/MMA-30/70-B	25.9	3.95	60.4	6.05	1,4-dioxane	113.49	10
CMS/MMA-50/50	39.6	6.04	39.6	3.96	DMF	136.82	10
CMS/MMA-55/45	42.6	6.51	34.9	3.49	1,4-dioxane	113.49	10
CMS/MMA-75/25	53.8	8.21	17.9	1.79	DMF	136.82	10
CMS/MMA-95/05	63.3	9.67	3.3	0.33	DMF	136.82	10
CMS/MMA-100/00	65.5	10.00	0.00	0.00	DMF	136.82	10

[a]All copolymerizations were performed at 90 °C with a target average molecular weight of 25 kg mol^{-1} and an initial molar ratio of SG1 relative to BlocBuilder-MA, where $r = [SG1]_0/ [BlocBuilder\text{-}MA]_0 = 0.10$.

During the initial stages of the polymerization chains are relatively short and homotermination is negligible; therefore, the concentration of reversibly deactivated species is assumed to be equal to the initial concentration of initiator ([P−SG1] = $[BlocBuilder]_0$). Finally, k_p is multiplied by K, and substituting the initial molar concentrations of SG1 and BlocBuilder-MA by r to give **eq 3.2**:

$$k_p K = k_p \frac{[SG1]_0[P]}{[BlocBuilder]_0} \quad (3.2)$$

Figure 3.1a expresses $\ln[(1-X)^{-1}]$ as a function of polymerization time where the slopes were used to measure k_p[P•] and k_pK (**Table 3.4**). **Figure 3.1b** demonstrates the increase in number-average molecular weight, $\bar{M}_n$, linearly with X. These plots justify the assumptions and makes eq 1 applicable. Therefore, we initially performed the polymerizations in DMF but found the removal of solvent often required several precipitations into hexanes, resulting in diminished yields due to the material loss associated with each operational step. We investigated the use of 1,4-dioxane as solvent which resulted in higher mass yields due to the lower number of precipitations required to remove the residual solvent; residual 1,4-dioxane is also readily removed via vacuum drying. To our surprise, we also observed that higher X's were achieved in 1,4-dioxane which we attributed to reduced chain transfer to solvent (compared to DMF) as reported with other systems.[52]

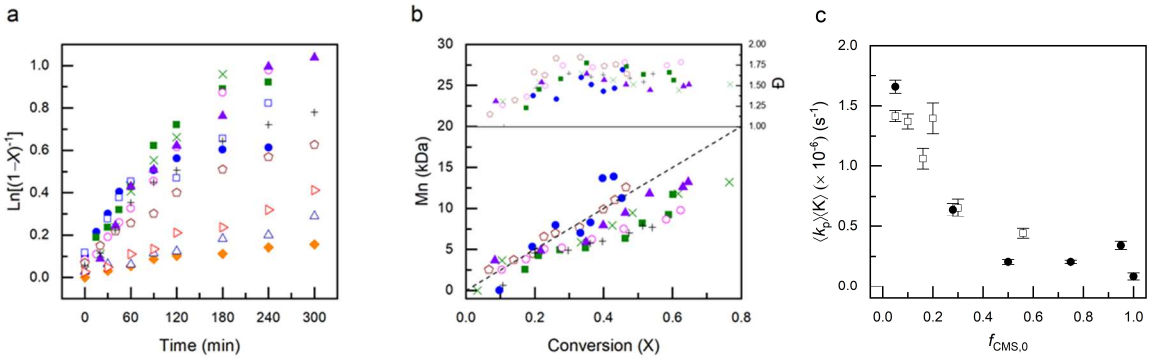

Figure 3.1 (a) Semilogarithmic plot of $\ln(1\text{-}X)^{-1}$) (X = conversion) versus time and (b) number-average molecular weight (M_n) & polymer dispersity (Đ) vs X for chloromethyl(styrene)/methyl methacrylate (CMS/MMA) copolymerization using 15 mol % SG1 relative to BlocBuilder-MA at 90 °C for various initial feeds performed in a 50 wt% 1,4-dioxane solution or DMF solutions. $f_{CMS,0}$ = 0.05 1,4-dioxane (●); $f_{CMS,0}$ = 0.05 DMF (□); $f_{CMS,0}$ = 0.10 1,4-dioxane (■); $f_{CMS,0}$ = 0.15 1,4-dioxane (○); $f_{CMS,0}$ = 0.20 1,4-dioxane (×); $f_{CMS,0}$ = 0.30 1,4-dioxane (▲); $f_{CMS,0}$ = 0.30 DMF (⬠); $f_{CMS,0}$ = 0.50 DMF (◆); $f_{CMS,0}$ = 0.55 1,4-dioxane (+); $f_{CMS,0}$ = 0.75 DMF (△); $f_{CMS,0}$ = 0.95 DMF (▷).(c) Product of average activation-deactivation equilibrium constant $\langle K \rangle$ and the average propagating rate constant $\langle k_P \rangle$, $\langle k_P \rangle \langle K \rangle$ as a function of the initial molar feed fraction of CMS, $f_{CMS,0}$. The experimentally obtained $\langle k_P \rangle \langle K \rangle$ values of reaction performed in DMF are represented by the filled circles and in 1,4-dioxane are represented by the open squares. The error bars were determined from the standard error of the slope from the semilogarithmic kinetic plots.

The change in $\langle k_P \rangle \langle K \rangle$ as a function of CMS feed composition for the copolymerization of MMA/CMS by using both DMF and 1,4-dioxane are very similar to the NMP of other methacrylate/styrenic copolymerization systems such as tertbutyl methacrylate/styrene,[53] benzyl methacrylate/styrene,[54] and 2-(2-methoxyethoxy)ethyl methacryate (MEO2MA)/9-(4-vinylbenzyl)-9H-carbazole (VBK).[55] In addition, the observed linear increase in $\bar{M}_n$ versus X and relatively low $\bar{M}_w/\bar{M}_n$ suggest that the copolymerization is well controlled. These characteristics are crucial for the design of well-defined copolymers and block copolymers and will help elucidate the effect of composition and molecular architecture to device performance.

To synthesize statistical copolymers with specific and predictable final composition, it is necessary to determine the copolymerization reactivity ratios. While the copolymerization of CMS and styrene has been reported by NMP,[56,57] to our knowledge, there has been no study showing the use of CMS as a controlling monomer for NMP of methacrylates. ^{1}H NMR was used to determine copolymer composition of samples taken at low conversion ($X < 0.1$), where we can assume no depletion of either monomer has yet taken place in the polymerization mixture. Eleven polymerizations with initial molar feed compositions of CMS relative to MMA, $f_{CMS,0}$ = 0.05−0.95, were copolymerized in 50 wt % solutions of DMF or 1,4-dioxane at 90 °C. The resulting copolymer composition (X < 0.1) as a function of feed composition are shown in **Figure 3.2** and listed in **Table 3.5**.

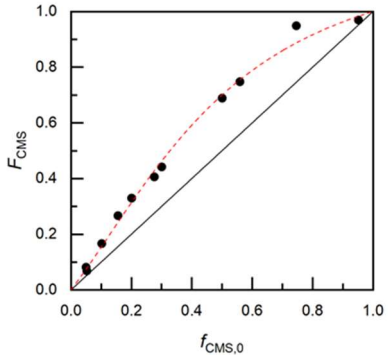

Figure 3.2 Mayo−Lewis plot of copolymer composition with respect to chloromethylstyrene (CMS), F_{CMS}, vs monomer feed composition, $f_{CMS,0}$, using CMS and methyl methacrylate reactivity ratios determined from nonlinear least-squares fitting of the Mayo−Lewis equation to the experimental data (r_{CMS} = 2.99 ± 0.39 and r_{MMA} = 0.71 ± 0.08). The fit is indicated by the dashed line while the experimental data points are found in **Table 3.5**. The straight line indicates the azeotropic composition.

The final composition of a copolymer is defined by the relative addition of each monomer to a propagating chain as represented by a terminal model[58] that defines reactivity ratios r_1 and r_2, where r_1 represents the preference for monomer "1" to add onto a propagating chain with a terminal unit "1" while r_2 represents the preference for monomer "2" to add onto a propagating chain with a terminal unit "2". To determine r_{CMS} and r_{MMA} for the CMS/MMA system, we employ the Mayo−Lewis[58] equation:

$$F_1 = \frac{r_1 f_1^2 + f_1 f_2}{r_1 f_1^2 + 2 f_1 f_2 + r_2 f_2^2} \tag{3.3}$$

where the instantaneous monomer feed compositions f_1 and f_2 are related to the final copolymer composition F and where the subscript "1" = CMS and "2" = MMA in this case. Reactivity ratios were determined to be r_{CMS} = 2.99 and r_{MMA} = 0.71 by performing a nonlinear least-squares fitting of the experimental data (**Table 3.5**) to the Mayo−Lewis equation. The Mayo−Lewis plot is shown in **Figure 3.2** by using the determined reactivity ratios against the experimental data. There has only been one report of CMS/MMA reactivity ratios which differed slightly from our values (r_{CMS} = 0.82 and r_{MMA} = 0.37) which could be due to the their use of conventional free radical polymerization rather than NMP.[59] In both cases, $r_{CMS} > r_{MMA}$, suggesting a favorable addition of the styrenic controlling comonomer relative to MMA which will produce a composition gradient within copolymer, where the propagating end of the polymer has more MMA and the initiation end has more CMS. Recently, studies have shown that with the addition of as little as 1−5 mol % of a styrenic comonomer it is possible to control the copolymerization of methacrylates by NMP when the reactivity ratios are favorable for styrenic addition.[60] The reactivity ratios calculated indicate that the copolymerization of CMS and MMA by NMP leads to well-defined copolymers with tunable and predictable compositions.

3.3.2 Synthesis of VBBI$^+$TFSI$^-$ Containing Statistical and Block Copolymers by Post-polymerization Coupling and Subsequent Anion Exchange.

The MMA/CMS statistical and block copolymers were functionalized by a quaternization reaction with 1-butylimidazole followed by an anion exchange to result in the final VBBI$^+$TFSI$^-$-containing copolymer (**Scheme 3.1**). It is a requirement that all residual CMS monomer be removed before the polymeric sample is functionalized. Otherwise, the CMS monomer will also

undergo the quaternization reaction, producing a VBBI$^+$TFSI$^-$ monomer, which is insoluble in the precipitating medium utilized (hexanes), and thus inseparable from the functionalized polymer. This post-polymerization approach was utilized as the polymer could easily be isolated from the unreacted monomers by precipitation, which was not the case for direct polymerization of the IL monomer.[46] Additionally, the final VBBI$^+$TFSI$^-$-containing polymers are incompatible with SEC columns; thus, the precursor approach facilitated the characterization for the prepolymers by SEC. The quaternization reaction and subsequent anion exchange were confirmed by ^{1}H NMR seen in **Figure 3.8**.

3.3.3 Statistical and Block Copolymer Molecular Weight and Thermal Characterization.

The respective differential scanning calorimetry (DSC) plots used to determine the glass transition temperatures (T_gs) are displayed in **Figure 3.3**. For the MMA/VBBI$^+$TFSI$^-$ statistical copolymers, there is a single relatively narrow T_g, which decreases from 75 to 45 °C with increasing VBBI$^+$TFSI$^-$ composition from 7.7 to 43.2 mol % (**Table 3.2**). As expected, the Tg values obtained for MMA/VBBI$^+$TFSI$^-$ copolymers are between the T_g of pure poly(MMA) ($T_{g,1}$) and poly(VBBI$^+$TFSI$^-$) ($T_{g,2}$) homopolymers. The experimental data were fit to the Gordon−Taylor equation[61] and are represented in **Figure 3.3**. The Gordon− Taylor equation is as follows:

$$T_g = \frac{w_1 T_{g,1} + K' w_2 T_{g,2}}{w_1 + K' w_2} \tag{3.4}$$

$$K' = \frac{T_{g,1}}{T_{g,2}} \tag{3.5}$$

where w_1 and w_2 are weight fractions of the two monomers, and K' is a fitting parameter. The solid line represents a $K' = 1$ and is defined as a fully miscible system when the Gordon−Taylor equation simplifies to the Fox equation. $K' = 0.52$ was identified as the best fit for our experimental data (**Figure 3.3c**). It is important to note that this value is different from $T_{g,1}/T_{g,2} = 0.40$, suggesting that the VBBI$^+$TFSI$^-$ and the MMA are not completely randomly distributed in the polymer chain. This is expected as the CMS/MMA reactivity ratios suggest a gradient copolymer would be produced. These results further suggest that copolymer T_g can be tuned through control of the copolymer composition. **Figure 3.4** illustrates a typical DSC thermogram

of the final functionalized poly(MMA-*r*-S)-*b*-poly(VBBI$^+$TFSI$^-$) block copolymer after quaternization and anion exchange with LiTFSI. The thermogram clearly demonstrates two second-order transitions which correspond to two unique T_gs: one for each block. Not all block copolymers exhibited two distinct T_gs (**Table 3.2**) which is common for polymer samples where one block is too small, resulting in miscibility in the larger block. This is not surprising because all block copolymers in this study were synthesized by using the same poly(MMA-r-S) macroinitiator and only differed in the length of the poly(VBBI$^+$TFSI$^-$) (**Table 3.2**).

Table 3.2 Thermal Properties of VBBI$^+$TFSI$^-$- Containing Statistical and Block Copolymers

Final copolymers [a]	*Polymer ID* [a]	$F_{\text{VBBI+TFSI}}$ [b]	wt %	T_g [c] (°C)	M_w [d] (kg/mol)	M_w/M_n [d]
poly(MMA-*st*-VBBI$^+$TFSI$^-$-7.7)	R-7.7	0.077	11.3	75	26.3	1.21
poly(MMA-*st*-VBBI$^+$TFSI$^-$-12.5)	R-12.5	0.125	17.9	67	29.1	1.19
poly(MMA-*st*-VBBI$^+$TFSI$^-$-14.7)	R-14.7	0.147	20.8	61	26.6	1.21
poly(MMA-*st*-VBBI$^+$TFSI$^-$-34.4)	R-34.4	0.344	44.4	48	20.5	1.18
poly(MMA-*st*-VBBI$^+$TFSI$^-$-43.2)	R-43.2	0.432	53.6	45	22.1	1.21
poly(MMA-*b*-VBBI$^+$TFSI$^-$-5.6)	B-5.6	0.056	8.2	85[e]	25.5	1.21
poly(MMA-*b*-VBBI$^+$TFSI$^-$-8.0)	B-8.0	0.080	11.7	78[e]	27.6	1.52
poly(MMA-*b*-VBBI$^+$TFSI$^-$-9.4)	B-9.4	0.094	13.7	73[e]	29.9	1.21
poly(MMA-*b*-VBBI$^+$TFSI$^-$-12.1)	B-12.1	0.121	17.3	59[e]	31.7	1.25
poly(MMA-*b*-VBBI$^+$TFSI$^-$-18.7)	B-18.7	0.187	25.9	42, 112	32.4	1.23
poly(MMA-*b*-VBBI$^+$TFSI$^-$-22.6)	B-22.6	0.226	30.8	41, 110	32.8	1.22

[a] Final copolymers are given by poly(MMA-st or b-VBBI$^+$TFSI$^-$-X), with MMA = methyl methacrylate, VBBI$^+$TFSI$^-$ = 1-(4-vinylbenzyl)-3- butylimidazolium bis(trifluoromethylsulfonyl)imide and *X* = molar composition of VBBI$^+$TFSI$^-$ determined from ^{1}H NMR spectroscopy. Polymer ID are an abbreviated form of the final copolymer as given by st-*X* or B-*X*, for statistical copolymer (R) or block copolymer (B) and where *X* = molar composition of VBBI$^+$TFSI$^-$ in the final polymer.

[b] $F_{\text{VBBI+TFSI}-}$ is the final molar composition of VBBI$^+$TFSI$^-$ in the copolymer, as determined by ^{1}H NMR spectroscopy.

[c] Determined by differential scanning (DSC) calorimetry using the midpoint method.

[d] Weight-average molecular weight ($\bar{M}_w$) and polymer dispersity ($\bar{M}_w/\bar{M}_n$) were determined for the MMA/CMS copolymer precursors.

[e] Only one single broad T_g was identified by DSC for the resulting block copolymers likely due to the small second block.

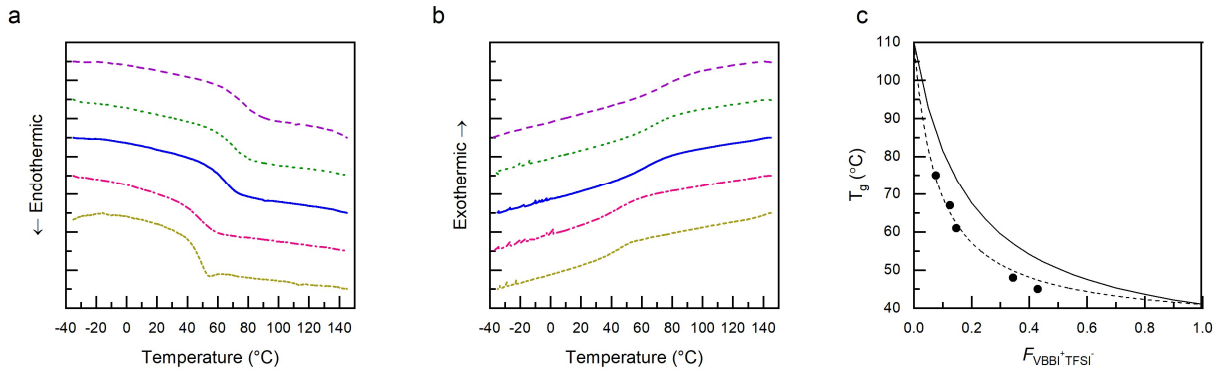

Figure 3.3. DSC exothermic thermograms (a) and DSC endothermic thermograms (b) of MMA/VBBI$^+$TFSI$^-$ statistical copolymers with molar composition of VBBI$^+$TFSI$^-$ ($F_{VBBI^+TFSI^-}$): $F_{VBBI^+TFSI^-}$ = 7.7 (purple dashed line); $F_{VBBI^+TFSI^-}$ = 12.5 (green dotted line); $F_{VBBI^+TFSI^-}$ = 14.7 (blue solid line); $F_{VBBI^+TFSI^-}$ = 34.4 (pink dash-dotted line); $F_{VBBI^+TFSI^-}$ = 43.2 (mustard short-dashed line). (c) Glass transition temperatures as a function of $F_{VBBI^+TFSI^-}$. The dashed line corresponds to the Gordon−Taylor equation with fitting parameter K = 0.52.

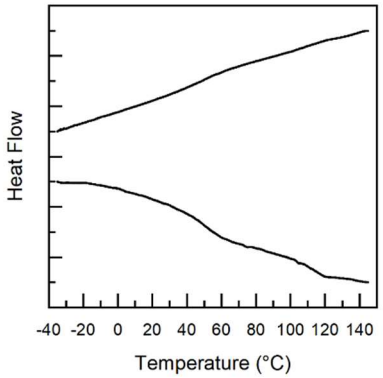

Figure 3.4 DSC thermogram of final functionalized block copolymer, poly(MMA-b-VBBI$^+$TFSI$^-$-22.6), (B-22.6), after quaternization and anion exchange with LiTFSI.

3.3.4 The Impedance Behavior of MMA/VBBI$^+$TFSI$^-$ Statistical and Block Copolymers as Electrolyte Dielectrics.

The metal−insulator−metal (MIM) capacitors were fabricated by spin-coating the VBBI$^+$TFSI$^-$-containing polymer between gold electrodes which were deposited by thermal evaporation as described in the Experimental Section. In the VBBI$^+$TFSI$^-$-containing statistical and block copolymers, the cation is covalently bound to the polymer backbone, whereas the TFSI$^-$ counter-anion can move freely during device operation. Applying a voltage to the MIM capacitor

leads to the movement of $TFSI^-$ anions and formation of electrical double layers (EDLs) at the electrolyte/electrode interfaces.

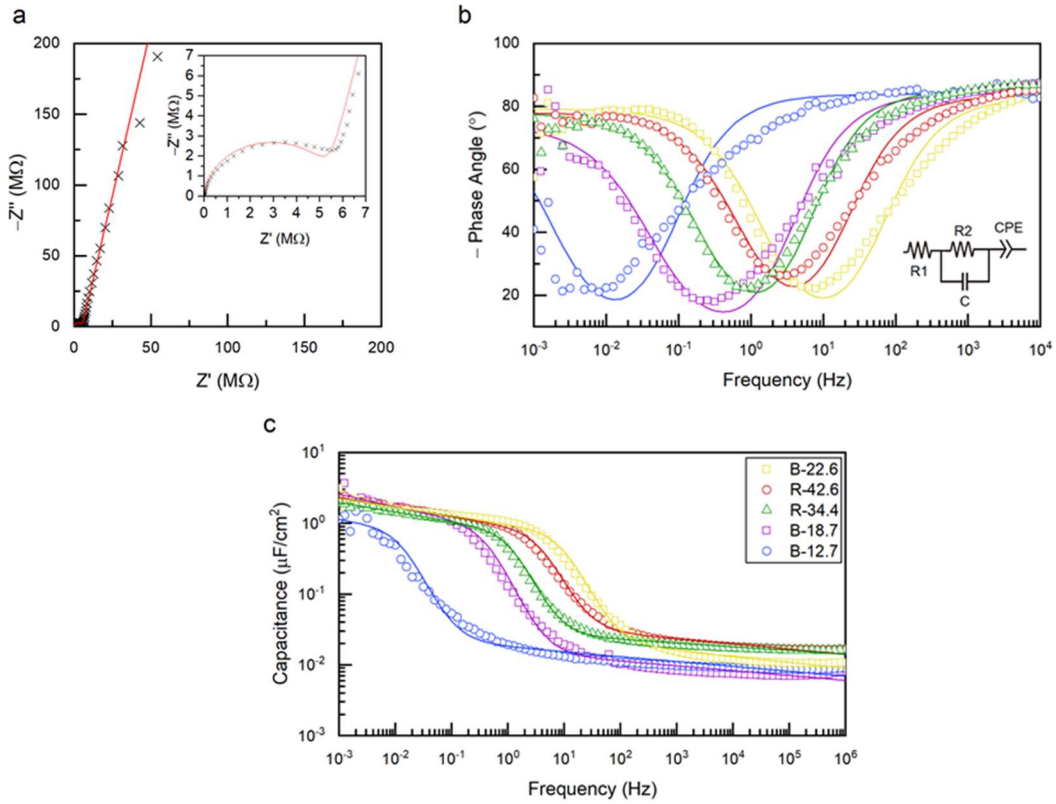

Figure 3.5 (a) Representative Nyquist plot, (b) phase angle vs frequency, and (c) specific capacitance of MIM capacitor with ~400 nm thick poly(MMA-r-S)-poly($VBBI^+TFSI^-$) insulator layer. The inset in (a) displays the high-frequency region of the Nyquist plot. In (b), the symbols represent the experimental data, and the solid line represents the equivalent circuit model fit (equivalent circuit model shown in corner). The equivalent circuit model R1, R2, C, and CPE, represent contact resistance, bulk resistance, dipolar polarization, and resistance from leakage current, respectively. The impedance of the constant phase element (CPE) is described by the equation $Z_{CPE} = Q_n^{-1}(j\omega)^{-n}$, where Q_n is a constant, j is the imaginary number, ω is the angular frequency ($\omega = 2\pi f$), and n is a constant in the range of $0 \leq n \leq 1$. The legend in (c) is valid for both (b) and (c).

Impedance spectroscopy experiments were performed on the series of $VBBI^+TFSI^-$-containing statistical and block copolymer MIM devices, and the corresponding plots are found in **Figure 3.5**. The Nyquist plot (Z'' vs Z') in **Figure 3.5a**, corresponding to $F_{VBBI^+TFSI^-}$ = 0.12, displays a semicircle in high-frequency regimes (10^6–10^0 Hz) and a slanted vertical line in low-

frequency regions (10^0–10^{-3} Hz), which is the expected behavior of an electrolyte with solid electrodes.[62] The phase angle versus frequency plots and corresponding specific capacitance versus frequency for all the $VBBI^+TFSI^-$-containing statistical and block copolymer that displayed ionic motion are compared in **Figures 3.5b and 3.5c**, respectively. As expected the polarization of polyelectrolytes often demonstrates both resistive and capacitive behavior.[18] The experimental impedance data were fit to using an equivalent circuit model, displayed in **Figure 3.5b**. The equivalent circuit model is represented by a capacitor (*C*), which represents the polarization of the polyelectrolyte dipoles, in parallel with a resistor (*R2*), which corresponds to the bulk resistance during high-frequency ion migration. The semicircle in the Nyquist plot (**Figure 3.5a**) is a result of R2, while the vertical line is due to the formation of EDLs at the polyelectrolyte/electrode interfaces and is represented by C in series. However, the nonideal behavior shown by the slanting of vertical line (**Figure 3.5a**) is likely due to the capacitance dispersion caused by the surface roughness of metals in contact with electrolyte at the interface.[62–64] To correct for the nonideal behavior caused by the differentiated EDLs and inhomogeneous interfaces, a constant phase element (CPE) is utilized instead of an ideal capacitor in the equivalent circuit. The impedance of the CPE is therefore defined by **eq 3.6**:[18,63,64]

$$Z_{CPE} = Q_n^{-1}(j\omega)^{-n} \tag{3.6}$$

where Q_n is a constant, j is the imaginary number, ω represents the angular frequency ($\omega = 2\pi f$), and n is a constant ranging from of $0 \leq n \leq 1$. The phase angle is described by $\theta_{CPE}\,(n) = -90n°$: where $n = 1$ represents ideal capacitor behavior with capacitance $C = Q_n$ and where $n = 0$ represents an ideal resistor with resistance $R = Q_n^{-1}$. Additionally, a resistor is placed in series to the equivalent circuit model representing nonideal contact resistance and leakage current of the electrolyte material, *R1*. The equivalent circuit model described is displayed in the **Figure 3.5b** inset. Ionic conductivity can then be found by using the equation $\sigma_{Ion} = dR^{-1}A^{-1}$ where *d* is the film thickness, *A* is the capacitor cross-sectional area, and *R* is the bulk resistance (*R2* from circuit modeling). The ionic conductivity and double-layer capacitance for the $VBBI^+TFSI^-$-containing copolymer films calculated from the experimental impedance data and the fitting parameters for copolymers of different architecture and composition are displayed in **Table 3.3**. The high-frequency dipolar relaxation is 2 orders of magnitude smaller than the EDL capacitance. The small

value of *R1* (~0 Ω for all), representing the nonideal contact resistance, is much lower compared to *R3* (~50 kΩ) representing resistance due to current leakage of the electrolyte. A value of n = ~ 0.9 suggests that the CPE is representing the capacitance caused by EDL formation.

Table 3.3. Fitting Parameters from the Equivalent Circuit Model Components of Poly(VBBI$^+$TFSI$^-$-*r*-MMA) Statistical and Block Copolymer MIM Capacitors

polymer ID [a]	$F_{\text{VBBI+TFSI}}$ [b]	architecture	conductivity [c] (S cm^{-1})	capacitance [c] (nF cm^{-2})	*n* [c]
B-5.6	0.056	block	- [d]	5.9	- [d]
R-7.7	0.077	statistical	- [d]	6.7	- [d]
B-8.0	0.080	block	- [d]	8.2	- [d]
B-9.4	0.094	block	- [d]	8.7	- [d]
B-12.1	0.121	block	2.1×10^{-9}	1,000	0.83
R-12.5	0.125	statistical	- [d]	7.8	- [d]
R-14.7	0.147	statistical	- [d]	8.4	- [d]
B-18.7	0.187	block	8.9×10^{-10}	1,183	0.87
B-22.6	0.226	block	2.4×10^{-9}	1,169	0.89
R-34.4	0.344	statistical	1.6×10^{-9}	1,089	0.85
R-42.6	0.426	statistical	1.8×10^{-9}	1,187	0.87

[a] Polymer ID is an abbreviated form of the final copolymer as given by R-*X* or B-*X*, for statistical copolymer (R) or block copolymer (B) and where *X* = molar composition of VBBI$^+$TFSI$^-$ in the final polymer.

[b] $F_{VBBI^+TFSI^-}$ is the final molar composition of VBBI$^+$TFSI$^-$ in the copolymer, as determined by ^{1}H NMR spectroscopy.

[c] Conductivity and capacitance were determined by electrical impedance spectroscopy (EIS). *n* is a constant as found in **eq 3.6**.

[d] Materials that did not exhibit any frequency dependence and thus no double layer capacitance; their constant capacitance is reported.

Figure 3.5c displays the effective specific capacitance versus frequency. The capacitance increases as frequency decreases and is >1 μF/cm^2 at frequencies under 1 Hz. Poly(MMA), which does not exhibit an EDL, has a constant capacitance independent of frequency. The large capacitance of the poly(MMA-r-S)-*b*-poly(VBBI$^+$TFSI$^-$) block copolymers is caused by the EDLs formed at the polyelectrolyte/electrode interface. Additionally, by use of the constant phase element, a frequency-independent effective capacitance can be calculated from *R* and the fitting parameters (**eq 3.7**):[62,64]

$$C = R^{((1/n)-1)} Q_n^{1/n} \qquad (3.7)$$

The frequency-independent capacitance calculated is ~1 μF/cm^2, which is comparable to other electrolytes that incorporate ionic liquids.[62,65] The impedance properties of the polyelectrolyte thin-film capacitors were also studied as a function of PIL composition and architecture. We performed EIS on the poly(MMA-*r*-VBBI$^+$TFSI$^-$) statistical copolymer with compositions of $F_{VBBI^+TFSI^-}$ = 0.07−0.426 and poly(MMA-*r*-S)-*b*-poly(VBBI$^+$TFSI$^-$) block copolymers of $F_{VBBI^+TFSI^-}$ = 0.056−0.226 (**Table 3.3**). Of the 11 copolymers examined by EIS, only six exhibited behavior suggesting EDL formation. All block copolymers above $F_{VBBI^+TFSI^-}$ > 0.094 resulted in EDL formation, in contrast to a minimum of $F_{VBBI^+TFSI^-}$ > 0.34 needed for the statistical copolymers. We attribute this to the MMA impeding the movement of the TFSI$^-$ anions in the insulating film whereas microdomains are formed in the block copolymer films which facilitate this migration.[66] It is interesting to note that the observed EDL formation roughly corresponds to the copolymer composition where two distinct T_gs were measured for the poly(MMA-*r*-S)-*b*-poly(VBBI$^+$TFSI$^-$) block copolymers by DSC, further suggesting microphase separation of larger blocks is desirable over smaller miscible blocks. Regardless, these results suggest that both copolymer composition and copolymer architecture are critical for the formation of the EDL. Furthermore, the use of block copolymers over statistical copolymers facilitates the formation of the EDL with less required VBBI$^+$TFSI$^-$ content in the polymer.

3.3.5 Unipolar Polyelectrolyte Dielectrics for n-Type EGTs.

We characterized the unipolar conduction behavior of a characteristic VBBI$^+$TFSI$^-$-containing block copolymer and compared it to the poly(MMA) homopolymer as the gating medium in TFTs. Because of the mobile anion in the VBBI$^+$TFSI$^-$-containing block copolymer, it was paired with an n-type semiconductor in top-gate transistors to avoid electrochemical doping. Applying a positive potential to the gate promotes the movement of TFSI$^-$ anions toward the gate, resulting in the polyelectrolyte/semiconductor interface to possess solely the large polycationic backbone. The large macromolecule is too large to penetrate the semiconductor layer, forming an EDL.[67] A solution-processable n-type semiconductor, poly(NDI20D-T2), was used to fabricate top gate bottom contact (TGBC) devices.[68]

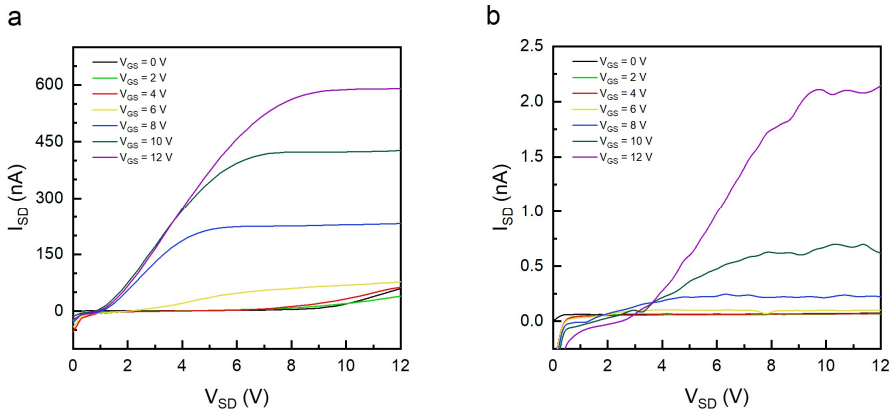

Figure 3.6 Example output curves for TGBC devices with n-type semiconductor using (a) poly(MMA-*b*-VBBI$^+$TFSI$^-$-22.6) and (b) poly(MMA) insulators. All data for devices are characterized in air.

Figures 3.6a and **3.6b** show the output characteristics of TGBC n-type poly(NDI2OD-T2) TFTs (W/L = 30 mm/50 µm) with a gating medium of ~400 nm poly(MMA-*r*-S)-b-poly(VBBI$^+$TFSI$^-$) block copolymer or poly(MMA) film, respectively. The measured specific capacitances of the polyelectrolyte films are about 2 orders of magnitude larger than that of the poly(MMA) films (**Table 3.3**), leading to higher drain currents (I_{SD}) for comparable operating voltage. As shown in **Figure 3.6**, devices using the polyelectrolyte demonstrated I_{SD} ranging between 1 and 2 orders of magnitude higher than those using poly(MMA) for a similar range of V_{GS} and V_{SD}, thus showing reduced operating voltage required to differentiate conduction state. For both materials, the presence of an injection barrier is evident in the delayed onset of the linear region, although this effect is particularly pronounced for the poly(MMA) devices. This barrier is often observed in TFTs with the bottom-contact device configuration or semiconductor−electrode energetic mismatch and could be remedied with device architecture or contact modifications to further reduce V_{SD} required for operation.[69]

Transfer characteristics for the polyelectrolyte and poly-(MMA) devices (**Figure 3.7**) were obtained by sweeping V_{GS} at a slow sweep rate of 200 mV/s to guarantee EDL formation while holding V_{SD} constant at 8 V. Poly(MMA) devices exhibited little hysteresis, observed as a difference in the forward and reverse sweeps, whereas the PIL-containing devices showed significant hysteresis stems from the slower polarization speed of the poly(MMA-*r*-S)-*b*-poly-(VBBI$^+$TFSI$^-$) block copolymer compared to the nonionic polarization of poly(MMA). Given a constant C, the saturation regime electron mobility can be determined from **eq 3.8**:

$$I_D = \frac{W}{2L} C\mu(V_{GS} - V_{th})^2 \qquad (3.8)$$

where W is the width of the channel, L is the length of the channel, V_{th} is the threshold voltage, and μ is electron field-effect mobility for the saturation region. To calculate the μ of poly(NDI2OD-T2) from the transfer data, specific capacitance (C) values of 5 and 1000 nF cm^{-2} were used for the poly(MMA) and polyelectrolyte devices, respectively, and were shown to be constant as a function of voltage (**Figure 3.9**). The saturation μ for both types of devices ranged similarly between 0.0004 and 0.0012 cm^2 V^{-1} s^{-1} for V_{DS} held at 8 V, while Vth for the PIL devices (~4 V) was slightly lower than for the poly(MMA) devices (~6 V). Because of the significant contact resistance observed, linear region characteristics could not be easily obtained. These results demonstrate that while VBBI$^+$TFSI$^-$-containing copolymers do not substantially impact the μ of poly(NDI2OD-T2), they do result in a minor decrease in V_{th} and a significant increase in capacitance and output current compared to poly(MMA) in TFTs. If the threshold voltage could be reduced along with the contact resistance, operating voltage requirements in terms of V_{GS} and V_{DS} could be further decreased.

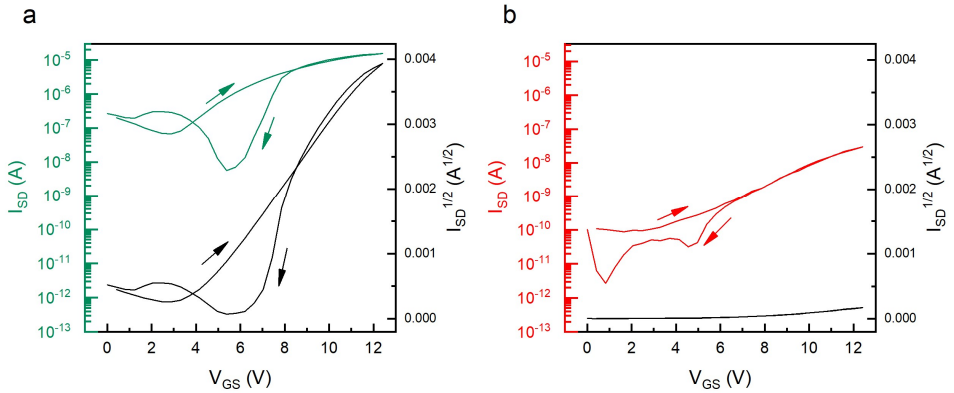

Figure 3.7 Example transfer characteristics of TGBC devices with n-type semiconductor using (a) polyelectrolyte and (b) poly(MMA) insulators. All data for devices are characterized in air with a constant V_{DS} of 8 V.

3.4 Conclusion

In this study, we demonstrated that the controlled copolymerization of methyl methacrylate (MMA) and chloromethylstyrene (CMS) is possible by nitroxide-mediated polymerization giving rise to well-defined copolymers with predictable kinetics, molecular weights, and copolymer

composition. We report the effect of feed composition on the copolymerization kinetics and on the final copolymer composition. Second, we synthesize a series of block copolymers using a MMA rich macroinitiator for the initiation of a second batch of CMS, resulting in well-defined CMS-containing block copolymers. We then successfully converted the CMS units in the statistical and block copolymers to 1-(4-vinylbenzyl)-3-butylimidazolium bis(trifluoromethylsulfonyl)-imide ($VBBI^+TFSI^-$) and tracked the complete conversion by ^1H NMR. We determined a relationship between the glass transition temperatures of the resulting $VBBI^+TFSI^-$-containing statistical/block copolymers and $VBBI^+TFSI^-$ composition. We then measured the capacitance behavior of these materials by using impedance spectroscopy and found that all $VBBI^+TFSI^-$-containing block copolymers with a molar copolymer composition of $F_{VBBI^+TFSI^-} > 0.094$ resulted in electric double layer (EDL) formation in contrast to a minimum of $F_{VBBI^+TFSI^-} > 0.34$ needed for the $VBBI^+TFSI^-$-containing statistical copolymers. Finally, we demonstrated that the $VBBI^+TFSI^-$-containing copolymers that form an EDL resulted in n-type TFT devices that show significantly greater output current at lower operating voltages compared to devices that utilized poly(MMA) homopolymer as the dielectric insulating material. These findings represent the beginning of crucial design rules for solid polymer electrolytes for TFTs: it is possible to introduce a significant portion of comonomers to impart secondary functionality, such as mechanical strength, while maintaining the desirable EDL. Second, this composition can be increased even further when using block copolymer architecture rather than a random distribution.

3.5 Experimental Section

Synthesis of Statistical Precursor Copolymer Poly-(MMA-r-CMS).

The polymerizations were performed in a 100 mL three-neck round-bottom flask equipped with a magnetic stir bar, thermal well, and condenser. The vessel was placed into a heating mantle with a magnetic stirrer. The experimental formulations are tabulated in **Table 3.1**. All polymerization feeds were calculated for a target number-average molecular weight ($\overline{M}_n$) of 25 kg mol^{-1} at complete conversion (X). The procedure for an initial molar feed composition of chloromethylstyrene (CMS) ($f_{CMS,0}$) equal to 0.20 is used as an example (CMS/MMA-20/80, Table 1): CMS (2.76 g, 18.1 mmol), MMA (7.24 g, 72.3 mmol), BlocBuilder-MA (152.6 mg, 0.4 mmol), SG1 (17.7 mg, 0.06 mmol), and 1,4-dioxane (10.00 g, 113.5 mmol) were added to the flask and

mixed with a stir bar. A thermocouple was placed into the thermal well in one of the reactor necks and connected to a temperature controller. A condenser fitted to a recirculating chiller, and a nitrogen line was connected to the second neck to prevent loss of solvent and monomer from evaporation. Prior to heating, the reaction solution was bubbled with nitrogen for at least 20 min with stirring to aid in the removal of dissolved oxygen. Next, the vessel was heated to 90 °C while under a constant nitrogen purge. The polymerization start time was taken when the reaction mixture reached a temperature of 90 °C. Samples were periodically collected with a syringe for 5 h, after which the reaction mixture was cooled and precipitated into hexanes (the polymerizations performed in DMF were precipitated into methanol). After precipitating, the polymer was isolated by filtration and redissolved in tetrahydrofuran (THF) and reprecipitated once more into hexanes to remove the unreacted CMS and residual solvents. The polymer was filtered and dried overnight in a vacuum oven at 70 °C to remove any unreacted monomer or solvent from the precipitated medium.

Synthesis of Statistical Copolymers Poly(MMA-r-VBBI$^+$TFSI$^-$) and Block Copolymers Poly(MMA-r-S)-b-Poly-(VBBI$^+$TFSI$^-$) from Respective Precursor Polymers.

The synthesis of the PIL statistical precursor copolymer poly(methyl methacrylate-*r*-1-(4-vinylbenzyl)-3-butylimidazolium chloride) (poly-(MMA-*r*-VBBI$^+$Cl$^-$)) is shown in **Scheme 3.1**. For example, poly(CMS-*r*-MMA) precursor polymer (1.0 g) was dissolved in DMSO (10 mL), and 1-butylimidazole (7.21 mmol, 0.90 g) was added to the mixture which was then heated to 50 °C under nitrogen for 20 h. The reaction mixture was cooled to room temperature and precipitated into diethyl ether, and then the polymer product was isolated by filtration to remove the excess 1-butylimidazole and bulk solvent. The crude product was then dried overnight in a vacuum oven at 70 °C. The anion exchange from Cl$^-$ to TFSI$^-$ from the respective polymer is shown in Scheme 1. Poly(MMA-*r*-VBBI$^+$Cl$^-$) (1 g) and LiTFSI (1.04 g, 3.61 mmol) were mixed with DMA (10 mL) and stirred at room temperature for 48 h. The reaction mixture was precipitated into excess DI water twice. The resulting poly(MMA-*r*-VBBI$^+$TFSI$^-$) copolymer was isolated by filtration and dried in an oven at 70 °C for 24 h. The same procedure was also performed on the block copolymers.

Preparation of Metal−Insulator−Metal (MIM) Capacitors.

MIM capacitors were fabricated under atmospheric conditions. The 1 in. × 1 in. glass slides cut from standard microscope slides were initially cleaned by sequential sonication steps in a series of solvents (soapy water, water, acetone, methanol) for 5 min each and blown dry with a nitrogen stream. The cleaned substrates were then patterned with Au bottom electrodes (30 nm) by physical vapor deposition (a 10 nm chromium adhesion layer was deposited prior to Au deposition) with aid of a shadow mask followed by an air plasma treatment process (10 min, Harrick Plasma Cleaner PDC-32G). Next, a solution of 50 mg/mL polymer (poly(MMA) or polyelectrolyte) in methyl ethyl ketone (MEK, 99%) was deposited by spin-coating at 2000 rpm on the patterned substrate and then annealed at 120 °C under vacuum for 2 h. Sequentially, the same polymer solution was applied again at 2000 rpm on the heat-treated substrate and annealing process repeated to give the final insulating film of ∼500 nm. The top Au electrodes (40 nm) were then deposited by physical vapor deposition producing the final MIM capacitors. The overlap of the bottom and top electrodes led to 16 unique devices with varying known areas ranging from 0.35 to 2.88 mm^2.

OTFT Device Fabrication.

Top-gate bottom-contact OTFTs were fabricated in an oxygen (<10 ppm) and moisture (<10 ppm) free glovebox. Prepatterned substrates with interdigitated indium tin oxide (ITO) finger electrodes having channel dimensions of 30 mm (W) × 50 μm (L) were purchased from Ossila. The prepatterned substrates were cleaned by the same process as capacitor substrates previously described. A solution of 15 mg/mL poly{[N,N′-bis(2-octyldodecyl)naphthalene-1,4,5,8-bis(dicarboximide)-2,6-diyl]-alt-5,5′-(2,2′-bithiophene)} (poly(NDI2OD-T2)) n-type semiconductor in dichlorobenzene (DCB) was deposited by spin-coating at 2000 rpm on the substrate, followed by annealing at 105 °C for 10 min. After that, the gating medium was spun-cast at 2000 rpm from a 50 mg/mL solution in MEK onto the semiconductor film, annealed, and repeated in a similar fashion to the polymer layers in the MIM capacitors. Finally, the gold gate electrode was deposited by thermal evaporation through a shadow mask on top of the insulating layer by using an Angstrom EvoVac system (base pressure $<3.0 \times 10^{-7}$ Torr).

3.6 Acknowledgements

The authors are very grateful for financial support from the NSERC Discovery Grant (2015-03987) to B.H.L. The authors also thank Dr. Adrien Metafiot and Professor Milan Maric (McGill University) for the use of SEC for characterization of the CMS/MMA copolymers used for the kinetic analysis and Prof Marc Dube' for the donation of the BlocBuilder-MA, which was originally obtained from Arkema. This work was also supported by an Ontario government Queen Elizabeth II Graduate Scholarship in Science and Technology (QEII GSST) to A.J.P. and Ontario Graduate scholarship (OGS) to O.A.M.

3.7 Supplementary Information

Copolymerization experimental conditions, Mayo−Lewis experimental data, representative NMRs of precursor and final functionalized polymer, representative capacitance−voltage impedance measurement of ionic-liquid containing copolymer.

3.7.1 Additional Tables & Figures

Table 3.4. Chloromethyl styrene/methyl methacrylate (CMS/MMA) statistical copolymerizations initiated by BlocBuilder-MA at 90 °C in 50 wt% DMF or 1,4-dioxane solution.

Exp ID [a]	$f_{CMS,0}$ [b]	$F_{CMS,10}$ [c]	$k_P[P]$ (s^{-1}) [d]	$k_P\langle K\rangle$ (s^{-1}) [e]	X [f]
CMS/MMA-05/95-A	0.05	0.07	$(1.11 \pm 0.04) \times 10^{-4}$	$(1.66 \pm 0.05) \times 10^{-5}$	0.46
CMS/MMA-05/95-B	0.05	0.08	$(9.43 \pm 0.30) \times 10^{-5}$	$(1.42 \pm 0.05) \times 10^{-5}$	0.56
CMS/MMA-10/90	0.10	0.17	$(9.14 \pm 0.42) \times 10^{-5}$	$(1.37 \pm 0.06) \times 10^{-5}$	0.60
CMS/MMA-15/85	0.16	0.27	$(7.05 \pm 0.56) \times 10^{-5}$	$(1.06 \pm 0.08) \times 10^{-5}$	0.62
CMS/MMA-20/80	0.20	0.33	$(9.31 \pm 0.85) \times 10^{-5}$	$(1.40 \pm 0.13) \times 10^{-5}$	0.77
CMS-MMA-30/70	0.28	0.41	$(4.27 \pm 0.34) \times 10^{-5}$	$(6.41 \pm 0.52) \times 10^{-6}$	0.47
CMS/MMA-30/70	0.30	0.44	$(4.38 \pm 0.49) \times 10^{-4}$	$(6.57 \pm 0.73) \times 10^{-6}$	0.65
CMS/MMA-50/50	0.50	0.69	$(1.37 \pm 0.14) \times 10^{-5}$	$(2.05 \pm 0.20) \times 10^{-6}$	0.14
CMS/MMA-55/45	0.56	0.75	$(2.94 \pm 0.27) \times 10^{-5}$	$(4.42 \pm 0.41) \times 10^{-6}$	0.54
CMS/MMA-75/25	0.75	0.95	$(1.37 \pm 0.01) \times 10^{-5}$	$(2.05 \pm 0.14) \times 10^{-6}$	0.30
CMS/MMA-95/05	0.95	0.98	$(2.27 \pm 0.23) \times 10^{-5}$	$(3.40 \pm 0.34) \times 10^{-6}$	0.32
CMS/MMA-100/00	1.00	1.00	$(5.67 \pm 1.95) \times 10^{-5}$	$(8.50 \pm 2.92) \times 10^{-7}$	0.37

a) Experimental identification (exp ID) for copolymerizations are given by CMS/MMA-X/Y, with CMS representing chloromethyl styrene, MMA = methyl methacrylate and X/Y = molar feed ratio of CMS relative to MMA.
b) $f_{CMS,0}$ is the initial molar fraction of CMS in the feed determined by ^{1}H NMR.
c) $F_{CMS,10}$ is the copolymer composition at $X = 0.10$ determined by ^{1}H NMR.
d) $k_P[P]$ is the apparent rate constant, determined from the slope of the linear region of the kinetic plots.
e) Product of the average propagation rate constant, $\langle k_P\rangle$, and the average equilibrium constant, $\langle K\rangle$. Error derived from the standard error in the slope of scaled conversion ($\ln(1\text{-}X)^{-1}$) versus time plots.
f) Final monomer conversion (X), as determined by ^{1}H NMR spectroscopy

Table 3.5. Chloromethyl styrene/methyl methacrylate (CMS/MMA) statistical copolymerizations initiated by BlocBuilder-MA at 90°C in 50 wt% DMF or 1,4-dioxane solutions.

Exp ID [a]	$f_{CMS,0}$ [b]	F_{CMS} [c]
CMS/MMA-05/95-A	0.05	0.08
CMS/MMA-05/95-B	0.05	
CMS/MMA-10/90	0.10	0.13
CMS/MMA-15/85	0.16	0.20
CMS/MMA-20/80	0.20	0.29
CMS-MMA-30/70	0.28	
CMS/MMA-30/70	0.30	0.45
CMS/MMA-50/50	0.50	0.72
CMS/MMA-55/45	0.56	0.77
CMS/MMA-75/25	0.75	
CMS/MMA-95/05	0.95	~0.99
CMS/MMA-100/00	1.00	

a) Experimental identification (exp ID) for CMS/MMA copolymerizations are given by CMS/MMA-X/Y, with CMS representing chloromethyl styrene, MMA = methyl methacrylate and X/Y = initial molar feed ratio of CMS to MMA.
b) $f_{PFS,0}$ is the initial molar fraction of CMS in the feed determined by ^{1}H NMR spectroscopy.
c) F_{CMS} is the final molar composition of CMS in the copolymer, as determined by ^{1}H NMR spectroscopy.

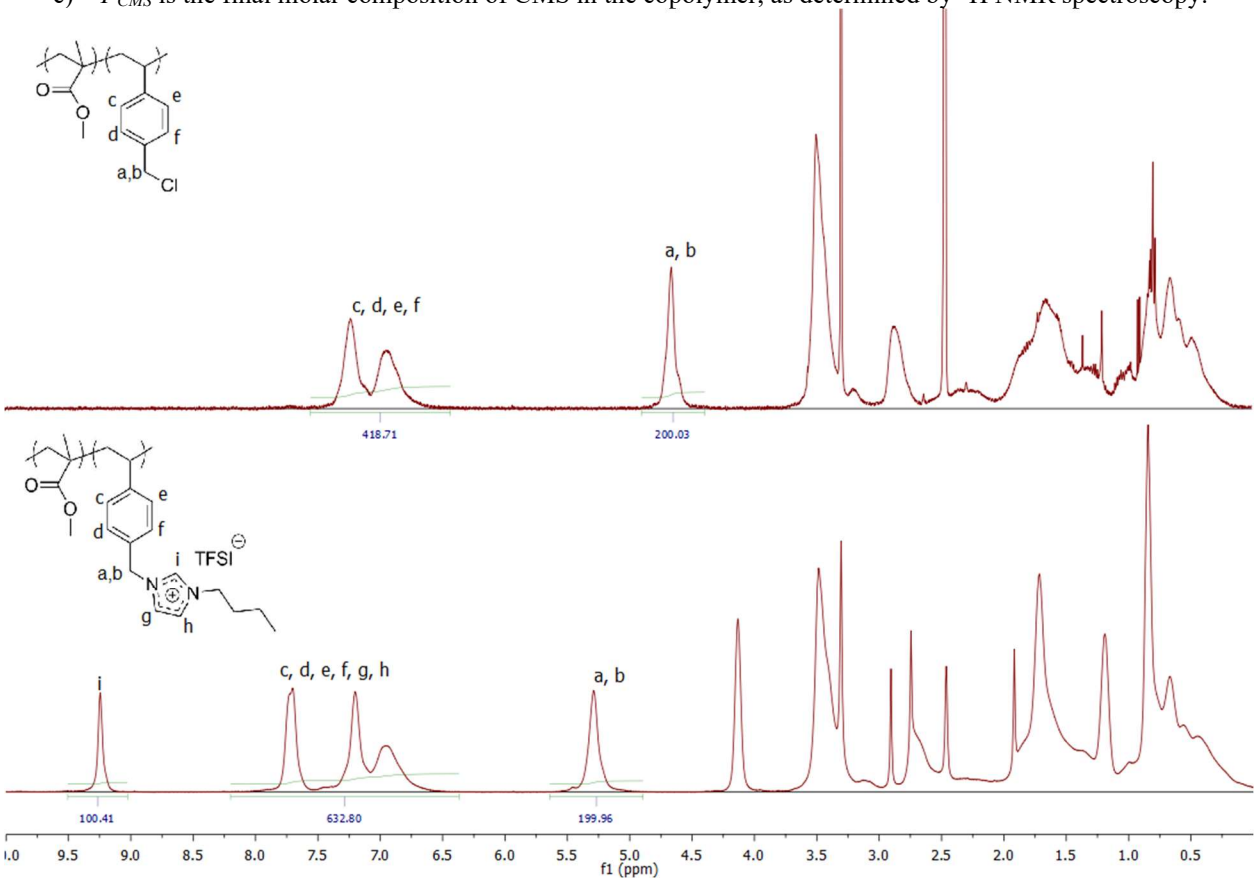

Figure 3.8. Precursor (poly(CMS-r-MMA)) and final polymer poly(VBBI$^+$TFSI$^-$-r-MMA) after quaternization and anion exchange reaction.

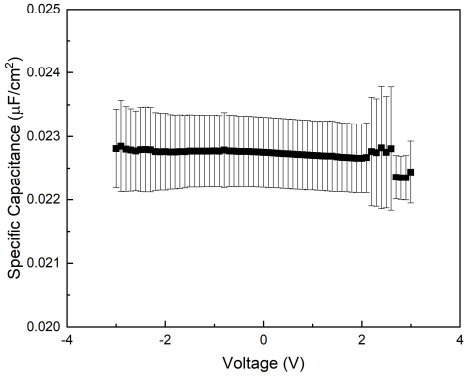

Figure 3.9. Representative capacitance versus voltage by Electrical Impedance Spectroscopy (EIS) for poly(IL-*b*-MMA) MIM.

3.7 References

(1) Berggren, M.; Nilsson, D.; Robinson, N. D. Organic Materials for Printed Electronics. *Nat. Mater.* **2007**, *6* (1), 3– 5.

(2) Berggren, M.; Richter-Dahlfors, A. Organic Bioelectronics. *Adv. Mater.* **2007**, *19* (20), 3201– 3213.

(3) Dodabalapur, A. Organic and Polymer Transistors for Electronics. *Mater. Today* **2006**, *9* (4), 24– 30.

(4) Kim, S. H.; Hong, K.; Xie, W.; Lee, K. H.; Zhang, S.; Lodge, T. P.; Frisbie, C. D. Electrolyte-Gated Transistors for Organic and Printed Electronics. *Adv. Mater.* **2013**, *25* (13), 1822– 1846.

(5) Braga, D.; Erickson, N. C.; Renn, M. J.; Holmes, R. J.; Frisbie, C. D. High-Transconductance Organic Thin-Film Electrochemical Transistors for Driving Low-Voltage Red-Green-Blue Active Matrix Organic Light-Emitting Devices. *Adv. Funct. Mater.* **2012**, *22* (8), 1623– 1631.

(6) Andersson, P.; Forchheimer, R.; Tehrani, P.; Berggren, M. Printable All-Organic Electrochromic Active-Matrix Displays. *Adv. Funct. Mater.* **2007**, *17* (16), 3074– 3082.

(7) Lin, P.; Yan, F. Organic Thin-Film Transistors for Chemical and Biological Sensing. *Adv. Mater.* **2012**, *24* (1), 34– 51.

(8) Xia, Y.; Zhang, W.; Ha, M.; Cho, J. H.; Renn, M. J.; Kim, C. H.; Frisbie, C. D. Printed Sub-2 V Gel-Electrolyte-Gated Polymer Transistors and Circuits. *Adv. Funct. Mater.* **2010**, *20* (4), 587– 594.

(9) Herlogsson, L.; Cölle, M.; Tierney, S.; Crispin, X.; Berggren, M. Low-Voltage Ring Oscillators Based on Polyelectrolyte-Gated Polymer Thin-Film Transistors. *Adv. Mater.* **2010**, *22* (1), 72– 76.

(10) Dimitrakopoulos, C. D.; Malenfant, P. R. L. Organic Thin Film Transistors for Large Area Electronics. *Adv. Mater.* **2002**, *14* (2), 99– 117.

(11) Facchetti, A.; Yoon, M. H.; Marks, T. J. Gate Dielectrics for Organic Field-Effect Transistors: New Opportunities for Organic Electronics. Adv. Mater. 2005, 17 (14), 1705–1725.

(12) Halik, M.; Klauk, H.; Zschieschang, U.; Schmid, G.; Dehm, C.; Schütz, M.; Maisch, S.; Effenberger, F.; Brunnbauer, M.; Stellacci, F. Low-Voltage Organic Transistors with an Amorphous Molecular Gate Dielectric. Nature 2004, 431 (7011), 963– 966.

(13) Xie, W.; Frisbie, C. D. Electrolyte Gated Single-Crystal Organic Transistors to Examine Transport in the High Carrier Density Regime. *MRS Bull.* **2013**, *38* (1), 43– 50.

(14) Shimotani, H.; Diguet, G.; Iwasa, Y. Direct Comparison of Field-Effect and Electrochemical Doping in Regioregular Poly(3-Hexylthiophene). *Appl. Phys. Lett.* **2005**, *86* (2), 022104.

(15) Yuan, H.; Shimotani, H.; Tsukazaki, A.; Ohtomo, A.; Kawasaki, M.; Iwasa, Y. High-Density Carrier Accumulation in ZnO Field-Effect Transistors Gated by Electric Double Layers of Ionic Liquids. *Adv. Funct. Mater.* **2009**, *19* (7), 1046– 1053.

(16) Thiemann, S.; Sachnov, S. J.; Pettersson, F.; Bollström, R.; Österbacka, R.; Wasserscheid, P.; Zaumseil, J. Cellulose-Based Ionogels for Paper Electronics. *Adv. Funct. Mater.* **2014**, *24* (5), 625– 634.

(17) Bubel, S.; Meyer, S.; Kunze, F.; Chabinyc, M. L. Ionic Liquid Gating Reveals Trap-Filled Limit Mobility in Low Temperature Amorphous Zinc Oxide. *Appl. Phys. Lett.* **2013**, *103* (15), 152102.

(18) Larsson, O.; Said, E.; Berggren, M.; Crispin, X. Insulator Polarization Mechanisms in Polyelectrolyte-Gated Organic Field-Effect Transistors. *Adv. Funct. Mater.* **2009**, *19* (20), 3334– 3341.

(19) Cho, J. H.; Lee, J.; Xia, Y.; Kim, B.; He, Y.; Renn, M. J.; Lodge, T. P.; Daniel Frisbie, C. Printable Ion-Gel Gate Dielectrics for Low-Voltage Polymer Thin-Film Transistors on Plastic. *Nat. Mater.* **2008**, *7* (11), 900– 906.

(20) Yomogida, Y.; Pu, J.; Shimotani, H.; Ono, S.; Hotta, S.; Iwasa, Y.; Takenobu, T. Ambipolar Organic Single-Crystal Transistors Based on Ion Gels. *Adv. Mater.* **2012**, *24* (32), 4392– 4397.

(21) Panzer, M. J.; Newman, C. R.; Frisbie, C. D. Low-Voltage Operation of a Pentacene Field-Effect Transistor with a Polymer Electrolyte Gate Dielectric. *Appl. Phys. Lett.* **2005**, *86* (10), 103503.

(22) Xie, W.; Frisbie, C. D. Organic Electrical Double Layer Transistors Based on Rubrene Single Crystals: Examining Transport at High Surface Charge Densities above 10 13 Cm −2. *J. Phys. Chem. C* **2011**, *115* (29), 14360– 14368.

(23) Thiburce, Q.; Campbell, A. J. Low-Voltage Polyelectrolyte-Gated Polymer Field-Effect Transistors Gravure Printed at High Speed on Flexible Plastic Substrates. *Adv. Electron. Mater.* **2017**, *3* (2), 1600421.

(24) Liu, Z.; Yin, Z.; Wang, J.; Zheng, Q. Polyelectrolyte Dielectrics for Flexible Low-Voltage Organic Thin-Film Transistors in Highly Sensitive Pressure Sensing. *Adv. Funct. Mater.* **2019**, *29* (1), 1806092.

(25) Yin, M. J.; Yin, Z.; Zhang, Y.; Zheng, Q.; Zhang, A. P. Micropatterned Elastic Ionic Polyacrylamide Hydrogel for Low-Voltage Capacitive and Organic Thin-Film Transistor Pressure Sensors. *Nano Energy* **2019**, *58*, 96– 104.

(26) Lee, J.; Kaake, L. G.; Cho, J. H.; Zhu, X.-Y.; Lodge, T. P.; Frisbie, D. Ion Gel-Gated Polymer Thin-Film Transistors: Operating Mechanism and Characterization of Gate Dielectric Capacitance, Switching Speed, and Stability. *J. Phys. Chem. C* **2009**, *113*, 8972–8981.

(27) Herlogsson, L.; Noh, Y. Y.; Zhao, N.; Crispin, X.; Sirringhaus, H.; Berggren, M. Downscaling of Organic Field-Effect Transistors with a Polyelectrolyte Gate Insulator. *Adv. Mater.* **2008**, *20* (24), 4708– 4713.

(28) Panzer, M. J.; Frisbie, C. D. Polymer Electrolyte-Gated Organic Field-Effect Transistors: Low-Voltage, High-Current Switches for Organic Electronics and Testbeds for Probing Electrical Transport at High Charge Carrier Density. *J. Am. Chem. Soc.* **2007**, *129* (20), 6599– 6607.

(29) Panzer, M. J.; Frisbie, C. D. High Carrier Density and Metallic Conductivity in Poly(3-Hexylthiophene) Achieved by Electrostatic Charge Injection. *Adv. Funct. Mater.* **2006**, *16* (8), 1051– 1056.

(30) Laiho, A.; Nguyen, H. T.; Sinno, H.; Engquist, I.; Berggren, M.; Dubois, P.; Coulembier, O.; Crispin, X. Amphiphilic Poly(3-Hexylthiophene)-Based Semiconducting Copolymers for Printing of Polyelectrolyte-Gated Organic Field-Effect Transistors. *Macromolecules* **2013**, *46* (11), 4548– 4557.

(31) Panzer, M. J.; Frisbie, C. D. Polymer Electrolyte Gate Dielectric Reveals Finite Windows of High Conductivity in Organic Thin Film Transistors at High Charge Carrier Densities Polymer Electrolyte Gate Dielectric Reveals Finite Windows of High. *J. Am. Chem. Soc.* **2005**, *127*, 6960– 6961.

(32) Ono, S.; Minder, N.; Chen, Z.; Facchetti, A.; Morpurgo, A. F. High-Performance n-Type Organic Field-Effect Transistors with Ionic Liquid Gates. *Appl. Phys. Lett.* **2010**, *97*, 143307.

(33) Uemura, T.; Yamagishi, M.; Ono, S.; Takeya, J. Low-Voltage Operation of n-Type Organic Field-Effect Transistors with Ionic Liquid. *Appl. Phys. Lett.* **2009**, *95*, 103301.

(34) Malti, A.; Gabrielsson, E. O.; Berggren, M.; Crispin, X. Ultra-Low Voltage Air-Stable Polyelectrolyte Gated n-Type Organic Thin Film Transistors. *Appl. Phys. Lett.* **2011**, *99*, 063305.

(35) Herlogsson, L.; Crispin, X.; Tierney, S.; Berggren, M. Polyelectrolyte-Gated Organic Complementary Circuits Operating at Low Power and Voltage. *Adv. Mater.* **2011**, *23* (40), 4684– 4689.

(36) Ye, Y.; Sharick, S.; Davis, E. M.; Winey, K. I.; Elabd, Y. A. High Hydroxide Conductivity in Polymerized Ionic Liquid Block Copolymers. *ACS Macro Lett.* **2013**, *2* (7), 575– 580.

(37) Choi, J. H.; Ye, Y.; Elabd, Y. A.; Winey, K. I. Network Structure and Strong Microphase Separation for High Ion Conductivity in Polymerized Ionic Liquid Block Copolymers. *Macromolecules* **2013**, *46* (13), 5290– 5300.

(38) Gu, Y.; Lodge, T. P. Synthesis and Gas Separation Performance of Triblock Copolymer Ion. *Macromolecules* **2011**, *44*, 1732– 1736.

(39) Yuan, J.; Antonietti, M. Poly(Ionic Liquid)s: Polymers Expanding Classical Property Profiles. *Polymer* **2011**, *52* (7), 1469– 1482.

(40) Yuan, J.; Mecerreyes, D.; Antonietti, M. Poly(Ionic Liquid)s: An Update. *Prog. Polym. Sci.* **2013**, *38* (7), 1009– 1036.

(41) Lee, M.; Choi, U. H.; Salas-De La Cruz, D.; Mittal, A.; Winey, K. I.; Colby, R. H.; Gibson, H. W. Imidazolium Polyesters: Structure-Property Relationships in Thermal Behavior, Ionic Conductivity, and Morphology. *Adv. Funct. Mater.* **2011**, *21* (4), 708– 717.

(42) Ye, Y.; Elabd, Y. A. Anion Exchanged Polymerized Ionic Liquids: High Free Volume Single Ion Conductors. *Polymer* **2011**, *52* (5), 1309– 1317.

(43) Marcilla, R.; Alcaide, F.; Sardon, H.; Pomposo, J. A.; Pozo-Gonzalo, C.; Mecerreyes, D. Tailor-Made Polymer Electrolytes Based upon Ionic Liquids and Their Application in All-Plastic Electrochromic Devices. *Electrochem. Commun.* **2006**, *8* (3), 482– 488.

(44) Horowitz, A. I.; Panzer, M. J. High-Performance, Mechanically Compliant Silica-Based Ionogels for Electrical Energy Storage Applications. *J. Mater. Chem.* **2012**, *22* (32), 16534– 16539.

(45) Hlalele, L.; Klumperman, B. In Situ Nmr and Modeling Studies of Nitroxide Mediated Copolymerization of Styrene and n -Butyl Acrylate. *Macromolecules* **2011**, *44* (17), 6683– 6690.

(46) Peltekoff, A. J.; Therrien, I.; Lessard, B. H. Nitroxide Mediated Polymerization of 1-(4-Vinylbenzyl)-3-Butylimidazolium Ionic Liquid Containing Homopolymers and Methyl Methacrylate Copolymers. *Can. J. Chem. Eng.* **2019**, *97* (1), 5– 16.

(47) Lessard, B. H.; Sampson, K. L.; Plint, T.; Bender, T. P. Boron Subphthalocyanine Polymers: Avoiding the Small Molecule Side Product and Exploring Their Use in Organic Light-Emitting Diodes. *J. Polym. Sci., Part A: Polym. Chem.* **2015**, *53* (17), 1996– 2006.

(48) Grubbs, R. B. Nitroxide-Mediated Radical Polymerization: Limitations and Versatility. *Polym. Rev.* **2011**, *51* (2), 104– 137.

(49) Nicolas, J.; Guillaneuf, Y.; Lefay, C.; Bertin, D.; Gigmes, D.; Charleux, B. Nitroxide-Mediated Polymerization. *Prog. Polym. Sci.* **2013**, *38* (1), 63– 235.

(50) Dire, C.; Belleney, J.; Nicolas, J.; Bertin, D.; Magnet, S.; Charleux, B. β-Hydrogen Transfer from Poly(Methyl Methacrylate) Propagating Radicals to the Nitroxide SG1: Analysis of the Chain-End and Determination of the Rate Constant. *J. Polym. Sci., Part A: Polym. Chem.* **2008**, *46* (18), 6333– 6345.

(51) Mchale, R.; Aldabbagh, F.; Zetterlund, P. B. The Role of Excess Nitroxide in the SG1 (N-Tert-Butyl-N-[1-Diethylphosphono-(2,2-Dimethylpropyl)] Nitroxide)-Mediated Polymerization of Methyl Methacrylate. *J. Polym. Sci., Part A: Polym. Chem.* **2007**, *45* (11), 2194– 2203.

(52) Lessard, B.; Tervo, C.; Marić, M. High-Molecular-Weight Poly(Tert-Butyl Acrylate) by Nitroxide-Mediated Polymerization: Effect of Chain Transfer to Solvent. *Macromol. React. Eng.* **2009**, *3* (5–6), 245– 256.

(53) Lessard, B.; Tervo, C.; De Wahl, S.; Clerveaux, F. J.; Tang, K. K.; Yasmine, S.; Andjelic, S.; D'Alessandro, A.; Maric, M. Poly(Tert -Butyl Methacrylate/Styrene) Macroinitiators as Precursors for Organo- and Water-Soluble Functional Copolymers Using Nitroxide-Mediated Controlled Radical Polymerization. *Macromolecules* **2010**, *43*, 868– 878.

(54) Zhang, C.; Lessard, B.; Maric, M. Synthesis and Characterization of Benzyl Methacrylate/Styrene Random Copolymers Prepared by NMP. *Macromol. React. Eng.* **2010**, *4* (6–7), 415– 423.

(55) Lessard, B. H.; Ling, E. J. Y.; Maric, M. Fluorescent, Thermoresponsive Oligo(Ethylene Glycol) Methacrylate/ 9-(4-Vinylbenzyl)-9 H -Carbazole Copolymers Designed with Multiple LCSTs via Nitroxide Mediated Controlled Radical Polymerization. *Macromolecules* **2012**, *45*, 1879.

(56) Gromadzki, D.; Makuška, R.; Netopilík, M.; Holler, P.; Lokaj, J.; Janata, M.; Štěpánek, P. Comb Copolymers of Polystyrene-Poly(Tert-Butyl (Meth)Acrylate) Prepared by Combination of Nitroxide Mediated Polymerization and Photoinduced Iniferter Technique. *Eur. Polym. J.* **2008**, *44* (1), 59– 71.

(57) Kazmaier, P.; Daimon, K.; Georges, M.; Hamer, G.; Veregin, R. Nitroxide-Mediated "Living": Free Radical Polymerization: A Rapid Polymerization of (Chloromethyl)Styrene for the Preparation of Random, Block, and Segmental Arborescent Polymers. *Macromolecules* **1997**, *30* (8), 2228– 2231.

(58) Mayo, F. R.; Lewis, F. M. Copolymerization I. A Basis for Comparing the Behavior of Monomers in Copolymerization; the Copolymerization of Styrene and Methyl Methacrylate. *J. Am. Chem. Soc.* **1944**, *66* (1939), 1594– 1601.

(59) Kondo, S.; Ohtsuka, T.; Ogura, K.; Tsuda, K. Convenient Synthesis and Free-Radical Copolymerization of P-Chloromethylstyrene. *J. Macromol. Sci., Chem.* **1979**, *13* (6), 767–775.

(60) Lessard, B. H.; Guillaneuf, Y.; Mathew, M.; Liang, K.; Clement, J. L.; Gigmes, D.; Hutchinson, R. A.; Marić, M. Understanding the Controlled Polymerization of Methyl Methacrylate with Low Concentrations of 9-(4-Vinylbenzyl)-9 H -Carbazole Comonomer

by Nitroxide-Mediated Polymerization: The Pivotal Role of Reactivity Ratios. *Macromolecules* **2013**, *46* (3), 805– 813.

(61) Gordon, M.; Taylor, J. S. Ideal Copolymers and the Second-Order Transitions of Synthetic Rubbers. i. Non-Crystalline Copolymers. *J. Appl. Chem.* **1952**, *2* (9), 493– 500.

(62) Lee, K. H.; Zhang, S.; Lodge, T. P.; Frisbie, C. D. Electrical Impedance of Spin-Coatable Ion Gel Films. *J. Phys. Chem. B* **2011**, *115*, 3315– 3321.

(63) Zhang, S.; Lee, K. H.; Frisbie, C. D.; Lodge, T. P. Ionic Conductivity, Capacitance, and Viscoelastic Properties of Block Copolymer-Based Ion Gels. *Macromolecules* **2011**, *44* (4), 940– 949.

(64) Brug, G. J.; van den Eeden, A. L. G.; Sluyters-Rehbach, M.; Sluyters, J. H. The Analysis of Electrode Impedances Complicated by the Presence of a Constant Phase Element. *J. Electroanal. Chem. Interfacial Electrochem.* **1984**, *176* (1–2), 275– 295.

(65) Lee, K. H.; Kang, M. S.; Zhang, S.; Gu, Y.; Lodge, T. P.; Frisbie, C. D. Cut and Stick" Rubbery Ion Gels as High Capacitance Gate Dielectrics. *Adv. Mater.* **2012**, *24* (32), 4457– 4462.

(66) Ye, Y.; Choi, J.; Winey, K. I.; Elabd, Y. A. Polymerized Ionic Liquid Block and Random Copolymers: Effect of Weak Microphase Separation on Ion Transport. *Macromolecules* **2012**, *45* (17), 7027– 7035.

(67) Choi, J. H.; Xie, W.; Gu, Y.; Frisbie, C. D.; Lodge, T. P. Single Ion Conducting, Polymerized Ionic Liquid Triblock Copolymer Films: High Capacitance Electrolyte Gates for N-Type Transistors. *ACS Appl. Mater. Interfaces* **2015**, *7* (13), 7294– 7302.

(68) Yan, H.; Chen, Z.; Zheng, Y.; Newman, C.; Quinn, J. R.; Dötz, F.; Kastler, M.; Facchetti, A. A High-Mobility Electron-Transporting Polymer for Printed Transistors. *Nature* **2009**, *457* (7230), 679– 686.

(69) Bürgi, L.; Richards, T. J.; Friend, R. H.; Sirringhaus, H. Close Look at Charge Carrier Injection in Polymer Field-Effect Transistors. *J. Appl. Phys.* **2003**, *94* (9), 6129– 6137.

Chapter 4: Ionic Liquid Containing Block Copolymer Dielectrics: Designing for High-Frequency Capacitance, Low-Voltage Operation, and Fast Switching Speeds

Context

This study was designed based on the results of the preceding chapter; it was clear block copolymers produced advantageous conductivities compared to random copolymers and that T_g was inversely proportional to conductivity. We decided to explore these findings by synthesizing a new series of block copolymer materials where the conductive block was a copolymer with T_g ranging from X to Y °C. We used a polystyrene macroinitiator due to its higher degree of pseudo-livingness compared to p(S-*r*-MMA) (as used in the previous chapter) resulting in improved re-initiation. Additionally, we exploited the post-polymerization functionalization synthetic approach to produce materials where we could easily compare the effect the mobile anion on resulting material properties. Lastly, we changed the OTFT device architecture to top gate top contact to reduce contact resistance effects, a new device structure that had not yet been employed in our group.

Contributions of Authors

I designed the study in consultation with Benoit Lessard. I synthesized & characterized the polymers, designed the experiments, and built the frequency tester. I built the capacitors and characterized them. I prepared all the films for SAXS and TEM and helped analyze the results. Samantha Brixi did the device fabrication & conventional characterization, we performed the frequency characterization together. Jukka Niskanen provided experimental guidance and characterization insight. I wrote the first draft of the manuscript. Benoit Lessard interpreted the SAXS results and edited the final manuscript.

Significance of Research

This research was significant as it led to structure property relationships between block copolymer T_g and anion choice to corresponding EDL formation and ion conductivity.

Additionally, we developed OTFT response time testing setup in the laboratory and established a relationship between choice of anion and OTFT switching speed. Ultimately, the conductivities of the new materials were greater than the previous study and the device performed improved with reduced contact resistance. This study establishes the start of design rules for high performance polyelectrolyte gating materials for solid state OTFTs.

*Chapter 4 has been published in JACS Au: Peltekoff, A. J., Brixi, A., Niskanen, J., & Lessard, B. H., **2021**, 1, 7, 1044–1056. doi:10.1021/jacsau.1c00133*

4.1 Abstract

Polymerized ionic liquids (PILs) are a potential solution to the large-scale production of low-power consuming organic thin-film transistors (OTFTs). When used as the device gating medium in OTFTs, PILs experience a double-layer capacitances that enables thickness independent, low-voltages operation. PIL microstructure, polymer composition, and choice of anion have all been reported to have an effect on device performance, but a better structure property relationship is still required. A library of 27 well defined, poly(styrene)-*b*-poly(1-(4-vinylbenzyl)-3-butylimidazolium-random-poly(ethylene glycol) methyl ether methacrylate) (poly(S)-*b*-poly(VBBI$^+$[X]-*r*-PEGMA)) block copolymers, with varying PEGMA/VBBI$^+$ ratios and three different mobile anions (where X = TFSI$^-$, PF_6^- or BF_4^-), were synthesized, characterized, and integrated into OTFTs. The fraction of VBBI$^+$ in the poly(VBBI$^+$[X]-*r*-PEGMA) block ranged from 25 mol% to 100 mol% and led to glass transition temperatures (T_g) between -7 °C and 55 °C for that block. When VBBI$^+$ composition was equal or above 50 mol% the block copolymer self-assembled into well-ordered domains with sizes between 22 and 52 nm, depending on the composition and choice of anion. The block copolymers double-layer capacitance (C_{DL}) and ionic conductivity (σ) were found to correlate to the polymer self-assembly and the Tg of the poly(VBBI$^+$[X]-*r*-PEGMA) block. Finally, the block copolymers were integrated into OTFTs as the gating medium that led to n-type devices with threshold voltages of 0.5-1.5V while maintaining good electron mobilities. We also found that the greater the σ of the PIL, the greater the OTFT operating frequency could reach. However, we also found that C_{DL} is not strictly proportional to OTFT output currents.

4.2 Introduction

Organic thin-film transistors (OTFTs) are carbon-based field-effect logic operators, which enables lightweight and flexible electronics through low-cost printing methods. An obstacle in the advancement of OTFT based technologies is the need for low operating voltages. Currently, large-area printed batteries provide voltages, typically around 1.35 V, that are far too low to power typical OTFTs.[1] Electrolytes are attractive gating materials as they provide an extremely high capacitance, responsible for the reduction of operating voltage that is independent of layer thickness, making them compatible with large scale printing technologies. Ionic liquids are room temperature molten salts, which exhibit capacitances that are two orders of magnitude greater than conventional dielectrics due to the formation of electrical double layers (EDLs). The high capacitances leads to a greater number of charge carriers in the semiconductor channels, which results in high on-current and low threshold voltages.[2] Unfortunately ionic liquids are problematic due to electrochemical doping of the semiconductor during operation leading to slow switching speeds.[3,4] In addition, ionic liquid are liquids which limits their potential for use in solid state devices. Blending the ionic liquid (ion gels)[5] with a polymer does lead to improved mechanical properties but this does not reduce the potential for electrochemical doping. The ideal material should have the mechanical properties of a polymer combined with the performance of ionic liquids.

Polymerized ionic liquids (PILs) are solid electrolyte materials that exhibit the same EDL capacitances as ionic liquids but are unipolar, where only one ion is mobile, and the complementary charge is bound to the polymer backbone. When paired with an appropriate semiconductor, the possibility of electrochemical doping is eliminated as the EDL at the dielectric/semiconductor interface is formed by the large macromolecule that is too large to penetrate the semiconductor.[6] Therefore, pairing polycation PIL (mobile anion) with n-type semiconductor and polyanion PIL (mobile cation) with p-type semiconductors, prevents the possibility of faradic oxidation and reduction of the organic semiconductor.[7] In The thickness independent high-capacitances and elimination of electrochemical doping (faradic effects) of unipolar PILs give them great potential to realize large scale production of low-power consuming OTFTs. However, PILs are plagued by sluggish response times due to their lower ionic conductivity compared to unpolymerized ionic liquids. There have been efforts to increase the

solid-state ionic conductivity of PILs to improve OTFT response times when utilized as the gating mediums.[8–10] For example, reducing the glass transition temperature (Tg) of PIL leads to an increase in ionic conductivity.[11] For example, poly(1-glycidyl-3-butylimidazolium TFSI) supporting an ethylene glycol backbone exhibited ionic conductivity of 10^{-5} S cm^{-1} at 30 °C with a low-T_g of -14 °C.[12] Intuitively, greater polymer chain flexibility facilitates ion transport through the materials in an analogous fashion to the correlation of viscosity and ionic conductivity for ionic liquids. Evidently, the ion dynamics and structural relaxation are strongly correlated above the Tg, leading to a significant trade-off between ionic conductivity and mechanical integrity.[13,14] Our group and others have shown that block copolymers exhibited ionic conductivities up to two orders of magnitude greater compared to random copolymers of similar compositions due to the microphase separation of the ionic segments forming conductive pathways through the material.[9,10,15] While these studies examine the ionic conductivity of the polymer, this does not correlate directly to OTFT performance. For example, an increased capacitance increases output currents, but decreases charge mobility (μ). This decreased μ is related to the way the EDL is formed by the charge carriers and electrolyte ions. Therefore, the choice of polymer, the mobile ion and the dielectric/semiconductor interface itself are critical and no studies have systematically and simultaneously examined all these parameters.

In this study we develop a series of 27 different block copolymers to probe the dielectric/semiconductor interface and the design of these critical materials. For example, we characterize the same polymer with different anions ($TFSI^-$, PF_6^-, BF_4^-) and their effect on device performance. In this example, the interface for each of these three devices is identical because the polymer is the same and it is only the anion that migrates. However, our materials have a different capacitance which will influence μ. We have designed a library of poly(styrene)-*b*-poly(1-(4-vinylbenzyl)-3-butylimidazolium -*random*-poly(ethylene glycol) methyl ether methacrylate), (poly(S)-*b*-poly(PIL-*r*-PEGMA)), block copolymers with three different anions ($TFSI^-$, PF_6^- or BF_4-). This will help elucidate structure-property relationships for the design of high performance PIL gating materials in n-type OTFTs and decouple the effect of ion conductivity, capacitance and the device μ.

4.3 Results & Discussion

We synthesized a series of diblock copolymers consisting of a high glass transition temperature (T_g) poly(styrene) block and a low T_g poly(ionic liquid) (PIL) containing second block (**Scheme 4.1**). The resulting materials were characterized, integrated into capacitor devices and studied by impedance spectroscopy to determine conductivity and double-layer capacitance. Finally, OTFT devices were fabricated, and electrical characterization was performed. The following explores the effect of molecular architecture and self assembly on the resulting electrical performance.

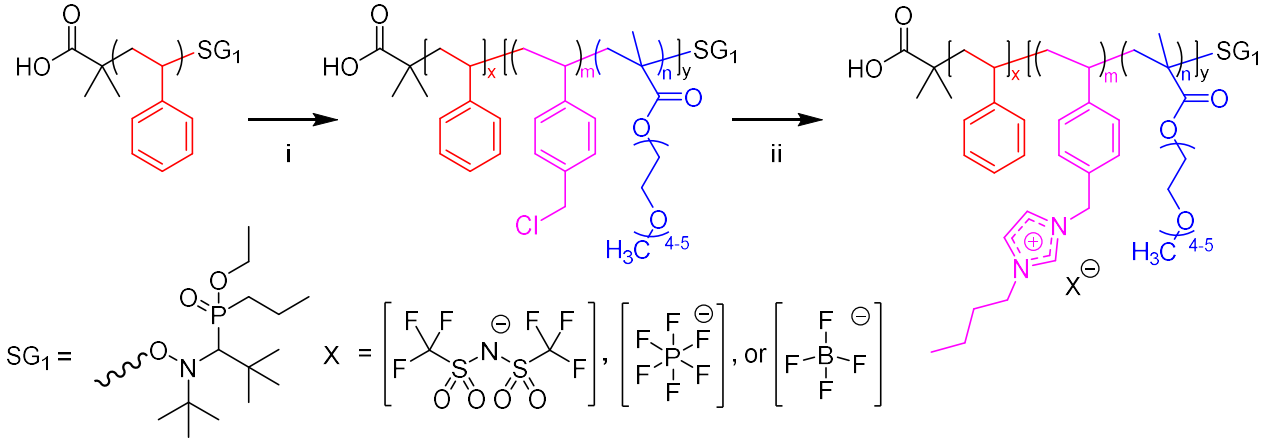

Scheme 4.1. Synthesis of poly(styrene)-b-poly(1-(4-vinylbenzyl)-3-butylimidazolium-random-poly(ethylene glycol) methyl ether methacrylate), (poly(S)-b-poly(VBBI$^+$[X]-*r*-PEGMA)), (where X = TFSI$^-$, PF_6^- or BF_4^-) poly(ionic liquid) gating material. i) chain extension of a poly(S) macroinitiator using chloromethyl styrene (CMS) and poly(ethylene glycol) methyl ether methacrylate (PEGMA), N-tert-butyl-N-[1-diethylphosphono-(2,2-dimethylpropyl)] nitroxide (SG1), 1,4-dioxane, 90 °C, 24 h; (iia) butylimidazole, dimethylacetamide, 50 °C, 24 h; (iib) Organic salt (LiTFSI, $LiPF_6$, or $NaBF_4$), dimethylacetamide, r.t., 48 h.

4.3.1 Block Copolymer Synthesis

All experimental conditions and formulations can be found in the experimental section (**Table 4.3**). Nitroxide mediated polymerization (NMP) is a controlled polymerization technique that can lead to well defined molecular architectures without the need for transition metal catalysts or laborious purification techniques; making it an ideal technique for the development of functional polymers for printable electronics.[16–19] Therefore, a single large batch of narrow dispersity and pseudo-living poly(styrene) (poly(S)) macroinitiator ($\bar{M}_w/\bar{M}_n = 1.06$; $\bar{M}_n = 22.5$ kg·mol^{-1},

Table 4.1) was synthesized by NMP, ensuring to stop the reaction at low-conversion to maintain a high-degree of livingness, with a target MW similar to our previous works.[15,20,21] Chain extension of the poly(S) macroinitiators was performed using chloromethyl styrene (CMS) and poly(ethylene glycol)methyl ether methacrylate (PEGMA) comonomers in varying comonomer feed ratios and with different target molecular weights (**Table 4.1**). We obtained nine different poly(S)-b-poly(CMS-*r*-PEGMA) diblock copolymers with unimodal molecular weight distributions ranging from $\bar{M}_w/\bar{M}_n = 1.07 - 1.24$ with $\bar{M}_n s$ ranging from 24.5 – 39.6 kg·mol-1 (**Table 4.1**). Representative size exclusion chromatography (SEC) chromatograms of the poly(S) macroinitiator and the corresponding poly(S)-b-poly(CMS-r-PEGMA) diblock copolymers P100/0-8 and P25/75-4 are shown in Figure S1. The chromatograms illustrate a clear monomodal shift from the poly(S) macroinitiator to the final poly(S)-b-poly(CMS-r-PEGMA) demonstrating a higher $\bar{M}_n$. Further examination of the trace from chain-extended products of high methacrylate content (shown in red) exhibit a slight tailing on the leading edge, which is indicative of termination by combination resulting in a broadening of molecular weight distributions.[22] This slight broadening is consistent with typical chain extensions by NMP[23,24] using PEGMA and other methacrylates. The final molar composition of PEGMA, CMS and styrene (F_{PEGMA}, F_{CMS} and F_S) of the block copolymers were determined by ^{1}H NMR and are presented in **Table 4.1**; a representative spectrum detailing composition calculation is presented in the supporting information (**Figure 4.10**). The composition of these second blocks varied between 100:0 (pure CMS) to 23:77 (mostly PEGMA) (**Table 4.1**). A small trend can be seen where the CMS integrated into the polymer is slightly higher than the feed, suggesting CMS preferentially reacts with itself and PEGMA due to favorable reactivity ratios. This was not a surprise as we have previously shown CMS and other styrenic monomers are controlling monomers in the NMP of methacrylates.[25,26] Overall, the pseudo-living poly(S) macroinitiator was effective in producing a library of poly(S)-b-poly(CMS-r-PEGMA) precursor block copolymers with relatively narrow, monomodal molecular weight distributions.

Table 4.1. Molecular Weight Distribution Data & Glass Transition for poly(S)-*b*-poly(CMS-*r*-PEGMA) Diblock Copolymer Precursors to Ionic Liquid Containing Block Copolymers

Exp ID[1]	$\partial n/\partial c$[2] $[mL\ g^{-1}]$	$\bar{M}_n$[2] $[kg\ mol^{-1}]$	Đ[2] $[\bar{M}_w/\bar{M}_n]$	F_{STY}[3]	F_{CMS}[3]	F_{PEGMA}[3]	$R_{CMS/PEGMA}$[3]	T_g[4] [X] (°C)
poly(S)	0.192	22.5	1.06	1.00	-	-	-	100
P25/75-2	0.190	27.0	1.10	0.86	0.10	0.04	0.88	TFSI (99); PF_6(99); BF_4(99)
P25/75-4	0.096	58.2	1.10	0.88	0.04	0.09	0.41	TFSI (99); PF_6(99); BF_4(99)
P25/75-6	0.179	28.0	1.07	0.95	0.02	0.03	0.64	TFSI (99); PF_6(99); BF_4(99)
P50/50-4	0.194	31.8	1.24	0.69	0.17	0.14	1.17	TFSI (-7,106); PF_6(21,105); BF_4(17,105)
P50/50-6	0.167	35.9	1.23	0.67	0.18	0.15	1.27	TFSI (-7,106); PF_6(22,105); BF_4(19,106)
P75/25-6	0.246	27.1	1.17	0.69	0.23	0.08	2.85	TFSI (2,107); PF_6(55,106); BF_4(48,105)
P75/25-8	0.202	31.4	1.12	0.74	0.20	0.06	3.17	TFSI (2,105); PF_6(52,105); BF_4(49,103)
P100/0-4	0.235	24.5	1.12	0.81	0.18	-	-	TFSI (12,105); PF_6(101); BF_4(98)
P100/0-8	0.154	39.6	1.17	0.70	0.30	-	-	TFSI (11,106); PF_6(104); BF_4(99)

[1] Experimental identification (Exp ID) we define the as PX/Y-Z where X/Y = the target ratio of chloromethyl styrene (CMS) versus poly(ethylene glycol) methyl ether methacrylate (PEGMA) and where Z corresponds to the weight of total comonomers (CMS + PEGMA) added to 1g of macroinitiator in chain extension polymerizations.

[2] The $\partial n/\partial c$ was determined by offline batch dRI measurements for each polymer. Number-average molecular weight ($\bar{M}_n$), weight-average molecular weight ($\bar{M}_w$), and the dispersity (M_w/M_n) were determined by size exclusion chromatography (SEC).

[3] Molar compositions were determined by ^{1}H NMR. $R_{CMS/PEGMA}$ is the molar ratio of CMS relative to PEGMA in the second block.

[4] Glass transition temperature (T_g) determined by differential scanning calorimetry (DSC) on the same base polymer with varying salts [X] = TFSI; PF_6 or BF_4

The final PIL containing block copolymers were prepared by subsequent quaternization and anion exchange reactions on the precursor polymers (**Scheme 4.1**). First, the quaternization reaction on the CMS moiety with 1-butylimidazole was performed leading to poly(styrene)-*b*-poly(1-(4-vinylbenzyl)-3-butylimidazolium-*r*-poly(ethylene glycol) methyl ether methacrylate), (poly(S)-*b*-poly(VBBI+-*r*-PEGMA)) block copolymers; this reaction mixture was then divided into three, so a subsequent anion exchange with 3 different organic salts was performed poly(S)-b-poly(VBBI$^+$[X]-r-PEGMA) (where [X] = BF_4^-, PF_6^-, or $TFSI^-$). These anions were selected for their delocalized charge and size which increases conductivities.[27] Isolation of the intermediate product was intentionally avoided as it could not be effectively obtained by precipitation and dialysis methods resulting in low yields. However, after substituting the Cl^- anion with the organic anions ($TFSI^-$, BF_4^-, PF_6^-), the macromolecule becomes completely insoluble in water, facilitating the isolation of the final product, which was purified by repetitive washing with water. A total of 27 final poly(S)-*b*-poly(VBBI$^+$[X]-*r*-PEGMA) block copolymers (**Table 4.1**) possessing three different mobile anions; X = BF_4^-, PF_6^-, and $TFSI^-$ were obtained and confirmed by ^{1}H NMR (see experimental section and supporting information).

4.3.2 Self Assembly of Poly(ionic liquid) Block Copolymers

All PIL containing block copolymers were first characterized by differential scanning calorimetry (DSC) and characteristic thermograms can be found in **Figure 4.1**. The glass transition temperature (T_g) of the materials was influenced by both the composition of the poly(VBBI$^+$[X]-*r*-PEGMA) block and the nature of the mobile anion. Block copolymers with an $R_{CMS/PEGMA} > 0.88$ (**Table 4.1**) exhibited two distinct T_g*s*: one corresponding to the poly(S) block and a second corresponding to the poly(VBBI$^+$[X]-*r*-PEGMA) block. Two distinct transitions suggests phase separation is occurring.[28] Block copolymers containing >75 mol% PEGMA displayed only one *Tg* that was below that of the poly(S) macroinitiator, suggesting the blocks are miscible and no phase separation is taking place (**Figure 4.1**).[28] The selection of anionic salt affected the T_g of the poly(VBBI$^+$[X]-*r*-PEGMA) block, where $TFSI^-$ containing polymers exhibited the lowest T_g followed by PF_6^- and BF_4^- (**Figure 4.1, Table 4.1**). This observation is consistent with studies that have shown the melting temperature of an ionic liquid decreases with increasing ion diameter.[29] It is interesting to note that both poly(S)-*b*-poly(VBBI$^+$[X]) block copolymers (i.e.: $F_{PEGMA} = 0$) with PF_6^- and BF_4^- anions exhibited only one T_g while the same polymer with $TFSI^-$ led to two T_gs

(**Table 4.1**). This suggests that not only polymer composition but also the choice of the anion play a critical role in the self-assembly of the resulting block copolymers.

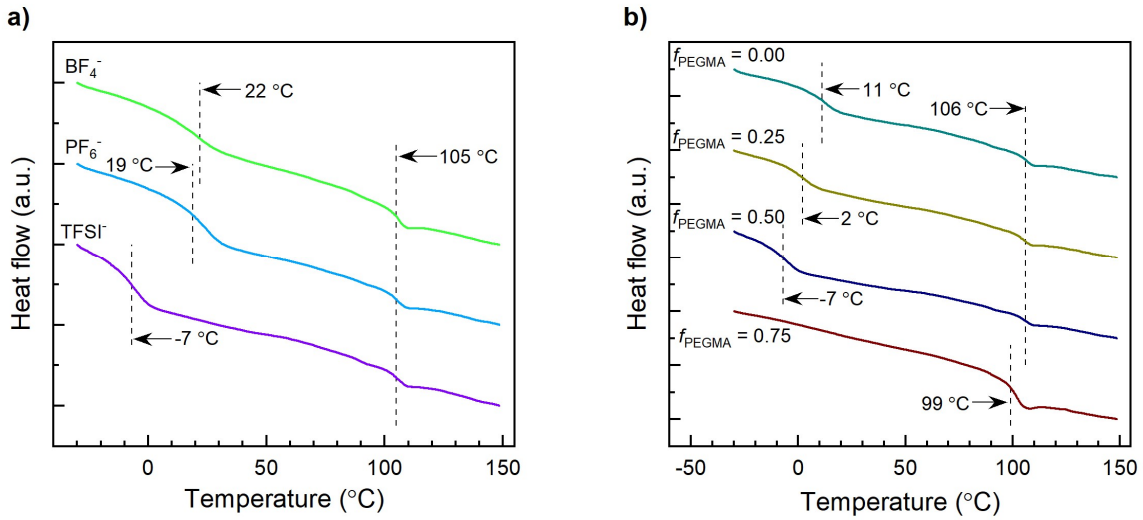

Figure 4.1. Characteristic differential scanning calorimetry (DSC) thermograms of poly(S)-*b*-poly(VBBI$^+$[X]-*r*-PEGMA) (where [X] = BF_4^-, PF_6^-, or $TFSI^-$) block copolymers where (a) compares the effect of 3 different salt forms; $TFSI^-$, PF_6^- and BF_4^- within the same polymer P50/50 and (b) compares the same salt, $TFSI^-$, on 4 different block copolymers with different PEGMA loadings, P100/0-8, P75/25-8, P50/50-6, and P25/75-6. The thermograms are from the second heat cycle in a heat/cool/heat experiment. The glass transition temperatures (T_g) for all materials are summarized in **Table 4.1**.

To study the effect of morphology on OTFT performance, the molecular architecture and choice of anion were characterized as a function of degree of microphase separation. The morphology of 12 characteristic PIL block copolymers, which demonstrated dual T_gs, (**Table 4.1**) were evaluated by both through-plane small angle x-ray scattering (SAXS) and transmission electron microscopy (TEM), **Figure 4.2** and **4.3**, respectively. Prior to morphological characterization materials were annealed to allow the self-assembled block copolymers to attain a thermodynamic minimum in regard to their organization.[30] In all cases microphase ordering with varying long-range periodicity are observed by SAXS. Variations in peak intensity as well as location suggests changes in morphology from lamella (LAM) to hexagonally packed cylinders (HEX) and mixtures of both. For example, samples exhibit the characteristic reflections at q*, 2q*, 3q*, 4q*, 5q* corresponds to LAM while reflections at q*, q*√3, 2q*, q*√7 and 3q* corresponds to HEX. Similar patterns have been reported for other PIL containing block copolymers.[8,31]

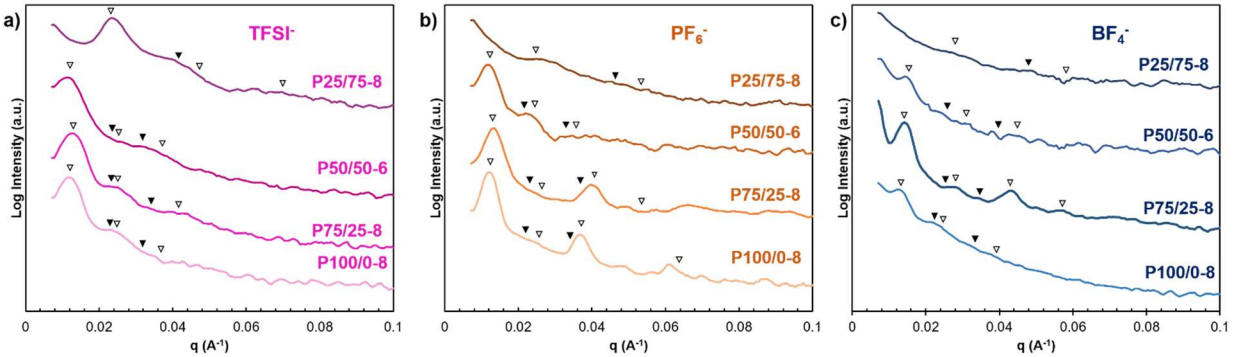

Figure 4.2. Through-plane small-angle X-ray scattering profiles of poly(s)-*b*-poly(PIL-*r*-PEGMA) block copolymers functionalized with a) $TFSI^-$, b) PF_6^- and c) BF_4^-. The inverted filled triangles (▼) of samples indicate expected peak positions at q*, √3q*, 2q*, and √7q* for hexagonally packed cylindrical (HEX) morphology. The inverted open triangles (▽) indicate expected peak positions at q*, 2q*, 3q*, and 4q* for lamellar (LAM) morphology.

Table 4.2. Domain size and long range order morphology as determined by SAXS

Exp. ID[a]	anion	Domain size (nm)[b]	Morphology[c]	σ (S cm^{-1})[d]
P25/75-8	BF_4^-	21.7	WLO	-
P50/50-6	BF_4^-	42.1	LAM	7.9×10^{-8}
P75/25-8	BF_4^-	44.2	LAM	1.2×10^{-8}
P100/0-8	BF_4^-	48.7	LAM+HEX	4.6×10^{-9}
P25/75-8	PF_6^-	22.7	WLO	-
P50/50-6	PF_6^-	52.4	LAM	4.1×10^{-9}
P75/25-8	PF_6^-	46.5	LAM	5.8×10^{-11}
P100/0-8	PF_6^-	49.1	LAM+HEX	7.4×10^{-11}
P25/75-8	$TFSI^-$	26.8	HEX	3.6×10^{-8}
P50/50-6	$TFSI^-$	52.0	HEX	3.4×10^{-7}
P75/25-8	$TFSI^-$	47.8	HEX	1.7×10^{-7}
P100/0-8	$TFSI^-$	52.0	HEX	1.4×10^{-9}

[a] Experimental identification (Exp. ID) we define the as PX/Y-Z where X/Y = the target ratio of chloromethyl styrene (CMS) versus poly(ethylene glycol) methyl ether methacrylate (PEGMA) and where Z corresponds to the weight of total comonomers (CMS + PEGMA) added to 1g of macroinitiator in chain extension polymerizations.

[b] Domain sizes ($d = 2\pi/q^*$) determined by small angle x-ray scattering.

[c] Morphology: hexagonally packed cylindrical (HEX) morphology; for lamellar (LAM) morphology and weak long-range microphase separation (WLO).

[d] Ionic conductivity (σ) was estimated using $\sigma = d/(R_b A)$, where d is the film thickness, R_b is the bulk resistance, and A is the area of the capacitor. Conductivity and capacitance were determined by electrical impedance spectroscopy (EIS).

The corresponding structures are represented in **Table 4.2**. In general, the q* decreases, corresponding to an increased domain sizes ($d = 2\pi/q^*$), as the anion size increase BF_4^- < PF_6^- < $TFSI^-$ (**Table 4.2**). P25/75-8 with BF_4^- and PF_6^- exhibited a broad scattering peak indicating weaker microphase separation without long-range periodicity. This weak long-range microphase separation (WLO) is likely due to the partial miscibility of the two blocks,[9] which can be seen in the DSC traces where only one T_g is present (**Table 4.1**). P25/75-8 with $TFSI^-$ exhibited a strong q* scattering peaks with broad 2q* and √3q* suggesting more significant microphase separation into a mixture of LAM and HEX compared to the same polymer with PF_6^- or BF_4^-. In all three cases, the calculated domain size was on the order of 20-26 nm and the TEM images show no significant long range order. All other polymers (P50/50-6, P75/25-8 and P100/0-8 with either salts) exhibited relatively larger domain sizes ranging from 42-52 nm and clearly visible long range order by TEM (**Figure 4.3**). Ye at al. observed an increase in domain size as PIL block increased relative to poly(MMA) block (i.e. poly(MMA) block remained the same length[9] and the PIL block size increased), while our study shows no correlation between PIL composition and domain size, likely due to the negligible changes in relative block length (i.e. as PIL content increase in our study, PEGMA content decreases keeping total block length comparable). P100/0-8 with BF4- and all block copolymers that were functionalized with $TFSI^-$ (**Figure 4.2**) experienced higher order reflections at q*√3 and q*√7 indicative of HEX morphology, which is consistent with the TEM images. Both P75/25 and P100/0-8 with PF_6^- and P75/25-8 with BF_4^- exhibited strong q* scattering peaks at q*, 3q* and 5q* with structure factor extinctions of 2q* and 4q*, indicative of a LAM morphology with apparent symmetric volume fractions of each block.8 The LAM morphology was supported using TEM. P50/50-6 with PF_6^- exhibited strong features at 2q* which was confirmed to correspond to LAM by TEM (**Figure 4.3**). P100/0-8 with PF6- exhibited strong features suggesting LAM morphology. However, small features at q*√3 and q*√7 indicative of HEX morphology were also detected by SAXS and the combination of HEX and LAM was also detected using TEM. These results indicate that the library of PIL block copolymers, with two distinct T_gs exhibit self-assembled microstructures with long range order and that the domain size and organizational structure (HEX vs LAM) depends on block copolymer architecture and choice of anion. This self assembly clearly demonstrates well defined domains comprised of the low T_g

PIL blocks, which can lead to improved anion transport through the film. This film morphology will therefore directly affect the device performance.

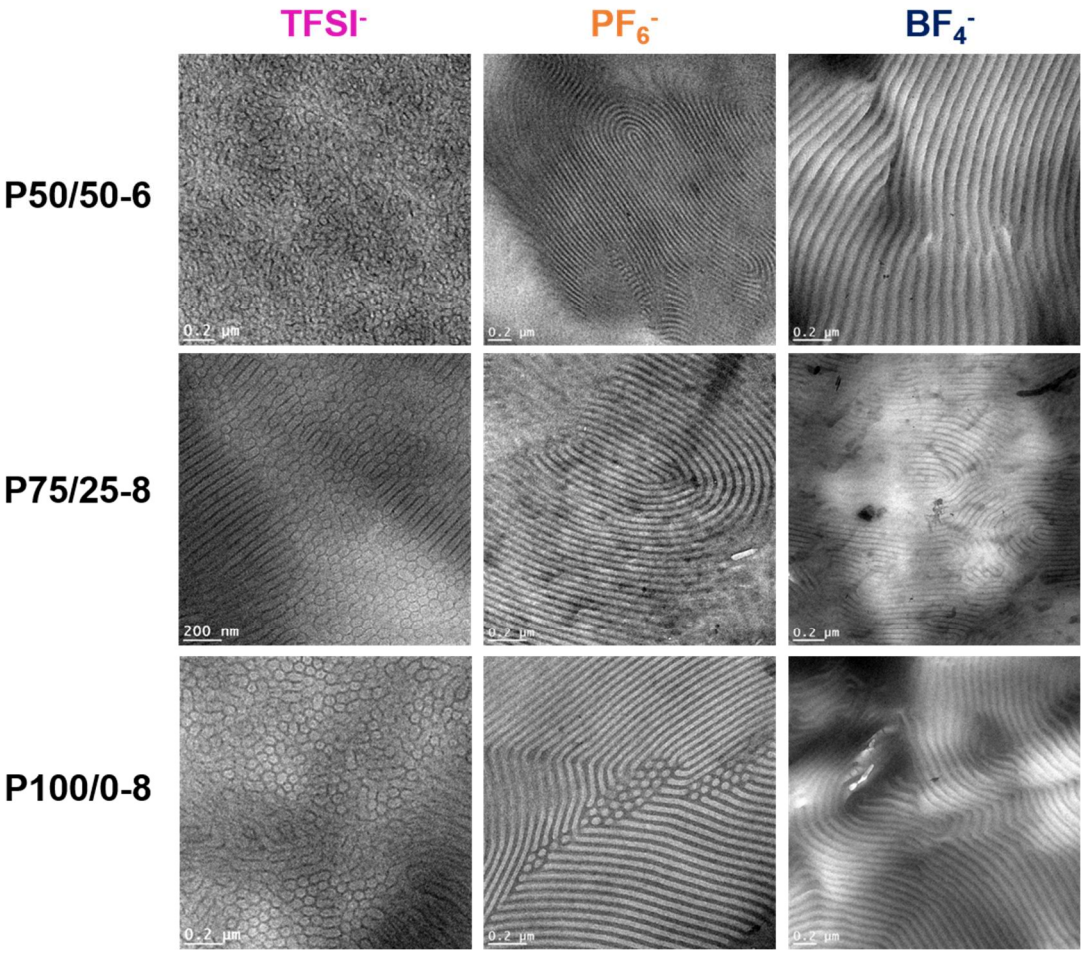

Figure 4.3. Transmission electron microscopy (TEM) images of poly(S)-*b*-poly(VBBI$^+$[X]-*r*-PEGMA) copolymers where the rows represent the polymer P50/50-6 (top), P75/25-8 (center) and P100/0-8 (bottom) and where the columns represent the choice of anions: TFSI$^-$ (left), PF_6^- (center) and BF_4^- (right). All samples were solvent cast from methyl ethyl ketone (MEK) over ~ 24 h at 130 °C in vacuum. Dark microdomains in TEM correspond to the poly(VBBI$^+$[X]-*r*-PEGMA) microphase.

4.3.3 Metal-Insulator-Metal Capacitors

The poly(S)-b-poly(VBBI$^+$[X]-r-PEGMA) (where [X] = BF_4^-, PF_6^-, or TFSI$^-$) block copolymers were used as the insulating layer in the fabrication of metal-insulator-metal capacitors and characterized using electrochemical impedance spectroscopy (EIS). The ionic conductivity (σ) was estimated using $\sigma = d/(R_b A)$, where d is the film thickness, R_b is the bulk resistance, and A

is the area of the capacitor. Nyquist plots (**Figure 4.12**) are obtained from the impedance data for each block copolymer. The R_b was determined by the radius of a circle fit to the ionic segment of the Nyquist plot produced from the EIS experiments. The resulting σ obtained for the block copolymers, which exhibited measurable conductivity, were plotted as a function of the lower *Tg*, which corresponds to the *Tg* of the PIL containing block (**Figure 4.4**).

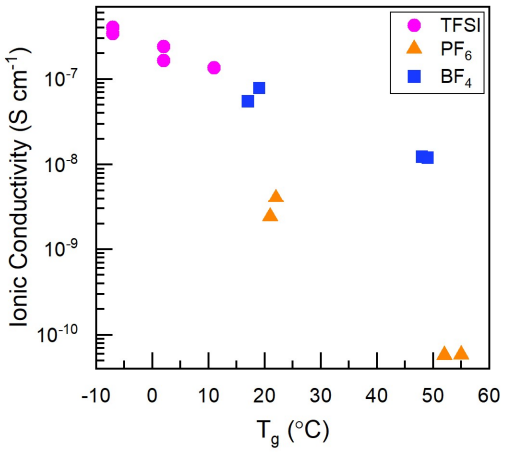

Figure 4.4. Conductivity versus the lower glass-transition temperature (T_g) of the poly(S)-*b*-poly(VBBI$^+$[X]-*r*-PEGMA) (where [X] = BF_4^-, PF_6^-, or $TFSI^-$) block copolymers. All experimentally obtained T_g are tabulated in **Table 4.1**.

In all cases, the σ increases as the *Tg* of the PIL block decreases resulting in three orders of magnitude increase in σ for a 65 °C drop in *Tg* (**Figure 4.4**), a well-established relation with this class of materials.[27,32] This observation extends from ionic liquids; where Angel et al.[33] found the σ of neat ionic liquids followed an inverse linear dependence on the viscosity, which is seemingly independent of the cation and anion. Observed discrepancies from this ideal dependence have been attributed to differences in the ion sizes, however most ionic liquid species in practice possess similar volumes.[34,35] The polymer architecture of similar PEO based single-ion conducting polymer electrolytes on conductivity has been explored. For example: Mapesa et al. showed the incorporation of a long alkyl spacer between charged imidazolium moieties and polymer backbones offered extra mobility to the ion pairs, leading to an increase in ionic conductivity.[36] This placement of the imidazolium moiety was further explored by Kuray et al. who found that materials with the charged moiety placed in a pendant had a greater σ than those with the functionalization directly in the polymer backbone.[37] Choi et al. explored the difference in σ

between materials with an alkyl spacer versus PEO spacers and showed the PEO containing PILs were significantly more conductive due to the relatively flexible and polar nature of the PEO spacer that behaves as a plasticizer and solvator.[38,39] Other PEO structures have also been explored such as linear side chain versus cyclic side-chain[40] as well as utilizing PEO as the polymeric backbone with imidazolium pendant moieties.[12] Ikeda et al. explored the length of tail off of the imidazolium pendant and found it has no major influence on *Tg* or conductivity.[41] We found that the effect of *Tg* was more significant than the ionic concentration itself, i.e. composition of the poly(VBBI$^+$[X]-r-PEGMA) block. These results are consistent with the SAXS and TEM results, suggesting that low *Tg* pathways through the film improve anion transport and therefore increase ionic conductivity. This corroborates observations by Chen et al. with butyl methacrylate imidazolium based PIL homopolymers with $TFSI^-$ and BF_4^- anions who showed that reduced *Tg* has a more significant effect on σ than the overall charge content.[11] Further examination into the influence of F_{PEGMA} for the poly(VBBI$^+$[X]-*r*-PEGMA) block, we can see that σ increases from $F_{PEGMA} = 0$ (pure PIL, P100/0-4, P100/0-8) to $F_{PEGMA} = 0.15$ (P50/50-4, P50/50-6). Interestingly, when $F_{PEGMA} > 0.75$, this trend no longer holds true. The resulting materials exhibited no σ (with the exception of P25/75-4-TFSI), which is likely due to unfavourable morphology as demonstrated by only exhibiting a single *Tg* and negligible self-assembly by TEM. These results demonstrate that block copolymer architecture and microphase separation both play a critical role in obtaining high σ. **Figure 4.4** further demonstrates that the choice of anion plays a significant role on the *Tg*, and thus, the resulting σ, where in all cases a trend of σ : $TFSI^- > PF_6^- > BF_4^-$ was observed. A similar trend was reported by Chen et al. for similar anions when using methacrylate based imidazolium PIL homopolymers with alkyl spacers.[42] Ganesan and coworkers have attributed ion size as a handle on σ within the respective physicochemical ion classes of PILs, while noting that large ions with delocalized charge can outperform some smaller ions, this corresponds to our observations where the TFSI- materials exhibited the highest conductivity.[43] In addition to σ, the electrical double-layer (EDL) capacitance is a critical characteristic necessary to understand prior to integration into organic thin film transistor (OTFT) devices. Very few reports exist on the characterization of ionic liquid EDL capacitance and even less on the characterization of PILs EDL capacitance. For example, typical electrolytes contain a solvent dipole and supporting electrolyte that are well understood using Helmholtz and Guoy-Chapman models.[44] Unlike typical

electrolytes, ionic liquids interfacial phenomena greatly effect of the EDL due to their direct contact with the electrode. Therefore, electrode properties such as work function and surface roughness have been shown to effect ionic liquid EDL capacitance, suggesting the importance of the interface.[45] However, it is established that polarizability and ion size effects the EDL.[46] For example, an increase in molecular volume will increase the static dielectric constant.[46] Colby and coworkers showed that the capacitance of imidazolium ionic liquids is increased when polymerized into PILs.[46] The specific capacitance as a function of frequency and the corresponding average = EDL capacitance for the poly(S)-b-poly(VBBI$^+$[X]-*r*-PEGMA) block copolymers as a function of anion ([X] = BF_4^-, PF_6^-, or $TFSI^-$) are plotted in **Figure 4.5**. The specific capacitance shown at intermediate frequencies (~10^{-3} to 10^{-1} Hz) is associated with the EDL capacitance. It is clear that the magnitude of EDL capacitance is dictated by the choice of mobile anion, where TFSI- producing the greatest value followed by PF_6- and BF_4^-. These results are consistent with the trend observed by Fujimoto et al. with ionic liquids based on 1-butyl-3-methylimidazolium (BMIM) cation.[47] At high frequencies (prior to EDL formation) all materials exhibited similar capacitances (**Figure 4.5a**). Choi et al. have shown that the capacitance is increased when the cation is physically further from the polymer backbone by use of a spacer, facilitating a response to an applied electric field, increasing their relaxation strength and thus dielectric constant, however, this increase is only seen in high frequency regime, prior to the EDL formation.[46] At lower frequencies block copolymers with elevated F_{PEGMA}, experienced a small secondary rise in capacitance (**Figure 4.5a**). This low frequency rise suggests an orientation of PEGMA chains or of the alkyl group on butyl-imidazole[48,49] Another important result of the formation of the EDL layer is that it provides a thickness independent dielectric, which is critical for the integration of these materials into large scale commercial printed electronics. To confirm that these block copolymers exhibited thickness-independent capacitance, we characterized ≈400 nm and ≈800 nm films of all block copolymers and obtained identical results (**Figure 4.13**).

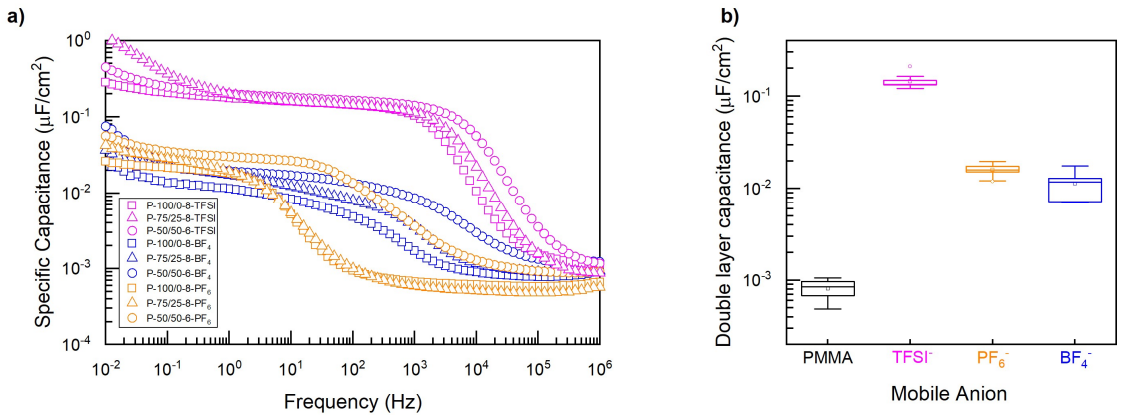

Figure 4.5. a) Representative Specific Capacitance versus Frequency curves and b) Double layer capacitance for poly(S)-*b*-poly(VBBI$^+$[X]-*r*-PEGMA) (where [X] = BF_4^-, PF_6^-, or $TFSI^-$) in MIM capacitors. The data in b) is presented in a standard box plot convention where the upper and lower lines of the box represent the 75th and 25th percentile while the middle horizontal lines represent the median. The outer whiskers represent the upper and lower quartile + 1.5 the interquartile range. Additionally, two symbols were used in the data representations (square and circle); the square represents the mean whereas the circle represents outliers.

The EDL capacitances achieved for these TFSI- based block copolymers were on the order of 200-300 nF·cm^{-2} (**Figure 4.5, Table 4.2**) which is lower than other $TFSI^-$ based PILs we have studied using the same characterization setup.[15,50] Previously we have reported triazole-based styrenic homopolymers[50] and poly(methyl methacrylate-r-styrene)-b-poly(VBBI$^+$TFSI$^-$) (poly(MMA-r-S)-b-poly(VBBI$^+$TFSI$^-$) block copolymers,[15] which were both characterized by an EDL capacitance of 1000-2000 nF·cm^{-2}. It is also important to note that in both cases those polymers were found to have a greater Tg and a reduced σ compared to these poly(S)-b-poly(VBBI$^+$[X]-r-PEGMA) block copolymers. Therefore high conductivity does not necessarily lead to high EDL capacitance. This comparison also illustrates that while the choice of anion is important, the molecular architecture, the self-assembly, the interfacial composition and the EDL formation is critical for high capacitance.

4.3.4 Poly(ionic liquid)-Gated Thin-Film Transistors

To ensure only electrostatic gating is present, which does not affect the band structure of the semiconductor as electrochemical doping does, ions in the electrolyte must only interact with the charge in the channel via Coulombic interactions.[51] One method to ensure electrostatic gating

while maintaining the benefits of high capacitances from electrolyte gating is the use of single-ion conductors which, when properly paired with an appropriate semiconductor, will result in only electrostatic gating.[52] Furthermore, Fullerton-Shirey and coworkers have shown single-ion conductors (mobile cation paired with p-type semiconductor) can achieve charge carrier densities in OTFTs of equivalent magnitude to that of dual ion conductors.[53] In this study, top-gate top-contact (TGTC) transistors were fabricated using P50/50-6 (**Table 4.1**), a poly(S)-*b*-poly(VBBI$^+$[X]-*r*-PEGMA) materials functionalized with either [X] = TFSI$^-$, PF_6^-, or BF_4^- as the mobile anions; gold contacts, and solution processable poly(NDI2OD-T2)[54] n-type semiconductor (**Figure 4.6, Table 4.6**). It is important to note that we paired a PIL with mobile anion with the complimentary n-type semiconductor to avoid electrochemical doping. Polymer layers were formed via spin-coating in atmospheric conditions and contacts were deposited by physical vapour deposition (PVD) under vacuum (see experimental section). It is important to note that the EDL capacitance is a function of the ionic conductivity and dielectric constants of the materials as well as the electrode geometry and type[55–57] this is why in all cases the same electrode materials were used for the MIM capacitors as well as the OTFTs. Furthermore, all poly(ionic liquid) materials were compared under the same conditions using the same electrode geometry and processing parameters to ensure adequate comparison. The top-contact architecture was selected in an effort to reduce contact resistance exhibited in similar devices from our previous work which utilized ITO contacts in a bottom-contact architecture.[15] High-contact resistance is commonly seen in OTFTs with bottom-contact configurations and from energetic mismatched semiconductor-electrode metal pairs.[58] The unipolar PIL gating materials were purposefully paired with an n-type semiconductor to prevent electrical doping of the semiconductor with the mobile ions during device operation. When a positive voltage is applied to turn on the device, the negative anions move to form an EDL at the gate; this leaves the semiconductor/PIL interface to consist solely of the large polycation backbone which is simply too big to penetrate the permeable semiconductor.[59] Since all materials were obtained from the same precursor block copolymer material (P50/50-6); this semiconductor/PIL interface should be identical for all devices fabricated irrespective of their mobile anion making any observed differences in drain-currents solely due to the effect of the mobile anion. To the best of our knowledge, this would be the only report of the identical polymer with different anions being used as gating material for n-type OTFTs. Small changes in polymer

structure (composition, molecular weight, polydispersity) can have significant effect on self-assembly and EDL formation making the comparison of different systems quite challenging; which again is avoided here by having the identical polymer precursor.

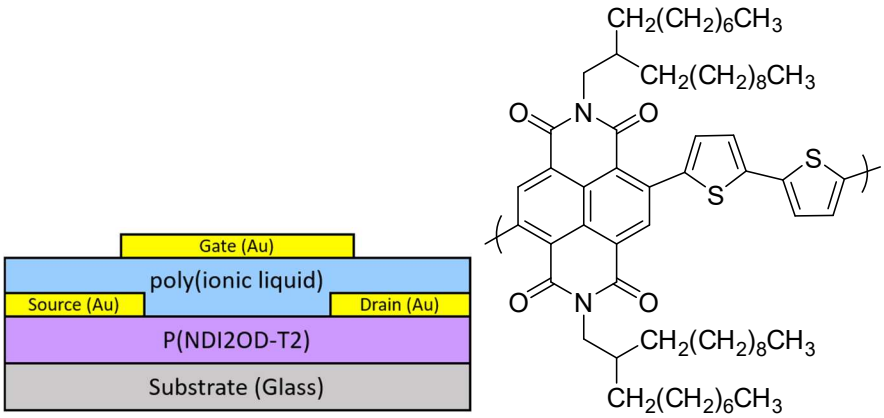

Figure 4.6. Schematic cross section of TGTC transistors based on poly(NDI2OD-T2) n-type semiconductor, poly(S)-*b*-poly(VBBI$^+$[X]-*r*-PEGMA) (where [X] = BF_4^-, PF_6^-, or $TFSI^-$) as poly(ionic liquid) gating medium, and gold contacts.

Figure 4.14 shows the drain current (I_{DS}) versus drain voltage (V_{DS}) output curves for poly(NDI2OD-T2) devices (W/L = 1 mm/30 µm) fabricated with P50/50-6 using $TFSI^-$, PF_6^-, or BF4-. P50/50-6 was selected as a point of comparison due to its high ionic conductivity. The output characteristics of all the transistors exhibit linear behavior up to 1 V, where $TFSI^-$ and BF_4^- devices start to display saturation behaviour. While the resulting devices displayed some degree of contact resistance; they represented a significant improvement over our earlier studies with similar dielectric materials in a top gate bottom contact architecture.[15] The greatest I_{DS} were obtained from devices made using P50/50-6 with the BF_4^- anion, followed by $TFSI^-$ and PF_6^-, respectively (**Figures 4.7 & 4.8**). These results indicate that the choice of anion plays a role on the device current even when the devices all had identical polycation backbone and semiconductor interface. Note that the anion moves away from the interface during operation and because we used the identical cation polymer for each device the interface should be identical. Additionally, the relative trend of I_{DS} obtained from these devices does not correspond to EDL capacitance values observed in capacitors where $TFSI^- > PF_6^- > BF_4^-$.

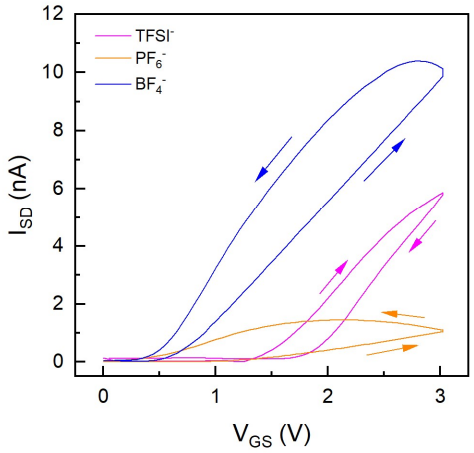

Figure 4.7. Representative transfer characteristics in the linear regime (V_{DS} = 1 V) of poly(S)-*b*-poly(VBBI$^+$[X]-*r*-PEGMA) (where [X] = BF_4^-, PF_6^-, or $TFSI^-$) OTFTs. The gate voltage was swept linearly at a rate of 250 mV/s. (L = 30 µm, W = 1000 µm)

The transfer characteristics for the OTFTs were obtained by sweeping the gate voltage (V_{GS}) at a sweep rate of approximately 250 mV/s to ensure EDL formation whilst holding the V_{SD} constant at 1 V. All materials displayed hysteresis which is commonly observed in electrolyte dielectrics as a consequence of the relatively slow movement of ions and moisture.[60–62] Several parameters were extracted by aid of linear fit to the transfer curves; the transconductance (g_m) equating to slope, and threshold V_T which corresponds to the V_G-intercept. The linear fits were performed on the forward sweep of all the transfer curves. P50/50-6 with $TFSI^-$ and BF_4^- devices exhibited similar gm whereas P50/50-6 with PF_6^- were smaller by over an order of magnitude (**Figure 4.7**). The V_T of $TFSI^-$ and PF_6^- ranged between 1 and 2 V whereas BF_4^- devices consistently turned on below 1 V. These VTs are significantly lower compared to BGBC devices made using the same poly(NDI2OD-T2) on SiO_2 (V_T = 33.9 V, tested in air) which possessed similar charge trap densities (**Table 4.6**).[63] This enabled the devices to operate at much lower operating voltages exhibited by the output curves (**Figure 4.14**).

The field-effect mobility (μ) was calculated from the g_m using the equation:

$$\mu = g_m \frac{LV_{SD}}{WC_i}$$

where, *Ci* is the capacitance of the gate insulator and L/W are the length and width of the OTFT, respectively. The *Ci* value utilized corresponds to the EDL capacitance determined in the capacitor experiments at the same frequency. The resulting μ for P50/50-6 with $TFSI^-$, PF_6^-, and BF_4^- devices were 0.9×10^{-3}, 1.1×10^{-3}, and 1.1×10^{-2} cm^2/Vs, respectively. These values are similar to what we obtained using poly(NDI2OD-T2)- based BGBC for devices on SiO_2 in air (3×10^{-2} cm^2/Vs).[63] The μs seen for devices from P50/50-6 with TFSI- are comparable to our previous reports using poly(MMA-r-S)-b-poly($VBBI^+TFSI^-$) with the same semiconductor.[15] It has often been noted that a higher capacitance dielectric results in a reduced μ,[64,65] which concurs with the greater μ obtained using devices fabricated using P50/50-6 with BF_4^- compared to $TFSI^-$. The reduced μ is mainly explained by referencing a microscopic model in which the charge carriers electrostatically accumulated at semiconductor surfaces undergo polaronic self-localization stemming from the interaction with polarizable dielectrics leading to Fröhlich polarons.[64,65] This induces a broadening of the density of states (DOS) at the semiconductor/gating material interface and decrease in DOS at the Fermi energy, reducing the hopping probability and thus reduce μ.[66] Previous reports by Fujimoto et al. using octathio[8]circulene (p-type semiconductor) based OTFTs with 1-butyl-3-methylimidozolium bis(trifluoromethylsulfonyl) (BMIM) cation based ionic liquids gating materials with different anions ($TFSI^-$, BF_4^-, PF_6^-, TFS^-) found a negative linear correlation between the μ and ionic liquid capacitance.[47] For our devices, the ON/OFF ratios were relatively low (**Table 4.6**). These ON/OFF ratios could potentially be improved by reducing off currents which could be achieved by eliminating parasitic leakage currents outside the gate controlled area.[67] Conventionally this is achieved by patterning the semiconductor layer, however, there have been relatively few reports involving the effective patterning of solution processed OTFTs.[68] The authors also found that V_T significantly depends on the structure of ionic liquid gating medium, suggesting choice of ionic liquid is correlated to device performance. To the best of our knowledge, no similar study has been reported for n-type operation using ionic liquids or PILs but our results suggest a similar dependency between choice of anion and device performance.

Thus far, from a device performance perspective, P50/50-6 with BF_4^- is the most suitable choice due to the resulting devices being characterized with relatively low V_T, high I_{SD} and high μ (**Figure 4.7**). However, these experiments were run slowly to ensure a comparison of the devices

once the EDL is formed and therefore do not properly characterize a device during intended operation. It is critical to study the device responsiveness to properly assess the potential of these materials. The responsiveness of the P50/50-6 (with either $TFSI^-$, PF_6^-, or BF_4^-) gated OTFTs was examined by applying a 3 V square-pulse waveform to the gate at frequencies of 20, 100, 200, 600, 800, and 1000 mHz while measuring the I_{SD} (**Figure 4.8**). It is clear that the I_{SD} of the devices follow the input signal of the gate, however, it is also clear that the response changes with frequency and with choice of anion. For example: the use of P50/50-6 with $TFSI^-$, the most conductive of the three, leads to devices that reach their maximum I_{SD} at very slow operations of 20 mHz and at fast operation of up to 1000 mHz, when we can see that the maximum is just barely reached within 0.5 sec before the device is turned off. For devices fabricated using BF_4^-, the maximum I_{SD} is almost 5x greater than those made using $TFSI^-$ at low frequencies (< 1000 mHz) but the I_{SD} reduces as the frequency is increased to a point where no current is detected at frequencies > 800 mHz (**Figure 4.8**). We surmise this drop is due to the device not reaching saturation, i.e not being completely "on" before being switched "off". For devices made using PF_6-, the least conductive gating material, we only detected a current at slow operations < 100 mHz. The difference in responsiveness is attributed to the ionic conductivity of the gating media; the device is turned on by the formation of an EDL, which form at lower frequencies for more conductive materials (as seen in the MIM section). The responsiveness thus follows the same order of increasing ionic conductivity with $TFSI^-$ being the highest, followed by BF_4^-, then PF_6^-. What is interesting to note is that the $TFSI^-$ containing materials led to more consistent current generation at all operating frequencies while the same polymer containing BF_4^-, (and possibly PF_6^-) led to a frequency dependent I_{SD}.

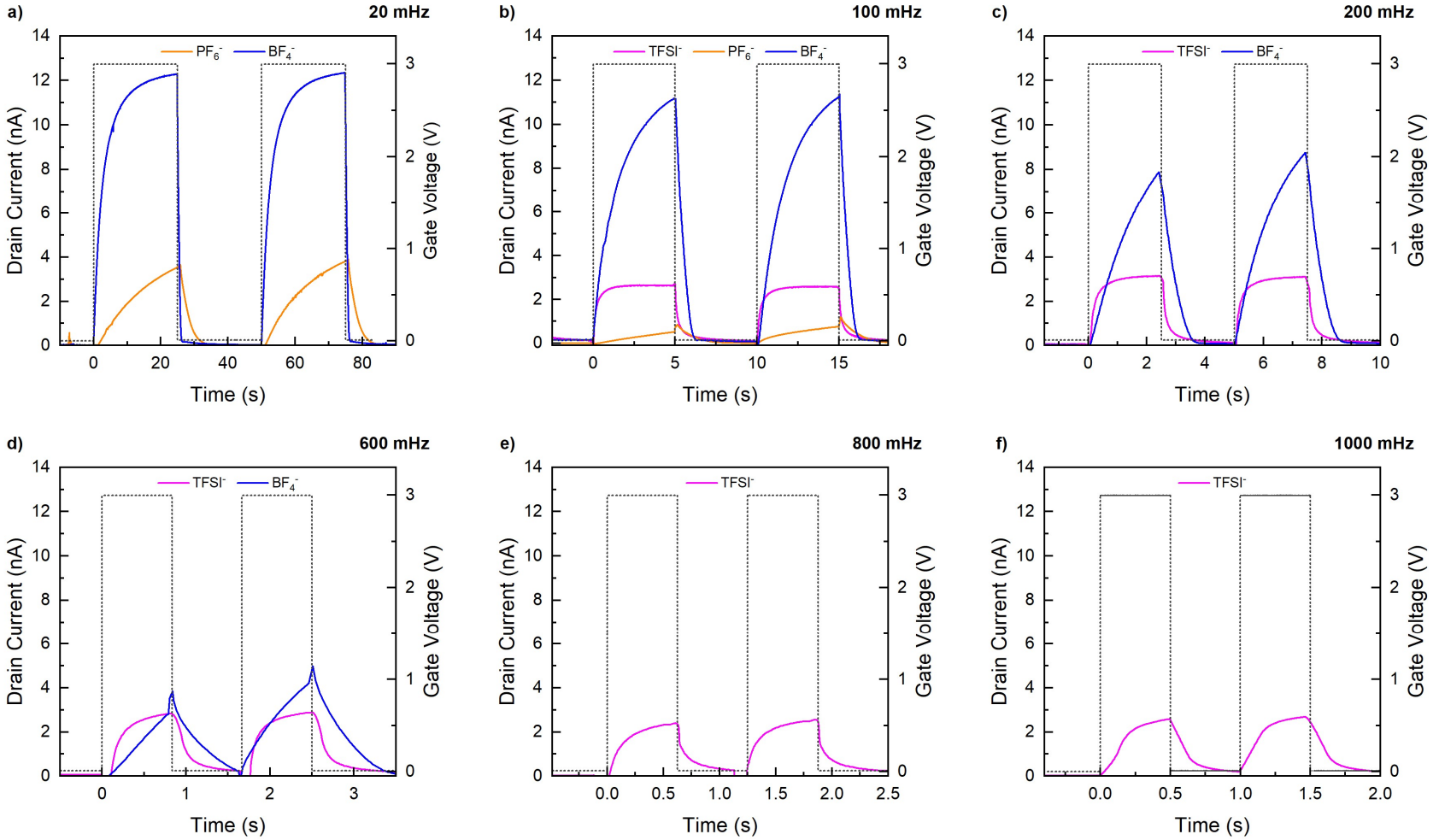

Figure 4.8. Frequency-dependent measurements of P50/50-6 a poly(S)-*b*-poly(VBBI$^+$[X]-*r*-PEGMA) (where [X] = BF_4^-, PF_6^-, or $TFSI^-$) gated OTFTs, where the traces correspond to the anion as $TFSI^-$ (magenta), PF_6^- (orange), and BF_4^- (blue). The drain current response to a 3 V gate voltage applied in a two-square wave burst at frequencies ranging from 20 mHz to 1000 mHz.

4.4 Conclusion

In this study, we prepared a series of poly(styrene)-*b*-poly(1-(4-vinylbenzyl)-3-butylimidazolium-*random*-poly(ethylene glycol) methyl ether methacrylate) (poly(S)-*b*-poly(VBBI$^+$[X]-*r*-PEGMA)) block copolymers, with varying PEGMA/VBBI$^+$ ratios and three different mobile anions (where X = TFSI$^-$, PF_6^- or BF_4^-) to study structure-property relationships to gain insights towards designing materials for low-operating voltage and responsive OTFTs. We showed a library of PIL block copolymer materials, with two distinct T_gs exhibit self-assembled microstructures with long range order, and that the domain size and organizational structure depended on block copolymer architecture and choice of anion. We demonstrated that the use of these PIL containing block copolymers leads to n-type OTFTs with comparable mobilities and very low threshold voltages ($V_T \approx 0.5$V). By comparing identical polymers with different anions, we were able to probe the semiconductor/PIL interface during OTFT operation. We found that reduced glass transition temperatures and greater conductivity in the PIL block copolymers led to faster OTFT switching speeds. We have also shown that double-layer capacitance measured by EIS does not directly translate to device output currents even when the semiconductor/PIL interface is identical, suggesting OTFT fabrication is needed to screen potential PIL gating material candidates.

4.5 Experimental Section

4.5.1 Synthesis of poly(styrene) macroinitiator (poly(S))

The poly(S) macroinitiator was synthesized by the polymerization of styrene (400 g, 3.84 mol) using BlocBuilder-MA (1.53 g, 4.00 mmol) with additional SG1 nitroxide mediating stable-free radical (117.7 mg, 0.4 mmol). The ratio of BlocBuilder-MA to styrene were selected to target a 100 kDa polymer at 100% conversion. The polymerization was performed in typical air-free conditions using a round-bottom flask fitted under a head of nitrogen with condenser. The reagents were first combined in the flask, the solvent was added (200 mL toluene), and the vessel was bubbled with nitrogen for 1 hour. After purging, the vessel was heated to 100 °C. GPC samples were periodically taken to measure the M_W with an effort to stop the reaction at a rough molecular weight of 25 kDa corresponding to 25% conversion, to produce an effective, highly living macroinitiator. The reaction was stopped at 6 h, left to cool, then precipitated twice into methanol

from tetrahydrofuran (THF). The final polymer was dried in vacuum, producing 112.5 g of the final poly(S) macroinitiator (M_n = 22.5 kDa, M_w/M_n = 1.11).

4.5.2 Synthesis of poly(styrene)-*b*-poly(chloromethyl styrene-*r*-poly(ethylene glycol) methacrylate) (poly(S)-*b*-poly(CMS-*r*-PEGMA)) precursor block copolymers

Precursor poly(styrene)-*b*-poly(chloromethyl styrene-*r*-poly(ethylene glycol) methacrylate) block copolymers were produced by performing a chain extension on the poly(S) macroinitiator. All of the formulations are listed in **Table 4.3** and a typical procedure is as follows using the formulation CMS/PEGMA-50/50-4: poly(S) macroinitiator (3.00 g), CMS (1.35 g, 8.84 mmol), PEGMA (2.65 g, 8.84 mmol), and 50 wt% DMSO were loaded into a round-bottom flask sealed under a nitrogen condenser and purged with nitrogen for 20 minutes before heating to 90 °C. The reactions were left to run overnight. Final material was isolated in a similar fashion to the poly(S): twice precipitating to methanol, re-dissolving into THF between steps, and finally drying in vacuum overnight. Precursor polymers were characterized by NMR and SEC (**Figures 4.9 & 4.11**).

4.5.3 Preparation of poly(ionic liquid) materials from precursor block copolymers

Quaternization reaction were performed with a 1.1 molar excess of butylimidazole on the block copolymers containing CMS group (calculated by assuming entire polymer was CMS homopolymer) at 70 °C for 24 h, forming a poly(S)-*b*-poly(VBBI$^+$Cl$^-$-*r*-PEGMA)) block copolymers possessing a Cl^- mobile anion. The post-reaction mixtures were then divided into three scintillation vials, and a subsequent anion exchange reaction was performed with a 1.1 molar excess of LiTFSI, $LiPF_6$, or $NaBF_4$ at room temperature for 48 h. The final poly(S)-*b*-poly(VBBI$^+$[X]-*r*-PEGMA)) block copolymers (where X = $TFSI^-$, PF_6^- or BF_4^-) were all isolated by precipitating into water and thoroughly washed with water to remove any salts and finally dried in a vacuum oven, at 70 °C, overnight. The final poly(ionic liquid) block copolymers were characterized by ^{1}H NMR to confirm quaternization was taken to full conversion and that the subsequent anion exchange was confirmed by shifting of neighbouring protons on the imidazole group.

4.5.4 Fabrication of metal-electrolyte-metal (MEM) capacitors

Metal-insulator-metal (MIM) capacitors were fabricated using one 25mm x 25mm glass slide as a substrate. The slides were first cleaned by sonication in soapy water, water, acetone and methanol for 5 minutes each, then blown dry with nitrogen. The cleaned slides were then patterned by physical vapour deposition (PVD) with bottom electrodes consisting of an initial 100 nm chromium adhesion layer followed by 400 nm of gold. The final poly(S)-*b*-poly(VBBI$^+$[X]-*r*-PEGMA)) block copolymers (where X = TFSI$^-$, PF_6^- or BF_4^-) were deposited by spin-coating 90 µL solution (two thicknesses were targeted using either 60 mg/mL and 100 mg/mL solutions) in methyl ethyl ketone (MEK) at 2000 rpm followed by annealing at 130 °C for 2 hours. Finally, top electrodes were deposited by PVD using a shadow mask; the pattern of the top and bottom electrodes results in 16 different capacitors on each slide with areas ranging from 0.35 mm^2 to 2.88 mm^2. For each poly(S)-*b*-poly(VBBI$^+$[X]-*r*-PEGMA)) block copolymers (where X = TFSI$^-$, PF_6^- or BF_4^-), two substrates were prepared with different insulating layer thickness' by changing the concentration of poly(ionic liquid) in MEK solutions. Capacitors were characterized by profilometry for thickness measurements and electrical impedance spectroscopy.

4.5.5 Fabrication of top-gate top-contact (TGTC) poly(ionic liquid)-gated organic thin-film transistors

Top-gate top-contact organic thin-film transistors (OTFTs) were fabricated on top of 15 x 20 mm quartz coated glass substrates. First the semiconducting layer, poly{[N,N-bis(2-octyldodecyl)-naphthalene-1,4,5,8-bis(dicarboximide)-2,6-diyl]-alt-5,5-(2,2-bithiophene)} (poly(NDI2OD-T2)) was deposited by spin coating from a 10 mg/mL *o*-dichlorobenzene solution at 2000 rpm followed by annealing at 100 °C for 1 hour. Next, 50 nm thick gold contacts were deposited for the source and drain electrodes using PVD aided by a shadow mask, with L = 30 µm and W = 1000 µm. Next, the poly(S)-*b*-poly(VBBI$^+$[X]-*r*-PEGMA)) block copolymers (where X = TFSI$^-$, PF_6^- or BF_4^-) gating medium was deposited from spin coating from a 60 mg/mL solution in MEK at 2000rpm. The OTFTs were then annealed at 130 °C for 1 hour to remove residual solvent and promote self-assembly of the block copolymer. A second layer of the poly(S)-*b*-poly(VBBI$^+$[X]-*r*-PEGMA)) block copolymer was deposited by spin coating and annealed using identical conditions. The substrates were left to cool and finally completed by depositing a 50 nm thick gold gate electrode using PVD and shadow mask.

4.5.6 Characterization

Size Exclusion Chromatography (SEC). The molecular weight and dispersity of the poly(S)-*b*-poly(CMS-*r*-PEGMA) precursor polymers was determined by size exclusion chromatography. SEC was performed using an Agilent 1260 Infinity with columns heated to 30 °C with THF as the eluent at a flow rate of 1 mL·min^{-1}. Wyatt detectors were utilized for the measurements; DAWN HELEOS II multi-angle light scattering (MALS) detector, ViscoStar II differential viscometer, and an Optilab T-rEX differential index detector. The system was fitted with two MZ-Gel SD plus Linear 5µm, 300 × 8.0mm columns. The $\partial n/\partial c$ for each material was determined using offline batch measurements with the RI detector, injecting a series of polymer in THF solutions of increasing concentration by a syringe pump and recording the dRI response. The dRI versus concentration was plotted, and the line of best-fit slope, equating to the dn/dc, was determined using a linear fit.

Nuclear magnetic resonance spectroscopy (NMR). The copolymer compositions and confirmation that polymer functionalization reactions were taken to completion was determined using nuclear magnetic resonance (^{1}H NMR) using a Bruker AVANCE II 400 MHz spectrometer. Samples were dissolved in deuterated chloroform ($CDCl_3$) or deuterated dimethyl sulfoxide DMSO-d_6 as the solvent. Determination of copolymer composition via ^{1}H NMR is described in the Supporting Information.

Differential Scanning Calorimetry (DSC). The glass transition temperatures (T_gs) of the final poly(S)-*b*-poly(VBBI$^+$[X]-*r*-PEGMA)) block copolymer were determined using Differential Scanning Calorimetry. DSC was performed using a TA Instruments Q2000 over a temperature range of -40 °C to 150 °C at a heating/cooling rate of 10 °C/min under an N_2 environment. The T_gs were determined using the midpoint method from the second thermogram heating cycle using the software, Universal Analysis, provided by TA Instruments.

Profilometry. The thickness of the poly(S)-*b*-poly(VBBI$^+$[X]-*r*-PEGMA)) block copolymer layer in MIM capacitors was measured using a Bruker Dektak XT profilometer. A series of 10 scratches were made with a diamond tip pen to create a step edge. The step edge was measured, and the average of the measurements ± SD are reported.

Electrochemical Impedance Spectroscopy (EIS). Impedance properties such as conductivity and double-layer capacitance of the poly(S)-*b*-poly(VBBI$^+$[X]-*r*-PEGMA)) block copolymers in the MIM capacitors were investigated with EIS. Measurements were conducted over a frequency range of 10^{-3} – 10^6 Hz with an AC amplitude of 10 mV under atmospheric conditions using a Metrohm PGSTAT204. The ionic conductivity (σ) was calculated using the equation: $\sigma = d/(R_b A)$, where d is the thickness, R_b is the bulk resistance, and A is the area of the capacitor. Bulk resistance, R_b, was found by using the diameter of a circular fit to the charge transfer regime, which appears as a semicircle, of the experimental data Nyquist plot of the experimental impedance data using Nova 2.1 software. A representative Nyquist plot with semicircular diameter fitting is shown in S4.

Transmission Electron Microscopy (TEM). Images of annealed bulk poly(S)-*b*-poly(VBBI$^+$[X]-*r*-PEGMA)) block copolymer sample section were obtained using Transmission Electron Microscopy. Samples were prepared by drop-casting 100 mg/ml polymer/MEK solution onto a Teflon watch-glass and left in a vacuum oven at 70 °C until solvent evaporated. The dried casted polymer samples were then annealed at 130 °C under vacuum for 2 hours and left to cool overnight. Liquid N_2 was then poured over the annealed-polymer coated Teflon watch-glasses', the casted polymer cracked, lifted from the watch-glass and collected. Sections were cut on a Leica UCT ultramicrotome (Leica Microsystems, Leica UCT Ultramicrotome) equipped with a diamond blade, placed onto copper grids, and exposed to 5 wt % aqueous RuO_4 solution for 1 h to preferentially stain the poly(styrene) block. TEM imaging was performed on the prepared samples using a FEI Titan 80-300.

Small-Angle X-ray Scattering (SAXS). The SAXS patterns were collected with a Bruker AXS Nanostar system equipped with a Microfocus Copper Anode at 45 kV / 0.65 mA, MONTAL OPTICS and a VANTEC 2000 2D detector. The distance, 106.95 cm from the detector to the sample, was calibrated with a Silver Behenate standard prior the measurements. The positioning fine tuning was done by Nanography; a 2 sec. per step scan sweep on X and Y to find the exact position of the samples. The diffracted intensities were integrated from 0.100 to 3.000 deg. 2-theta on 360 degrees. Collection exposures were 200 to 400 seconds

Transistor Characterization. Transistor characterization was performed in ambient conditions using a probe station equipped with a 2614B Keithley 2-channel source-measure unit (SMU) to control the gate and source-drain potentials, V_G and V_{DS}, respectively. Output curves were generated measuring the source-drain current (I_{SD}) and linearly sweeping V_{DS} while fixing V_{GS} at a fixed potential, performing a series of steps in V_{GS}. Transfer curves were generated by fixing V_{SD} at 1 V and sweeping V_{GS}. Frequency dependence of transfer characteristics were examined by measuring I_{SD} and using a function generator (AFG 3011C) to apply the gate voltage in a square-pulse waveform of selected frequencies. In the response time experiments, the gate potential was supplied by the waveform generator and measured using a Keithley Digital Multimeter (DMM 6500) to digitize the voltage. While the source-drain potential was set using one channel of the Keithley SMU connected in series with the device-under-testing and simultaneously measured the drain current, I_{SD}.

4.6 Acknowledgements

The Natural Sciences and Engineering Research Council of Canada (NSERC RGPIN-2020-04079 to B.H.L) and the University of Ottawa are acknowledged for financial support. The research was undertaken, in part, thanks to funding from the Canada Research Chair program which B.H.L is a member. The authors would like to thank Marcia Reid, Carmen Adrei, and Andreas Korinek (Canadian Centre for Electron Microscopy, McMaster University) for cross-sectional TEM sample preparation and imaging. The authors would also like to thank Marc Dubé (University of Ottawa) for donating BlocBuilder-MA, which was originally acquired from Arkema and Daniel Fortin (Université de Sherbrooke) for SAXS measurements. We are also grateful to Ontario government for the Queen Elizabeth II Graduate Scholarship in Science and Technology (QEII GSST) to A.J.P.

4.7 Supplementary Information

Synthetic chemistry formulations and molecular weights for chloromethyl/poly(ethylene glycol) methyl ether methacrylate chain extension from poly(styrene) macroinitiator, along with representative characterization example; NMR spectra, determination of composition, and GPC trace; example Nyquist plot from polyelectrolyte capacitor with circular-best-fit used for conductivity calculation; detailed table of MIM capacitors including material, glass transitions, conductivity, and thickness; detailed transistor characterization results including; output curves, transfer characteristics (by the decade); and summary table with ON/OFF ratio, threshold voltage, capacitance, mobility, subthreshold swing, and charge trap density.

4.7.1 Calculation of Copolymer Composition

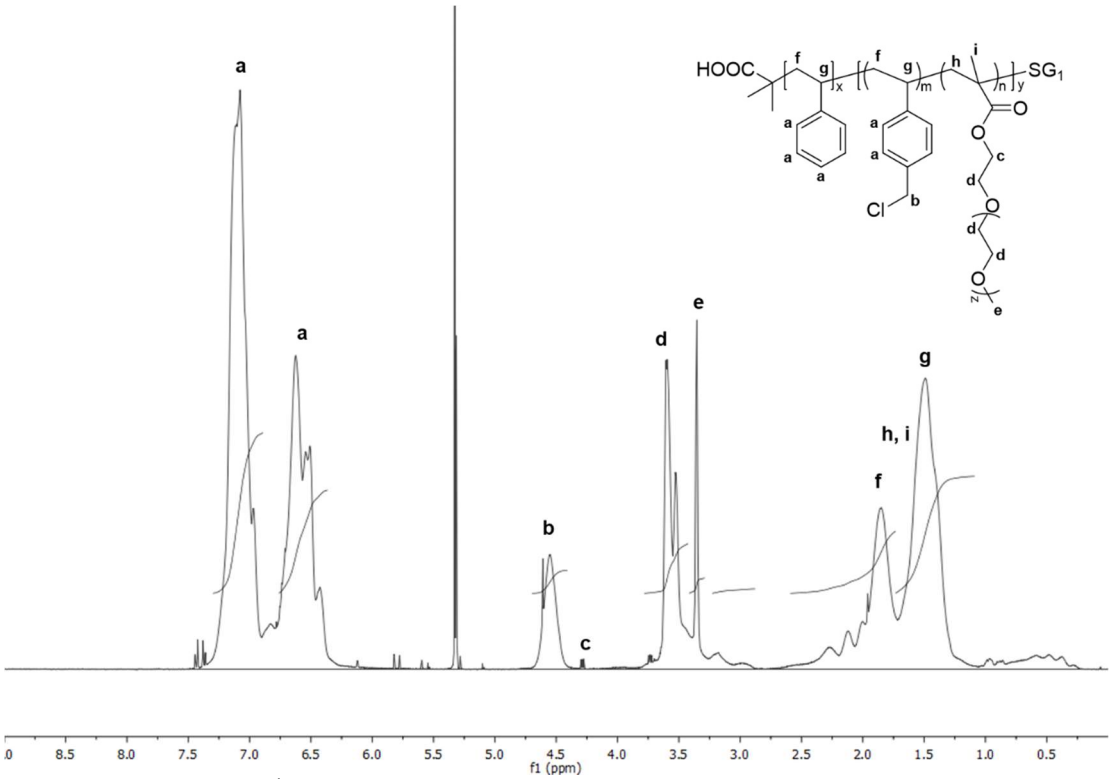

Figure 4.9. Representative ^{1}H NMR spectra of the precursor block copolymer in $CDCl_2$ (poly(S)-b-poly(CMS-r-PEGMA)-25/75-6g. Compositions are determined using the relative integrations of a, b, c, d, and e.

The molar ratio of Styrene, CMS, PEGMA was calculated:

$$ST : CMS : PEGMA$$

$$\frac{I_a - 2I_b}{5} : \frac{I_b}{2} : \frac{I_c + I_d + I_e}{21}$$

The composition of the entire polymer was calculated:

$$F_{ST} = \frac{ST}{ST+CMS+PEGMA} \quad ; \quad F_{CMS} = \frac{CMS}{ST+CMS+PEGMA} \quad ; \quad F_{PEGMA} = \frac{PEGMA}{ST+CMS+PEGMA}$$

The composition of the 2nd block was calculated:

$$F_{CMS} = \frac{CMS}{CMS+PEGMA} \quad ; \quad F_{PEGMA} = \frac{PEGMA}{CMS+PEGMA}$$

4.7.2 Additional Tables & Figures

Table 4.3. Formulations chloromethyl styrene/poly(ethylene glycol) methyl ether methacrylate chain extensions from poly(styrene) macroinitiator.

Exp. ID [a]	**CMS**		**PEGMA**	
	mmol	g	mmol	g
CMS/PEGMA-100/0-4g	26.21	4.00	-	-
CMS/PEGMA-100/0-8g	52.42	8.00	-	-
CMS/PEGMA-25/75-2g	1.90	0.29	5.70	1.71
CMS/PEGMA-25/75-4g	3.80	0.58	11.40	3.42
CMS/PEGMA-25/75-6g	5.70	0.87	17.10	5.13
CMS/PEGMA-50/50-4g	8.84	1.35	8.84	2.65
CMS/PEGMA-50/50-6g	13.26	2.02	13.26	3.98
CMS/PEGMA-75/25-4g	15.83	2.42	5.28	1.58
CMS/PEGMA-75/25-6g	23.75	3.62	7.92	2.38
CMS/PEGMA-75/25-8g	31.67	4.83	10.56	3.17

[a] Experimental identification (Exp. ID) is given by CMS/PEGMA-Y: where CMS and PEGMA correspond to chloromethyl styrene (CMS) and poly(ethylene glycol) methyl ether methacrylate (PEGMA), respectively. And the following number fraction refers to the molar feed of CMS to PEGMA, followed by the grams of total chain extension monomer.

[b] All experiments were performed utilizing the same amount of poly(styrene) macroinitiator (3.00 g).

Table 4.4. Molecular Weight Distribution Data for poly(S)-*b*-poly(CMS-r-PEGMA) Block Copolymer Precursors to Ionic Liquid Containing Block Copolymers Determined using poly(MMA) Standards.

Exp. ID	$\bar{M}_p$ (Da) $[kg\ mol^{-1}]$	$\bar{M}_w$ (Da) $[kg\ mol^{-1}]$
poly(S) macro.		
CMS/PEGMA-100/0-4g	37.3	39.5
CMS/PEGMA-100/0-8g	39.6	41.6
CMS/PEGMA-25/75-2g	41.8	43.4
CMS/PEGMA-25/75-4g	44.5	46.2
CMS/PEGMA-25/75-6g	40.2	40.9
CMS/PEGMA-50/50-4g	43.6	46.8
CMS/PEGMA-50/50-6g	39.2	43.7
CMS/PEGMA-75/25-4g	45.3	46.1
CMS/PEGMA-75/25-6g	42.8	45.9
CMS/PEGMA-75/25-8g	38.9	42.2

b) Number-average molecular weight ($\bar{M}_n$), weight-average molecular weight ($\bar{M}_w$), and dispersity (M_w/M_n) were determined by size exclusion chromatography (GPC). $\partial n/\partial c$ was determined by offline batch dRI measurements for each polymer.

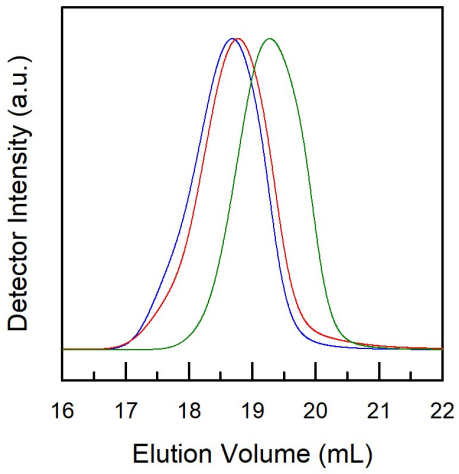

Figure 4.10. Representative SEC refractive index and light-scattering chromatograms of poly(styrene) macroinitiator (green) and poly(S)-b-poly(CMS-*r*-PEGMA)-100/0-8g (red) and poly(S)-*b*-poly(CMS-*r*-PEGMA)-25/75-4g (blue) diblock copolymers. The red line represents data from the light-scattering detector, and the blue line represents data from the RI detector.

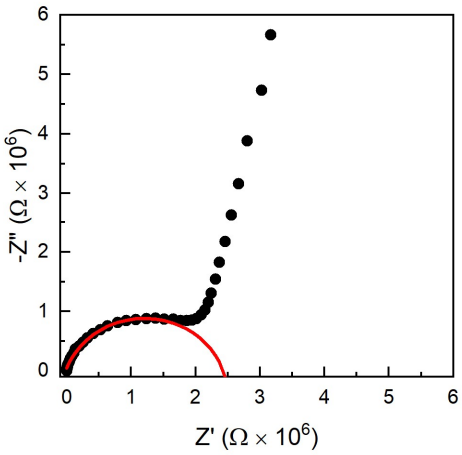

Figure 4.12. Representative Nyquist plot from metal-insulator-metal (MIM) capacitors. The conductivity was determined by performing a fit to the circular portion of the plot (red).

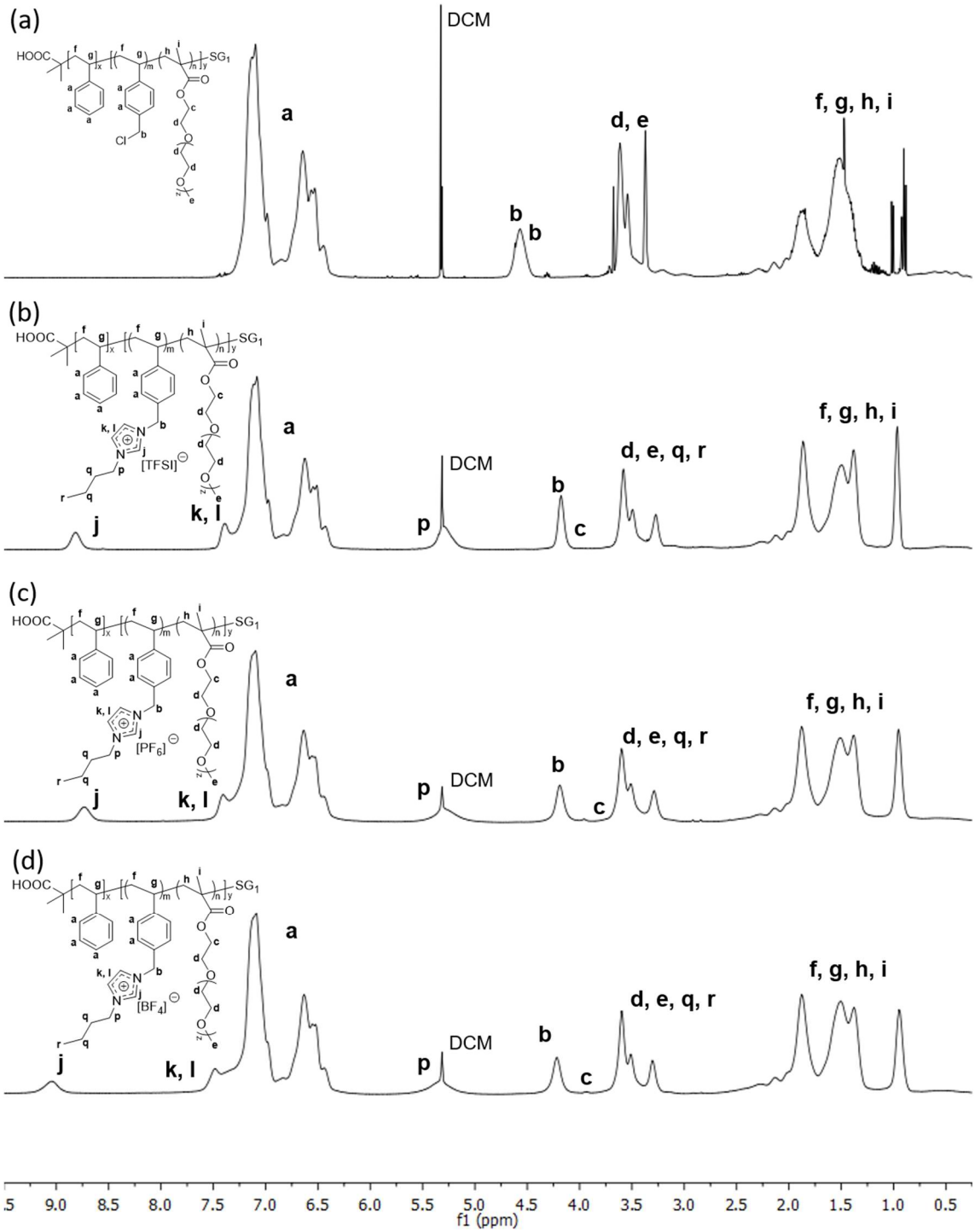

Figure 4.11. ^{1}H NMR spectra of (a) poly(S)-*b*-poly(CMS-*r*-PEGMA) precursor polymer, (b) poly(S)-*b*-poly(VBBI^{+}[X]-*r*-PEGMA)) block copolymers where X = TFSI^{-}, (c) poly(S)-*b*-poly(VBBI^{+}[X]-*r*-PEGMA)) block copolymers where X = PF_6^- anion, and (d) poly(S)-*b*-poly(VBBI^{+}[X]-*r*-PEGMA)) block copolymers where X = BF_4^- anion in $CDCl_2$. All polymers are from experiment CMS/PEGMA-75/25-8g.

Table 4.5. Glass transition, conductivity, and profilometry data for poly(ionic liquid)s. Two capacitor sets of differing thickness were fabricated and characterized for each material.

EXP-ID	$T_{g,1}$	$T_{g,2}$	Conc. [mg/mL]	Thickness [nm]	Conductivity S cm^{-1}	Conc. 2 [mg/mL]	Thickness [nm]	Conductivity [S cm^{-1}]
poly(S) macro.	-	-	60	323 ± 24	-			
P100/0-4g-TFSI	105	12	60	427 ± 44	1.8×10^{-9}	100	1069 ± 107	3.3×10^{-9}
P100/0-4g-PF_6	101	-	60	481 ± 47	3.5×10^{-11}	100	935 ± 44	3.5×10^{-11}
P100/0-4g-BF_4	98	-	60	531 ± 244	-	40	285 ± 35	5.7×10^{-10}
P100/0-8g-TFSI	106	11	60	439 ± 22	1.3×10^{-7}	100	677 ± 68	1.4×10^{-7}
P100/0-8g- PF_6	104	-	60	480 ± 45	6.1×10^{-11}	100	794 ± 40	8.7×10^{-11}
P100/0-8g-BF_4	99	-	60	702 ± 47	7.7×10^{-9}	40	380 ± 13	1.5×10^{-9}
P25/75-2g-TFSI	99	-	60	444 ± 32	-	100	1069 ± 107	-
P25/75-2g-PF_6	99	-	60	416 ± 22	-	100	1138 ± 26	-
P25/75-2g-BF4	99	-	60	887 ± 59	-	100	1069 ± 107	-
P25/75-4g-TFSI	99	-	60	466 ± 32	2.5×10^{-8}	100	967 ± 59	4.6×10^{-8}
P25/75-4g-PF_6	99	-	60	486 ± 36	-	100	1085 ± 77	-
P25/75-4g-BF_4	99	-	60	560 ± 21	-	100	1513 ± 60	-
P25/75-6g-TFSI	99	-	60	399 ± 35	-	100	887 ±75	-
P25/75-6g-PF_6	99	-	60	381 ± 13	-	100	1081 ± 107	-
P25/75-6g-BF_4	99	-	60	401 ± 24	-	100	999 ± 85	-
P50/50-4g-TFSI	106	-7	60	421 ± 60	3.3×10^{-7}	100	756 ± 52	4.7×10^{-7}
P50/50-4g-PF_6	105	21	60	504 ± 57	1.8×10^{-9}	100	972 ± 62	3.0×10^{-9}
P50/50-4g-BF_4	105	17	60	989 ± 49	7.6×10^{-8}	40	262 ± 13	3.4×10^{-8}
P50/50-6g-TFSI	105	-7	60	430 ± 42	3.6×10^{-7}	100	682 ± 19	3.2×10^{-7}
P50/50-6g- PF_6	105	22	60	562 ± 80	4.9×10^{-9}	100	1031 ± 116	3.2×10^{-9}
P50/50-6g-BF_4	106	19	60	747 ± 95	1.4×10^{-7}	40	243 ± 17	1.7×10^{-8}
P75/25-6g-TFSI	107	2	60	382 ± 35	2.0×10^{-7}	100	849 ± 90	2.8×10^{-7}
P75/25-6g-PF_6	106	55	60	497 ± 69	5.9×10^{-11}	100	936 ± 284	5.8×10^{-11}
P75/25-6g-BF_4	105	48	60	847 ± 13	1.9×10^{-8}	40	231 ± 15	5.8×10^{-9}
P75/25-8g-TFSI	105	2	60	408 ± 119	1.4×10^{-7}	100	802 ± 75	1.9×10^{-7}
P75/25-8g-PF_6	105	52	60	591 ± 46	7.9×10^{-11}	100	919 ± 71	3.7×10^{-11}
P75/25-8g-BF_4	103	49	60	871 ± 54	2.0×10^{-8}	40	382 ± 17	4.2×10^{-9}

Table 4.6. OTFT Characterization: ON/OFF, transconductance, threshold voltage, and field-effect mobility for each material.

Gating material[1]	ON/OFF[2]	Transconductance[3] [μSV^{-1}]	Threshold Voltage [V]	Capacitance[4] [Fcm^{-2}]	Mobility[5] [$cm^2V^{-1}s^{-1}$]	S_w [V/dec]	N_{it} [$cm^{-2}V^{-1}$]
$TFSI^-$	10^1	$(4.32 \pm 0.271) \times 10^{-8}$	1.5 ± 0.056	$(1.44 \pm 0.138) \times 10^{-6}$	$(9.0 \pm 1.03) \times 10^{-4}$	0.1	9.7×10^{12}
PF_6^-	10^1	$(5.87 \pm 0.557) \times 10^{-9}$	1.3 ± 0.093	$(1.60 \pm 0.687) \times 10^{-7}$	$(1.1 \pm 0.118) \times 10^{-3}$	0.5	8.3×10^{12}
BF_4^-	10^2	$(4.19 \pm 0.554) \times 10^{-8}$	0.7 ± 0.102	$(1.14 \pm 0.223) \times 10^{-7}$	$(1.1 \pm 0.234) \times 10^{-2}$	0.3	3.4×10^{12}
SiO_2[6]	10^2	-	33.9	1.50E-11	3.0E-2	5.1	8.0×10^{12}

1. All devices were fabricated from either SiO2 (taken from Brixi et al.[1]) or the P50/50-6 [X] material (where [X] = BF_4^-, PF_6^-, or $TFSI^-$)
2. ON/OFF ratios were obtained from the 100 mHz frequency plots
3. Transconductance obtained from the slope on the forward sweep of transfer curves
4. Obtained by EIS of capacitors fabricated with the poly(MMA-r-S)-b-poly(VBBI+[X]-r-PEGMA) (where [X] = BF_4^-, PF_6^-, or $TFSI^-$). Mean of the values summarized in Figure 6B.
5. Determined using device dimensions W/L = 1000µm/30µm
6. Calculated for a 230 nm SiO_2 dielectric thickness with dielectric constant = 3.9 using the equation: $C = \varepsilon\varepsilon_0 A/d$ where C is the capacitance, A is the area, ε is the dielectric constant, and ε_0 is the vacuum permittivity

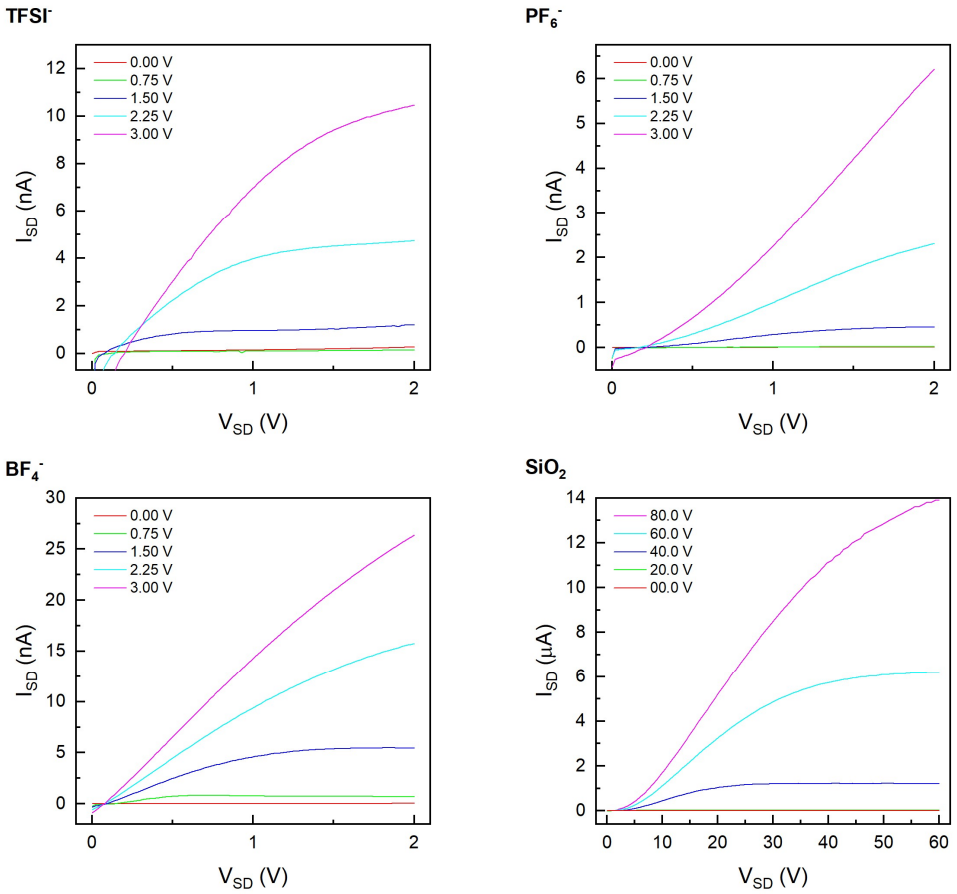

Figure 4.13. Representative output curves for TGTC devices with poly(NDI2OD-T2) n-type semiconductor using PF_6^-, BF_4^-, and $TFSI^-$ dielectrics. The dielectric layers ranged between 375 - 715 nm.

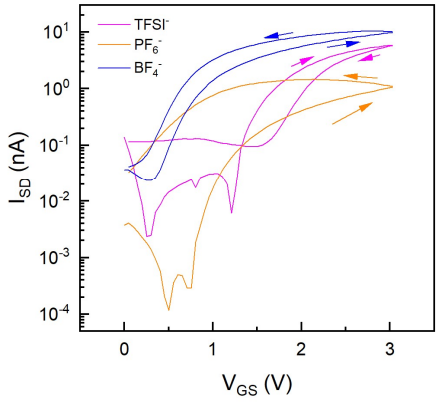

Figure 4.14. Representative transfer characteristics in the linear regime (V_{DS} = 1 V) of poly(S)-*b*-poly(VBBI$^+$[X]-*r*-PEGMA)) block copolymers (where X = $TFSI^-$, PF_6^- or BF_4^-) based OTFTs displayed with logarithmic scaling. The gate voltage was swept linearly at a rate of 250 mV/s. (L = 30 µm, W = 1000 µm)

4.8 References

(1) Saidi, A.; Desfontaines, L.; Champeval, A.; Lebreux, J. D.; Lecomte, C.; Pruneau, M.; Grondein, A.; Izquierdo, R.; Bélanger, D. The Effect of Ink Formulation and Electrode Geometry Design on the Electrochemical Performance of a Printed Alkaline Battery. *Flex. Print. Electron.* **2017,** *2* (1).

(2) Fujimoto, T.; Awaga, K. Electric-Double-Layer Field-Effect Transistors with Ionic Liquids. *Phys. Chem. Chem. Phys.* **2013**, *15* (23), 8983–9006.

(3) Kaake, L. G.; Zou, Y.; Panzer, M. J.; Frisbie, C. D.; Zhu, X. Y. Vibrational Spectroscopy Reveals Electrostatic and Electrochemical Doping in Organic Thin Film Transistors Gated with a Polymer Electrolyte Dielectric. *J. Am. Chem. Soc*. **2007**, *129* (25), 7824–7830.

(4) Yuen, J. D.; Dhoot, A. S.; Namdas, E. B.; Coates, N. E.; Heeney, M.; McCulloch, I.; Moses, D.; Heeger, A. J. Electrochemical Doping in Electrolyte-Gated Polymer Transistors. *J. Am. Chem. Soc*. **2007**, *129* (46), 14367–14371.

(5) Lee, J.; Kaake, L. G.; Cho, H. J.; Zhu, X. Y.; Lodge, T. P.; Frisbie, C. D. Ion Gel-Gated Polymer Thin-Film Transistors: Operating Mechanism and Characterization of Gate Dielectric Capacitance, Switching Speed, and Stability. *J. Phys. Chem. C* **2009**, *113* (20), 8972–8981.

(6) Kim, S. H.; Hong, K.; Xie, W.; Lee, K. H.; Zhang, S.; Lodge, T. P.; Frisbie, C. D. Electrolyte-Gated Transistors for Organic and Printed Electronics. *Adv. Mater.* **2013**, *25* (13), 1822–1846.

(7) Larsson, O.; Laiho, A.; Schmickler, W.; Berggren, M.; Crispin, X. Controlling the Dimensionality of Charge Transport in an Organic Electrochemical Transistor by Capacitive Coupling. *Adv. Mater.* **2011**, *23* (41), 4764–4769.

(8) Weber, R. L.; Ye, Y.; Schmitt, A. L.; Banik, S. M.; Elabd, Y. A.; Mahanthappa, M. K. Effect of Nanoscale Morphology on the Conductivity of Polymerized Ionic Liquid Block Copolymers. *Macromolecules* **2011**, *44* (14), 5727–5735.

(9) Ye, Y.; Choi, J. H.; Winey, K. I.; Elabd, Y. A. Polymerized Ionic Liquid Block and Random Copolymers: Effect of Weak Microphase Separation on Ion Transport. *Macromolecules* **2012**, *45* (17), 7027–7035.

(10) Choi, J. H.; Ye, Y.; Elabd, Y. A.; Winey, K. I. Network Structure and Strong Microphase Separation for High Ion Conductivity in Polymerized Ionic Liquid Block Copolymers. *Macromolecules* **2013**, *46* (13), 5290–5300.

(11) Chen, H.; Choi, J. H.; Cruz, D. S. D. La; Winey, K. I.; Elabd, Y. A. Polymerized Ionic Liquids: The Effect of Random Copolymer Composition on Ion Conduction. *Macromolecules* **2009**, *42* (13), 4809–4816.

(12) Hu, H.; Yuan, W.; Lu, L.; Zhao, H.; Jia, Z.; Baker, G. L.; Yuan, W. Low Glass Transition Temperature Polymer Electrolyte Prepared From Ionic Liquid Grafted Polyethylene Oxide. *J. Polym. Sci., Part A Polym. Chem* **2014**, *52*, 2104–2110.

(13) Wang, S. W.; Liu, W.; Colby, R. H. Counterion Dynamics in Polyurethane-Carboxylate Ionomers with Ionic Liquid Counterions. *Chem. Mater.* **2011***, 23* (7), 1862–1873.

(14) Snyder, J. F.; Carter, R. H.; Wetzel, E. D. Electrochemical and Mechanical Behavior in Mechanically Robust Solid Polymer Electrolytes for Use in Multifunctional Structural Batteries. *Chem. Mater.* **2007**, *19* (15), 3793–3801

(15) Peltekoff, A.; Hiller, V. E.; Lopinski, G. P.; Melville, O. A.; Lessard, B. H. Unipolar Polymerized Ionic Liquid Copolymers as High Capacitance Electrolyte Gates for N-Type Transistors. *ACS Appl. Polym. Mater.* **2019**.

(16) Lessard, B. H. Novel Materials : From Nanoporous Materials To. In *Nitroxide Mediated Polymerization: From Fundamentals To Applications in Materials Science*; **2015**; pp 441–493.

(17) Lessard, B. H.; Sampson, K. L.; Plint, T.; Bender, T. P. Boron Subphthalocyanine Polymers: Avoiding the Small Molecule Side Product and Exploring Their Use in Organic Light-Emitting Diodes. *J. Polym. Sci. Part A Polym. Chem.* **2015**, *53* (17), 1996–2006.

(18) Lessard, B. H.; Beouch, L.; Goubard, F.; Wantz, G.; Maric, M.; Gigmes, D.; Dumur, F. Poly(2-(N-Carbazolyl)Ethyl Acrylate) as a Host for High Efficiency Polymer Light-Emitting Devices. *Org. Electron.* **2015**, *17* (January), 377–385.

(19) Lamontagne, H. R.; Lessard, B. H. Nitroxide-Mediated Polymerization: A Versatile Tool for the Engineering of Next Generation Materials. *ACS Appl. Polym. Mater*. **2020**, *2* (12), 5327–5344.

(20) Lessard, B.; Tervo, C.; De Wahl, S.; Clerveaux, F. J.; Tang, K. K.; Yasmine, S.; Andjelić, S.; D'Alessandro, A.; Marić, M. Poly(Tert-Butyl Methacrylate/Styrene) Macroinitiators as Precursors for Organo- And Water-Soluble Functional Copolymers Using Nitroxide-Mediated Controlled Radical Polymerization. *Macromolecules* **2010**, *43* (2), 868–878.

(21) Lessard, B.; Marić, M. Effect of Acrylic Acid Neutralization on 'Livingness' of Poly[Styrene- Ran -(Acrylic Acid)] Macro-Initiators for Nitroxide-Mediated Polymerization of Styrene. *Polym. Int.* **2008**, *57* (10), 1141–1151.

(22) Mchale, R.; Aldabbagh, F.; Zetterlund, P. B. The Role of Excess Nitroxide in the SG1 (N-Tert-Butyl-N-[1-Diethylphosphono-(2,2-Dimethylpropyl)] Nitroxide)-Mediated Polymerization of Methyl Methacrylate. *J. Polym. Sci. Part A Polym. Chem.* **2007**, *45* (11), 2194–2203.

(23) Lessard, B.; Marić, M. Incorporating Glycidyl Methacrylate into Block Copolymers Using Poly(Methacrylate- Ran -Styrene) Macroinitiators Synthesized by Nitroxide-Mediated Polymerization. *J. Polym. Sci. Part A Polym. Chem.* **2009**, *47* (10), 2574–2588.

(24) Lessard, B. H.; Ling, E. J. Y.; Marić, M. Fluorescent, Thermoresponsive Oligo(Ethylene Glycol) Methacrylate/9-(4- Vinylbenzyl)-9H-Carbazole Copolymers Designed with Multiple Lcsts via Nitroxide Mediated Controlled Radical Polymerization. *Macromolecules* **2012**, *45* (4), 1879–1891.

(25) Peltekoff, A. J. A. J.; Therrien, I.; Lessard, B. H. B. H. B. H. Nitroxide Mediated Polymerization of 1-(4-Vinylbenzyl)-3-Butylimidazolium Ionic Liquid Containing

Homopolymers and Methyl Methacrylate Copolymers. *Can. J. Chem. Eng.* **2019**, *97* (1), 5–16.

(26) Lessard, B. H.; Guillaneuf, Y.; Mathew, M.; Liang, K.; Clement, J. L.; Gigmes, D.; Hutchinson, R. A.; Marić, M. Understanding the Controlled Polymerization of Methyl Methacrylate with Low Concentrations of 9-(4-Vinylbenzyl)-9 H -Carbazole Comonomer by Nitroxide-Mediated Polymerization: The Pivotal Role of Reactivity Ratios. *Macromolecules* **2013**, *46* (3), 805–813.

(27) Qian, W.; Texter, J.; Yan, F. Frontiers in Poly(Ionic Liquid)s: Syntheses and Applications. *Chem. Soc. Rev.* **2017**, *46* (4), 1124–1159.

(28) Parizel, N.; Lauprêtre, F.; Monnerie, L. N.m.r. and d.s.c. Investigations of the Miscibility of Poly(Methyl Methacrylate)/ Poly(Ethylene Oxide) Blends. *Polymer (Guildf)*. **1997**, *38* (15), 3719–3725.

(29) Lamperski, S.; Outhwaite, C. W.; Bhuiyan, L. B. The Electric Double-Layer Differential Capacitance at and near Zero Surface Charge for a Restricted Primitive Model Electrolyte. *J. Phys. Chem. B* **2009**, *113* (26), 8925–8929.

(30) Zhang, X.; Harris, K. D.; Wu, N. L. Y.; Murphy, J. N.; Buriak, J. M. Fast Assembly of Ordered Block Copolymer Nanostructures through Microwave Annealing. *ACS Nano* **2010**, *4* (11), 7021–7029.

(31) Choi, J. H.; Ye, Y.; Elabd, Y. A.; Winey, K. I. Network Structure and Strong Microphase Separation for High Ion Conductivity in Polymerized Ionic Liquid Block Copolymers. *Macromolecules* **2013**, *46* (13), 5290–5300.

(32) Ohno, H.; Yoshizawa, M.; Ogihara, W. Development of New Class of Ion Conductive Polymers Based on Ionic Liquids. *Electrochim. Acta* **2004**, *50* (2-3 SPEC. ISS.), 255–261.

(33) Xu, W.; Cooper, E. I.; Angell, C. A. Ionic Liquids: Ion Mobilities, Glass Temperatures, and Fragilities. *J. Phys. Chem. B* **2003**, *107* (25), 6170–6178.

(34) Abbott, A. P.; Harris, R. C.; Ryder, K. S. Application of Hole Theory to Define Ionic Liquids by Their Transport Properties. *J. Phys. Chem. B* **2007**, *111* (18), 4910–4913.

(35) Nilsson-Hallén, J.; Ahlström, B.; Marczewski, M.; Johansson, P. Ionic Liquids: A Simple Model to Predict Ion Conductivity Based on DFT Derived Physical Parameters. *Front. Chem.* **2019**, *7* (MAR), 1–6.

(36) Mapesa, E. U.; Chen, M.; Heres, M. F.; Harris, M. A.; Kinsey, T.; Wang, Y.; Long, T. E.; Lokitz, B. S.; Sangoro, J. R. Charge Transport in Imidazolium-Based Homo- and Triblock Poly(Ionic Liquid)S. *Macromolecules* **2019**, *52* (2), 620–628.

(37) Kuray, P.; Noda, T.; Matsumoto, A.; Iacob, C.; Inoue, T.; Hickner, M. A.; Runt, J. Ion Transport in Pendant and Backbone Polymerized Ionic Liquids. *Macromolecules* **2019**, *52* (17), 6438–6448.

(38) Choi, U. H.; Price, T. L.; Schoonover, D. V.; Xie, R.; Gibson, H. W.; Colby, R. H. Role of Chain Polarity on Ion and Polymer Dynamics: Molecular Volume-Based Analysis of the Dielectric Constant for Polymerized Norbornene-Based Ionic Liquids. *Macromolecules* **2020**, *53* (23), 10561–10573.

(39) Juger, J.; Meyer, F.; Vidal, F.; Chevrot, C.; Teyssié, D. Synthesis, Polymerization and Conducting Properties of an Ionic Liquid-Type Anionic Monomer. *Tetrahedron Lett*. **2009**, *50* (1), 128–131.

(40) Geng, Z.; Schauser, N. S.; Schauser, N. S.; Lee, J.; Lee, J.; Schmeller, R. P.; Barbon, S. M.; Segalman, R. A.; Segalman, R. A.; Segalman, R. A.; et al. Role of Side-Chain Architecture in Poly(Ethylene Oxide)-Based Copolymers. *Macromolecules* **2020**, *53* (12), 4960–4967.

(41) Ikeda, T.; Moriyama, S.; Kim, J. Imidazolium-Based Poly(Ionic Liquid)s with Poly(Ethylene Oxide) Main Chains: Effects of Spacer and Tail Structures on Ionic Conductivity. *J. Polym. Sci. Part A Polym. Chem.* **2016**, *54* (18), 2896–2906.

(42) Chen, M.; Dugger, J. W.; Li, X.; Wang, Y.; Kumar, R.; Meek, K. M.; Uhrig, D. W.; Browning, J. F.; Madsen, L. A.; Long, T. E.; et al. Polymerized Ionic Liquids: Effects of Counter-Anions on Ion Conduction and Polymerization Kinetics. *J. Polym. Sci. Part A Polym. Chem.* **2018**, *56* (13), 1346–1357.

(43) Keith, J. R.; Rebello, N. J.; Cowen, B. J.; Ganesan, V. Influence of Counterion Structure on Conductivity of Polymerized Ionic Liquids. *ACS Macro Lett.* **2019**, *8* (4), 387–392.

(44) Oldham, K. B. A Gouy-Chapman-Stern Model of the Double Layer at a (Metal)/(Ionic Liquid) Interface. *J. Electroanal. Chem.* **2008**, *613* (2), 131–138.

(45) Islam, M. M.; Alam, M. T.; Ohsaka, T. Electrical Double-Layer Structure in Ionic Liquids: A Corroboration of the Theoretical Model by Experimental Results. *J. Phys. Chem. C* **2008**, *112* (42), 16568–16574.

(46) Choi, U. H.; Mittal, A.; Price, T. L.; Gibson, H. W.; Runt, J.; Colby, R. H. Polymerized Ionic Liquids with Enhanced Static Dielectric Constants. *Macromolecules* **2013**, *46* (3), 1175–1186.

(47) Fujimoto, T.; Matsushita, M. M.; Awaga, K. Ionic-Liquid Component Dependence of Carrier Injection and Mobility for Electric-Double-Layer Organic Thin-Film Transistors. *J. Phys. Chem. C* **2012**, *116* (8), 5240–5245.

(48) Chan, C. H.; Kammer, H. W. Impedance Spectra of Polymer Electrolytes. *Ionics (Kiel)*. **2017**, *23* (9), 2327–2337.

(49) Chan, C. H.; Kammer, H. W. Low Frequency Dielectric Relaxation and Conductance of Solid Polymer Electrolytes with PEO and Blends of PEO and PMMA. *Polymers (Basel)*. **2020**, *12* (5).

(50) Niskanen, J.; Tousignant, M. N.; Peltekoff, A. J.; Lessard, B. H. 1,2,3-Triazole Based Poly(Ionic Liquids) as Solid Dielectric Materials. *Polymer (Guildf)*. **2021**, *212*, 123144.

(51) Xu, K.; Fullerton-Shirey, S. K. Electric-Double-Layer-Gated Transistors Based on Two-Dimensional Crystals: Recent Approaches and Advances. *J. Phys. Mater.* **2020**, *3* (3), 032001.

(52) Xu, K.; Liang, J.; Woeppel, A.; Bostian, M. E.; Ding, H.; Chao, Z.; McKone, J. R.; Beckman, E. J.; Fullerton-Shirey, S. K. Electric Double-Layer Gating of Two-Dimensional Field-Effect Transistors Using a Single-Ion Conductor. *ACS Appl. Mater. Interfaces* **2019**, *11* (39), 35879–35887.

(53) Woeppel, A.; Xu, K.; Kozhakhmetov, A.; Awate, S.; Robinson, J. A.; Fullerton-Shirey, S. K. Single- versus Dual-Ion Conductors for Electric Double Layer Gating: Finite Element Modeling and Hall-Effect Measurements. *ACS Appl. Mater. Interfaces* **2020**, *12* (36), 40850–40858.

(54) Yan, H.; Chen, Z.; Zheng, Y.; Newman, C.; Quinn, J. R.; Dötz, F.; Kastler, M.; Facchetti, A. A High-Mobility Electron-Transporting Polymer for Printed Transistors. *Nature* **2009**, *457* (7230), 679–686.

(55) Serghei, A.; Tress, M.; Sangoro, J. R.; Kremer, F. Electrode Polarization and Charge Transport at Solid Interfaces. *Phys. Rev. B - Condens. Matter Mater. Phys.* **2009**, *80* (18), 1–5.

(56) Sokolov, A. N.; Tee, B. C. K.; Bettinger, C. J.; Tok, J. B. H.; Bao, Z. Chemical and Engineering Approaches to Enable Organic Field-Effect Transistors for Electronic Skin Applications. *Acc. Chem. Res.* **2012**, *45* (3), 361–371.

(57) Krause, C.; Sangoro, J. R.; Iacob, C.; Kremer, F. Charge Transport and Dipolar Relaxations in Imidazolium-Based Ionic Liquids. *J. Phys. Chem. B* **2010**, *114* (1), 382–386.

(58) Bürgi, L.; Richards, T. J.; Friend, R. H.; Sirringhaus, H. Close Look at Charge Carrier Injection in Polymer Field-Effect Transistors. *J. Appl. Phys.* **2003**, *94* (9), 6129–6137.

(59) Choi, J. H.; Xie, W.; Gu, Y.; Frisbie, C. D.; Lodge, T. P. Single Ion Conducting, Polymerized Ionic Liquid Triblock Copolymer Films: High Capacitance Electrolyte Gates for N-Type Transistors. *ACS Appl. Mater. Interfaces* **2015**, *7* (13), 7294–7302.

(60) Kim, S. H.; Nam, S.; Jang, J.; Hong, K.; Yang, C.; Chung, D. S.; Park, C. E.; Choi, W. S. Effect of the Hydrophobicity and Thickness of Polymer Gate Dielectrics on the Hysteresis Behavior of Pentacene-Based Field-Effect Transistors. *J. Appl. Phys.* **2009**, *105* (10).

(61) Gu, G.; Kane, M. G. Moisture Induced Electron Traps and Hysteresis in Pentacene-Based Organic Thin-Film Transistors. *Appl. Phys. Lett.* **2008**, *92* (5), 2006–2009.

(62) Noh, Y. H.; Young Park, S.; Seo, S. M.; Lee, H. H. Root Cause of Hysteresis in Organic Thin Film Transistor with Polymer Dielectric. *Org. Electron.* **2006**, *7* (5), 271–275.

(63) Brixi, S.; Melville, O. A.; Mirka, B.; He, Y.; Hendsbee, A. D.; Meng, H.; Li, Y.; Lessard, B. H. Air and Temperature Sensitivity of N-Type Polymer Materials to Meet and Exceed the Standard of N2200. *Sci. Rep.* **2020**, *10* (1), 1–10.

(64) Hulea, I. N.; Fratini, S.; Xie, H.; Mulder, C. L.; Iossad, N. N.; Rastelli, G.; Ciuchi, S.; Morpurgo, A. F. Tunable Fröhlich Polarons in Organic Single-Crystal Transistors. *Nat. Mater.* **2006**, *5* (12), 982–986.

(65) Fratinil, S.; Xie, H.; Hulea, I. N.; Ciuchi, S.; Morpurgo, A. F. Current Saturation and Coulomb Interactions in Organic Single-Crystal Transistors. *New J. Phys.* **2008**, *10*.

(66) Veres, J.; Ogier, S. D.; Leeming, S. W.; Cupertino, D. C.; Khaffaf, S. M. Low-k Insulators as the Choice of Dielectrics in Organic Field-Effect Transistors. *Adv. Funct. Mater.* **2003**, *13* (3), 199–204.

(67) Dickey, K. C.; Subramanian, S.; Anthony, J. E.; Han, L. H.; Chen, S.; Loo, Y. L. Large-Area Patterning of a Solution-Processable Organic Semiconductor to Reduce Parasitic Leakage and off Currents in Thin-Film Transistors. *Appl. Phys. Lett.* **2007**, *90* (24), 1–4.

(68) Tang, W.; Feng, L.; Jiang, C.; Yao, G.; Zhao, J.; Cui, Q.; Guo, X. Controlling the Surface Wettability of the Polymer Dielectric for Improved Resolution of Inkjet-Printed Electrodes and Patterned Channel Regions in Low-Voltage Solution-Processed Organic Thin Film Transistors. *J. Mater. Chem. C* **2014**, *2* (28), 5553–5558.

(69) Hlalele, L.; Klumperman, B. In Situ Nmr and Modeling Studies of Nitroxide Mediated Copolymerization of Styrene and n -Butyl Acrylate. *Macromolecules* **2011**, *44* (17), 6683–6690.

Chapter 5: Overall Conclusions and Recommendations for Future Work

5.1 Overall Conclusions

Alleviating organic thin-film transistor manufacturability concerns continues to be a necessity towards bringing these technologies to commercialization. Developing novel polyelectrolyte dielectric materials to improve the manufacturability of the gating layers is starting to seem like a viable solution as shown; highly responsive devices can be fabricated; however, higher output currents are desired.

Chapter 2 explored the synthetic groundwork utilized to produce the materials in the remaining chapters. I showed that ionic liquid polymers could be obtained by nitroxide mediated polymerization by various routes resulting in low dispersity and highly living polymers. I identified the most desirable route to was to take a post-polymerization functionalization approach due to the ease of purification and compatibility with GPC.

Chapter 3 was our groups first demonstration of polyelectrolyte gated transistors. The performance of these transistors were comparable to devices of other groups with similar dielectrics and semiconductor. However, they exhibited high degrees of contact resistance, which we hypothesized could possibly be improved by changing the device architecture and contact electrode material. From a materials perspective, it was shown that the content of ionic liquid moieties in the final polymer was not proportional to the double-layer capacitance. Additionally, we saw the polymeric structure (block vs. random) influenced important properties such as conductivity. These findings were instrumental in designing the study presented in Chapter 4.

Chapter 4 built off of the findings of Chapter 3; Further polymer-structure to material-property to device-performance relations were improved. Ultimately, both the materials and devices were improved; final materials had a higher conductivity and the devices had reduced contact resistance. I showed the structure-property relationships to improve the conductivity of the ionic gating medium; most notably the need for self-assembly to form ionically conductive channels and the dependence on T_g of the conductive block. I showed the T_g can be easily tuned by the copolymer composition of the second block using a low-T_g monomer copolymerized with

the ionic liquid comonomer. Additionally, I showed the EDL capacitance was most related to the mobile anion of the material, however, this did not translate to higher output currents in our devices as one would have thought.

Overall, this thesis is entirely focused on the development of novel polyelectrolyte materials to be employed as the gating medium in organic thin-film transistors. A question raised in the introduction, whether device performance in regard to switching speeds and field-effect mobility can be further improved by developing polyelectrolytes of higher conductivity was explored. My research ultimately demonstrated that the sluggish response times of polyelectrolyte gated transistors can be improved by increasing the ionic conductivity of the polyelectrolyte material.

5.2 Recommendations for Future Work

I recommend a target application be selected to determine what transistor response times are required in order to direct whether the response times shown in this work are satisfactory or if work towards higher conductivity materials is needed. If slightly higher conductivities are required some work implementing a spacer for higher conductivity may be useful as well as selecting a lower T_g comonomer than PEGMA.

In addition to material conductivity-device response time relationships, I had also attempted to begin the work to further the understanding of the other critical component for dielectrics; the double layer capacitance produced at the semiconductor polyelectrolyte backbone interface that drives the device. A fundamental gap in understanding from my completed research are the specific reasons the device output currents differ so drastically for different mobile anions. In isolated metal-polyelectrolyte-metal experiments I showed the mobile anion (material structure) was the critical component that impacted the capacitance (material property). However, this did not directly translate to OTFT performance; the material with the lowest capacitance seen in capacitors produced devices with the highest output currents. I recommend that this line of research examining the dielectric/semiconductor interface with ionic dielectrics continue to be explored. Further measurement techniques such as Hall measurements may elucidate the reasons behind this discrepancy.

The driving motivation of this thesis was to alleviate solution processed thin-film transistor manufacturing and scalability concerns by molecular design. Keeping with the strong desire to bring these technologies to market we can also scrutinize the viability of the synthetic chemistry in an industrial setting. The limited availability (or unavailability) of BlocBuilder due to its sole supplier ultimately adds significant supply chain risk and will ultimately require the chemistry to be re-tooled to other controlled free radical techniques if there is a desire to utilize a candidate material into a commercial product. Despite the many advantages NMP has to offer over other CRP techniques, the limited availability of its key components makes it undesirable. I recommend future polymer work in the group utilize other controlled free radical polymerization techniques where the critical components can be acquired from a multitude of vendors. I also recommend the scalability of chemistry & purification techniques continue to be a high priority and not side-lined in the purely academic pursuit of structure property relationships.

Chapter 6: Additional Contributions

6.1 Controlled Synthesis of Poly(pentafluorostyrene-ran-methyl methacrylate) Copolymers by Nitroxide Mediated Polymerization and Their Use as Dielectric Layers in Organic Thin-Film Transistors

Alexander J. Peltekoff, Mathieu N. Tousignant, Victoria E. Hiller, Owen A. Melville, Benoît H. Lessard

MDPI Polymers

Published: May 29, 2020

DOI: 10.3390/polym12061231

Abstract

A library of statistically random pentafluorostyrene (PFS) and methyl methacrylate (MMA) copolymers with narrow molecular weight distributions were produced using nitroxide mediated polymerization (NMP) to study the effect of polymer composition on the performance of bottom-gate top-contact organic thin-film transistors when utilized as the dielectric medium. Contact angle measurements confirmed the ability to tune the surface properties of copolymer thin films through variation of its PFS/MMA composition, while impedance spectroscopy determined the effect of this variation on dielectric properties. Bottom-gate, top-contact copper phthalocyanine (CuPc) based organic thin-film transistors were fabricated using the random copolymers as a dielectric layer. We found that increasing the PFS content led to increased field-effect mobility until a point after which the CuPc no longer adhered to the polymer dielectric.

Contributions

I designed the study and oversaw the experiments performed by Victoria (polymer synthesis) and Mathieu (device fabrication). I performed the data analysis for all experiments and wrote the manuscript.

6.2 Improving Polyvinyl Alcohol (PVA) Thin Film Properties Through the Addition of Low Weight Percentages of Cellulose Nanocrystals

Mathieu N. Tousignant, Nicole A. Rice, Alexander Peltekoff, Chithiravel Sundaresan, Chuanwei Miao, Wadood Y. Hamad, Benoît H. Lessard

Langmuir 36, 13, 3550-3557

Published: March 12, 2020

DOI: 10.1021/acs.langmuir.0c00068

Abstract

The increased demand for electronic devices, combined with a desire to minimize the environmental impact, necessitates the development of new eco-friendly materials. One promising approach is the incorporation of renewable and green materials that possess the desired mechanical and electrical properties while allowing for more ecologically friendly disposal of these devices. The addition of low-weight percentages (0.25–0.75 wt %) of cellulose nanocrystals (CNCs) was investigated as an environmentally friendly additive in aqueous dispersions of poly(vinyl alcohol) (PVA). It was found that these low CNC loadings were sufficient to induce a favorable increase in viscosity, which in turn dramatically enhanced the film quality of the PVA blends through an improvement in the critical radius of the spun film, overall film thickness, and homogeneity of the thin film. This corresponded to an increase in the number of functioning organic electronic devices that could be fabricated by spin coating, including metal–insulator–metal (MIM) capacitors and organic thin-film transistors (OTFTs). Most importantly, the incorporation of CNCs into PVA did not significantly alter the native dielectric properties of the polymer thin films when incorporated into both MIM capacitors and OTFTs.

Contributions

I developed the procedure to fabricate and test MIM capacitor and coached Mathieu through the process and aided in the impedance data analysis.

6.3 Contact Engineering using Manganese, Chromium and Bathocuproine in Group 14 Phthalocyanine Organic Thin-Film Transistors

Owen A. Melville, Trevor M. Grant, Kate Lochhead, Benjamin King, Ryan Ambrose, Nicole A. Rice, Nicholas T. Boileau, Alexander J. Peltekoff, Mathieu Tousignant, Ian G. Hill, Benoît H. Lessard

ACS Applied Electronic Materials

Published: March 24, 2020

DOI: 10.1021/acsaelm.0c00104

Abstract

Silicon and tin(IV) phthalocyanines, which have been demonstrated as simple-to-synthesize materials for n-type organic thin-film transistors (OTFTs), have relatively shallow lowest unoccupied molecular orbital (LUMO) levels that create a Schottky barrier with the gold source–drain contacts typically used in device fabrication. To reduce the contact resistance (RC) associated with this barrier and improve the OTFT performance, we fabricated bottom-gate top-contact (BGTC) devices using low-work-function metals (Mn/Cr) and an electron dopant material (bathocuproine, BCP) as contact interlayers. We characterized two tin phthalocyanines (SnPcs), tin bis(pentafluorophenoxy)phthalocyanine (F_{10}-SnPc) and tin bis(2,4,6-trifluorophenoxy)phthalocyanine (246F-SnPc), as organic semiconductors (OSCs) and compared them to their silicon phthalocyanine (SiPc) analogues. We found that using Mn and Cr interlayers with SiPc OTFTs reduces RC to as low as 11.8 kΩ cm and reduces the threshold voltage (V_T) to as low as 7.8 V while improving linear region characteristics compared to devices using silver or gold electrodes only. BCP interlayers appear to reduce V_T in all SiPc and SnPc devices and increase the off-state conductivity of SnPc devices if covering the entire OSC. Overall, this work demonstrates the potential for metal interlayers and solid-state organic interlayers for improving electron transport in low-cost, n-type OTFTs using group 14 phthalocyanines.

Contributions

I aided in the troubleshooting using the impedance tester I built associated with the study.

6.4 1,2,3-triazole based poly(ionic liquids) as solid dielectric materials

Jukka Niskanen, Mathieu Tousignant, Alexander J. Peltekoff, Benoît H. Lessard

Elsevier Polymer

Published: October 15, 2020

DOI: 10.1016/j.polymer.2020.123144

Abstract

1,2,3-triazole based polyionic liquids (PIL) are an emerging field among polymeric dielectrics in organic electronics. 1,2,3-triazole based PILs can be obtained from poly(4-vinylbenzylchloride) by copper-catalyzed azide-alkyne cycloaddition (CuAAC) 'click' reaction. The polymer architecture and the charge of the PILs can be manipulated by choosing a suitable alkyne, azide containing moiety, and by the alkylation of the 1,2,3-triazole group. Thus, we were able to prepare PILs carrying either inorganic (Na^+ or Cl^-) or the organic counterions 1-butyl-3-methyl-imidazolium ($C4mim^+$) or 1-butyl-3-methyl-imidazolium ($TFSI^-$). Metal-insulator-metal capacitors were fabricated and the dielectric properties were characterized through electrochemical impedance spectroscopy. The PILs demonstrated an increase in capacitance density with decreasing frequency, characteristic for the polarization of the polymer layer and electrical double layer formation. Substitution of inorganic counterions with organic counterions improved the transition frequency of the capacitors and the conductivity of the polymers. This was due to increased ion mobility and decreased glass transition temperatures.

Contributions

I aided in the analysis and interpretation of the impedance data from the polyelectrolyte capacitors and contributed to the associated parts of the manuscript.

6.5 Cyanophenoxy-Substituted Silicon Phthalocyanines for Low Threshold Voltage n-Type Organic Thin-Film Transistors

Benjamin King, Andrew J Daszczynski, Nicole A Rice, Alexander J Peltekoff, Nathan J Yutronkie, Benoît H Lessard, Jaclyn L Brusso

ACS Applied Electronic Materials

Published: May 13, 2021

DOI: 10.1021/acsaelm.1c00175

Abstract

Silicon phthalocyanines (SiPcs) based organic thin-film transistors (OTFTs) typically have threshold voltages (V_T) above 10 V, limiting their usage in commercial devices due to exceedingly high power consumption. Herein, we report the synthesis and characterization of three SiPcs with phenoxy axial substituents containing nitrile and fluorine functional groups. These SiPcs, along with 3,5-difluorophenoxy SiPc were evaluated as candidate materials for n-type OTFTs. We found that further increasing the electron-withdrawing character of the pendant phenoxy groups of the SiPc resulted in a significant decrease in average V_T with the lowest reported value being 4.8 V, the lowest V_T reported for a phenoxy-SiPc-based OTFT exceeding the previous record low of 7.8 V attributed to F10-SiPc. Furthermore, it was noted that dewetting occurred when the phenoxy pendant group of the SiPc was substituted at the para position with a nitrile group combined with ortho- or meta-substituted fluorines, which was attributed to interactions at the semiconductor/dielectric interface. Depositing these SiPcs on silane-terminated poly(styrene) brush modified substrates improved long-term stability, demonstrated by a minimal change in surface morphology according to atomic force microscopy (AFM) images.

Contributions

I synthesized and characterized poly(styrene) and poly(methyl methacrylate) polymers with NHS-functional end groups by nitroxide-mediated polymerization which were used and grafted polymer brush layers in the OTFT devices.

6.5 Enthalpy of the Complexation in Electrolyte Solutions of Polycation and Polyzwitterions of Different Structures and Topologies

Jukka Niskanen, Alexander J. Peltekoff, Jean-Richard Bullet, Benoît H. Lessard, Francoise M. Winnik

ACS Applied Electronic Materials

Published: May 13, 2021

DOI: 10.1021/acs.macromol.1c00586

Abstract

Our understanding of the intricate complexation behavior of polyzwitterions with polycations is less than that of polyanion−polycation complexes. In addition, the effect of the topology of polyzwitterions on the complexation of polyzwitterions with polycations is also unclear. We investigated the complexation of methacrylate-based linear, star, and branched poly(sulfobetaine methacrylate)s (PB) with the cationic poly(methacryl oxyethyl trimethylammonium chloride) (PMOTAC), as well as the complexation of linear imidazolium-based polyzwitterions and polycations, by isothermal titration calorimetry (ITC) in saline media. The complexation enthalpies increased with increasing salt concentration and molecular weight up to 0.25 M NaCl. A low degree of branching had little effect on the complexation, whereas highly branched PB did not form complexes. The obtained complexes had nonstoichiometric composition, with high enthalpies per mole of injected polycation due to additional water being released by cascading complexation. Understanding the complexation behavior of polyzwitterions with polycations provides alternatives to traditional polyanion−polycation complexes.

Contributions

I synthesized and characterized the poly(VBIm) polymer which was used at the precursor material to form the final zwitterionic polymer featured in the study.